

LOUGHBOROUGH
UNIVERSITY OF TECHNOLOGY
LIBRARY

AUTHOR

TUMINELLO W H

COPY NO.

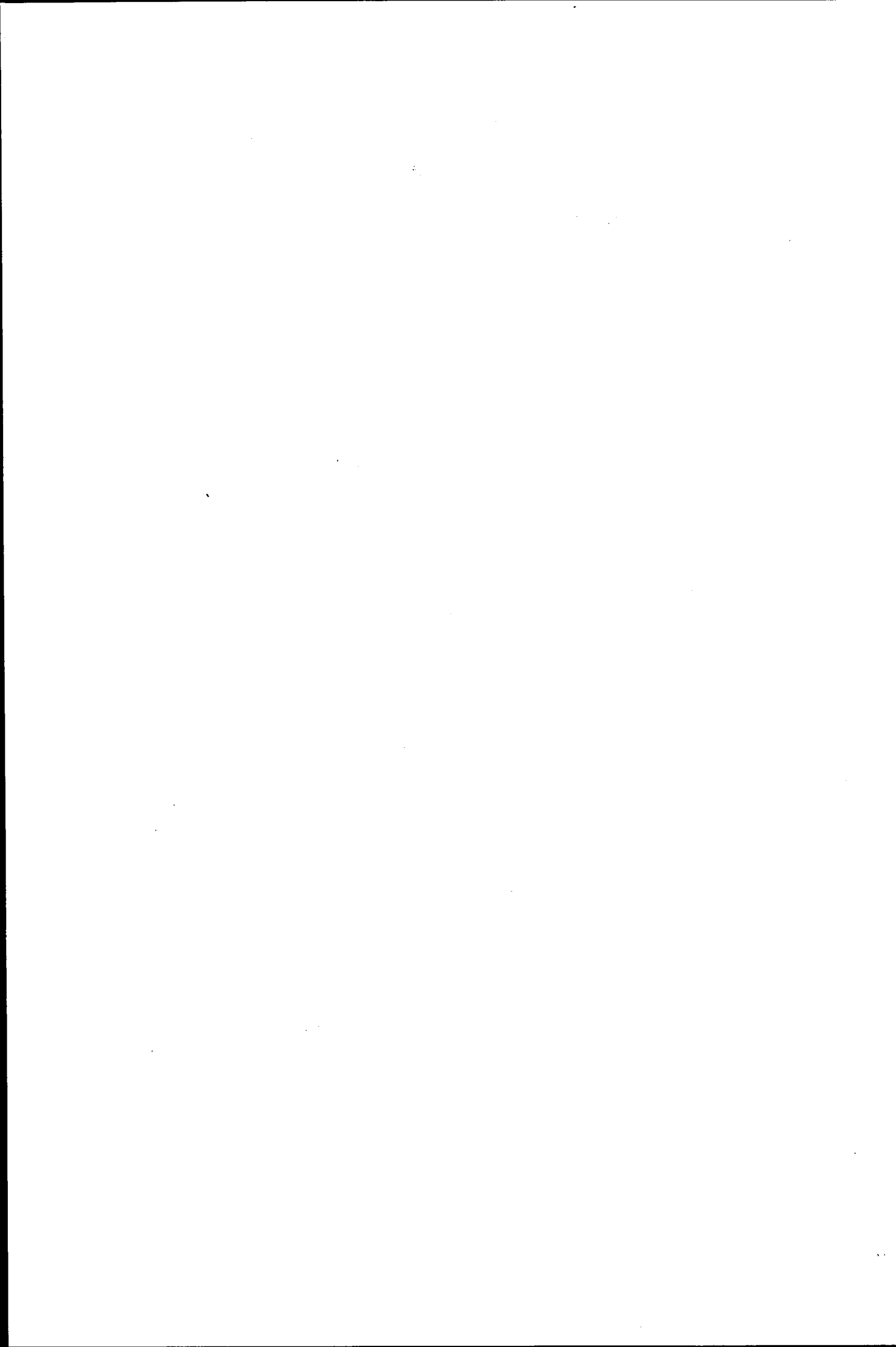
001895/01

VOL NO.

CLASS MARK

ARCHIVES COPY

FOR REFERENCE ONLY



STRUCTURE - PROPERTY RELATIONSHIPS IN
SOME THERMOPLASTIC RUBBERS

by

W. H. TUMINELLO

Supervisor:

DR. R. E. WETTON

Submitted for the Degree of Doctor of Philosophy
of Loughborough University of Technology

September, 1973

Department of Chemistry

© by William Howard Tuminello, 1973

Loughborough University of Technology Library	
Date	18 DEC 1973
Class	
Acc. No.	001895/01

ACKNOWLEDGEMENTS

The author wishes to express his gratitude to Dr. R. E. Wetton for supervising this work and for his help and encouragement throughout and the U. S. government for awarding an educational stipend for this period of study.

The author also wishes to thank: Dr. D. S. Brown for his valuable assistance in interpreting x-ray data, Dr. J. V. Dawkins for many helpful suggestions, Mr. John Greenfield and Mr. Alan Stevens for their technical assistance in assembling various pieces of apparatus, and most of all my wife, Priscilla, for typing this manuscript and her constant encouragement throughout.

ORIGINALITY

All the work presented in this thesis has been carried out by the author, except where otherwise acknowledged and has not previously been presented for a degree at this University or any other institution.

CONTENTS

<u>CHAPTER 1. INTRODUCTION.</u>	<u>Page.</u>
1.1 Thermoplastic Rubbers - General Survey	1
1.2 Structural Parameters for Thermoplastic Rubbers	5
1.3 Introduction to the Present Work	6
 <u>CHAPTER 2. THEORETICAL BACKGROUND</u>	
2.1 Elasticity of Rubber Networks	8
2.2 Viscoelastic Behaviour and Definition of Terms	10
2.3 Phenomenological Concepts of Viscoelasticity	15
2.4 Molecular Interpretation of Viscoelastic Behaviour	18
2.5 Time - Temperature Superposition Principle	21
2.6 Phase Separation and Transitions in Two - Phase Systems	23
2.7 Mechanical Models For Two - Phase Systems	32
2.8 Orientation in Block Copolymers	36
2.9 Small Angle X-ray Scattering (SAXS) in Polymers	38
 <u>CHAPTER 3. EXPERIMENTAL</u>	
3.1 Details of the Polymers Measured	45
3.2 Wide Frequency Scanning Dynamic Mechanical Apparatus	48

3.3	Torsion Pendulum	61
3.4	Differential Scanning Calorimetry (DSC)	68
3.5	Small Angle X-ray Scattering (SAXS)	71

CHAPTER 4. RESULTS

4.A	Hydrogenated Polymers	
4.A.1	Dynamic Mechanical Measurements	74
4.A.2	Differential Scanning Calorimetry	75
4.A.3	Small Angle X-ray Scattering	77
4.B	Siloxane Block Copolymers	
4.B.1	Small Angle X-ray Scattering	78
4.B.2	Wide Frequency Scanning Dynamic Mechanical Measurements	81
4.B.3	Torsion Pendulum Data	83
4.B.4	Differential Scanning Calorimetry	84

CHAPTER 5. DISCUSSION

5.A	Hydrogenated Polymers	
5.A.1	Dynamic Mechanical Measurements	86
5.A.2	Melting Behaviour and DSC Scans	87
5.A.3	Surface Area of the Crystalline Phase	95
5.A.4	Modulus Calculations	96
5.B	Siloxane Block Copolymers	
5.B.1	Polymer Morphology	110

5.B.2	Rubbery Relaxation	120
5.B.3	Temperature Dependence of Dynamic Mechanical Properties	127
5.B.4	Crystallinity in the Siloxane Phase	130

CHAPTER 6 CONCLUSIONS 132

REFERENCES

APPENDICES

CHAPTER 1 INTRODUCTION

1.1 Thermoplastic Rubbers - General Survey

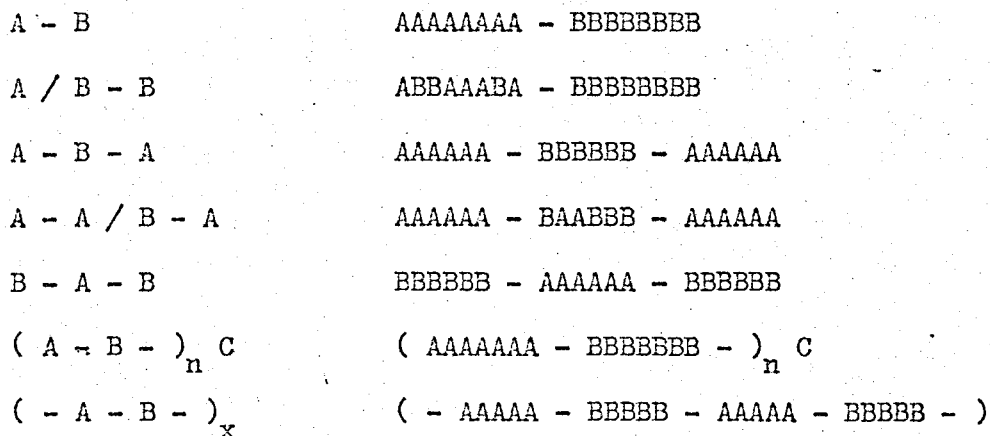
The ASTM definition of a rubber is, "a material which at room temperature can be stretched repeatedly to at least twice its original length and upon immediate release of the stress will return with force to its approximate original length." Materials which behave this way have long flexible chains which are interconnected by crosslinks and in many cases contain hard filler particles dispersed throughout the rubbery matrix. This results in the great majority of the flexible chains being interconnected in a three-dimensional network. In conventional rubbers, the crosslinks are covalent chemical bonds. These can be thought of as permanent crosslinks because once they are formed the rubbers cannot be dissolved or melt-processed. Thermoplastic rubbers have thermolabile crosslinks, so that rubbery behaviour occurs up to a temperature at which these crosslinks become unstable; above this transition temperature the polymer will flow.

At present, all thermoplastic elastomers are two-phase systems. However, attempts are being made to develop rubbers with thermolabile covalent bonds (1). Plastic flow is being sought at high temperatures by virtue of rapid reversible exchange reactions of covalent chemical crosslinks.

The ionomers are difficult to classify as having one or two-phases. Duck et. al. (2) have prepared carboxylated poly(butadiene) which was subsequently neutralized via metal salts. The rubbery products were thought to be crosslinked through ionic bundles.

Duck et. al. (3) have also developed unique two-phase thermoelastomers. These are partially hydrogenated poly (butadienes) and poly (butadiene-co-styrenes). At certain optimum degrees of hydrogenation (ca. 50%) they behave like true rubbers with fairly high tensile strength. The rubbery behaviour is due to the flexible butadiene chains being crosslinked and filler-reinforced by poly (ethylene) crystallites.

The largest class of thermoplastic elastomers are the block copolymers. The molecules of block copolymers consist of two or more chemically dissimilar segments, covalently bonded end-to-end. This latter feature distinguishes them from graft copolymers. Each segment, or block, is usually a long sequence of units of a single monomer, but may also be a long sequence of randomly copolymerized units. Therefore, even with only two monomers, A and B, there can be many combinations, some of which are given below:



The (A - B -)_n C type polymers are "star - shaped" where n = 3 and 4 when C is a tri- and tetrafunctional coupling agent, respectively. In the (- A - B -)_x type, as the block length

decreases, an alternating copolymer is approached. Block copolymers which are thermoplastic rubbers are of the (A - B - A),
 $(A - B -)_n C$ or $(- A - B -)_x$ type. At temperatures where rubbery behaviour occurs, the A segment is hard (glassy or crystalline) and the B segment is flexible. Block length and weight fraction of A and B are also crucial in achieving rubbery performance.

When the A segment (hard block) is crystalline, elastomeric behaviour is maintained until the segment starts to melt. The poly (urethanes) are the most widely known of these types. They are condensation polymers of flexible poly (ether) and/or poly (ester) diol segments interconnected by hard segments (diisocyanate - low molecular weight diol or diamine) of varying length. Cooper and coworkers (4 - 7) published a series of papers on the physical behaviour of SPANDEX and ESTANE urethane elastomers (8,9). These poly (ester - urethane) elastomers have been shown to be segmented linear polymers with two glass transitions. Imperial Chemical Industries has recently marketed their DALTOMOLD poly (ether) and poly (ester) urethanes which are rubbers with high tensile strength and elongation (10).

Similar to the poly (urethanes) are the HYTREL elastomers developed by Du Pont (11-13). They are described as random, segmented block copolymers consisting of tetramethylene terephthalate hard blocks and poly (tetramethylene ether) glycol terephthalate soft segments.

Elastomeric block copolymers, whose hard phases are glassy are

by far the best known. Of these, the polymers with poly (styrene) hard segments and poly (butadiene) and poly (isoprene) soft segments have been the most widely studied. They are commercially available as KRATON and THERMOLASTIC from Shell Chemical Company (14-15). Polymers with higher use temperatures based on poly (isoprene) soft segments have been developed by replacing the poly (styrene) with poly (α - methylstyrene) (16,17).

Of growing importance, are the elastomeric copolymers based on soft segments of poly (dimethylsiloxane) because of this polymer's excellent heat and light stability. A recent review has been written by Matzner et. al. (18). Poly (styrene) and poly (α - methylstyrene) based copolymers possessing both A - B - A and $(-A - B -)_x$ structures have been reported by several authors (19-24). Noshay and coworkers have developed poly (sulfone - b - dimethylsiloxane) elastomers (25,26) with continuous use temperatures of 443^oK and elastomers derived from 2,2,4,4 - tetramethyl-1,3 - cyclobutanediol polycarbonate displaying excellent UV stability (27-28). Copolymers derived from bisphenol A polycarbonate were prepared and investigated in detail by workers at the General Electric Laboratory (29-33). Methyl methacrylate - siloxane block copolymers have also been synthesized (34-35).

Alternating elastomeric block copolymers having the structure $(-A - B -)_x$ have been prepared where A is a polycarbonate and B is a polyether (193-5). The polycarbonate hard segment is made up of either crystalline units or bulky three-dimensional polycyclic groups.

1.2 Structural Parameters for Thermoplastic Rubbers

Rubbery behaviour is only found when flexible chains are interconnected. For the vast majority of thermoplastic rubbers these interconnections consist of crystallizable or glass forming chain segments covalently bonded to both sides of the flexible chains. It is thermodynamically favourable for the crystallizable or glass forming segments of many different chains to come together forming hard domains which act as both crosslinks and fillers for the soft matrix. Above the softening temperature of the thermoplastic segment, the system becomes a viscoelastic fluid and thus may be melt-processed. On cooling, it behaves like a rubber vulcanizate again, and the thermal cycle can be repeated indefinitely.

An uncrosslinked, linear, amorphous polymer will show dynamic modulus - temperature behaviour as depicted in curve A of Figure (1.1). The drop in modulus by a factor of 10^3 to 10^4 through the glass transition, $T_g (1)$, is typical of linear amorphous polymers. The rubbery plateau region (10^5 to 10^6 Nm^{-2}) is sensitive to the molecular weight of the polymer. Crosslinking extends the rubbery plateau to much higher temperatures (curve B).

Thermoplastic elastomers (curve C) can be semicrystalline or block polymers with a low percentage of hard segments. Rubbery behaviour occurs in the region between the glass transition of the rubber phase, $T_g (1)$, to the glass transition, $T_g (2)$, or melting point, T_m , of the hard phase. Below $T_g (1)$ the material is a glass while above $T_g (2)$ or T_m it can be melt-processed. There is a range of weight fractions of the hard phase such that true

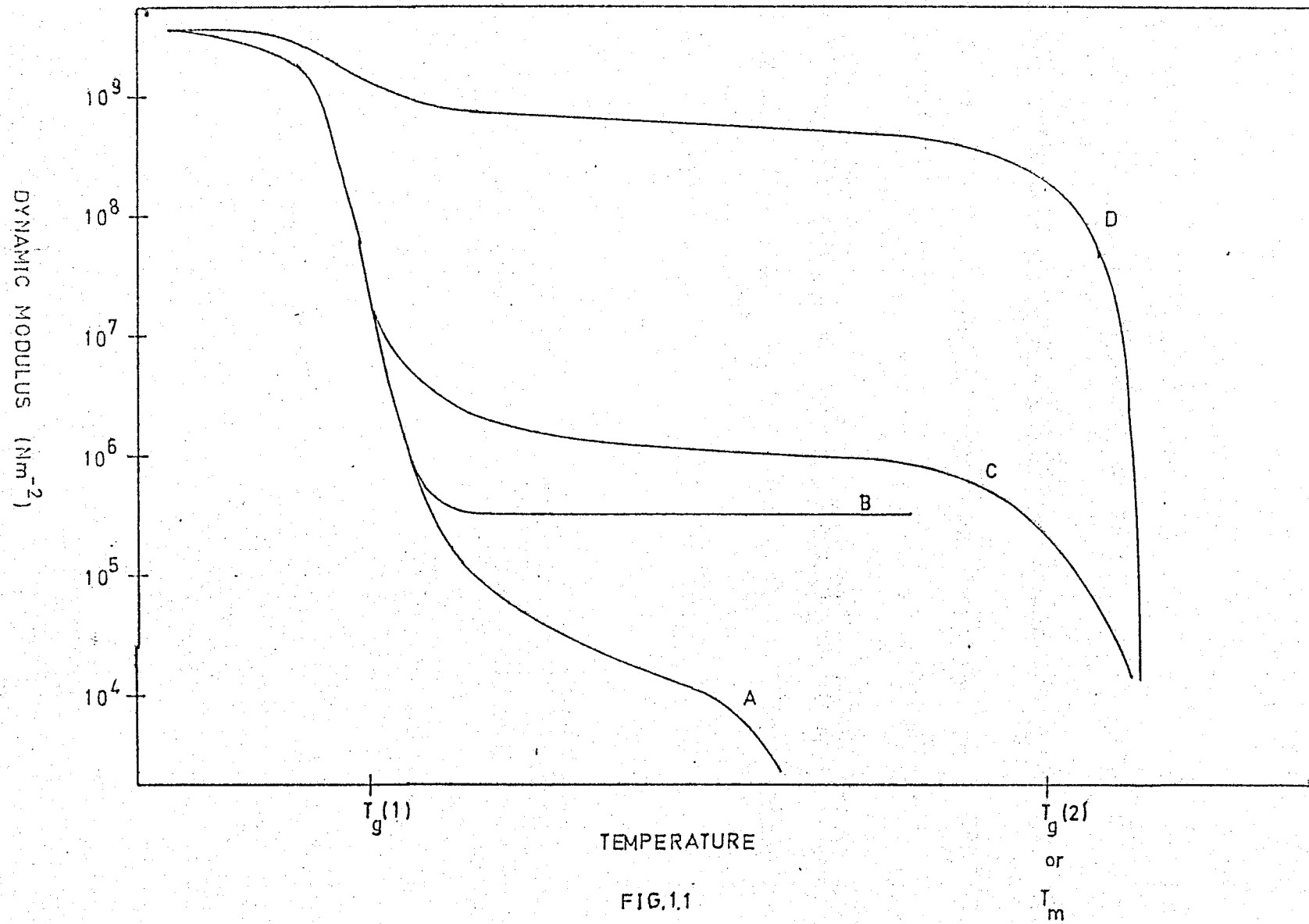


FIG.1.1

rubbery behaviour is achieved. At low fractions, the behaviour is similar to that of an undercured gum vulcanizate. At a certain critical weight fraction, hard segment content will be too low for phase separation to occur and behaviour similar to that represented by curve A will be observed. Polymers with high hard segment contents will be very stiff in the plateau region between $T_g (1)$ and $T_g (2)$ or T_m . This is illustrated by curve D.

1.3 Introduction to the Present Work

A great deal of work has been done relating the structures in elastomeric block copolymers to their physical properties, with most of this work being done on styrene - butadiene systems. The subject has been reviewed by several authors (36-38). It is the purpose of this study to relate this previous work to new thermo-elastomer systems. The structure of some non-block, partially hydrogenated polymers prepared by Duck et. al. (3) and a poly (dimethylsiloxane-b- α -methylstyrene), as determined via small angle x-ray scattering and calorimetric properties, were compared with their dynamic mechanical properties.

X-rays are reflected by inhomogeneities of matter. If the inhomogeneities are of colloidal dimensions, the effect will be confined to very small angles with respect to the primary beam of incident x-rays. The details of this scattering will depend upon the morphological structure of the system. It was decided to use SAXS to observe the morphology of the various systems.

Calorimetric properties were determined using a differential

scanning calorimeter (DSC). This method of analysis is capable of detecting glass transitions and the presence of crystallinity by temperature scanning. In this study, structural inferences will be drawn primarily from melting behaviour.

Figure (1.1) shows the two-step nature of dynamic modulus-temperature curves for thermoplastic rubbers. The general shape of the curve and the magnitudes and positions of the transitions have been related to structure for many block copolymers. It was thus decided to relate the dynamic mechanical properties of these samples, over a wide temperature and frequency range, to their structure, as determined by SAXS and DSC.

CHAPTER 2 THEORETICAL BACKGROUND

2.1 Elasticity of Rubber Networks

The moduli of glasses and crystals are in the range 10^9 to 10^{12} Nm^{-2} with elastic limits of less than 1%. Natural and synthetic rubbers on the other hand can be reversibly stretched to several hundred per cent of their equilibrium elongation, displaying moduli in the range 10^5 to 10^7 Nm^{-2} . The theory of rubberlike elasticity, reviewed by several authors (39-41), adequately describes this rubbery behaviour. In the treatment presented below, only the behaviour at very low strain will be considered.

Materials displaying rubberlike elasticity consist of three-dimensional networks of flexible molecular chains. This three-dimensional network can be temporary or permanent. In the case of high molecular weight linear polymers, rubberlike elasticity is displayed in a small temperature range where chain entanglements form temporary crosslinking points. In most thermoplastic rubbers the network is held together by a crystalline or glassy phase; above the melting point or T_g of the hard phase melt flow occurs. Permanent networks are formed by vulcanization processes whereby covalent bonds interconnect the different chains. When a rubbery network is stretched, a restoring force (X) is produced, as a result of entropy changes, which attempts to restore the network to its original dimensions.

In the unstretched state, a flexible chain in a network can attain Ω_u possible conformation between its crosslinks.

Stretching the network reduces the number of conformations attainable by the chain to Ω . It can be shown that the entropy difference between the stretched (S) and unstretched (S_u) states is:

$$S - S_u = k \ln \frac{\Omega}{\Omega_u} \quad (2.1)$$

where k is the Boltzmann constant. Using statistical theory to evaluate $\ln \frac{\Omega}{\Omega_u}$, Equation (2.1) becomes:

$$S - S_u = -\frac{1}{2}uk \left(\alpha^2 + \frac{2}{\alpha} - 3 \right) \left(\frac{\langle r^2 \rangle_i}{\langle r^2 \rangle_o} \right) \quad (2.2)$$

where u is the number of network chains in the system.

α is the extension ratio, defined as the extended length (L) divided by the unextended length (L_u).

$\langle r^2 \rangle_i$ is the mean square chain displacement length in the absence of strain imposed by an external stress.

$\langle r^2 \rangle_o$ is the mean square chain displacement length for free chains unconstrained by unit junctions.

Using thermodynamic arguments, the restoring force (X) in a flexible network under simple tension has been shown to be:

$$X = -T \left(\frac{\partial S}{\partial L} \right)_T \quad (2.3)$$

where T is the absolute temperature.

Combining Equations (2.2) and (2.3):

$$X = \frac{ukT}{L_u} \left(\frac{\langle r^2 \rangle_i}{\langle r^2 \rangle_o} \right) \left(\alpha - \frac{1}{\alpha^2} \right) \quad (2.4)$$

Dividing both sides of Equation (2.4) by A_u , the cross-sectional

area of the unstretched system:

$$\sigma = \left(\frac{\nu}{V}\right) kT \left(\frac{\langle r^2 \rangle_i}{\langle r^2 \rangle_o}\right) \left(\alpha - \frac{1}{\alpha^2}\right) \quad (2.5)$$

where σ is the tensile stress (X / A_u) applied to the system.

V is the volume of the system ($A_u L_u$)

$\frac{\nu}{V}$ is the number of network chains per unit volume.

The extension ratio may be written:

$$\alpha = 1 + \epsilon \quad (2.6)$$

where ϵ is the tensile strain $(L - L_u) / L_u$ in the system.

Using the binomial expansion:

$$\alpha^{-2} = (1 + \epsilon)^{-2} = 1 - 2\epsilon + \dots \quad (2.7)$$

Higher order terms in Equation (2.7) may be neglected at the low strains considered. Combining Equations (2.5) to (2.7):

$$\frac{\sigma}{\epsilon} = E = 3 \left(\frac{\nu}{V}\right) kT \left(\frac{\langle r^2 \rangle_i}{\langle r^2 \rangle_o}\right) \quad (2.8)$$

2.2 Viscoelastic Behaviour and Definition of Terms

The nature of polymer viscoelasticity has been outlined in standard texts (42-44). Polymers have intermediate properties between perfect (Hookean) solids and perfect (Newtonian) liquids, for which theories have been developed over the last century (45-46). Perfect solids obey Hooke's Law, which states that stress is proportional to strain. In perfect liquids, stress is proportional to the rate of strain, which is Newton's viscosity law. A polymer, however, deforms with time (creeps) when under a constant stress. Under a

constant strain, the stress needed to maintain polymer deformation is observed to decay (stress relaxation). For a sinusoidally oscillating stress, the strain is observed to be neither in phase (as for a Hookean solid) nor 90° out of phase (as for a Newtonian Liquid). There are instead in phase (storing energy) and out of phase (dissipating energy) components of the resultant strain.

In order to measure viscoelastic properties, three types of deformation are usually employed; simple shear, bulk compression and simple elongation as illustrated in Figure (2.1). In simple shear there is a change in shape without change in volume. Bulk compression requires that there be a volume change with no change of shape. In simple tension there is change of volume and shape. The moduli and compliances for these various deformations are related as follows:

$$E(t) = \frac{9 G(t) K(t)}{G(t) + 3 K(t)} \quad (2.9)$$

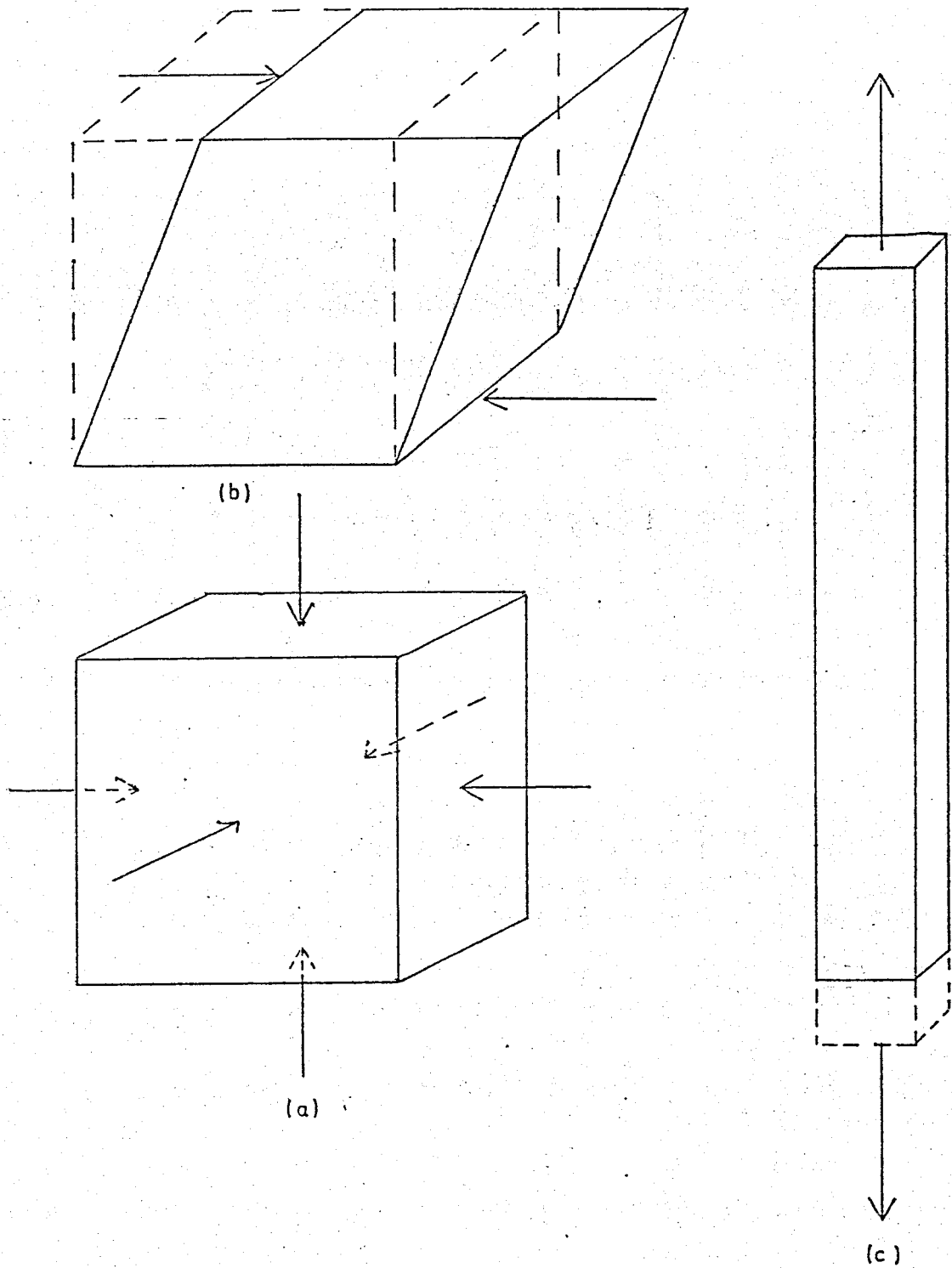
$$D(t) = \frac{J(t)}{3} + \frac{B(t)}{9} \quad (2.10)$$

where $E(t)$, $D(t)$ are the tensile relaxation modulus and creep compliance, respectively.

$G(t)$, $J(t)$ are the shear relaxation modulus and creep compliance, respectively.

$K(t)$, $B(t)$ are the bulk relaxation modulus and creep compliance, respectively.

In a rubber, $K(t) \gg G(t)$ changing Equations (2.9) and (2.10) to:



GEOMETRICAL ARRANGEMENT FOR
 (a) SIMPLE SHEAR (b) BULK DEFORMATION (c) SIMPLE EXTENSION

$$E(t) = 3G(t) \quad (2.11)$$

$$D(t) = \frac{J(t)}{3} \quad (2.12)$$

This behaviour is a result of the change in volume, for simple extension, being almost negligible when compared with the change in shape. Equations (2.11) and (2.12) can also be obtained by re-writing Equation (2.9) as:

$$E(t) = 2G(t) (1 + \nu) \quad (2.13)$$

where ν is Poisson's ratio and is expressed as:

$$\nu = \frac{1}{2} \left[1 - \frac{1}{V} \left(\frac{\partial V}{\partial \epsilon} \right) \right] \quad (2.14)$$

ν is $\frac{1}{2}$ for a rubber thus reducing Equation (2.13) to Equation (2.11).

The most important methods for viscoelastic measurements are creep, stress relaxation and dynamic mechanical tests. In the following description of these tests J and G have been used exclusively. However, D , B and E , K can be substituted for J and G respectively.

Creep experiments involve placing a specimen under constant stress and following the change in strain as a function of time. The creep compliance is given by:

$$J(t) = \frac{\epsilon_0}{\sigma(t)} \quad (2.15)$$

Figure (2.2) is a typical creep compliance curve for linear and crosslinked polymers. At very short times the polymer chains have not begun to "stretch" and the compliance is given by J_U , that of the unrelaxed or glassy state. As the time scale of the exper-

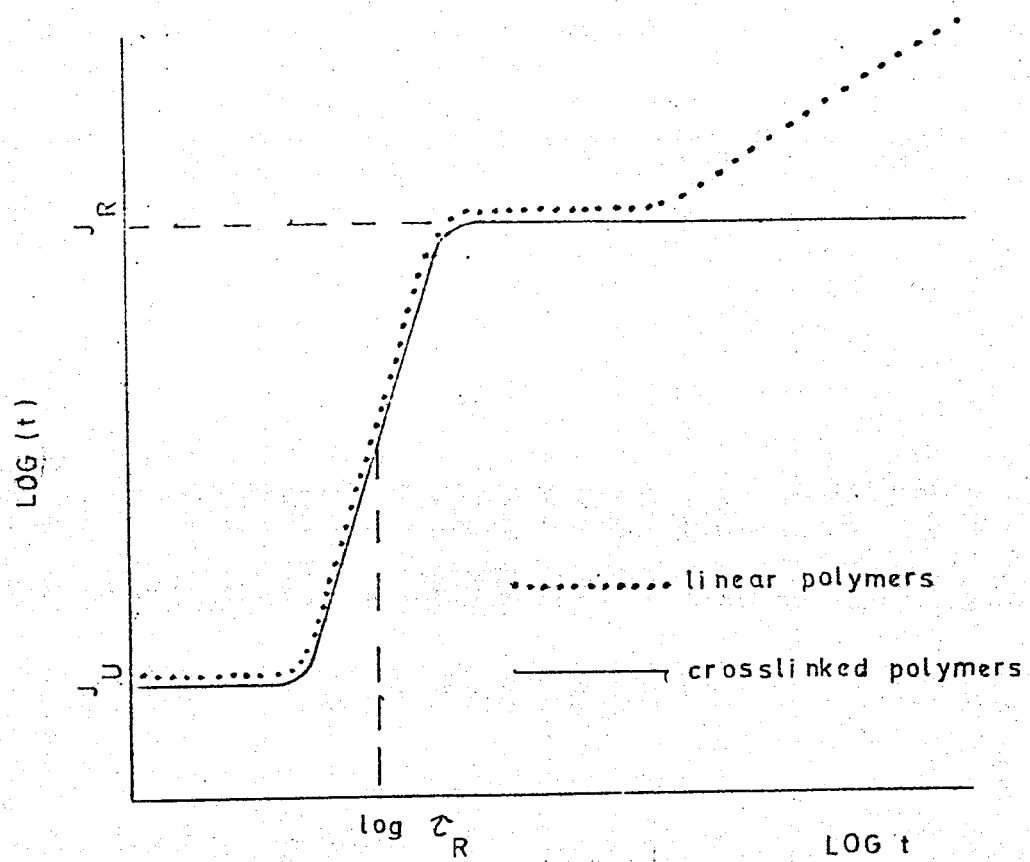


FIG. 2.2

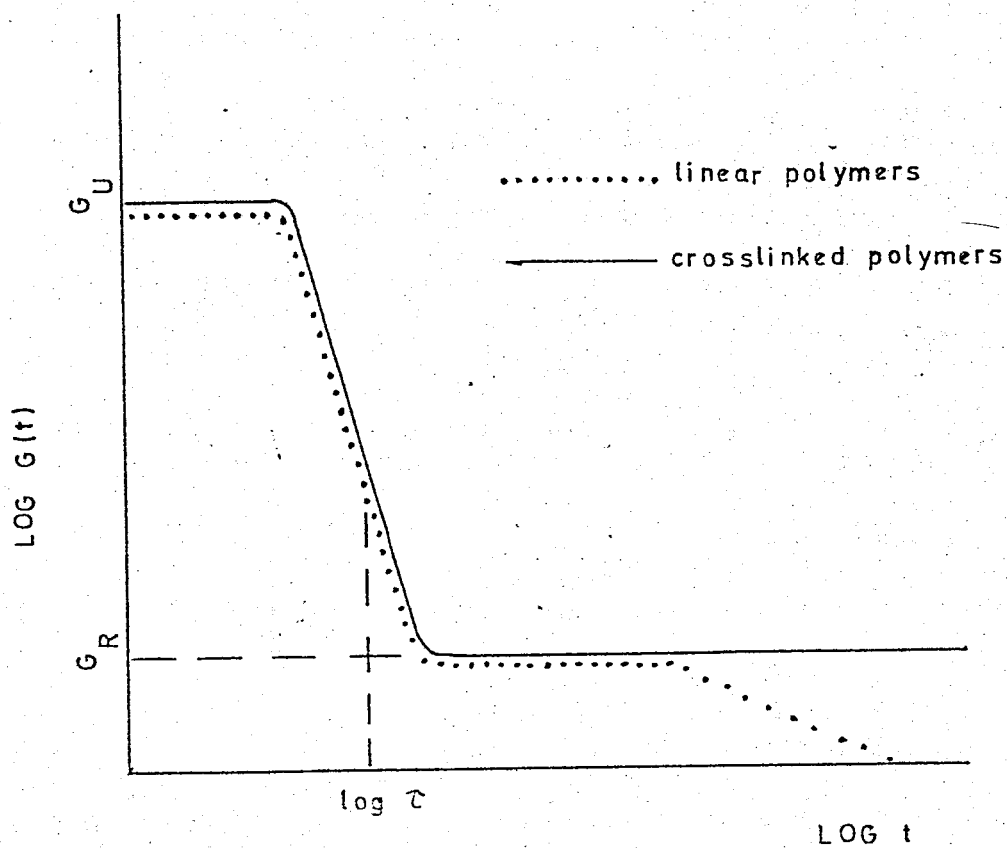


FIG. 2.3

iment nears that of the average retardation time (τ_R) of the sample, a transition occurs to a more relaxed state. Following the transition the compliance is that of a rubber J_R , the relaxed compliance. In crosslinked polymers, the compliance remains constant at J_R as a further function of time. For linear polymers, a second relaxation occurs with the unravelling of chain entanglements and the onset of Newtonian flow.

If a sample is subjected to an instantaneous strain and the stress decay is followed as a function of time, a stress relaxation experiment has been performed. The relaxation modulus is given as:

$$G(t) = \frac{\sigma_0}{\epsilon(t)} \quad (2.16)$$

Figure (2.3) illustrates the behaviour of $G(t)$ as a function of time for typical crosslinked and linear polymers. Again, at short times, the unrelaxed condition of the polymer gives it a glassy modulus (G_U). A transition region is encountered near the average relaxation time (τ) of the polymer which is followed by a plateau region where the relaxed (rubbery) state is reached with modulus G_R . For the crosslinked polymer the relaxation modulus remains constant while the modulus of the linear polymer gradually decreases with the onset of flow, as a further function of time.

In dynamic mechanical experiments a sinusoidal stress (or strain) is applied to a specimen and the resulting strain (or stress) is followed as a function of frequency. The situation is illustrated in Figure (2.4). An oscillating stress of frequency

STRESS
OR
STRAIN

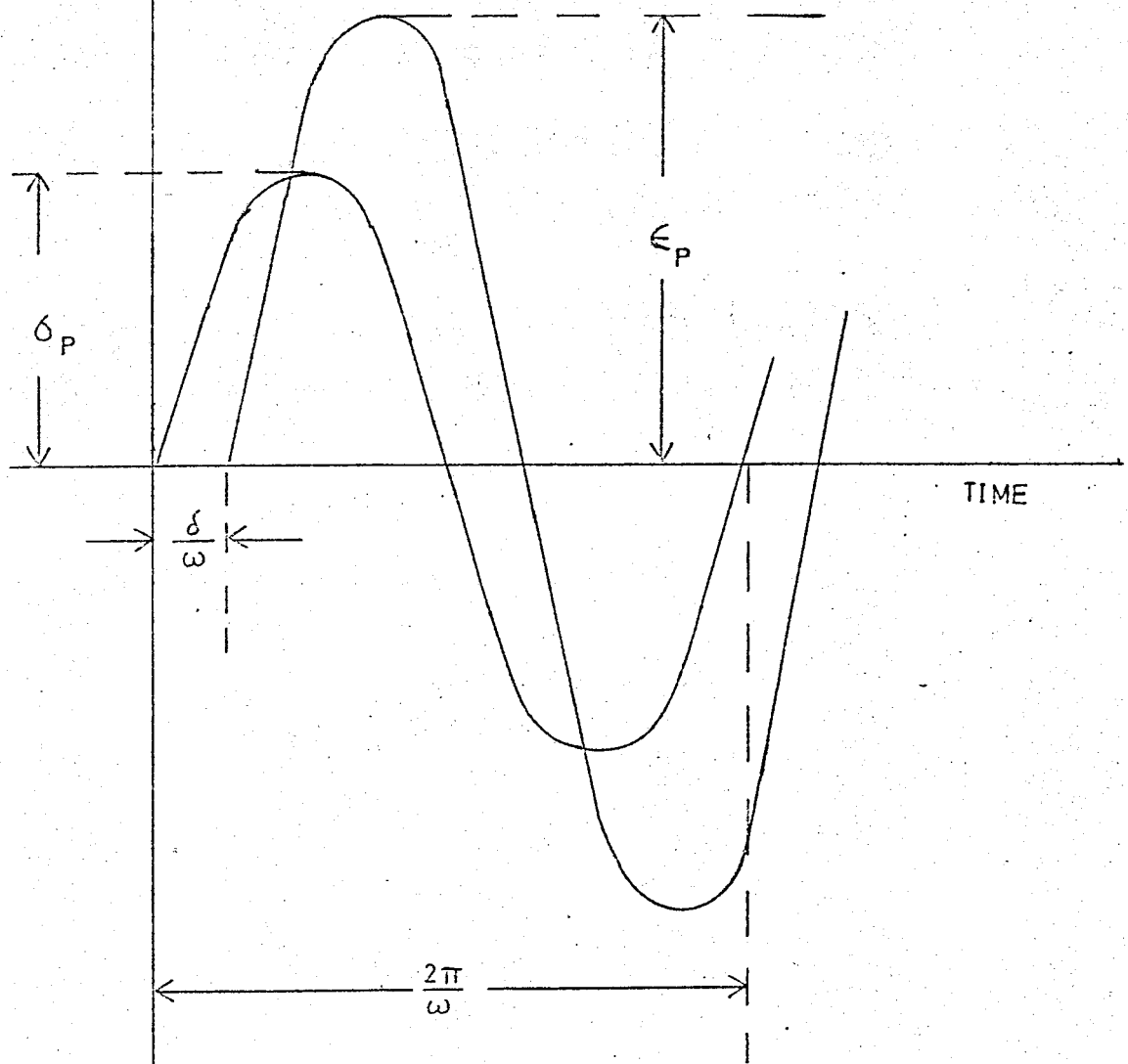


FIG. 2.4

(ω) is applied to the sample:

$$\sigma = \sigma_p \sin \omega t \quad (2.17)$$

where σ_p is the stress amplitude.

The strain is found to oscillate at the same frequency (ω) as the stress and to lag it by a phase angle (δ):

$$\varepsilon = \varepsilon_p \sin (\omega t - \delta) \quad (2.18)$$

where ε_p is the strain amplitude.

A complex compliance $J^*(\omega)$ and modulus $G^*(\omega)$ can be defined which have in phase $J'(\omega)$ and $G'(\omega)$, and out of phase, $J''(\omega)$ and $G''(\omega)$, components with the oscillating strain and stress, respectively. The absolute values of the complex compliance and modulus can be written:

$$\frac{\varepsilon}{\sigma} = |J^*(\omega)| = J'(\omega) \sin \omega t + J''(\omega) \cos \omega t \quad (2.19)$$

$$\frac{\sigma_p}{\varepsilon_p} = |G^*(\omega)| = G'(\omega) \sin \omega t + G''(\omega) \cos \omega t \quad (2.20)$$

$J'(\omega)$ and $G'(\omega)$, the storage compliance and modulus, represent input energy which is stored by the sample. $J''(\omega)$ and $G''(\omega)$, the loss compliance and modulus, represent input energy which has been dissipated by the sample as heat. Figures (2.5) and (2.6) illustrate the behaviour of $J'(\omega)$, $J''(\omega)$ and $G'(\omega)$, $G''(\omega)$ as a function of frequency, respectively. At high frequencies, glassy behaviour is attained where $J'(\omega) = J_U$ and $G'(\omega) = G_U$. At frequencies near $\frac{1}{\tau_R}$ and $\frac{1}{\tau}$, $J'(\omega)$ increases

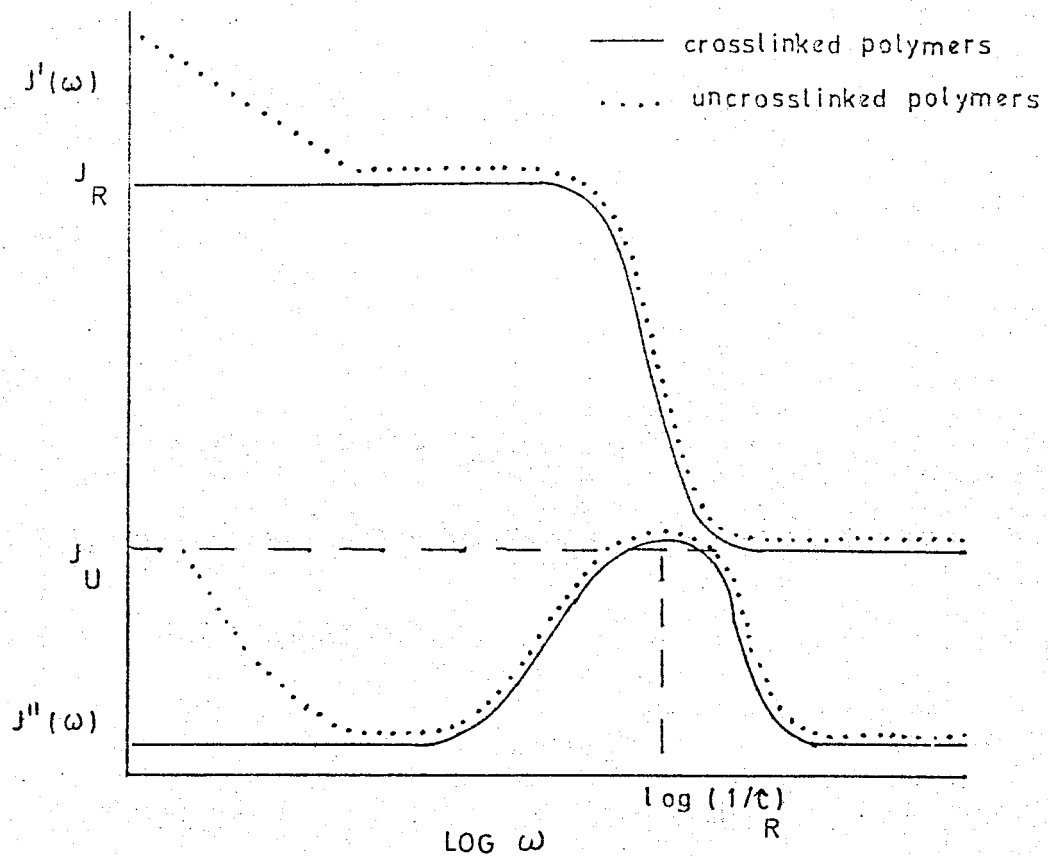


FIG.2.5

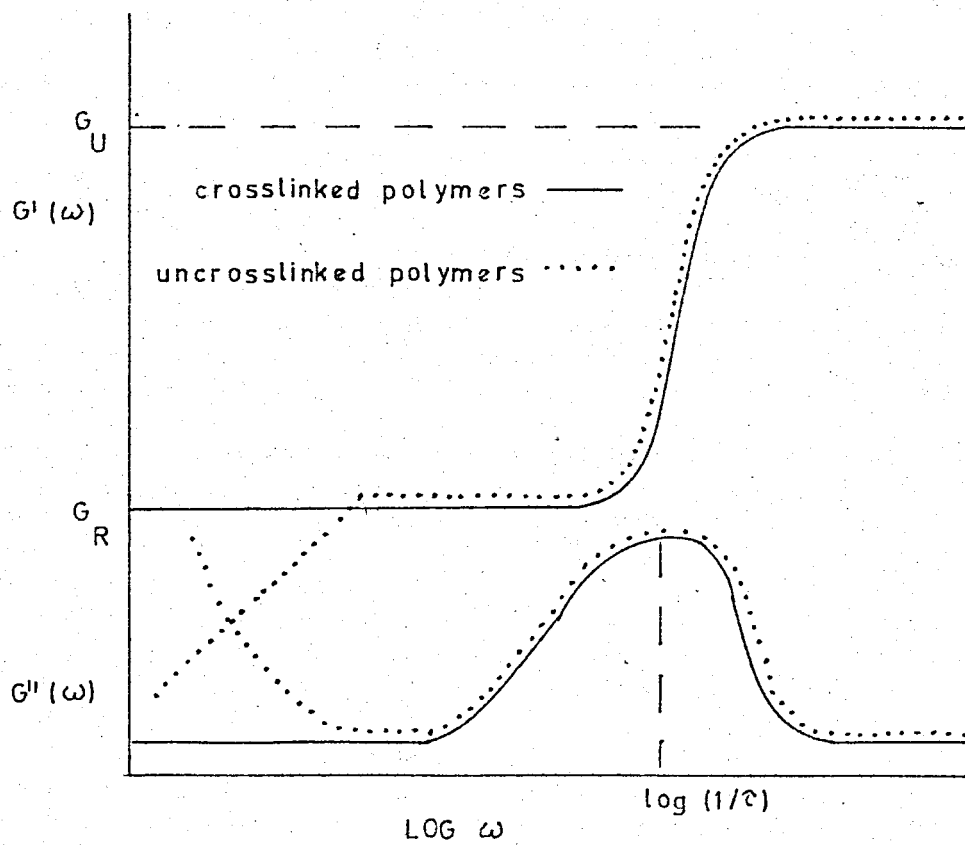


FIG.2.6

and $G'(\omega)$ decreases rapidly as frequency decreases. $J''(\omega)$ and $G''(\omega)$ attain a maximum value at $\frac{1}{\tau_R}$ and $\frac{1}{\tau}$, respectively. With further decrease in frequency $J'(\omega) = J_R$ and $G'(\omega) = G_R$ as the polymer is in the rubbery state. At the onset of flow the linear polymer goes through a second relaxation with $J'(\omega)$, $J''(\omega)$ and $G''(\omega)$ increasing, and $G'(\omega)$ decreasing with decreasing frequency.

Figure (2.7) illustrates the relationship between $J^*(\omega)$ and $G^*(\omega)$ and their components as expressed in Equations (2.19) and (2.20). From this illustration another viscoelastic parameter, the loss tangent ($\tan \delta$) can be defined.

$$\tan \delta = \frac{J''(\omega)}{J'(\omega)} = \frac{G''(\omega)}{G'(\omega)} \quad (2.21)$$

It should also be apparent that:

$$J^*(\omega) = \frac{1}{G^*(\omega)} \quad (2.22)$$

However, it should be noted that $J'(\omega) \neq \frac{1}{G'(\omega)}$ and

$$J''(\omega) \neq \frac{1}{G''(\omega)} .$$

If $G'(\omega)$ and $J'(\omega)$ are plotted against $\log(1/\omega)$, the curves are found to coincide with $G(t)$ and $J(t)$ plotted against $\log t$ on the same scale. This is a consequence of linear viscoelastic behaviour and establishes the reciprocal relationship between frequency and time.

2.3 Phenomenological Concepts of Viscoelasticity

The phenomenological theory is a purely mathematical description

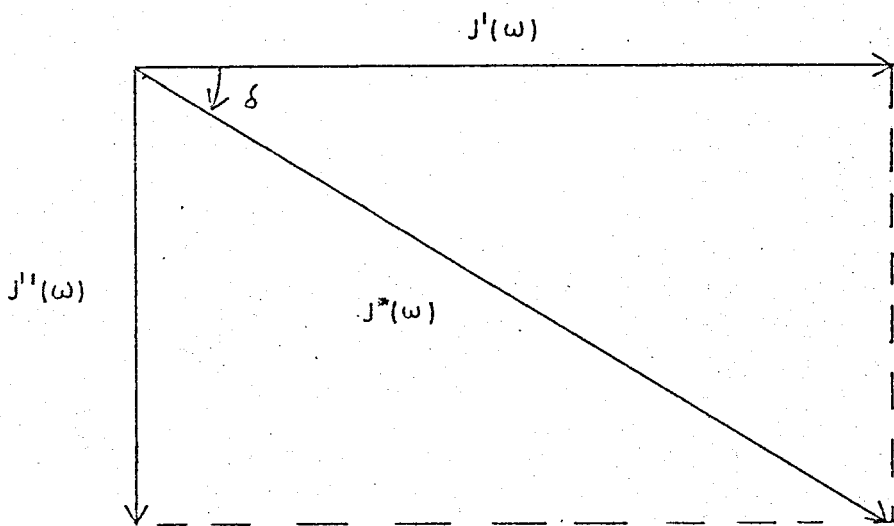
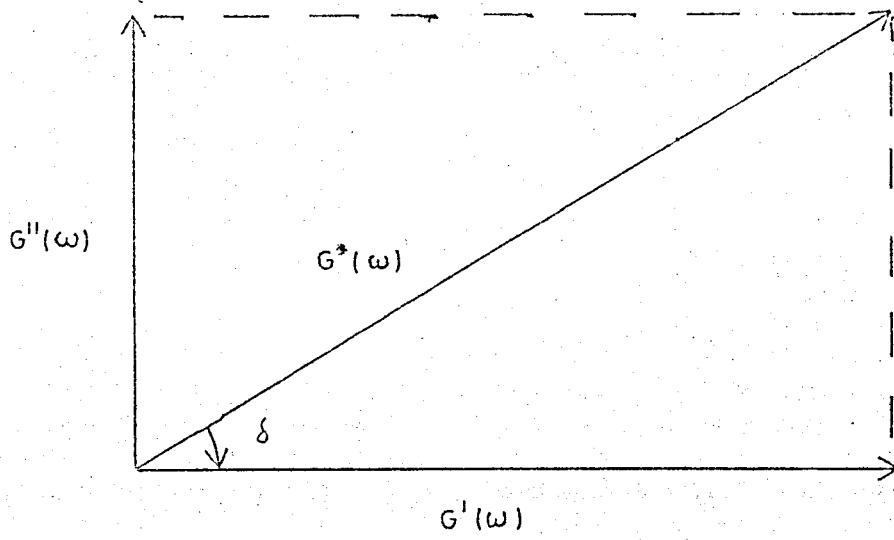


FIG. 2.7

of viscoelastic behaviour developed from Boltzmann's Superposition Principle (47). In this superposition principle Boltzmann stated that, if a number of deformations are applied to a material displaying linear mechanical response:

(1) Each deformation is independent of all others.

(2) The specimen's response can be calculated by adding the effects of the individual deformations.

This principle is applied to combinations of springs (Hookean solids) and dashpots (Newtonian liquids), whose motion can be precisely mathematically defined. Thus, once the correct model for a viscoelastic system has been chosen, all linear mechanical response can be predicted. The various mathematical forms of linear viscoelasticity are discussed in a number of works (42, 44, 47-51).

Single relaxation time models are the simplest combinations of springs and dashpots. Three types are illustrated in Figure (2.8) and their behaviour will be discussed below. The Maxwell model consists of a spring of modulus E_m and a dashpot of viscosity η_m in series. Its motion is described by Equation (2.23).

$$\sigma + \tau \left(\frac{d\sigma}{dt} \right) = E_m \tau \left(\frac{d\varepsilon}{dt} \right) \quad (2.23)$$

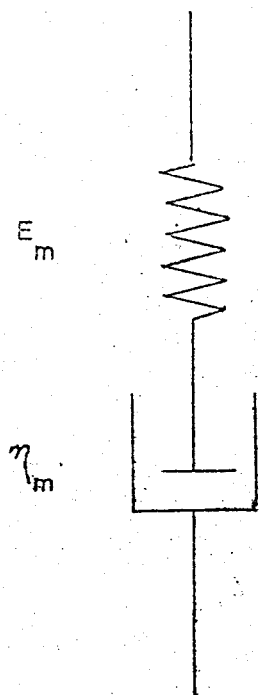
where σ is the applied stress.

ε is the extension.

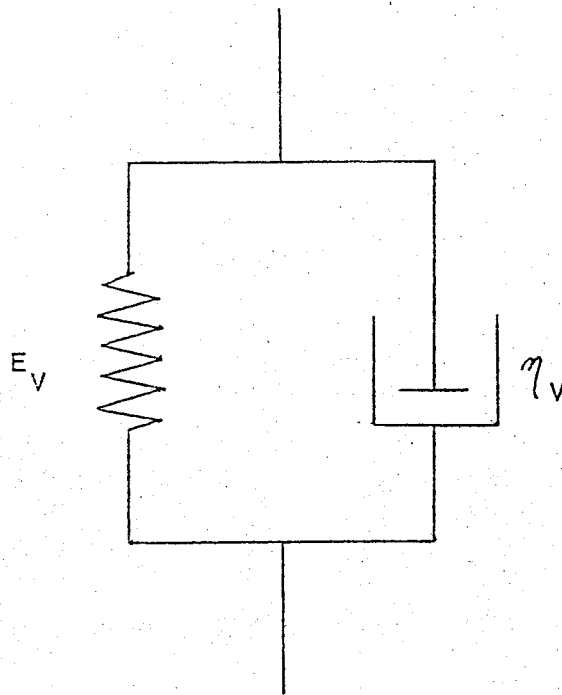
τ is the relaxation time (η_m / E_m).

For the Voigt model, a spring of modulus E_v connected in parallel to a dashpot of viscosity η_v , the load-extension relationship is:

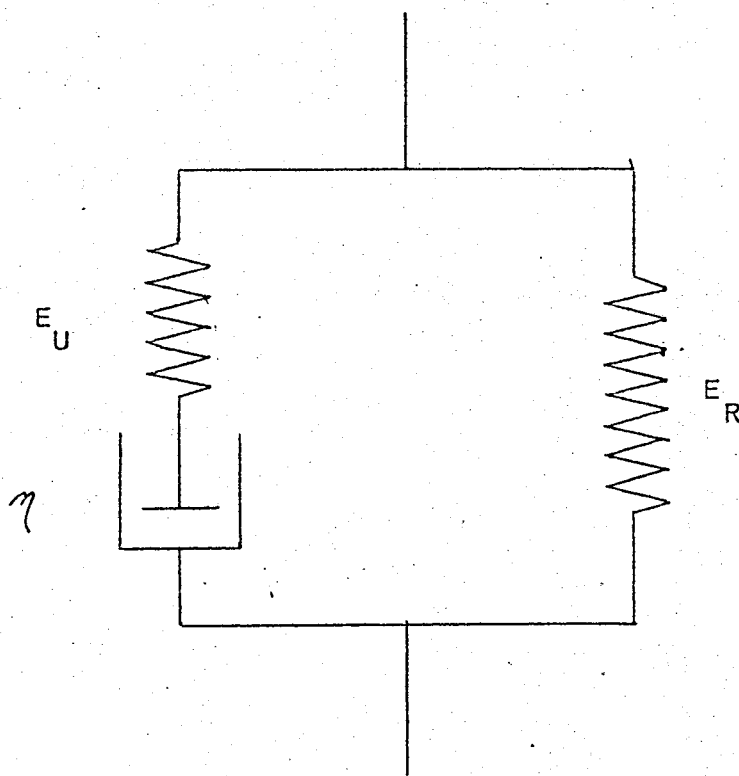
$$\sigma = \varepsilon E_v + E_v \tau_v \left(\frac{d\varepsilon}{dt} \right) \quad (2.24)$$



MAXWELL MODEL



VOIGT MODEL



STANDARD LINEAR BODY

FIG.2.8

where τ_R is the retardation time (η_V / E_V).

Although some aspects of polymer viscoelasticity are represented by these simple models, in most cases it is just a crude approximation.

The "standard linear body", represented by a Maxwell body in parallel with a spring is a simplified model for an ideal cross-linked polymer. It possesses single relaxation and retardation times and a relaxed and unrelaxed modulus (and compliance). Thus when its behaviour is followed as a function of frequency, plots similar to those for crosslinked polymers, in Figures (2.5) and (2.6), are obtained. The dynamic moduli parameters for this model are described by Equations (2.25), (2.26) and (2.27).

$$E'(\omega) = E_R + \frac{(E_U - E_R) \omega^2 \tau^2}{1 + \omega^2 \tau^2} \quad (2.25)$$

$$E''(\omega) = \frac{(E_U - E_R) \omega \tau}{1 + \omega^2 \tau^2} \quad (2.26)$$

$$\tan \delta = \frac{(E_U - E_R) \omega \tau}{(E_U E_R)^{\frac{1}{2}} (1 + \omega^2 \tau^2)} \quad (2.27)$$

The compliances of the system, defined in Section (2.2) will be given by similar equations and by replacing τ with τ_R . Also, shear or bulk moduli can be described by similar equations.

Real polymers display much broader transitions than described by these simple models. Mathematically, this is equivalent to a superposition of the behaviour of many models each with its own single relaxation (or retardation) time. Thus relaxation, $H(\tau)$,

and retardation, $L(\tau_R)$, time spectra were introduced to describe real polymer behaviour, which were first introduced by Weichert (52) and Thomson (53). In general, a continuous relaxation time spectra can be conveniently defined as $H(\tau)$ where $Hd(\ln\tau)$ is the contribution to the modulus of relaxation times whose logarithms lie between $(\ln\tau)$ and $(\ln\tau + d \ln\tau)$. A corresponding retardation time spectra, $L(\tau_R)$, may be defined as a similar contribution to the compliance. The expressions for the dynamic moduli, analogous to Equations (2.25) and (2.26), but in terms of the relaxation spectra H , and the retardation spectra L , are:

$$E'(\omega) = E_R + \int_{-\infty}^{+\infty} \frac{H(\tau) \omega^2 \tau^2 d(\ln\tau)}{1 + \omega^2 \tau^2} \quad (2.28)$$

$$E''(\omega) = \int_{-\infty}^{+\infty} \frac{H(\tau) \omega \tau d(\ln\tau)}{1 + \omega^2 \tau^2} \quad (2.29)$$

$$J'(\omega) = J_U + \int_{-\infty}^{+\infty} \frac{L(\tau_R) \omega^2 \tau_R^2 d(\ln\tau_R)}{1 + \omega^2 \tau_R^2} \quad (2.30)$$

$$J''(\omega) = \int_{-\infty}^{+\infty} \frac{L(\tau_R) \omega \tau_R d(\ln\tau_R)}{1 + \omega^2 \tau_R^2} \quad (2.31)$$

In principle, once $H(\tau)$ and $L(\tau_R)$ have been obtained, all viscoelastic behaviour can be determined (43, 47, 50, 54).

2.4 Molecular Interpretation of Viscoelastic Behaviour

The molecular theory is used to predict viscoelastic response using molecular parameters. Rouse (55) and Bueche (56) have each

used arguments based on a polymer molecule envisioned as a number of bead-like masses connected by weightless springs moving in a viscous medium. The combined theory has been reviewed by several authors (42, 43, 57, 58).

Rouse's (55) treatment deals with polymer solutions. Each polymer chain is divided into N submolecules, each with a gaussian distribution of end-to-end distances. There are thus N springs and $N + 1$ beads. If there are q monomer units per submolecule, the root mean square end-to-end distance (σ) is $a\sqrt{q}$, by virtue of its gaussian behaviour (' a ' is a geometric parameter). When a uniaxial stress is applied to the polymer the viscous surroundings retard the movement of the chains. This retardation is represented by a friction coefficient (f_0) which equals $q \zeta_0$. (ζ_0 is the monomeric friction coefficient.) The response to an applied stress may be described by a series of co-operative modes (p). Each mode represents motion away from a given instantaneous configuration and corresponds to a discrete contribution to a relaxation spectrum (H), characterized by a relaxation, τ_p . In these terms H is given by:

$$H = nkT \sum_{p=1}^N \tau_p \delta(\tau - \tau_p) \quad (2.32)$$

$$\tau_p = \frac{\sigma^2 N^2 f_0}{6 \pi^2 p^2 kT} \quad (2.33)$$

where n is the number of molecules per cm^3 . δ is the Dirac delta function.

The theory can extend to bulk polymers on the grounds that the

same kind of motions occur in an amorphous polymer as in solution, although very much slower. Ferry (43) has done this and obtained the following expressions for the relaxation and retardation time spectra based on Rouse's treatment:

$$H(\tau) = \left(\frac{a \rho N_0}{2 \pi M_0} \right) \left(\frac{\xi_0 kT}{6} \right)^{\frac{1}{2}} \tau^{-\frac{1}{2}} \quad (2.34)$$

$$L(\tau) = \left(\frac{2M_0}{\pi a \rho N_0} \right) \left(\frac{6}{\xi_0 kT} \right)^{\frac{1}{2}} \tau^{\frac{1}{2}} \quad (2.35)$$

where ρ is the polymer density.

N_0 is Avogadro's number.

M_0 is the monomer molecular weight.

Bueche (56) has formulated a theory to apply to both linear and crosslinked bulk polymers. In his treatment, thermal motion is only inferred by the introduction of an entropy spring constant. The expressions obtained for $H(\tau)$ and $L(\tau)$ are similar to those obtained from the Rouse theory, Equations (2.34) and (2.35):

$$H(\tau) = 2^{\frac{1}{2}} H(\tau) \text{ (Rouse)} \quad (2.36)$$

$$L(\tau) = 2^{-\frac{1}{2}} L(\tau) \text{ (Rouse)} \quad (2.37)$$

Viscoelastic functions calculated from the Rouse-Bueche theory agree well with experimental values where the sample moduli are below 10^6 Nm^{-2} (i.e. at low frequencies or long times). The theory predicts only one transition for linear polymers (from the rubber to the melt). For this reason, Ferry, Landel and Williams (59) postulated a second friction factor operating at higher frequencies

to account for the second transition (from rubber to glass). However, Williams (60) has stated that this modification predicts, at best, an unrelaxed modulus more than two orders of magnitude smaller than experimentally determined values. This is apparently caused by employing terms which are applicable only to the rubber-like motion encountered at lower frequencies. Tobolsky (61) has pointed out that equations of motion can be written and solved employing terms more realistically describing the motions of the glassy state.

2.5 Time-Temperature Superposition Principle

In order to plot viscoelastic functions over as much as ten logarithmic decades of time or frequency at a particular temperature an extrapolation method must be used. At best, stress relaxation, creep and dynamic mechanical experiments will only cover six decades.

An extrapolation method involving time-temperature superposition was first suggested by Leaderman (50, 62), who observed that creep recovery curves could be superimposed by translation along the time axis. Thus, a factor A_T can be determined so that multiplying the data at one temperature (T) will superimpose it upon the data at a reference temperature (T_0). The factor (A_T) is experimentally determined at each temperature by noting the amount of shift needed to make the data at T and T_0 coincide. When all data at all temperatures has been treated in such a way, a master curve at the reference temperature is obtained covering many more logarithmic decades of time than were determinable experimentally. Furthermore, if the material in question obeys linear viscoelastic theory, similar

alteration in the time or frequency variable (A_T) will also effectively superimpose stress relaxation-time curves (63, 64) and dynamic modulus-frequency curves (65, 66).

This method of producing master curves is applied to polymers only in the transition region between glass-like and rubber-like behaviour. Polymer density (ρ) is affected by temperature. Also, the modulus is proportional to absolute temperature since in the transition region amorphous polymers are assumed to obey the laws of rubberlike elasticity. The dynamic and transient moduli and compliances must thus be adjusted before plotting against the reduced variables (T / A_T) and (ωA_T), as shown below:

$$(1) G(t) \left(\frac{T_0 \rho_0}{T \rho} \right) \text{ plotted against } \left(\frac{T}{A_T} \right) .$$

$$(2) J(t) \left(\frac{T \rho}{T_0 \rho_0} \right) \text{ plotted against } \left(\frac{T}{A_T} \right) .$$

$$(3) G'(t) \left(\frac{T_0 \rho_0}{T \rho} \right) \text{ and } G''(t) \left(\frac{T_0 \rho_0}{T \rho} \right) \text{ plotted against } (\omega A_T) .$$

It was previously described how A_T can be calculated empirically. Williams, Landel and Ferry (67) have defined A_T as the ratio of relaxation times (τ) at T to the relaxation times (τ_0) at T_0 . Since τ is related to the steady flow viscosity (η_T) at temperature T , knowledge of η_T and η_{T_0} (steady flow viscosity at T_0) enables one to calculate A_T by the following expressions:

$$A_T = \frac{T_0 \rho_0 \eta_T}{T \rho \eta_{T_0}} = \frac{\tau}{\tau_0} \quad (2.38)$$

For many polymers (68-71) in the transition region the data are found to superimpose quite well, using Equation (2.38) when plotted in the form of the reduced modulus or compliance versus the reduced time or frequency. For dynamic experiments in which both G' and G'' are measured, it is essential that the same values of A_T be used for both sets of data.

The variation of A_T with temperature is usually exponential and an activation enthalpy (ΔH_R) for the relaxation process can be obtained from the expression:

$$\Delta H_R = R \frac{d(\ln A_T)}{d(1/T)} \quad (2.39)$$

Therefore, ΔH_R is proportional to the slope of the linear plot of $\log A_T$ against $1/T$. However, a linear relationship between $\log A_T$ and temperature is frequently not found indicating that ΔH_R may itself be a function of temperature. This is often the case with block copolymers (72-79) and semi-crystalline homopolymers (44). In block copolymers this behaviour is attributed to the occurrence of relaxation mechanisms for both the domains and the matrix.

2.6 Phase Separation and Transitions in Two-Phase Systems

The two-phase nature of all thermoelastomers is the basis for their thermoplastic nature. The various theories of phase separation in copolymers is therefore worth mentioning. The following discussion will be divided into phase separation in crystalline and amorphous copolymer systems. Two excellent reviews on the subject have been written by Dawkins (36) and Folkes and Keller (37).

CRYSTALLINE COPOLYMERS

The primary requirements for crystallinity in homopolymers is the presence of chemical and structural regularity along the chain (80). The degree of crystallinity depends on chemical structure and crystallization conditions. Even in the most favourable situations, 100% crystallinity cannot be attained and a two-phase, semi-crystalline system is the result. In high crystallinity systems, the morphology is a lamellar matrix of crystallites with amorphous surfaces. Low crystallinity systems consist of dispersed crystallites in an amorphous matrix. Flory (81) has described the thermodynamic stability of crystallites for homopolymers monodisperse in molecular weight:

$$\frac{1}{T} - \frac{1}{T_m^0} = \frac{R}{\Delta H_U} \left(\frac{1}{n\lambda} + \frac{1}{n-1+1} \right) \quad (2.40)$$

where λ is the fraction of material which is amorphous at temperature T .

n is the degree of polymerization.

l is crystallite thickness.

T_m^0 is the equilibrium melting point of a crystallite when n and l are infinite.

ΔH_U is the heat of fusion per mole of repeat unit.

R is the gas constant.

Hoffman and Weeks (82) have described the stability of a crystallite more directly in terms of its length:

$$l = \frac{2\sigma_e}{\Delta F_U} \quad (2.41)$$

where δ_e is the surface free energy of the crystallite faces perpendicular to chain extension.

ΔF_U is the free energy of fusion at the crystallite melting point.

This equation is only valid for crystallites whose lateral dimensions are at least three times l .

In mixtures of two homopolymers, non-crystallizable chains are rejected from the crystal lattice in the great majority of cases. Flory (8/83) therefore assumed in his theory of crystallization of copolymers that for systems made up of M_1 crystallizable units differing chemically and structurally from M_2 units, the latter are excluded from the crystal lattice. The equilibrium crystallization of copolymers is described by Equation (2.42):

$$\frac{1}{T_m} - \frac{1}{T_m^0} = - \frac{R \ln p}{\Delta H_U} \quad (2.42)$$

where T_m is the equilibrium melting point of the copolymer (highest temperature at which crystallinity can exist).

p is the sequence propagation probability (probability of an M_1 unit being succeeded by another M_1 unit).

For random copolymers $p = x_A$ (the mole fraction of M_1 units) and Equation (2.41) becomes:

$$\frac{1}{T_m} - \frac{1}{T_m^0} = - \frac{R \ln x_A}{\Delta H_U} \quad (2.43)$$

The presence of randomly distributed M_2 units reduces the size of crystallites and causes them to be of varied lengths. This is the

reason for the very wide melting ranges and depressed melting points in copolymers. Flory's theory has been experimentally confirmed for random copolymers of ethylene and α - olefines (84-86).

Crystallization in block copolymers is similar to that described for homopolymers. However, a critical sequence length is required for crystallites of length l to be stable, according to Equations (2.40) and (2.41). Kovacs and coworkers (87,88) studied crystallinity in AB poly(ethylene oxide-b-styrene) observing lamellar crystallites and similar crystal habits to those of the corresponding homopolymer. The melting points of block copolymers obey Equation (2.42). The sequence propagation probability (p) in this case approaches unity so that T_m is similar to T_m^0 . This view is verified by the work of Theil and Mandelkern (89) on $(AB)_n$ poly(ethylene sebacate-b-propylene adipate).

AMORPHOUS COPOLYMERS

If two homopolymers (A and B) are mixed, the thermodynamics of mixing can be described by Equation (2.44):

$$\Delta G = \Delta H - T\Delta S \quad (2.44)$$

where ΔG is the Gibb's Free Energy of Mixing.

ΔH , ΔS are the enthalpy and entropy of mixing, respectively. Phase separation will occur when $\Delta G > 0$. For polymers, ΔS is small and positive so that miscibility is determined by the sign and magnitude of ΔH . When ΔH is just positive, phase separation occurs. The heat of mixing for non-polar homopolymers is (90):

$$\Delta H = V (\delta_A - \delta_B)^2 v_A v_B \quad (2.45)$$

where V is the total molar volume of the system.

δ_A, δ_B are the solubility parameters of homopolymers A and B, respectively.

v_A, v_B are the volume fractions of A and B, respectively. Thus if the solubility parameters are different, ΔH is positive and phase separation occurs.

In block copolymers of A and B blocks, phase separation is favoured because of incompatibility and is retarded by the chemical links between blocks. Thus, the same basic principles apply here as in the case of homopolymers except that the entropy contribution is larger due to the chemically linked blocks. Also, domain sizes tend to be much greater in the homopolymer case accounting for the term microphase, when referring to block copolymers. Krause (91, 92) has treated microphase separation thermodynamically and derived the following equation for the entropy of mixing:

$$\frac{\Delta S}{k} = \ln (v_A)^{v_A} (v_B)^{v_B} - 2(m-1) \left(\frac{\Delta S_{dis}}{R} \right) + \ln(m-1) \quad (2.46)$$

where k is Boltzmann's Constant.

m is the number of blocks in a copolymer molecule, assuming all molecules have the same average molecular weight, composition and sequence distribution.

$\left(\frac{\Delta S_{dis}}{R} \right)$ is the entropy lost when one unit of a copolymer molecule is immobilized.

This treatment shows that:

(1) ΔS increases as the number of blocks increases in a copolymer molecule of given length, so that phase separation is more difficult.

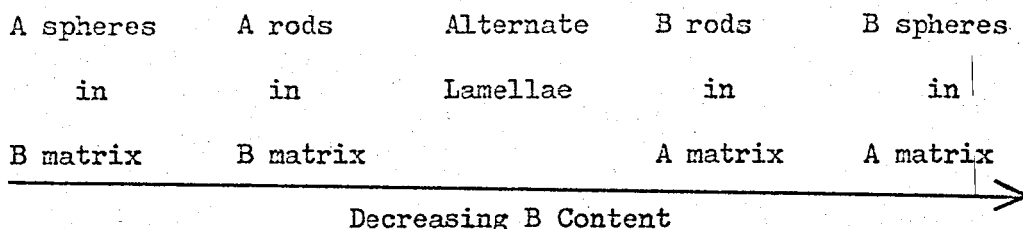
(2) For constant copolymer composition and the same number of blocks per molecule, phase separation becomes easier as molecular weight increases.

(3) For molecules having the same chain length and the same number of blocks, a copolymer with $v_A = .25$, $v_B = .75$ undergoes phase separation less readily than when $v_A = v_B = .50$.

Several authors have treated the problem of domain size, relating it to the conformational entropy and interfacial energy between phases. Bianchi et. al. (93) assumed sharp interfacial boundaries in their treatment while Meier (94) and Leary and Williams (95) allowed for the possibility of an interface. All of these workers limited their calculations to systems of glassy spheres in a rubbery matrix. Meier (94) has related domain size to A block length in AB poly(styrene-b-butadiene) with reasonable experimental agreement. La Flair (57) has extended the work of Leary and Williams (56) to cylindrical and lamellar morphologies, evaluating both domain dimensions and the size of the interface and their dependence on temperature.

The same factors which affect domain size also affect type. Three morphological types have been discovered using SAXS and electron microscopy - spheres, rods (cylinders) and lamellae. The relationship between domain type and B polymer content (A content

assumed constant) is qualitatively summarized below:



Meier (97), Kromer et. al. (98) and Inoue et. al. (99) report comprehensive thermodynamic theories of microphase separation taking into account an interfacial layer. Meier (97) related domain type to the ratio of block lengths of A and B in AB type polymers in the absence of solvents. He calculated the free energy of each domain type and plotted against M_A for a constant M_B and temperature; a representative plot is shown in Figure (2.9). At equilibrium, therefore, the morphology displaying minimum free energy is assumed to exist for a specific $\frac{M_B}{M_A}$ ratio. His calculations were insensitive to interfacial surface tension (γ) from $\gamma=0$ to 15 dyne cm^{-1} indicating universal application to most polymer types. Specifically, he concluded that the transition from spheres to cylinders occurs at $\frac{M_B}{M_A} = 4$, and from cylinders to lamellae occurs at $\frac{M_B}{M_A} = 3.33$ where M_B , M_A are the molecular weights of B and A, respectively. The pattern of results predicted by Meier is also shown by the work of Kromer et. al. (98) and Inoue et. al. (99).

Complete microphase separation is most likely to occur when equilibrium conditions exist, but sample preparation usually affects the kinetic factors thus inhibiting separation. Thermal history and casting solvent are among the most important factors affecting this behaviour. Krause's treatment (91, 92) of phase separation predicts

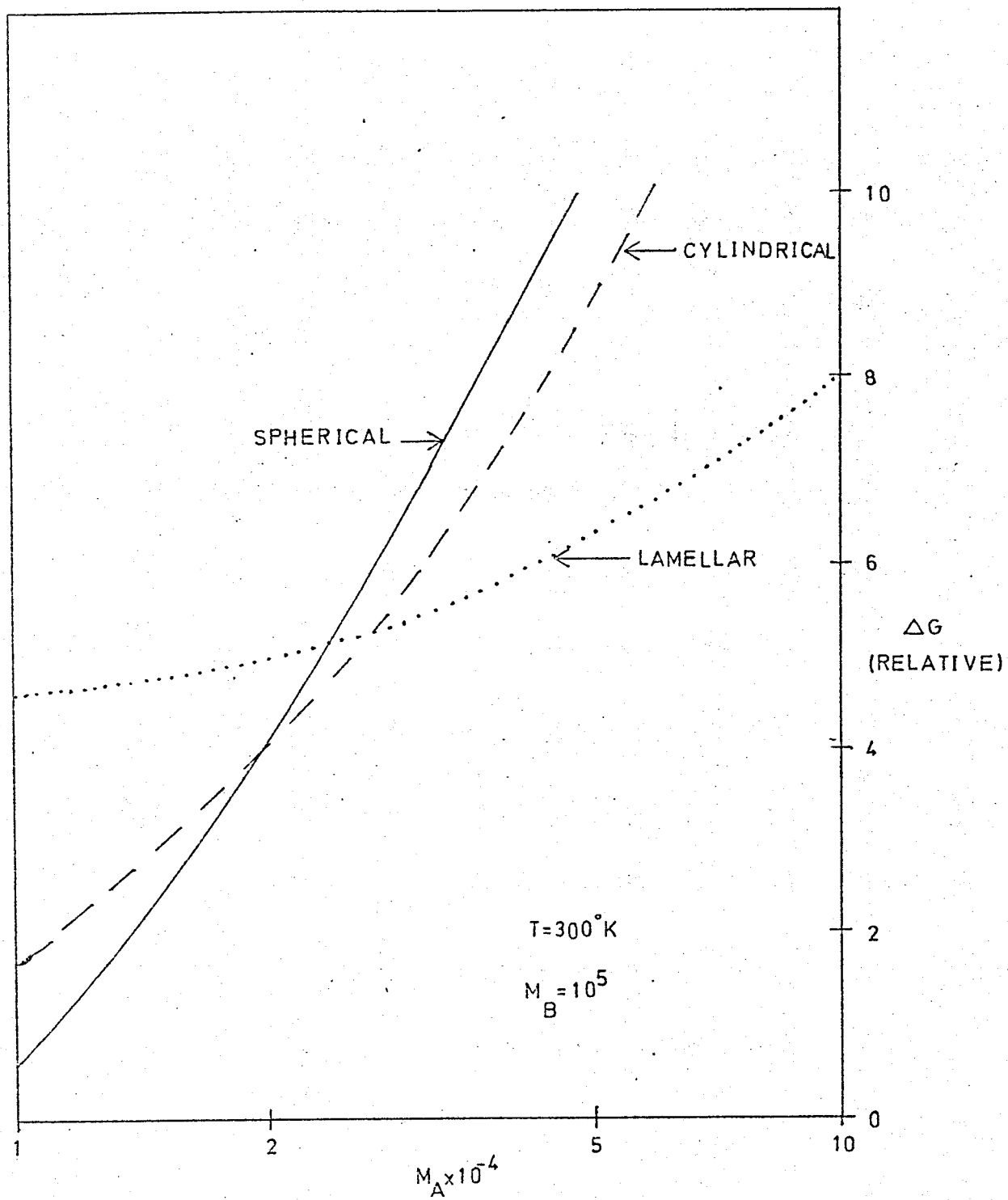


FIG.2.9

less complete separation of phases for $(AB)_n$ type polymers. In line with this prediction, Saam and Fearon (22) showed that $(AB)_n$ poly(styrene-b-dimethylsiloxane) had a much less well defined morphology than the AB or ABA polymers. Likewise, Le Grand (100,31) concluded from SAXS and dynamic mechanical measurements that partial microphase separation occurs in $(AB)_n$ poly(bisphenol-A-carbonate-b-dimethylsiloxane) despite the wide differences in solubility parameters.

The degree of phase separation is, as explained above, dependent on many characteristics of the system and dictates the number, position and sharpness of the glass transitions observed. If phase separation is complete, a transition for each phase is observed at similar temperatures and with similar sharpness as the individual homopolymers. If no phase separation occurs, one transition is observed intermediate between those of the homopolymers. Partial microphase separation leads to a glass transition for each phase and possibly a third transition for a mixed interface.

Childers and Kraus (76) have presented damping ($\tan \delta$) curves for block copolymers where complete microphase separation exists. The peaks occurred at temperatures expected for the respective homopolymers. The Fox-Flory equation (101) shows how the T_g of a homopolymer is affected by its \bar{M}_n :

$$T_g = T_g^\infty - \frac{C}{\bar{M}_n} \quad (2.47)$$

where T_g^∞ is the T_g at $\bar{M}_n = \infty$.

C is a constant varying with each polymer.

This treatment indicates a dependence of the T_g of each phase on its block length.

Complete phase mixing is akin to the situation encountered with random copolymers. Gordon and Taylor (102) have predicted that the T_g of random copolymers is intermediate between those of the homopolymers A (T_g, A) and B (T_g, B) and is dependent on the weight fraction of each monomer present:

$$(T_g - T_{g,A}) w_1 + K (T_g - T_{g,B}) w_2 = 0 \quad (2.48)$$

where w_1 , w_2 are the weight fractions of each monomer.

K is a constant dependent on the thermal expansion coefficients of the homopolymers in the glassy and rubbery states.

This equation is sometimes applicable to block copolymers where complete mixing occurs. The improbable situation of complete phase mixing in block copolymers with long block lengths has been observed accompanied by a single transition intermediate between those of the homopolymers but did not obey Equation (2.48) (103-4). A single glass transition was observed for $(AB)_n$ poly(ester 1-b-ester 2), with short and not too dissimilar blocks, and is close to the transition temperature predicted by Gordon and Taylor (105).

In a case where a mixed interface existed between two pure phases, three transitions were observed (72). Two of the transitions were attributed to the pure phases and the third transition, intermediate between the first two, was attributed to the mixed interface.

Kambour (52) observed two transitions in an $(AB)_n$ poly(bisphenol-A-carbonate-b-dimethylsiloxane) where the matrix had been shown to be a mixed phase.

2.7 Mechanical Models for Two-Phase Systems

GUTH - SMALLWOOD EQUATION

There have been several attempts to derive formulae giving the apparent modulus due to a dispersion of particles in rubber. Smallwood (106) described the reinforcing affect of spherical particles dispersed in a rubbery matrix using an analogy to the Einstein viscosity equation (107):

$$E = E_0 (1 + 2.5 \phi) \quad (2.49)$$

where E is the modulus of the filled rubber.

E_0 is the modulus of the rubber matrix.

ϕ is the volume concentration of filler.

However, this equation holds only for low concentrations of filler and amendments were derived (108 - 111). That of Guth and Gold (110), by considering the interactions between pairs of particles, added the term involving the square of the concentration of filler to Smallwood's equation and obtained:

$$E = E_0 (1 + 2.5 \phi + 14.1 \phi^2) \quad (2.50)$$

For nonspherical particles, Guth (112), introduced a shape factor (f) and proposed:

$$E = E_0 (1 + 0.67 f \phi + 1.62 f^2 \phi^2) \quad (2.51)$$

where f is expressed as the ratio of diameter to width of particles. These equations were derived on the assumption that the medium wets the filler particles, but does not chemically react with the filler surface. Cohan (///) applied these last equations to data obtained for a variety of fillers in several rubbers by measuring the initial stress required for extension to 400%, and found that the shape factor (f), thus deduced, corresponded closely to values observed directly in the electron microscope. In general, the relationships for these complex systems is only useful as an empirical description.

DEFORMATION OF PARALLEL LAMELLAR SYSTEM IN SIMPLE SHEAR

Parallel glassy lamellae, of thickness L , interconnected by flexible chains, in a rubbery layer of thickness l , can be deformed in three ways using simple shear. Two of the deformation geometries can be analyzed directly using Takayanagi models for parallel and series coupling (//3-6). The third geometry requires a more sophisticated analysis. In the following analyses, one coupling, defined as one glassy lamella coupled with one rubbery layer, is analyzed for each geometry as it is assumed to be representative of the behaviour of n couplings.

In the Takayanagi model, the mechanical properties of a two-phase system are considered to be duplicated by a unit cube of glassy and rubbery material with moduli G_g and G_R , respectively. The rubbery region is of volume $\phi \lambda$, and the glassy region is $(1 - \phi \lambda)$. The modulus of the combined model (G_M) is:

$$G_M = \left[\frac{\phi}{\lambda G_R + (1 - \lambda) G_g} + \frac{1 - \phi}{G_g} \right]^{-1} \quad (2.52)$$

Shear in geometry 1 is illustrated in Figure (2.9)¹⁰. G_g is assumed to be about three orders of magnitude greater than G_R so that all of the strain can be considered to be in the rubbery phase. If A is the area (defined as unity) over which the shear force (F) is applied, the shear stress is $F / A = F$. In all the illustrations in this section, the shear strains are assumed to be very small. Thus, if Θ is the angle of shear strain, $\Theta \cong \sin \Theta \cong \tan \Theta$. The shear strain in the rubbery phase is $\Theta = x / l$. Thus,

$$G_R = \frac{Fl}{x} \quad (2.53)$$

The strain experienced by the entire system of n couples is $x / (L + 1)$ while stress is F . Therefore, the measured shear modulus (G_M) is:

$$G_M = \frac{F(L + 1)}{x} = \left(\frac{L + 1}{l} \right) G_R \quad (2.54)$$

The Takayanagi model for series coupling is also pictured in Figure (2.9)¹⁰, describing the situation of the stress being everywhere constant but not the strain. λ is defined as unity for series coupling so that Equation (2.52) becomes:

$$\frac{1}{G_M} = \frac{1}{(L + 1) G_R} + \frac{L}{(L + 1) G_g} \quad (2.55)$$

Since $G_g \gg G_R$, this rearranges to:

SHEAR IN GEOMETRY 1

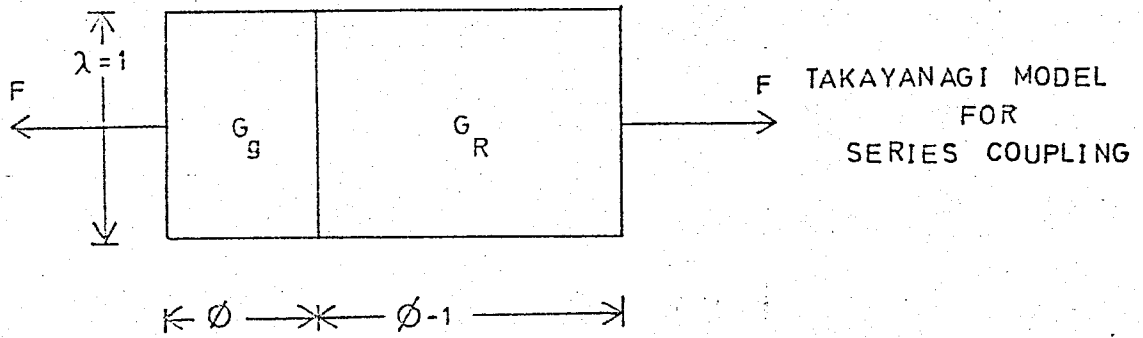
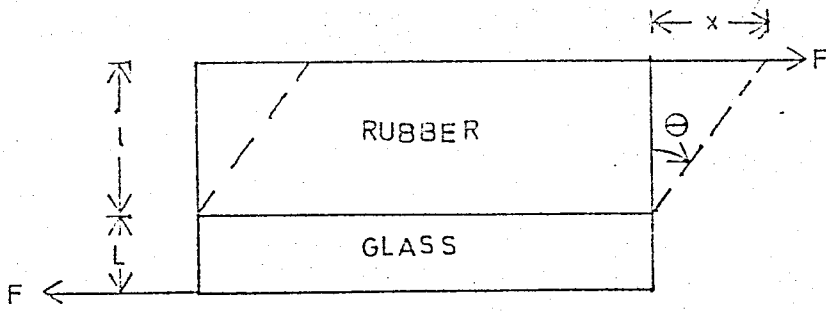


FIG.2.10

SHEAR IN GEOMETRY 3

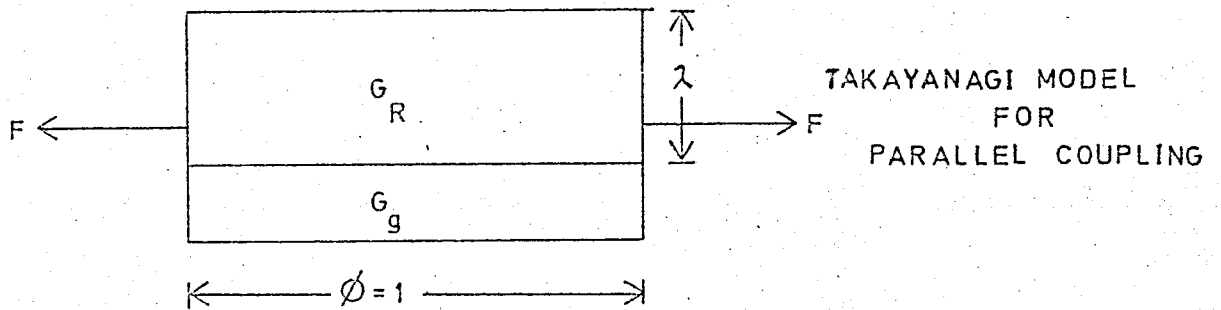
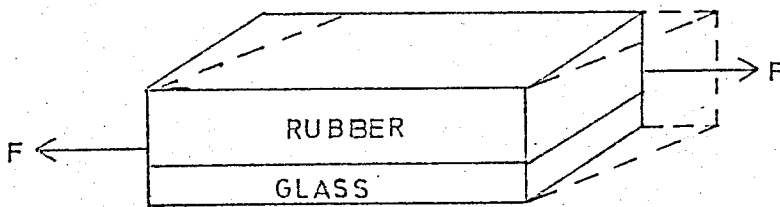


FIG.2.11

$$G_M = \left(\frac{L+1}{1} \right) G_R \quad (2.56)$$

This is the same answer obtained using the first principles approach.

Figure (2.11) illustrates the situation for shear in geometry 3. (The reason for numbering the geometries in this way will become apparent in Chapters 4 and 5). In this situation glassy lamellae are being deformed such that the strain in the system is everywhere constant but not the stress. This is equivalent to the Takayanagi model for parallel coupling also pictured in Figure (2.11). ϕ is defined as unity for this case and $\lambda = 1 / (L + 1)$. Equation (2.52) therefore becomes:

$$G_M = \left(\frac{L}{L+1} \right) G_g \quad (2.57)$$

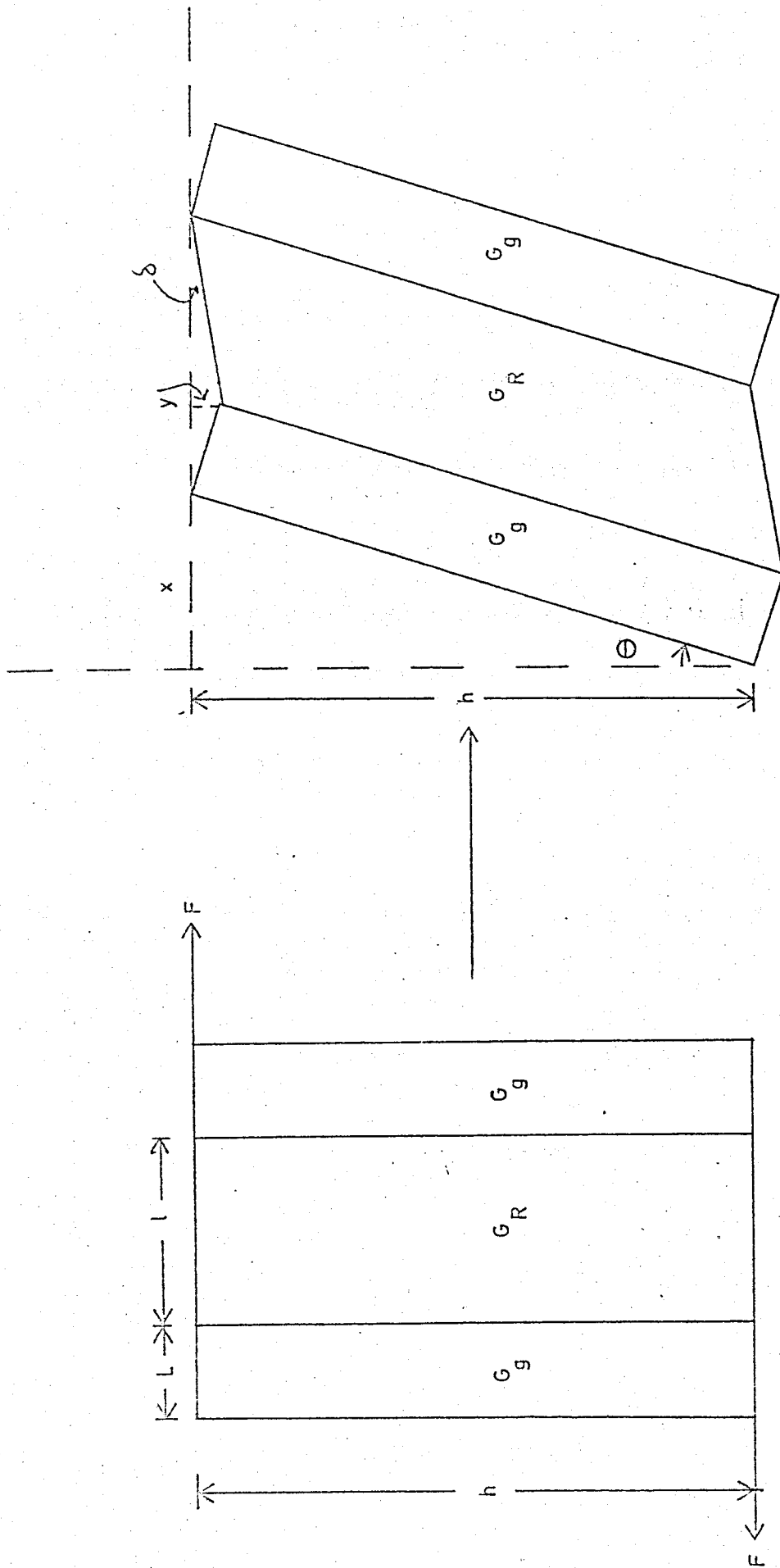
Geometry 3 should therefore be much stiffer than geometry 1.

The situation in geometry 2, pictured in Figure (2.12) is somewhat akin to geometry 1 in that the glassy lamellae are assumed to be infinitely stiff so that the strain is once again limited to the rubbery phase. The strain in the rubber is:

$$\text{rubber strain} = \Theta + \delta = \frac{x}{h} \left(\frac{L}{1} + 1 \right) \quad (2.58)$$

The strain for n couples is $\Theta = \frac{x}{h}$. The shear stress is $F / (1 + L)$ so that:

$$G_R = \frac{\frac{F}{1+L}}{\left(\frac{x}{h} \right) \left(\frac{L}{1} + 1 \right)} \quad (2.59)$$



SHEAR IN GEOMETRY 2

FIG.2.12

$$G_M = \frac{\frac{F}{l + L}}{\left(\frac{x}{h}\right)} \quad (2.60)$$

Combining Equations (2.58) and (2.59):

$$G_M = G_R \left(\frac{L + l}{l} \right) \quad (2.61)$$

Therefore, geometries 1 and 2 should have the same moduli.

2.8 Orientation in Block Copolymers

Keller and coworkers (117-119) have demonstrated a remarkable degree of orientation in an extruded plug of a styrene - butadiene-styrene block copolymer (SBS), with 25% styrene and \bar{M}_n styrene = 10,000. Small angle x-ray scattering (SAXS) photographs indicated the presence of glassy rods, parallel to the extrusion direction and in an hexagonal array. Furthermore, this morphology is present in a "single crystal" type structure. These properties were in line with the electron microscope photographs, mechanical properties and birefringence of this plug.

Lewis and Price (120) experimented on two different SBS copolymers (Sample 1 - 26 weight % styrene, $\bar{M}_n = 13,000$; Sample 2 - 28 weight % styrene, $\bar{M}_n = 10,000$). They showed that casting from benzene produced isotropic films while compression moulding produced orientation as a result of flow in the mould. Orientation was determined by the variation in intensity of the x-ray scattering as a function of the direction of the incident beam, birefringence and variation of the mechanical properties as a function of the stress

direction.

Krigbaum et. al. (121) found orientation in SBS (53% styrene, \bar{M}_n styrene = 14,100) films cast from butanone and toluene. Only slit-smearred SAXS was collected with the incident beam normal to film faces and edges. The butanone cast system showed greater reflected intensity with the beam normal to the film edge and greater long-spacing with the beam normal to the film face. The toluene cast system showed approximately equal intensity for both directions with, again, a greater long-spacing for the face view. The ratio of spacings of consecutive orders was consistent with a regular, periodic arrangement of lamellae of infinite lateral extension. These workers proposed that ordered convection currents are set up within the polymer solution giving rise to the orientation observed. This theory was proposed based on the "orange-peel" surface observed on the solution cast films and the writings of Thomson (122), Benard (123) and Pearson (124). Thomson and Benard explained the phenomenon in terms of density gradients set up within the solution by solvent evaporation cooling the surface, while Pearson explained it in terms of surface tension.

Many workers have demonstrated the mechanical anisotropy of oriented polymers and the subject has been extensively reviewed by Ward (125). Takayanagi et. al. (126) and Stachurski and Ward (127-9) have shown how the direction of applied stress specifically affects the dynamic modulus (E') and loss tangent ($\tan \delta$). The latter workers used the anisotropy of $\tan \delta$ for assigning relaxations to different molecular processes. Folkes and Keller (118)

have demonstrated one of the most striking examples of mechanical anisotropy in their measurements of Young's modulus (E) on "single crystal" SBS. They found that with stress applied parallel to the rods, $E = 4.1 \times 10^8 \text{ Nm}^{-2}$. When stress was applied perpendicular to the rods, $E = 5 \times 10^6 \text{ Nm}^{-2}$.

2.9 Small Angle X-ray Scattering (SAXS) in Polymers

The scattering of x-rays is due to inhomogeneities in electron density from one point to another in a material. The Bragg equation, Equation (2.62), relates the scattering angle (2Θ) to the spacings (d) of the reflecting planes formed by these inhomogeneities.

$$n\lambda = 2d \sin \Theta \quad (2.62)$$

where n is the reflection order (i.e. 1,2,3, . . .).

λ is the wavelength of the x-rays.

With $\text{CuK}\alpha$ radiation, $\lambda = 1.542 \text{ \AA}$, inhomogeneities of colloid dimensions (30 to 1000 \AA) will cause scattering at $2\Theta < 2$ degrees. Thus, systems such as semicrystalline polymers, block copolymers and filled rubbers can be analyzed using SAXS. Excellent reviews on the theory of SAXS and the application of x-ray diffraction methods to polymers exist (131-7). Folkes and Keller (37) have reviewed the subject for block copolymers.

Scattering at small angles can occur in three ways. Coherent scattering results from x-rays being affected by electron density differences in the sample such that the Bragg equation is obeyed. Incoherent, or inelastic, scattering results in x-rays of different

wavelengths from the incident radiation. The maximum intensity of this scattering occurs at zero degrees decreasing in intensity at higher angles. Monochromatic detectors, as used in this work, will thus filter out this incoherent scattering for counter detection methods while the backstop, minimizes its effects in film detection methods. Parasitic scattering is caused by reflection off the collimating system. It can be determined, for counter detection only, by placing the sample in an absorbing position just in front of the detector. When subtracted from the sample scattering, the coherent scattering remains.

The intensity of small angle scattering (\tilde{I}_2) is governed by the following equation:

$$\tilde{I}_2 = (\rho_1 - \rho_2)^2 v_1 v_2 \quad (2.63)$$

where ρ_1 , ρ_2 are the electron density of phases 1 and 2, respectively.

v_1 , v_2 are the volume fractions of phases 1 and 2 respectively. Thus the intensity is relatively large for a system of discrete particles in a matrix of different electron density. It is relatively small, however, for a heterogeneous system of regions of slightly different density.

There are two basic collimating systems used in x-ray analysis, pin-holes and slits. The diffraction pattern ^{for pin-holes} on a flat, photographic film for an unoriented lattice is a series of circles of equal intensity; the lowest order circle is shown in Figure (2.13). If the scattered intensity (I) of this photograph is plotted against

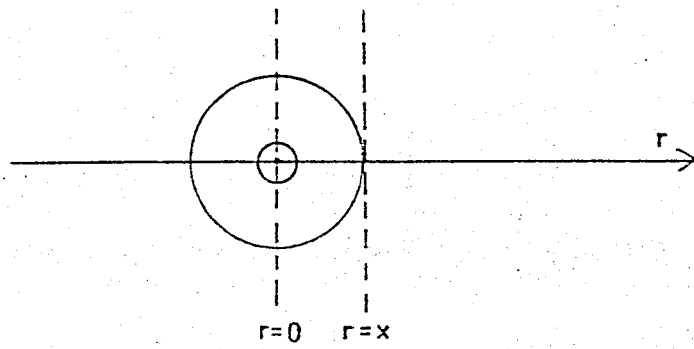


FIG. 2.13

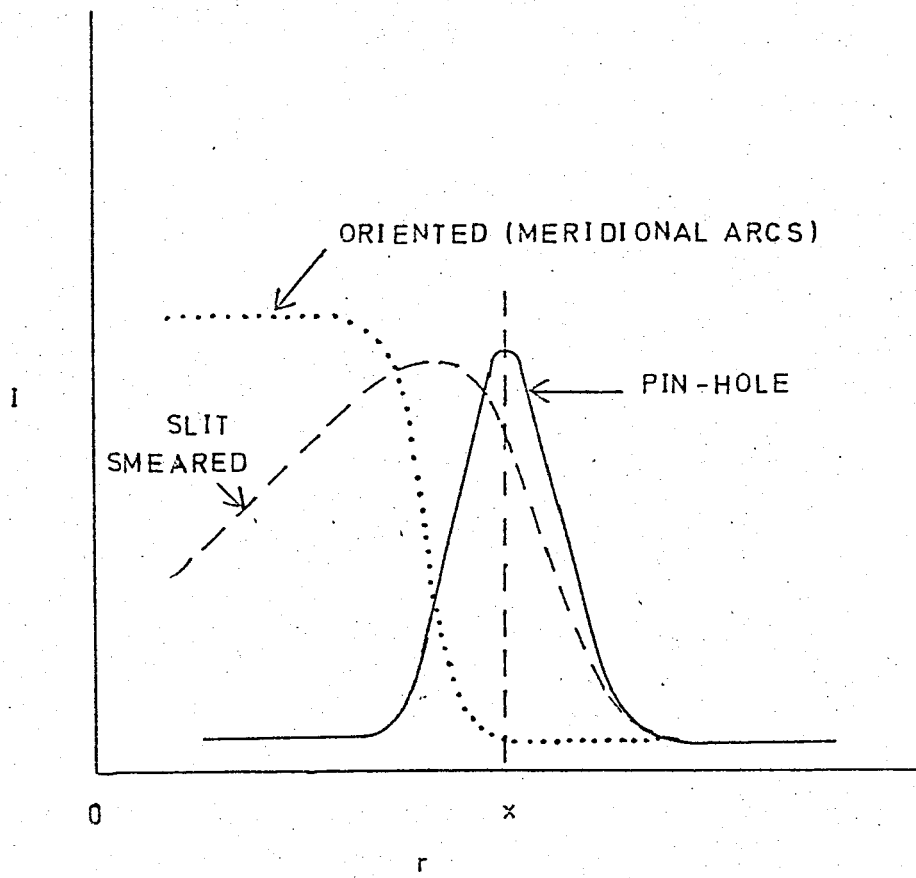
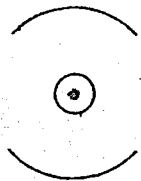


FIG. 2.14

distance (r), the solid line peak shown in Figure (2.14) is obtained. The situation is more complicated using slit optics. A slit can be thought of as a large number of pin-holes. Thus, photographic detection would reveal an intensity distribution that was a superposition of many pin-hole photographs in the direction of slit height. The intensity-distance plot for this situation is illustrated by the broken line curve in Figure (2.14). The, so-called, slit-smeared data shows the peak shifted to lower angles and indicates much more breadth to the diffraction pattern on the low angle side. This curve can be adjusted using desmearing formulae so that the spacing of the slit data coincides with that using pin-holes.

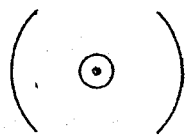
This type of desmearing cannot apply to oriented systems, as will be shown. If a sample is oriented such that its diffraction pattern consists of meridional arcs, as shown in Figure (2.15), the slit-smeared data is in the form of a plateau, as illustrated by the dotted line curve in Figure (2.14). Desmearing will obviously give a smaller spacing than obtained with pin-hole data. If the sample were oriented such that equatorial arcs were obtained using pin-holes, as in Figure (2.16), the slit-smeared spacing would be almost identical with that of pin-holes. In this case, desmearing would give a larger spacing than pin-holes.

An additional correction to the scattering curve is needed to account for all orientations of the reflecting planes (138). Thus, the experimentally determined intensity of scattering at an angle, S , $I(S)$ is corrected using Equation (2.64), where $S = \frac{2 \sin \Theta}{\lambda}$:



MERIDIONAL ARCS

FIG. 2.15



EQUATORIAL ARCS

FIG. 2.16

$$i(S) = 4 \pi S^2 I(S) \quad (2.64)$$

where $i(S)$ is the real intensity.

SURFACE AREA DETERMINATIONS

The problem of determining the interfacial surface area (S) of two phase systems via SAXS was first solved by Porod (139-40) using the following relationship:

$$S = \frac{8 \pi v_1 v_2 \left\{ \lim \left[\tilde{I}(M) M^3 \right] \right\}}{a \lambda \tilde{Q} \rho} \quad (2.65)$$

where $\left\{ \lim \left[\tilde{I}(M) M^3 \right] \right\}$ is the limiting value of the scattered intensity, at high angles, times M^3 .

$M = a (2 \Theta)$, where 'a' is the sample to plane of registration distance.

\tilde{Q} is the total integral of the scattering curve.

ρ is the polymer density.

Porod's method is generally applicable to any two-phase system. A second method, developed by Debye et. al. (141), can only be used on systems with dispersed particles of random size and shape. By Debye's method:

$$S = \frac{4 w_1 w_2}{\rho C} \quad (2.66)$$

where w_1 , w_2 are the weight fractions of phases 1 and 2, respectively.

$$C = \frac{\lambda}{2 \pi} \left(\frac{A}{B} \right)^{\frac{1}{2}} \quad (2.67)$$

where A and B are the slope and intercept, respectively, of the straight line drawn from the plot of $I^{-2/3}$ versus $(2\Theta)^2$.

(I is the scattered intensity minus parasitic scattering).

Warner et. al. (142) used both methods to determine the surface area of a silica filler dispersed in silicone rubber. They obtained excellent agreement, for both methods, with the accepted gas adsorption procedure.

DETERMINATION OF BLOCK COPOLYMER MORPHOLOGY

The fact that block copolymers have spherical, cylindrical or lamellar morphologies is coincident with the same situation in soaps. The morphology of soaps has been studied in detail by Luzatti et. al. (143) and Hussan et. al. (144) and this technology can thus be directly related to the study of block copolymers. The ratios of the Bragg spacings of consecutive reflection orders were found to form certain systematic sequences. These sequences are outlined in Table (2.1) with their corresponding morphologies. The outline is limited to morphologies known to occur in block copolymers.

ORIENTATION EFFECTS

The discussion will be limited to uniaxial orientation in which all the 'c' axes of a three-dimensional lattice are inclined at an angle, α , to the orientation axis, Z. In addition, the directions of the other two axes are uniformly distributed around the c axis. The situation is illustrated in Figure (2.17), where O is defined as the origin of the unit cell. A very complete treatment of orientation effects in polymers has been given by Kakudo and

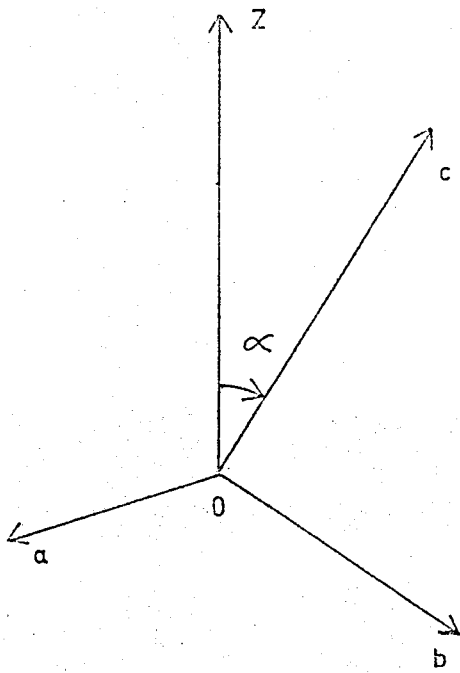


FIG. 2.17

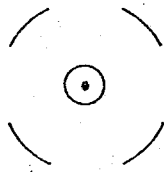


FIG. 2.18

Kasai (1957).

TABLE 2.1

RATIO OF CONSECUTIVE ORDERS	MORPHOLOGY
1 : .500 : .333 : .250	Regular periodic arrangement of parallel lamellae of infinite lateral extension.
1 : .577 : .500 : .378	Regular hexagonal arrangement of cylinders of infinite length.
1 : .866 : .612 : .522	Spheres packed in a face-centred cubic lattice.
1 : .706 : .577 : .500	Spheres packed in a simple cubic lattice. or Spheres packed in a body-centred cubic lattice.

There are three types of uniaxial orientation; these will be discussed below. In simple fibre structure, α is zero degrees (i.e. - c and Z axes coincide). With the x-ray beam normal to the fibre axis a four arc diffraction pattern is obtained, as shown in Figure (2.18). A uniform intensity circular pattern (Debye ring) is obtained with the beam parallel to Z, as shown in Figure (2.13). When $0^\circ < \alpha < 90^\circ$, spiral fibre structure (spiral orientation)

exists. This is distinguished by observing many arcs in the diffraction pattern with the beam normal to Z. Ring fibre structure (ring orientation) exists when $\alpha = 90^\circ$ and is distinguished by two situations. If, when the beam is normal to Z, equatorial arcs are distinguishable, a Debye ring must be observed with the beam parallel to Z. If, on the other hand, a Debye ring is observed with the beam normal to Z, equatorial arcs must be observed with the beam parallel to Z.

Consider the simple case of a one-dimensional lattice (i.e. - lamellae) oriented at an angle ϕ to the Z axis. An orientation function, $\langle \cos^2 \phi \rangle$, can be determined which represents the mean-square cosine (averaged over all the lamellae) of the angle between a given lamellae and Z. This orientation function has values of 1, 1/3, and 0 for lamellae with parallel, random and perpendicular orientations to Z, respectively. It is evaluated using the following equation (146-7):

$$\langle \cos^2 \phi \rangle = \frac{\int_0^{\pi/2} I(\phi) \sin \phi \cos^2 \phi \, d\phi}{\int_0^{\pi/2} I(\phi) \sin \phi \, d\phi} \quad (2.68)$$

For uniaxial orientation, $I(\phi)$ is the intensity of the diffraction pattern of a pin-hole photograph at the angle ϕ from the Z direction.

CHAPTER 3. EXPERIMENTAL

3.1 DETAILS OF THE POLYMERS MEASURED

Two different types of polymers were studied. The first was a series of poly(butadienes) and poly(butadiene-co-styrenes) hydrogenated to varying extents and supplied by Mr. J. Hawkins, International Synthetic Rubber Company (ISR). The other was a block copolymer, poly(dimethylsiloxane-b- α -methylstyrene), supplied by Mr. D. Jones, Dow Corning. Dow Corning also supplied some poly(dimethylsiloxane) homopolymer for comparison with the block copolymer.

HYDROGENATED POLYMERS

ISR supplied three base polymers characterised as shown in Table 3.1 with cis to trans butadiene isomer ratios of approximately unity. They were prepared in hydrocarbon solution using n-butyl lithium as the polymerization catalyst. Approximately 20 gm samples were then dissolved in 800 ml of dry toluene containing the hydrogenation catalyst (5 mM of butyl lithium and 1 mM of bis 3,5-diisopropyl salicylate nickel II). Hydrogen was bubbled through the mixture at 348°K, atmospheric pressure. The time of reaction was varied to vary the degree of saturation (3) as shown in Table 3.2. The mole % saturation refers to the percentage of hydrogenated double bonds and was determined via the iodine number of each polymer.

Each sample was compression moulded into strips at 393°K, 1000 psi for 15 minutes. They were then allowed to cool slowly to 323°K and held there for one hour. They were then allowed to

cool to room temperature where they were left for a period of weeks prior to testing. The moulded strips had average dimensions of approximately: length = 6.3 cm; width = 1.0 cm; thickness = 0.2 cm.

Table 3.1 Characteristics of the Base Polymers

Base Polymer	Styrene Content		Vinyl Content		\bar{M}_n (Osmometry)
	WT. %	Mole %	WT. %	Mole %	
A	0	0	9	9	150,000
B	6	3	9	8	200,000
C	13	7	8	7	130,000

Table 3.2 Degree of Hydrogenation

<u>Sample</u>	<u>Saturation (Mole %)</u>
A1	53
A2	84
B1	57
B2	60
B3	76
C1	65
C2	68
C3	72

The Dow Corning polymer is an $(AB)_4C$ "star" block copolymer where,

A is poly(α - methylstyrene)

B is poly(dimethylsiloxane)

C is a tetrafunctional coupling agent.

The copolymer contains 37.5 % A(w/w) and the A segment molecular weight is 9,000. It was synthesized by the sequential anionic copolymerization of α - methylstyrene and hexamethylcyclotrisiloxane. Narrow molecular weight distributions for each segment and the entire copolymer were confirmed by gel permeation chromatography (GPC), light scattering and membrane osmometry (19,148-50).

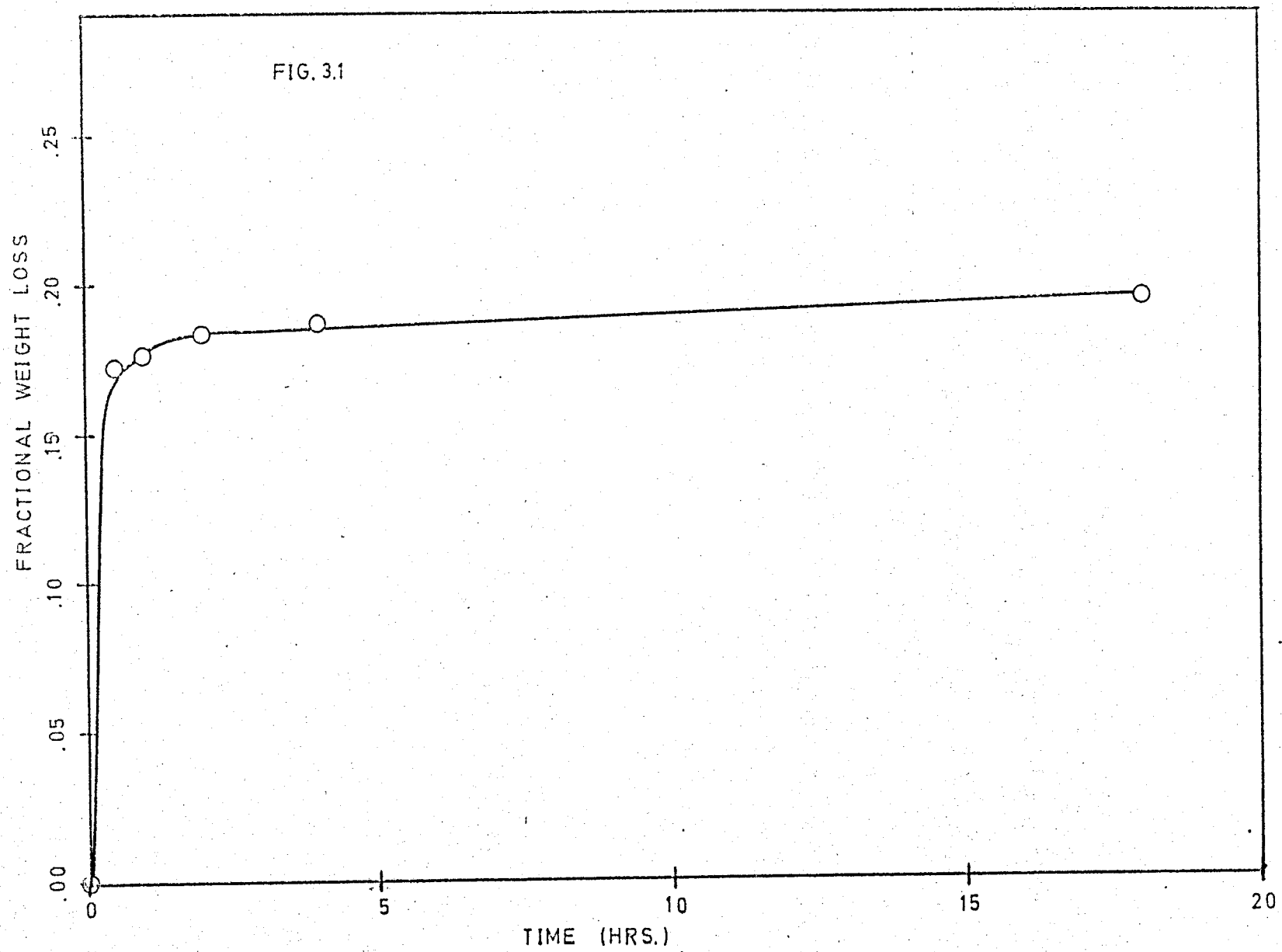
Sheets of polymer were prepared in three ways: casting from benzene, casting from cyclohexane and compression moulding. Films .1 to .2 cm thick were prepared by casting 10 % solutions (in benzene and cyclohexane) on to clean mercury and allowing the solvent to evaporate slowly (ca. 2 days) before removing from the mercury surface. The benzene cast sample was allowed to air dry for a month and then dried at 363°K , 1 torr pressure overnight to remove any remaining solvent. The cyclohexane cast sample was allowed to stand for a period of months at room temperature after casting and needed no further drying prior to testing. A compression moulded sheet ca. .15 cm thick was prepared at 523°K , 2000 psi for 20 minutes then rapidly cooled to room temperature (ca. 3 minutes).

DIMETHYLSILOXANE HOMOPOLYMER

The homopolymer was synthesized via ring opening polymerization by Mr. D. Jones, Dow Corning, and characterized in this laboratory. Prior to characterization the polymer was heated at 437°K , 1 torr pressure for 18 hours to remove 19.5 wt. % of low molecular weight cyclic homologues, $[(\text{CH}_3)_2\text{SiO}]_n$, where $n = 3, 4, 5$. The fractional weight loss was followed as a function of time and is shown in Fig. 3.1. The number average molecular weight (\bar{M}_n) was determined with a Hewlett-Packard 502 High Speed Membrane Osmometer, using toluene as solvent, at 298°K . \bar{M}_n was found to be $218,000 \pm 10,000$.

The polydispersity (\bar{M}_n / \bar{M}_w) was determined via gel permeation chromatography (GPC). (\bar{M}_w = weight average molecular weight). A Waters ALC/GPC 501 was used at room temperature, with tetrahydrofuran (THF) as solvent. Although neither the absolute values of \bar{M}_n or \bar{M}_w were determined, their ratio was found to be 1.4.

FIG. 3.1



3.2 WIDE FREQUENCY SCANNING DYNAMIC MECHANICAL APPARATUS

The storage (E' , G') and loss (E'' , G'') moduli were determined at various temperatures and frequencies on the wide frequency scanning dynamic mechanical apparatus. This information was used to assess molecular motion in the different samples under these varied conditions.

DESIGN OF APPARATUS

Measurements were made on the same apparatus described by Tan (1957) except for modifications and improvements to the arrangement of the electronic apparatus and driving coil. The apparatus was used to measure either Young's or rigidity (shear) moduli, depending on the deformation applied to the test specimen. Referring to Figure 3.2, for Young's moduli, a rectangular beam specimen (S) was clamped rigidly at both ends to two brass plates (P) and oscillated in bending geometry by a drive clamp (D), centrally located between the brass plates. Each of the brass plates is brazed to a brass three-quarter cylinder (T) which is free to move in a vertical direction. This allows the length of the specimen to be varied. The movement of the cylinders is controlled by the two 2BA screws (E).

Figure 3.3 shows how two disc specimens (J), can be oscillated by a central plate (H) in shear sandwich geometry for determination of shear moduli. The samples were pressed between the central plate and two stationary plates mounted on brass cylinders (K). The brass cylinders are interchangeable with the brass three-quarter cylinders, and their movement can also be controlled by E. The drive clamp and central plate are interchangeable and driven by magnets suspended from thin wires in the centre of a coil. The magnets are

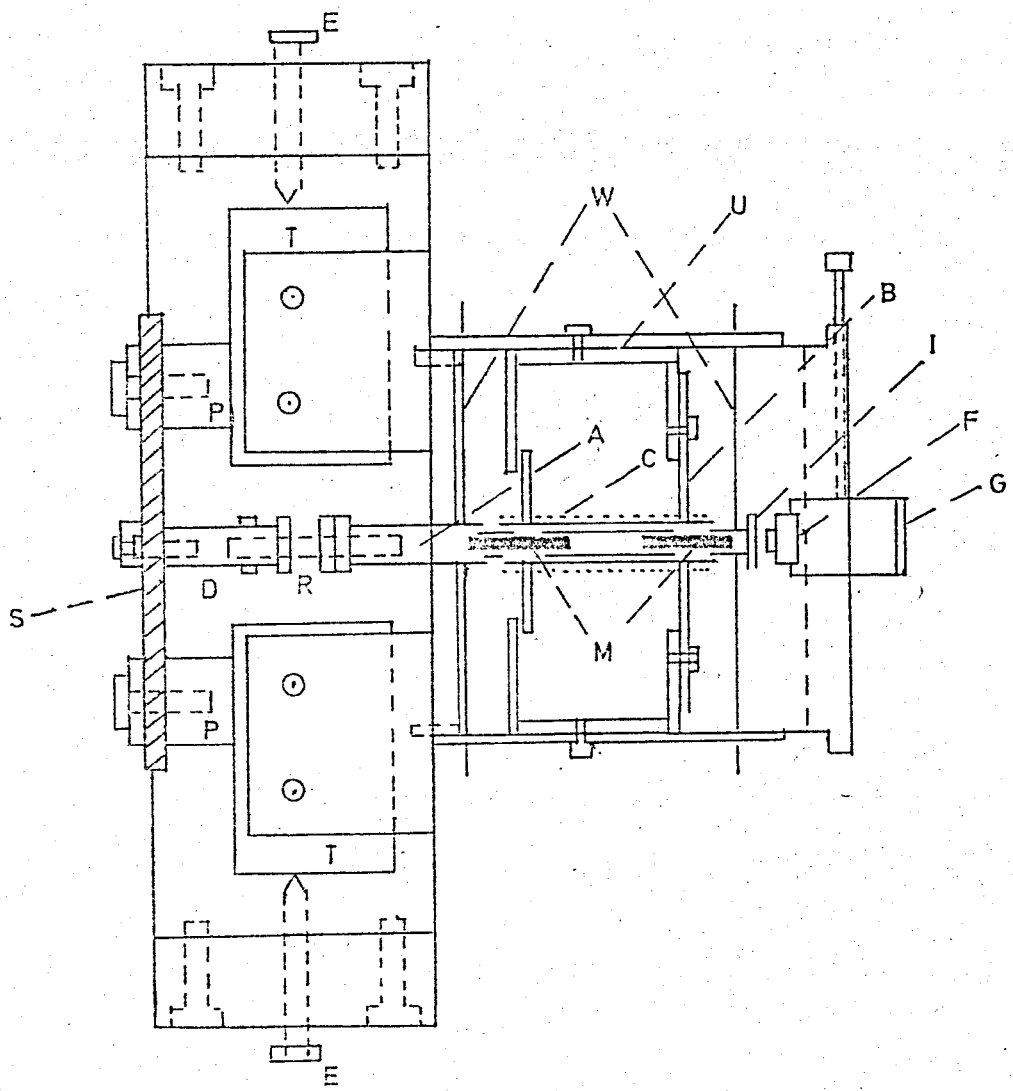


FIG. 3.2

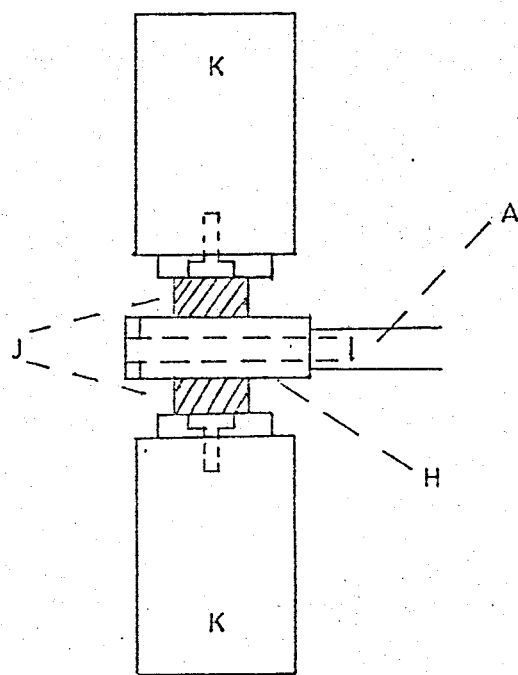


FIG. 3.3

connected to the drive, or central clamp by an aluminium spacer (A) and a 6BA threaded aluminium rod (R).

The two magnets (M) are suspended in the centre of the system of coils (C) by two sets of three stainless steel wires (W) (38 gauge). Figure 3.4 shows how the coil is wound about the bobbin in three sections. The magnets are oriented with like poles facing each other and bisected by the coil section boundaries. .0044" diameter, enamel coated copper wire is wound clockwise around the outer sections and counterclockwise around the inner section. Approximately 175m of wire was used with a calculated resistance of 307Ω , quite close to the calculated value. It was also determined that the wire is not shorting out on the bobbin. The bobbin is fastened (by three screws) to a brass cylinder (U) which is in turn screwed to another brass cylinder $1\frac{3}{4}$ " length and 2" diameter. This latter cylinder is fastened to the main body of the apparatus and also provides anchor points for the suspension wires. A brass case slides tightly into the open end of this cylindrical tube and holds a brass cylindrical rod (G), with a probe (F) at one end. The probe and the soft iron disc (I), on the vibrating system, form the transducer unit.

The apparatus is attached to a thick, flanged, brass plate by two L-shaped brackets. This enables it to be placed into a brass container and evacuated.

The vibrating system is shown schematically in Fig. 3.5. It consists of the aluminium drive clamp (D), the 6BA threaded aluminium rod (R), four soft-iron nuts, the aluminium spacers (A), the magnets (M) and the soft iron disc (I). The drive clamp is free to move in the horizontal direction and is locked in position by two 6BA

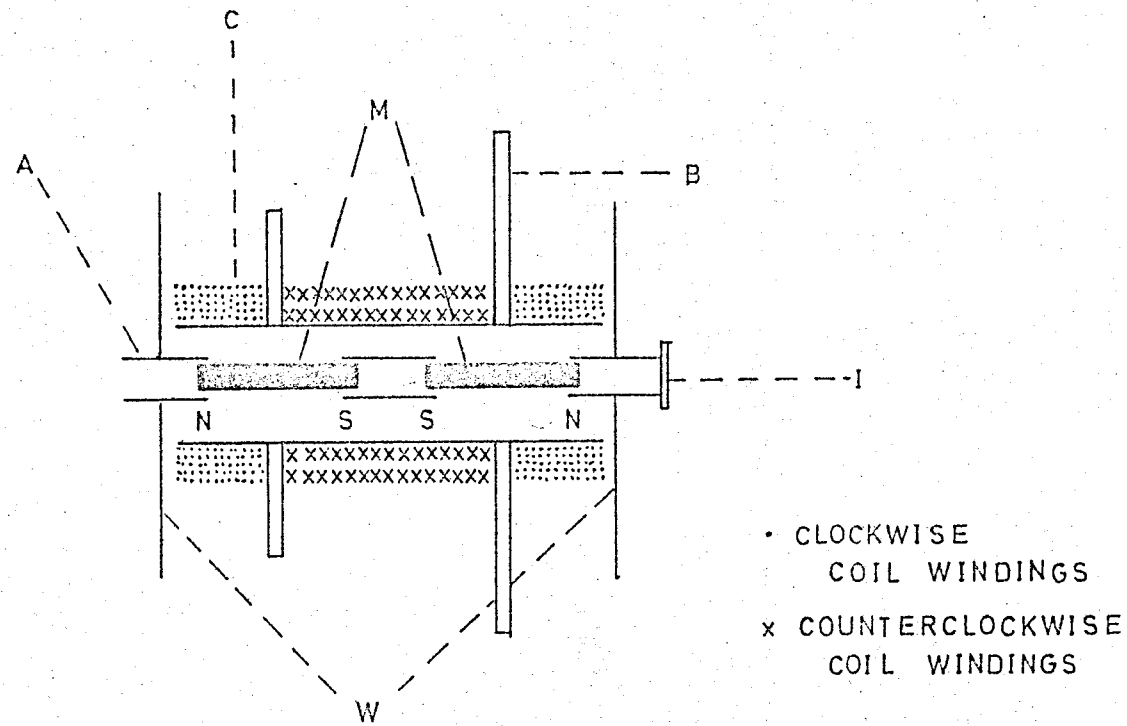


FIG. 3.4

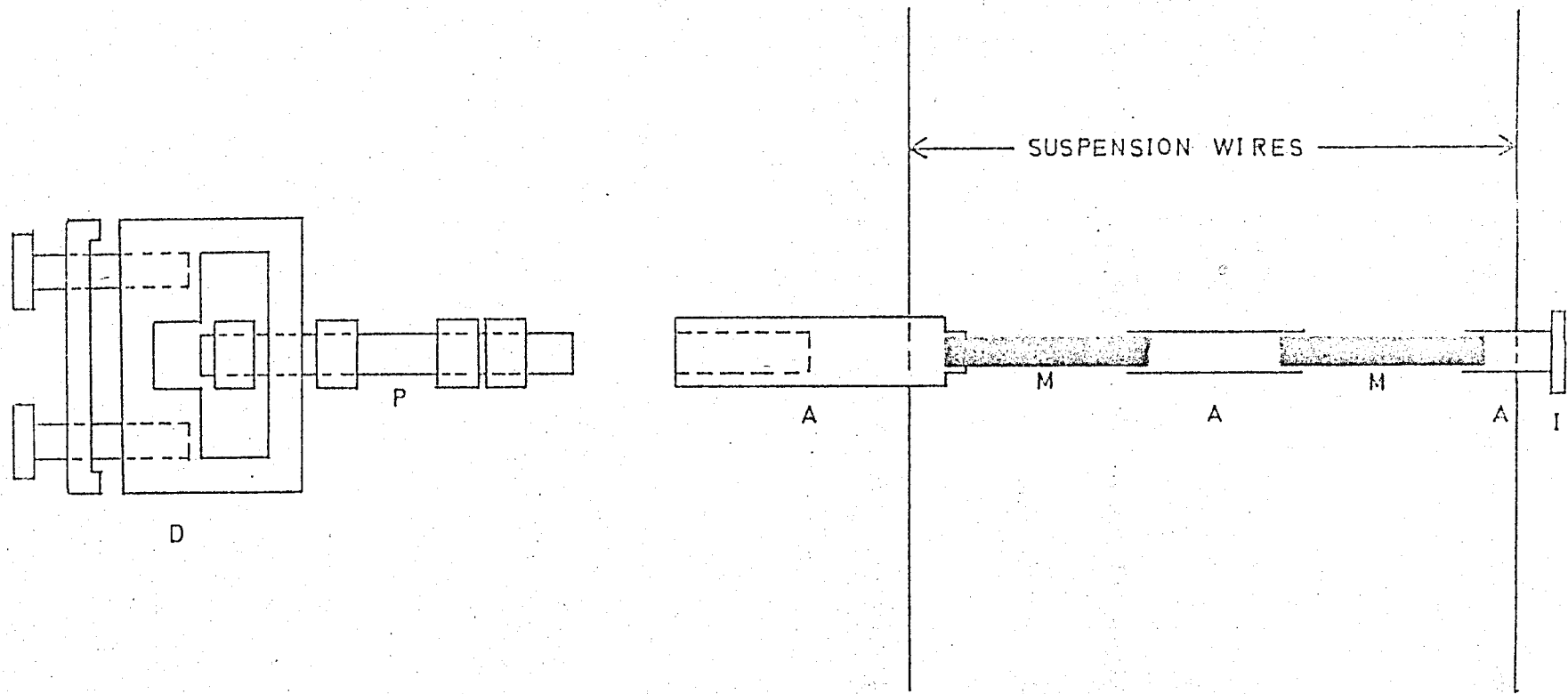


FIG. 3.5

nuts. The drive clamp can be replaced by a central plate for oscillating two similar disc specimens in shear sandwich geometry as described previously.

Tan (57) found that the soft-iron disc provides the most sensitive electrically conductive surface for the Bently probe to sense. The disc is $\frac{1}{2}$ " diameter and $\frac{1}{16}$ " thickness and is stuck to the vibrating system with "Araldite". Alternative metals like tin, copper, stainless steel and aluminium give less sensitivity.

The Bently probe (Bently-Nevada 304) is fitted onto the end face of the one inch long cylindrical rod. The rod is free to slide in a horizontal direction, through the centre of the thick cover of the brass case and is solidly locked in position by a screw pressing against it. The probe and the soft-iron disc are parallel to each other. The initial gap between them can be adjusted by moving the rod.

Figure 3.6 shows the tensioning device used in tightening the suspension wires. Each wire is anchored to the vibrating system by a soldered knot. The wire then passes through the fine hole in the centre of the tensioning device. The wires are tightened and locked in tension by two 4BA nuts, turning in opposite directions. The tensioning device sits in a hole through the supporting brass cylindrical tube and is clamped tightly by a 4BA nut.

The arrangement of the electronic apparatus, shown in Figure 3.7, represents a major change in apparatus design. The most significant difference is the incorporation of a Digital Transfer Function Analyzer (Solartron TFA JM1600) which digitally displays output voltage (proportional to the strain), input voltage (proportional

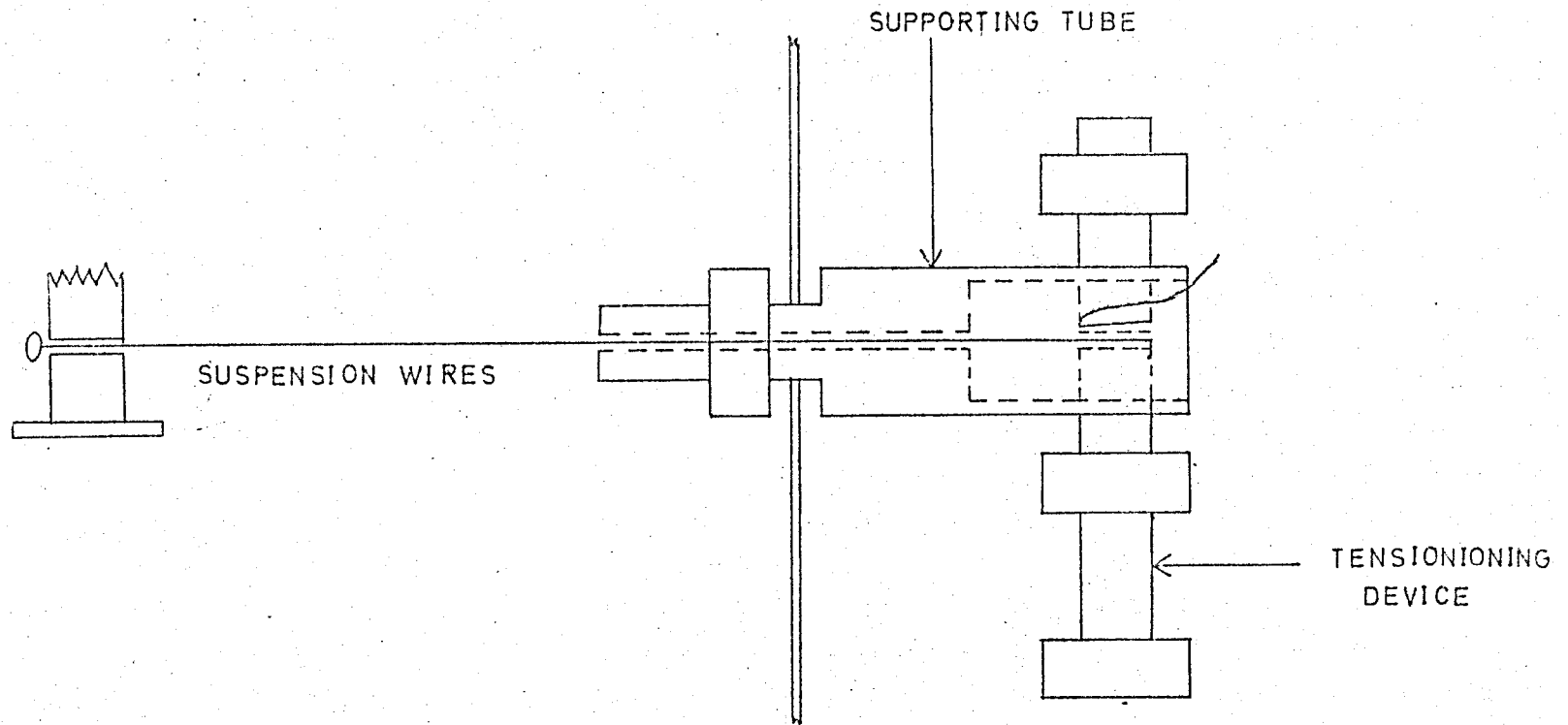


FIG. 3.6

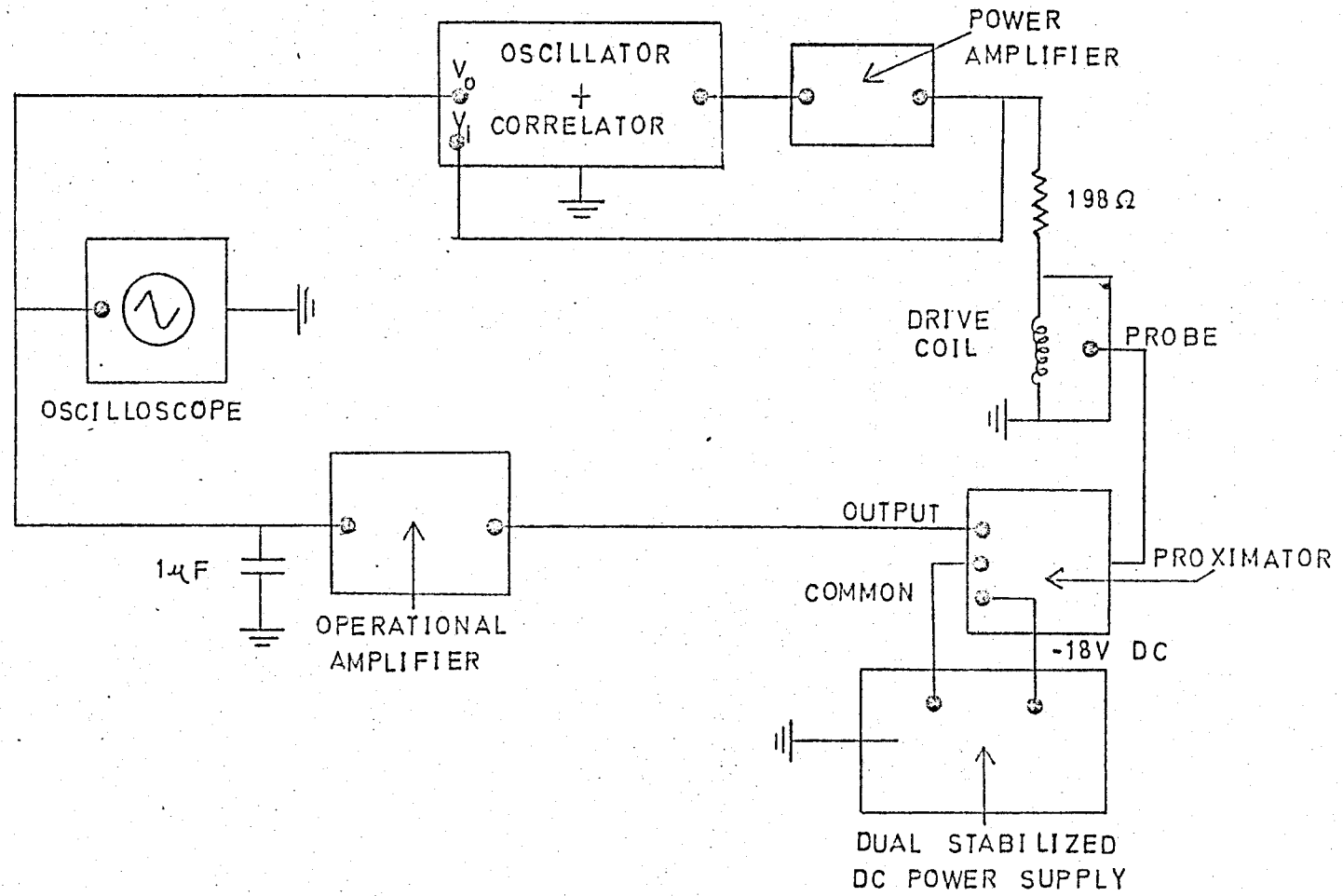


FIG. 3.7

to the stress) and the phase angle between input and output voltage. Thus, sample modulus (stress divided by strain) and loss tangent (tangent of the phase angle) are conveniently determinable. The Solartron Digital TFA comprises an oscillator with a 10V rms maximum output power supply and a Digital Correlator which computes dynamic response for display by an in-line digital read-out. With the Solartron High Frequency Extension Unit JX1639 attached, frequencies of 1.60×10^5 to 1.00×10^{-5} Hz $\pm 0.05\%$ are available. The signal from the Digital TFA is fed into the power amplifier (AIM WPA 116) which supplies the amplified signal to a 198Ω resistance (four resistors in parallel) in series with the driving coil. This resistance helps to reduce the phase lag between drive current and voltage due to inductance. Since the coil has a resistance of 276Ω the total resistance in this part of the circuit is 474Ω .

The Bently probe operates in conjunction with a proximator (Bently-Nevada 310G) and a power supply (Advance Dual Stabilised D.C. Supply PP3) to form a tuned resonance circuit. The proximator supplies electrical energy from the power supply to the probe and senses the signal return from the probe to provide a voltage signal that is proportional to the displacement variation of the vibrating system detected by the probe. The transducer system, which works on an eddy current principle, has a sensitivity ca. 8V per millimetre of motion and applies negligible stress to the vibrating elements. The voltage from the proximator is fed into an operational amplifier (Burr-Brown 1632A/16) with switch-selected gains of 1, 10 and 100. The signal is then monitored by an oscilloscope (Solartron CD 1014.2), to ensure that it is an undistorted sine wave, and fed into the cor-

relator. The amplitude of a carrier frequency (ca. 10^6 Hz) was minimized by shunting through a $1\mu\text{F}$ capacitor to earth. The Bently probe and proximator operate with a regulated -18V D.C. power supply, in the present case, balanced to obtain output signal about earth. This allows the probe gap to be monitored on the oscilloscope. The digital read-out on the correlator is the R.M.S. value of output voltage (V_o) and the phase angle (β), read to a precision of $10'$ of arc. The input voltage (V_i), from the Power Amplifier, can also be read by switching to the correlator. To minimize the effects of fluctuations in mains voltage, the entire apparatus is connected to an Advance Volstat (CVN 500/A) which is plugged into the mains. This results in the mains voltage being stabilized to $\pm 0.5\%$.

PRINCIPLE OF OPERATION

For rectangular beam samples undergoing bending deformation:

$$M\ddot{x} + kE^*x + Ax = F_p \exp(i\omega t) \quad (3.1)$$

where

M is the mass of the vibrating system,

x is the linear displacement of the driven clamp,

E^* is the complex Young's modulus of the specimen,

F_p is the maximum driving force,

ω is the angular frequency of the driving current,

t is time

A is the restoring force per unit displacement, of the suspension wires,

k is a geometrical factor = $\frac{2bh^3}{l^3}$

b is sample width,

h is sample thickness,

l is the length of each half of the sample between each rigid clamp and the central clamp.

For shear sandwich geometry E^* is replaced by G^* (complex shear modulus) in Equation (3.1) and the geometrical factor becomes:

$$k = \frac{2Q}{l} \quad (3.2)$$

where Q is the cross-sectional area of each disc and l the sample length as previously defined.

The following expressions can be derived from Equation (3.1), as shown in Appendix I. These expressions relate the viscoelastic parameters E' , E'' and $\tan\delta$ to measurable quantities.

$$E' = C \left(\frac{V_i}{V_o} \cos\beta \right) + \frac{M}{k} (\omega^2 - \omega_R^2) \quad (3.3)$$

$$E'' = C \left(\frac{V_i}{V_o} \sin\beta \right) \quad (3.4)$$

$$\tan\delta = \frac{E''}{E'} \quad (3.5)$$

where C is a constant.

As will also be shown in Appendix I, these parameters can be calculated at the system's resonant frequency (ω_o) providing the sample-free resonant frequency (ω_R) is known. Thus, at resonance only:

$$E'_S = \frac{M}{k} (\omega_o^2 - \omega_R^2) \quad (3.6)$$

$$\tan \delta_S = \tan \delta_0 \frac{\omega_0^2}{\omega_0^2 - \omega_R^2} \quad (3.7)$$

$$E_S'' = E_S' \tan \delta_S \quad (3.8)$$

where E_S' , E_S'' are the in-phase and out-of-phase Young's moduli at resonance, respectively.

$\tan \delta_S$ is the loss tangent of the sample at resonance.

$\tan \delta_0$ is the loss tangent of the sample plus wires at resonance.

For shear-sandwich geometry, G' , G'' , G_S' , G_S'' would replace E' , E'' , and E_S' and E_S'' .

DYNAMIC MECHANICAL MEASUREMENTS AND ERROR ANALYSIS

Measurements were made at various temperatures and frequencies. The temperature was controlled below ambient by placing the entire apparatus in a large dewar flask filled with methanol or acetone. Solid CO_2 was used to maintain temperatures within $\pm .5^\circ\text{K}$ for the period of time necessary to collect data at different frequencies. This method could only be used to 194°K , the transition temperature of CO_2 (solid) to CO_2 (gas). Temperatures as low as 103°K were achieved by passing N_2 (liquid) through a coil placed in the dewar. However, the temperature could only be maintained to within $\pm 1^\circ\text{K}$ using this method. For temperatures between ambient and 373°K , the apparatus was placed in a thermostatted paraffin bath where the temperature was controlled to $\pm .1^\circ\text{K}$. 373°K was not exceeded for fear of damage to the insulation of the electronics. Once the desired temperature had been reached, it was maintained for at least half an hour prior to measurements to

to ensure that the sample had reached equilibrium. A copper-constantan thermocouple was placed near the sample for temperature measurement. It was calibrated at the boiling points of N_2 and H_2O , the melting point of H_2O and several intermediate temperatures using calibrated thermometers.

Although the oscillator has a very broad frequency generating capability, measurements were limited to the range 1×10^{-3} to 1×10^3 Hz due to power limitations, variations in the voltage supplied to the proximator and changes in proximator sensitivity with temperature. Within the quoted range, frequencies could be dialled to three digit accuracy. Allowance had to be made for coil inductance causing the current through the coil to lag V_i . The resistance of the coil combined with the 198Ω resistance in series helped to reduce this effect. To measure this current lag, which would cause V_o to lag V_i by the same amount, an 18Ω resistance was placed between the coil and earth. The Digital TFA was used to measure the voltage and phase change across this resistance. Since the voltage across the 18Ω resistance was in phase with the current which passed through the coil, the measured phase angle would be that of the current and V_o . Table 3.3 summarizes these measurements as a function of frequency. For this circuit with resistance (R) and inductance (L) in series:

$$\tan\beta_1 = \left(\frac{2\pi L}{R} \right) f \quad (3.9)$$

Thus plotting $\tan\beta_1$ against f should give a straight line of slope

$\left(\frac{2\pi L}{R} \right)$ and intercept zero if β_1 is due primarily to inductance.

This plot is shown in Fig. 3.8 and demonstrates the agreement with

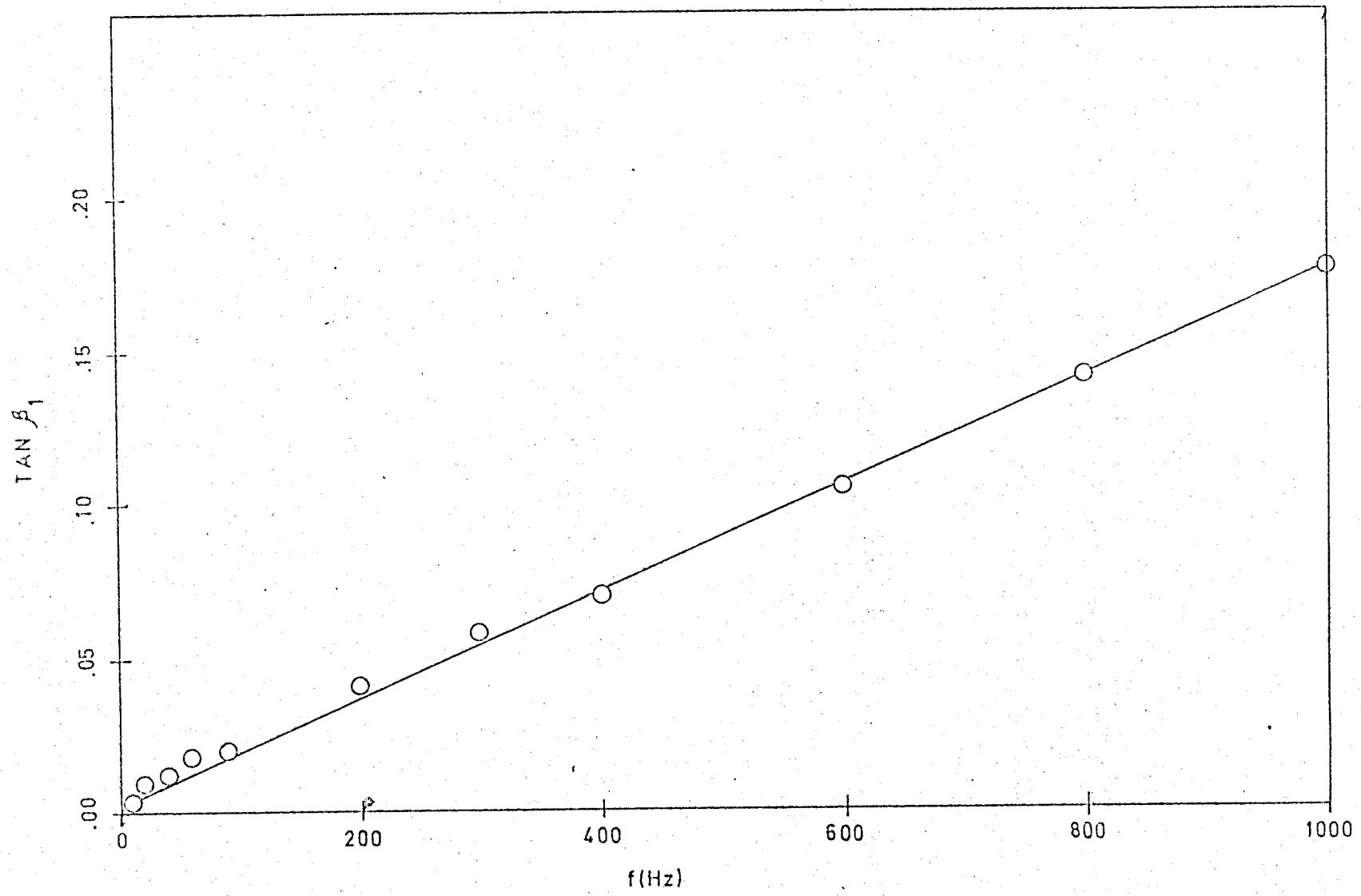


FIG. 3.8

Equation (3.9).

Table 3.3 Phase Angle (β_1) of the Current Through the Coil With Respect to V_i

<u>Frequency (Hz) (f)</u>	<u>β_1</u>	<u>$\tan \beta_1$</u>
1.00	0°10'	.003
3.00	0°10'	.003
10.0	0°10'	.003
20.0	0°30'	.009
40.0	0°40'	.012
60.0	1°00'	.018
90.0	1°10'	.020
200	2°20'	.041
300	3°20'	.058
400	4°00'	.070
600	6°00'	.105
800	8°00'	.141
1000	10°00'	.176

Thus, using the information in Table 3.3, at frequencies of 20 Hz and above, β_1 was subtracted from the measured phase angle to give the correct value of β . Figure 3.9 shows a frequency scan at room temperature for a high carbon steel bar for which E' and $\tan \delta$ are known to be constant, with the latter very small, in the frequency range shown. Values of kE'_S and $\tan \delta_S$, calculated at ω_0 , are represented by filled circles. All values of the modulus agree to within $\pm 1\%$ and the values of $\tan \delta$ agree to within $\pm .005$ except at frequencies of 100 Hz to resonance where phase angle and amplitude are starting to

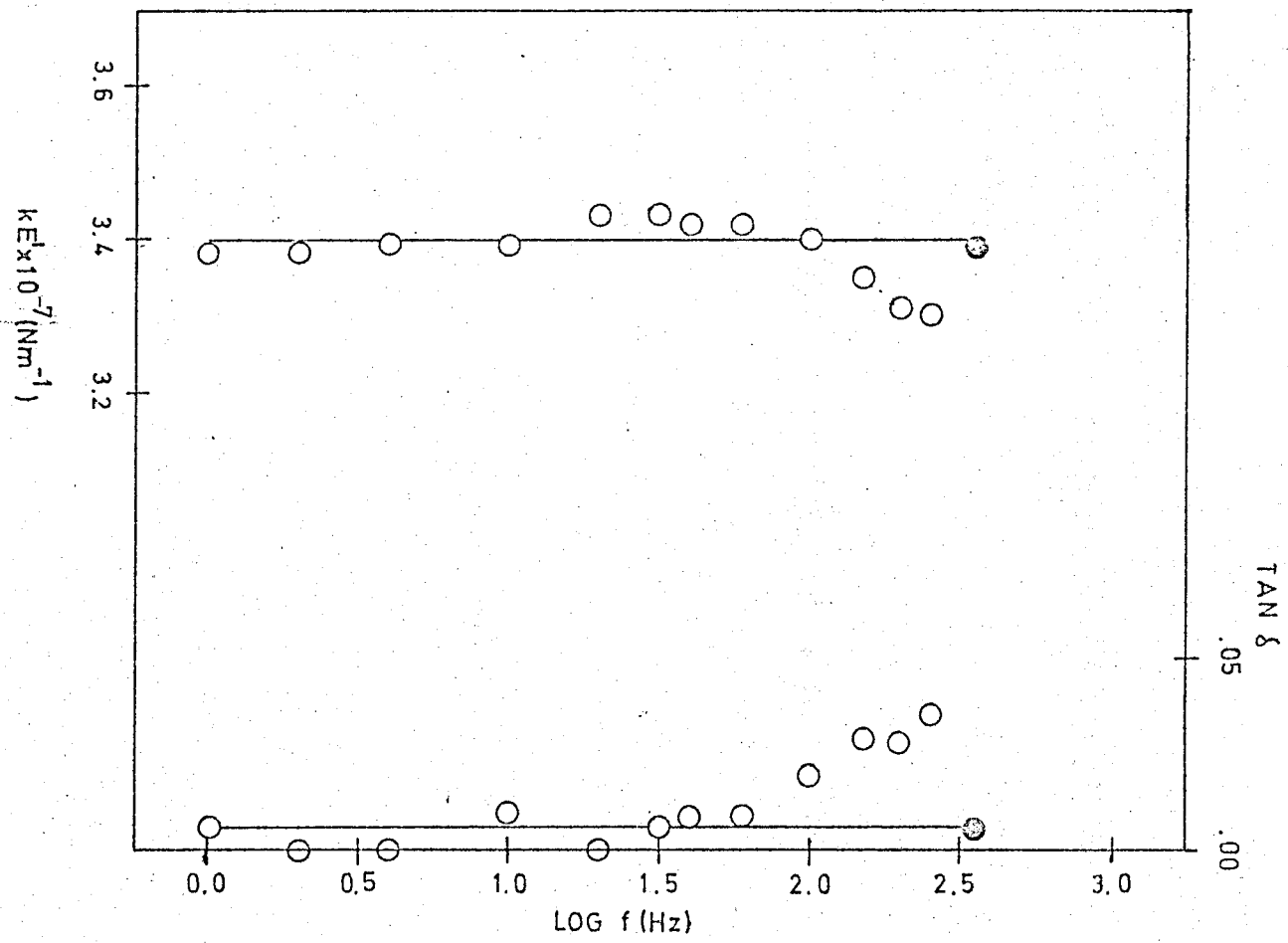


FIG. 3.9

be affected by the resonance phenomenon. It is not certain precisely why this deviation should occur, even after correction for current lag, but since it does, data was not collected in the resonance region.

Sample preparation for the hydrogenated polymers was described in section 3.1. The moulded polymers were clamped into place carefully ensuring that they were under no strain. Measurements were taken while cooling the samples to below their T_g . Measurements above ambient were taken only for sample B2. Data was collected as the sample warmed. Dow Corning polymers were measured in both bending and shear sandwich deformations. Samples measured in the bending mode were cut from the prepared sheets of block copolymer in the shape of strips approximately 8 cm long, 1 cm wide and .2 cm thick. The poly(dimethylsiloxane) was moulded into a strip at 343°K after being heated under vacuum for 48 hours to remove low molecular weight homologues. Since all polymers were partially crystalline below 233°K , the apparatus was first cooled to 194°K at about $2^\circ\text{K}/\text{min}$. This temperature was held for about 12 hours to maximally crystallize the poly(dimethylsiloxane) and then cooled to below the siloxane T_g (150°K) whereupon measurements were taken while the apparatus warmed to ambient. Samples measured in shear sandwich deformation were cut from the sheets in the form of cubes with their edges deviating from the average value by no more than 5%. Once again, all samples were clamped so that they were not strained.

Sample dimensions had to be carefully measured to minimize errors since, for bending, l and h are raised to the third power in calculating modulus. For bending, h and b were measured with a micrometer to $\pm 1 \times 10^{-3}$ cm. l was measured with a vernier calipers to $\pm 5 \times 10^{-3}$ cm.

Typical sample dimensions were:

$$l = 1 \text{ to } 2 \text{ cm}$$

$$b = 1 \text{ cm}$$

$$h = .1 \text{ to } .2 \text{ cm}$$

It is important to realize that sample dimensions influence the type of deformation occurring. Tan (157) has shown that, for bending deformation, as the l/h ratio decreases, a deflection due to shearing becomes more pronounced and the measured Young's modulus of the material (E_A) becomes smaller than the actual value (E). His findings are summarized in Table 3.4 for varying values of Poisson's Ratio (ν).

Table 3.4 The Effect of l/h Ratio on Measured Modulus

ν	$h(\text{cm})$	$l(\text{cm})$	E_A / E
0.50	0.1	1.5	.99
	0.1	1.0	.98
	0.2	1.5	.95
	0.3	1.5	.89
0.35	0.1	1.5	.99
	0.3	1.5	.90
0.20	0.1	1.5	.99
	0.3	1.5	.91

Sample dimensions were adjusted so that E_A / E was always larger than .90.

Rivlin and Saunders (154) have shown how sample dimensions affect the measured rigidity modulus. Using cylinders of varying lengths, they have predicted the ratio of measured (G_A) to actual (G) rigidity modulus assuming that as the cylinder length increases, more of a deflection due to bending, rather than shearing, occurs. They have also

compared these theoretical results with experimental measurements. Read (1955) also assumed that a fraction of the deflection was due to bending and using a different mathematical approach, predicted a range of G_A / G values depending on the ratio of the cylinder radius (r) to length (l). The results of these two papers are summarized in Figure 3.10 assuming a Poisson's Ratio of 0.5. Experimental points are shown to agree well with theoretical predictions and the experimentally found corrections were used in this work. Only the siloxane block copolymers were measured in shear. Unfortunately, restrictions in sample dimensions required measurements to be made at l/r equals 2.00.

An important step in calculating E' and E'' was the calibration of the apparatus i.e. - determination of the constant, C , in Equations (3.3) and (3.4). This was accomplished by first plotting $\frac{V_i}{V_o} \cos\beta$ against $\log \omega$ at values of ω where $\frac{M\omega^2}{k} \ll E'$. At these frequencies,

$$E' = C \left(\frac{V_i}{V_o} \cos\beta \right) - \frac{M\omega^2}{k} \quad (3.10)$$

Extrapolating this set of points to $\log \omega_o$, where E'_S was known, one could set Equation (3.10) equal to (3.6), so that:

$$C = \frac{M\omega_o^2}{k} \div \left(\frac{V_i}{V_o} \cos\beta \right)_{\omega_o} \quad (3.11)$$

where $\left(\frac{V_i}{V_o} \cos\beta \right)_{\omega_o}$ is the value of $\frac{V_i}{V_o} \cos\beta$ extrapolated to

$\log \omega_o$. It should be remembered that C was defined as N/kB

(see Appendix I), therefore, C is dependent on the properties of the

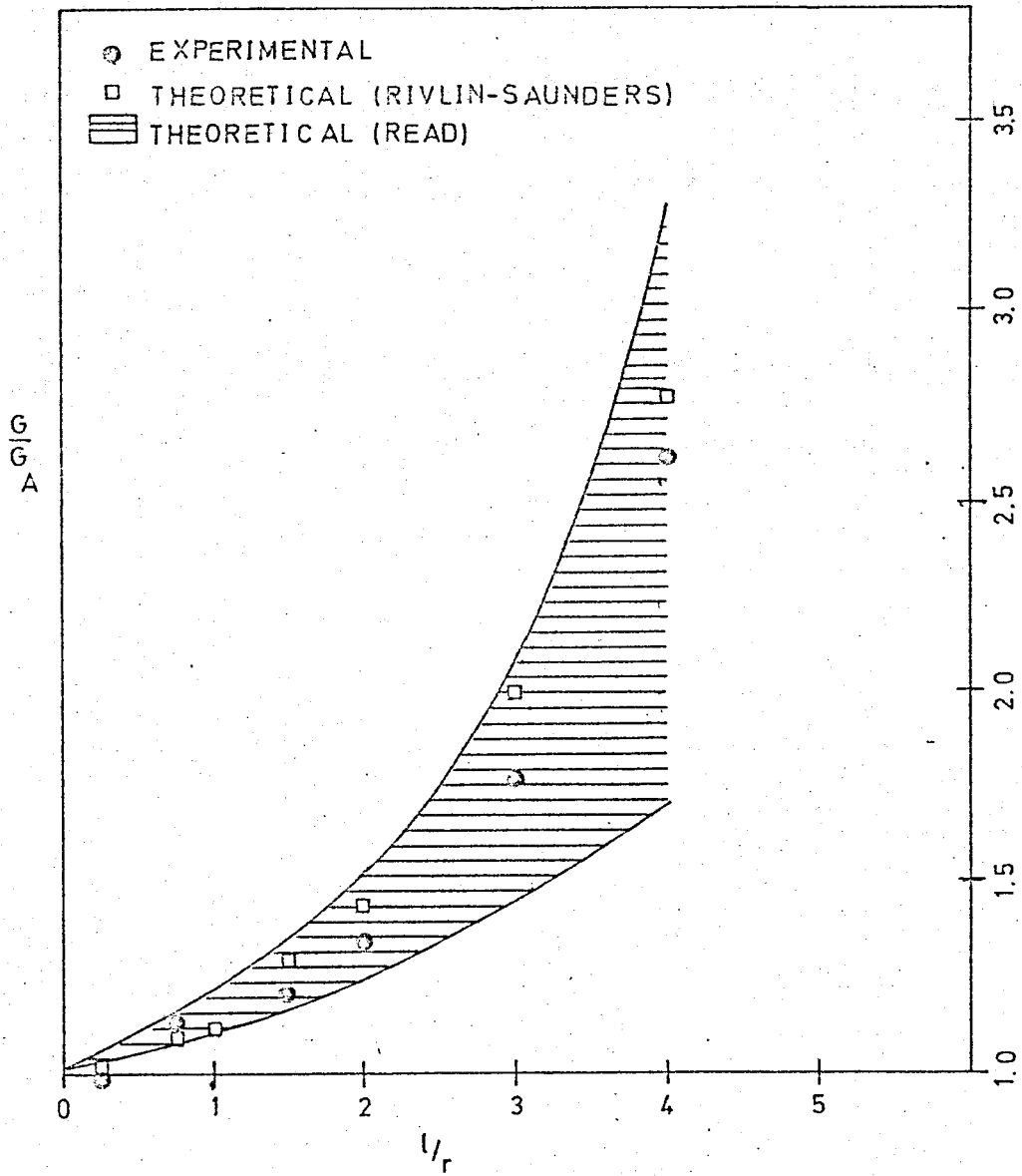


FIG. 3.10

coil and magnets (N) and of the transducer system (B); k will be constant for a particular sample geometry. The properties of the coil and magnets remain fairly constant, thus N should remain constant. The properties of the transducer system, however, have been found to vary. Tan (157) found that C varied with temperature largely as a result of differential expansions, altering the gap between probe and soft iron disc, and changes in probe sensitivity. The author has also found that proximator sensitivity is greatly affected by small changes in ambient temperature.

When performing the above mentioned extrapolation, a very accurate calibration can be accomplished when E' varies slowly with $\log \omega$ as in steel at room temperature or polymers well below T_g . The faster E' varies with frequency the more uncertain the extrapolation becomes. Also, at very high damping, resonance cannot be detected and C must be interpolated from a knowledge of C at neighbouring temperatures.

Uncertainty in calculating E' , E'' and $\tan \delta$ was a result of the degree of precision in determining the geometry constant (k), mass of the vibrating system (M), resonance of the specimen free system (ω_R), the calibration constant (C) and the digital read out from the TFA (V_i , V_o , β). Of these, determining k was usually the largest source of error. For bending, k could be determined to $\pm 5\%$. However, in shear sandwich geometry it should be recalled that in measuring the siloxane block copolymers, cubes were cut with a 5% uncertainty in edge dimensions. Thus k could only be determined to within $\pm 15\%$. Under certain conditions, discussed previously, C had a considerable uncertainty estimated to be as high as 5%. M was determined, by weighing, to be 7.21 and 4.27gms $\pm < .1\%$ for bending and shearing,

respectively. ω_R was 267 and 320 radions/sec $\pm < .5\%$ for bending and shearing, respectively. V_i and V_o were determined to $< \pm 1\%$ and β to $\pm 10'$ arc. Thus, for a single sample at constant temperature E' and $\tan \delta$ were found to agree to better than $\pm 1\%$ and $\pm .005$, respectively, in a frequency range of as large as five logarithmic decades. Absolute determinations of E' were made to within $\pm 10\%$ and determinations of G' to within $\pm 15\%$.

3.3 TORSION PENDULUM

DESIGN OF APPARATUS

The wide frequency scanning apparatus can be used for measurements to 373°K , only, for fear of damage to the circuitry at higher temperatures. In order to make dynamic measurements on the siloxane block copolymers, higher temperature capabilities were necessary to investigate relaxations of the organic phase. To accomplish this, a torsion pendulum was designed and built in this laboratory.

The apparatus was designed to measure the elastic shear modulus (G') and logarithmic decrement (Δ) of rectangular beam samples from 77°K to 573°K . During the description of the apparatus reference will be made to Figure (3.11), an overall view, and to Figure (3.12), a close-up of the clamped sample enclosed by the temperature control unit.

The sample is clamped at its top and bottom. Each clamp (A) is a brass cylinder with a half cylinder section removed so that it can be screwed back into position thus holding the sample in place. Both clamps are brazed to stainless steel tubes (B) (I.D. = .37cm;

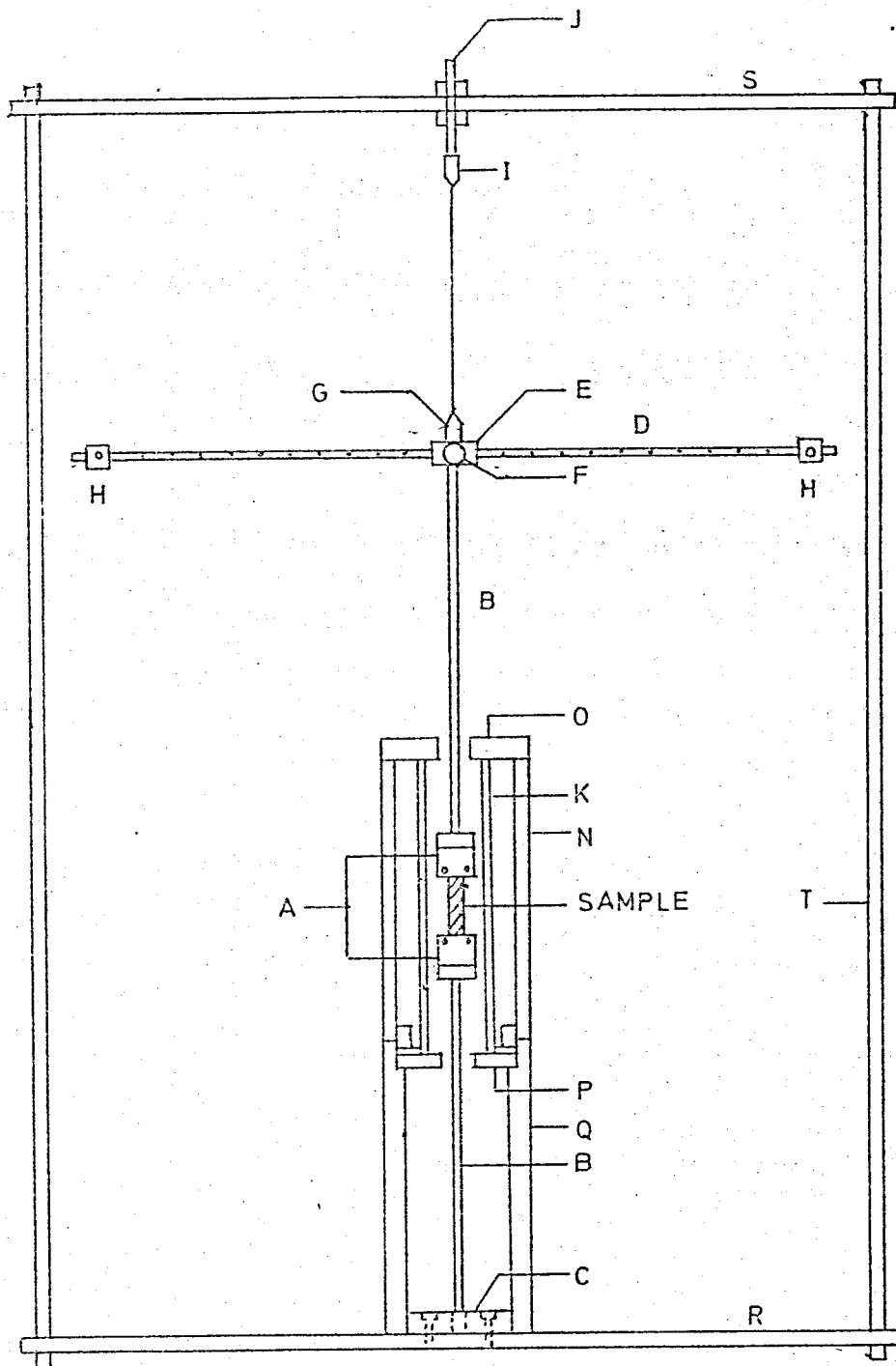
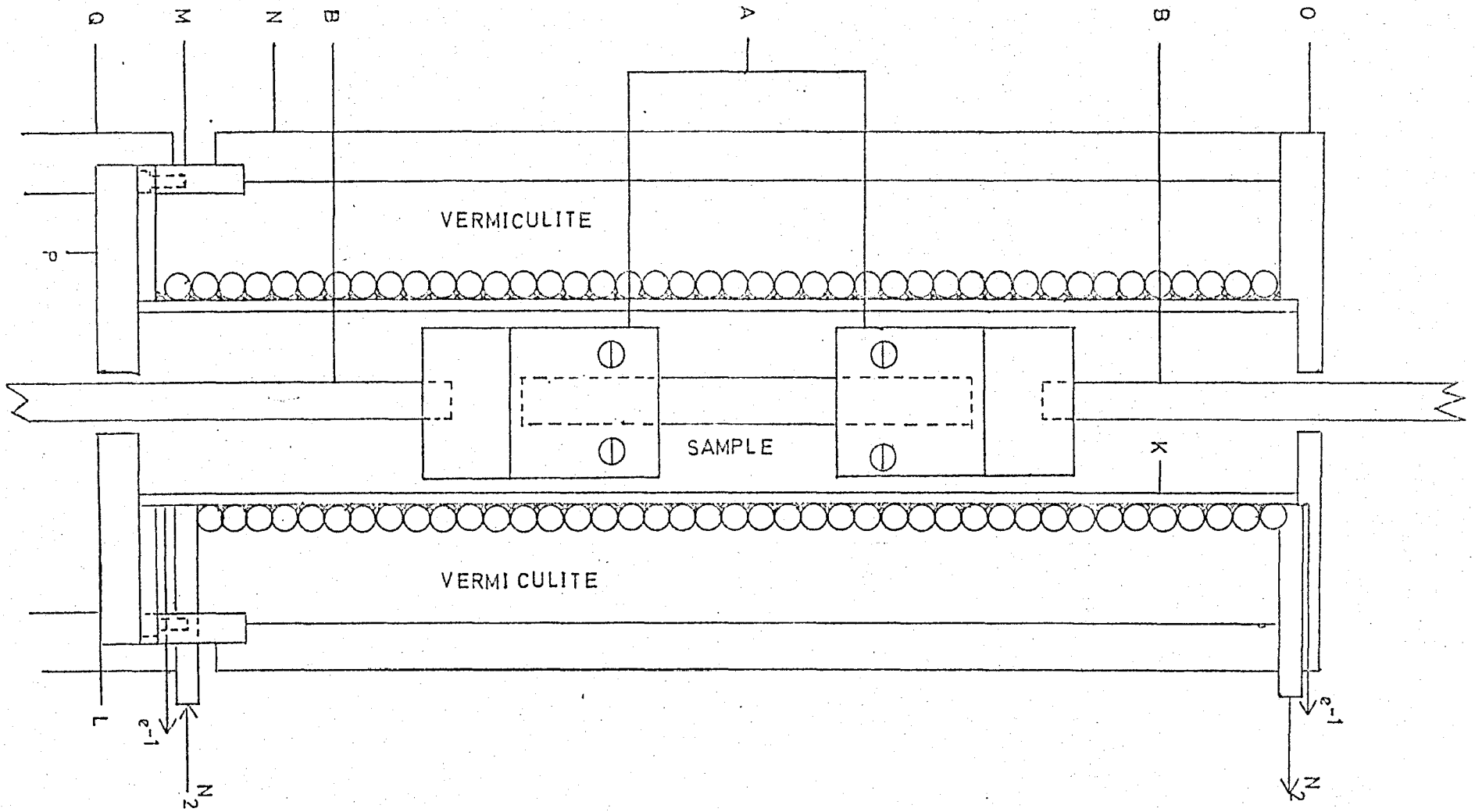


FIG. 3.11

FIG. 3.12



O.D. = 1.15cm). The stainless steel tube attached to the lower clamp is brazed to a steel plate (C) which is screwed to the steel base plate (R) thus holding the lower clamp rigidly in place. The stainless steel tube attached to the upper clamp is brazed to the inertia bar (D) via a machined brass cylinder (E). Also attached to the cylinder (E) is a highly polished mirror (F) and a pin vice (G). Two pairs of weights (H), 104.2 and 167.1 g, were made to slide over the inertia bar and were held fast in precisely drilled positions via a knurled screw. The positions drilled into the inertia bar are 26, 24, 22, 20, 18, 16, 12, and 10 cm \pm .01 cm from the centre of the bar. The inertia bar and upper clamp are supported by a thin high carbon steel wire gripped by the pin vice (G) and the pin vice (I). The upper vice is brazed to a threaded rod (J) attached to the upper steel plate (S) by two knurled nuts. The threaded rod-knurled nut assembly was adjusted so that the upper clamp is precisely centred over the lower clamp. Sample length can be varied by adjustment of the knurled nuts. The upper steel plate is supported by four 2.4 cm diameter steel bars (T) attached to the steel base plate.

The temperature controlling device consists of copper tubing (O.D. = .7 cm; I.D. = .5 cm) helically wound around a steel tube (K) (I.D. = 3.6 cm; .1 cm wall thickness) through which a coolant can be passed. Heating wire is also wrapped helically around the steel tube (K) between each winding of the copper tube. In Figure (3.12), open circles represent the copper tube and small crosses, the heating wire. The steel tube (K) is brazed to a steel ring (L) which is screwed into an asbestos ring (M). The ring (M) is stuck to the asbestos

cylinder (N) with fireplace cement. The gap between the copper coil and the cylinder (N) is filled with Vermiculite for insulation. The temperature controlling unit is capped with a split asbestos lid (P) which fits into the supporting asbestos cylinder (Q). The cylinder (Q) fits snugly around the plate (C).

PRINCIPLE OF OPERATION

Operating principles for torsion pendulums are described by several authors (43-4, 153, 156-7). Referring to Figures (3.11) and (3.12), the sample is set in torsional oscillation by moving the inertia bar from its equilibrium position. Oscillations will continue freely at a constant frequency (ω_0) and gradually decreasing amplitude. The viscoelastic properties are calculated from the characteristic frequency and amplitude decrement. For a sample undergoing torsional oscillations,

$$G' = \left(\frac{\omega_0^2 I}{b} \right) \left(1 + \frac{\Lambda^2}{4\pi^2} \right) \quad (3.12)$$

where I is the moment of inertia of the oscillating system.

b is the form factor depending on sample geometry.

Λ is the logarithmic decrement of the amplitude.

In this work $\frac{\Lambda^2}{4\pi^2} \ll 1$ and was ignored. Only for a few measurements did Λ approach 1 which would make $\frac{\Lambda^2}{4\pi^2} = .025$ and thus cause G' to be 2.5% in error. Thus, assume,

$$G' = \frac{\omega_0^2 I}{b} \quad (3.13)$$

Since this system has a wire contributing a term to the modulus Equation (3.13) becomes:

$$bG' + W' = I\omega_0^2 \quad (3.14)$$

where bG' , W' are the elastic restoring forces per unit angular displacement of the sample and wire, respectively. b is the form factor for the sample. If the sample is removed from the system and the system is then set into motion, it will oscillate at a set frequency (ω_R) for a particular moment of inertia (I_R). Thus,

$$W' = I_R \omega_R^2 \quad (3.15)$$

Combining Equations (3.14) and (3.15),

$$bG' = I\omega_0^2 - I_R \omega_R^2 \quad (3.16)$$

To calculate $\tan \delta$ the logarithmic decrement (Λ) must be determined. Λ is defined as the natural logarithm of the ratio between two successive displacements.

$$\tan \delta = \frac{\Lambda}{\pi} \quad (3.17)$$

For the system consisting of the sample and the wire the measured loss tangent ($\tan \delta_M$) is

$$\tan \delta_M = \frac{\Lambda}{\pi} = \frac{bG'' + W''}{bG' + W'} \quad (3.18)$$

where bG'' , W'' are the out of phase restoring forces per unit angular displacement for sample and wire, respectively.

The loss tangent ($\tan \delta$) for the sample only is:

$$\tan \delta = \frac{G''}{G'} \quad (3.19)$$

Since $W'' \ll bG''$ and combining Equations (3.14), (3.15), (3.18) and (3.19):

$$\tan \delta = \frac{\lambda}{\pi} \left(\frac{I\omega_o^2}{I\omega_o^2 - I_R\omega_R^2} \right) \quad (3.20)$$

MEASUREMENTS

Measurements were made on samples of the siloxane block copolymer moulded and cast from benzene and cyclohexane. Strips with rectangular cross sections were cut and data was collected as the samples were heated from ambient to above the T_g of the organic phase. The heating rate was less than $1^\circ/10$ mins. so that the sample temperature was assumed to be very close to the recorded temperature. The temperature was measured using a Copper - Constantan thermocouple calibrated at the melting and boiling points of H_2O and several other temperatures in the range $273^\circ K$ to $473^\circ K$ using a calibrated thermometer.

The frequency (ω_o) and decrement (λ) were measured by following the oscillations of a beam of light reflected by the mirror (F) onto a graduated screen. The oscillations were timed with a stop watch to $\pm .1$ second. The natural logarithm of amplitude decay was plotted against number of oscillations to determine λ , which was the slope of this line.

In order to calculate the system's moment of inertia (I), a spring steel wire of known radius (r), ($\pm .33\%$) was clamped between both pin vices. The distance (h) between the pin vices was precisely measured ($\pm .1\%$). With no sample in place and using Equation (3.15):

$$\frac{W'}{b_R} = I_R \omega_R^2 \quad (3.21)$$

$$\text{where } I_R = I_0 + mR^2 \quad (3.22)$$

I_0 is the moment of inertia of the system without weights attached.

m is the mass of each weight.

R is the distance of each weight from the rotational axis.

$$b_R = \frac{\pi r^4}{h} \quad (3.23)$$

Combining Equations (3.21) and (3.22):

$$mR^2 = \frac{W'}{b} - I_0 \left(\frac{\omega_0^2}{b_R} \right) \quad (3.24)$$

ω_0 varied with changing R . Thus, mR^2 was plotted against $\frac{\omega_0^2}{b_R}$ to obtain a straight line with slope = $-I_0$. Linear regression was performed on nine experimental points with a correlation coefficient = .9999 and $I_0 = 1.560 \times 10^{-3} \text{ kg m}^2 \pm 1.4\%$, the uncertainty depending on the precision obtained in determining b_R . Using Equation (3.22) I was determined at each value of R obtainable as is shown in Table (3.5).

The form factor (b) for strips with rectangular cross-sections is defined by Equation (3.25)

$$b = \frac{a t^3 \mu}{16l} \quad (3.25)$$

where a is sample width.

t is sample thickness.

l is sample length.

μ is a function of $\frac{a}{t}$.

a and t were measured with a micrometer to $\pm .001$ cm and l was determined with a vernier calipers to $\pm .005$ cm. μ varies from 2.249 to 5.232 for $\frac{a}{t}$ ratios of 1.00 to 40.00 respectively (156).

Table 3.5

R (cm)	I (kg m ²) x 10 ³	
	m = 104.2 g	m = 167.1 g
No Weights	1.56	1.56
10	2.60	3.23
12	3.06	3.97
14	3.60	4.84
16	4.23	5.84
18	4.94	6.97
20	5.73	8.24
22	6.60	9.65
24	7.56	11.2
26	8.60	12.9

One disadvantage in using a torsion pendulum is the inability to measure systems with high damping ($\lambda > 1$). In the apparatus under discussion, this problem can be circumvented by increasing the contribution of the W' term in Equation (3.14) by using larger diameter wires. This procedure was in fact followed for the three samples measured.

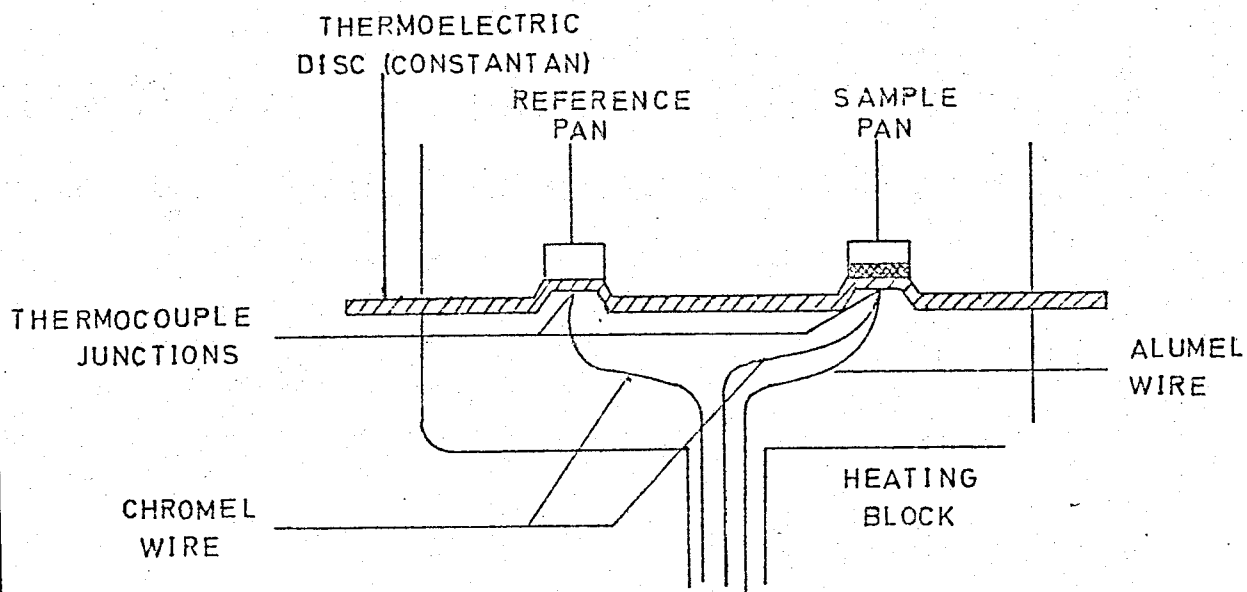
The apparatus described is capable of measuring E' and λ very precisely. If the sample is clamped so that it is under no tension, yet not slack, l is at least 3 cm and the wire is sufficiently thin so that $W' \ll bG'$ in Equation (3.14), the accuracy of G' will be dependent only on I , ω_0 and b . Thus G' should be determinable to within $\pm 6\%$ under the best of conditions. λ is determinable under these same conditions to within $\pm 1\%$. It has been stated

that W' was adjusted to give a sizable contribution in Equation (3.14). This of course decreased the accuracy and precision of measurements the larger its contribution. This became especially relevant when going through T_g where G' decreased markedly. Sample tension was found to affect the magnitudes of ω_0 and Λ . It was the major source of error when measuring at different temperatures, due to thermal expansion. Equation (3.25) shows that sample thickness (t) is the principal variable controlling sample stiffness. Since t for the samples measured was fixed, it was necessary to use very short sample lengths (< 1 cm) to compensate. It is possible that this was a considerable source of error since it seems likely that some torsion of the sample was occurring inside the clamp. Therefore, the larger l is, the smaller this error becomes.

3.4 DIFFERENTIAL SCANNING CALORIMETRY (DSC)

Differential Scanning Calorimetry (DSC) was used to measure the glass transitions, degree of crystallinity and melting ranges of the samples.

The DuPont DSC cell (Catalog 900600) was used in conjunction with the DuPont 900 Thermal Analyzer. A diagram of the cell cross section is shown in Figure (3.13). An aluminium pan containing a sample and an empty reference pan, are placed on raised portions of the constantan thermoelectric disc. The Chromel-Alumel thermocouple junction under the sample pan is coupled with the heating block to precisely control the heating rate. The temperature at the raised sample and reference platforms is monitored by a Chromel-Constantan



DSC CELL CROSS SECTION

FIG. 3.13

thermocouple formed by the junction of the Constantan disc with the Chromel wire at each platform position. The temperature difference (ΔT) between the Chromel-Constantan thermocouples is monitored on the Y-axis of the recorder and sample temperature, measured by the Chromel-Alumel thermocouple, is monitored on the X-axis.

Glass transitions (T_g), melting points (T_m), melting peaks (T_p) and degree of crystallinity (w_c) were determined. To illustrate the principles involved, Figure (3.14) a thermogram of a quenched hypothetical polymer capable of crystallizing fairly rapidly, will be referred to. Scanning starts below the polymer's T_g and proceeds from left to right. The shift in baseline occurs as a result of an increase in the heat capacity of the polymer, which is characteristic of a polymer changing from a glass to a rubber. The T_g is defined, in this work, as the midpoint of the straight line drawn between the onset and conclusion of this baseline shift. As the polymer warms it reaches a temperature where crystallization is kinetically favourable, accounting for the exothermic peak. As temperature increases further, the crystallites become unstable and melt, indicated by the endothermic peak. Since polymer melting occurs over a range of temperatures, the melting point is not so clear cut and simply defined as it is with small molecules. In this series of experiments, the melting point (T_m) is defined as the highest temperature at which crystallinity can exist and is represented on the thermogram by the point at which the endothermic peak returns to the baseline. The melting peak (T_p) is the temperature at which the maximum rate of melting occurs. When determining T_g , T_m or T_p , it must be realised that the position of points on the thermogram

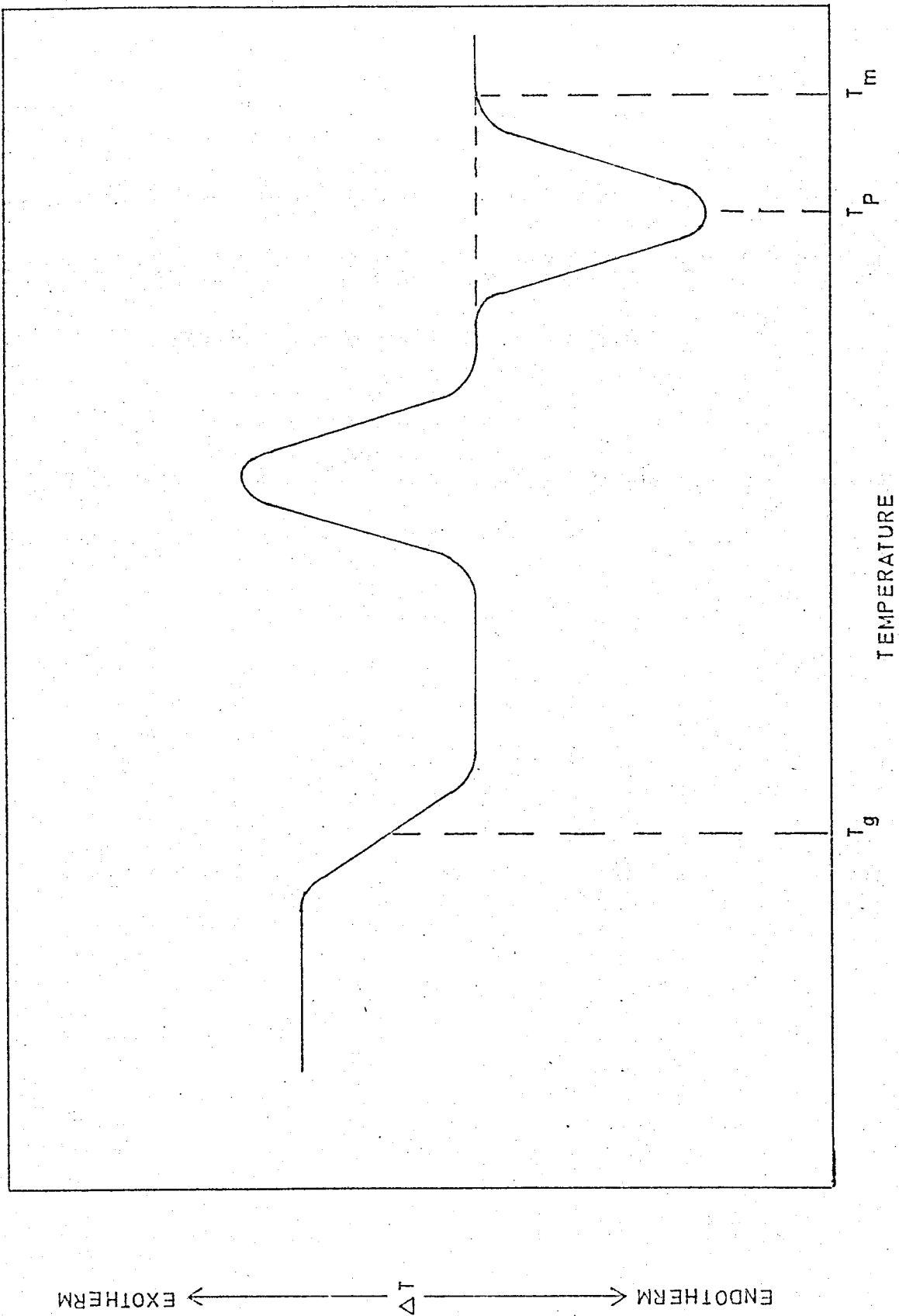


FIG. 3.14

rely on heat diffusing through the polymer to the thermocouples. Thus, it was necessary to extrapolate all data to the zero sample mass. Table 3.6 illustrates how T_m and T_p vary with sample mass. The dependence of transition temperatures on sample mass varies according to the sample's heat conductivity and the magnitude of ΔH_S . The temperature axis thermocouple was calibrated with mercury, gallium and indium.

Table 3.6 Variation of T_m and T_p with Sample Mass

Sample Mass (mg)	T_p ($^{\circ}$ K)	T_m ($^{\circ}$ K)
12.6	419	435
4.3	412	421
1.5	408	415
0.5	405	408
0.1	405	407

The degree of crystallinity (w_c) was determined using Equation (3.26):

$$w_c = \frac{\Delta H_S}{\Delta H} \quad (3.26)$$

where ΔH_S is the enthalpy change per g sample.

ΔH is the enthalpy change per g crystal.

ΔH was obtained from the literature. ΔH_S was calculated from the area of the melting peak using Equation (3.27):

$$\Delta H_S = \frac{EA\Delta T_S T_S}{Ma} \quad (3.27)$$

where E is the calibration coefficient.

A is the peak area.

ΔT_S is Y-axis sensitivity.

T_S is X-axis sensitivity.

M is sample mass.

a is heating rate.

The calibration coefficient was determined from ca. 233°K to 510°K using mercury, gallium, indium and tin. Peak area was determined by tracing onto graph paper with 1 mm divisions and counting squares.

It is estimated that T_g , T_p , and T_m are reproducible to $\pm 1^\circ\text{K}$, from duplicate runs. w_c was determinable to within $\pm 3\%$, due to uncertainty in measuring E(1%), A(1%) and M(1%).

3.5 SMALL ANGLE X-RAY SCATTERING (SAXS)

Small Angle X-ray Scattering (SAXS) was used to measure the surface area of the crystalline phase in a hydrogenated polymer and the morphology of the block copolymer macrolattice.

A Rigaku Denki small angle camera was used with either slit or pin-hole collimation and counter and film detection, respectively. Figure (3.15) illustrates the apparatus set up for slit collimation and counter detection. The x-ray beam ($\text{CuK}\alpha$) passes through slits 01, 02 and 03. Reflections by the sample at 2θ degrees pass through the scattering and receiving slits before being registered on the counter. With the aid of a multichannel analyzer (Laben Spectrascope Model 100) angles from $2\theta = .055$ degrees were traversed at .01 degree intervals. The counting time at each angle was variable from milliseconds to ∞ . The parasitic scattering at a particular angle was

SLIT COLLIMATION WITH COUNTER DETECTION

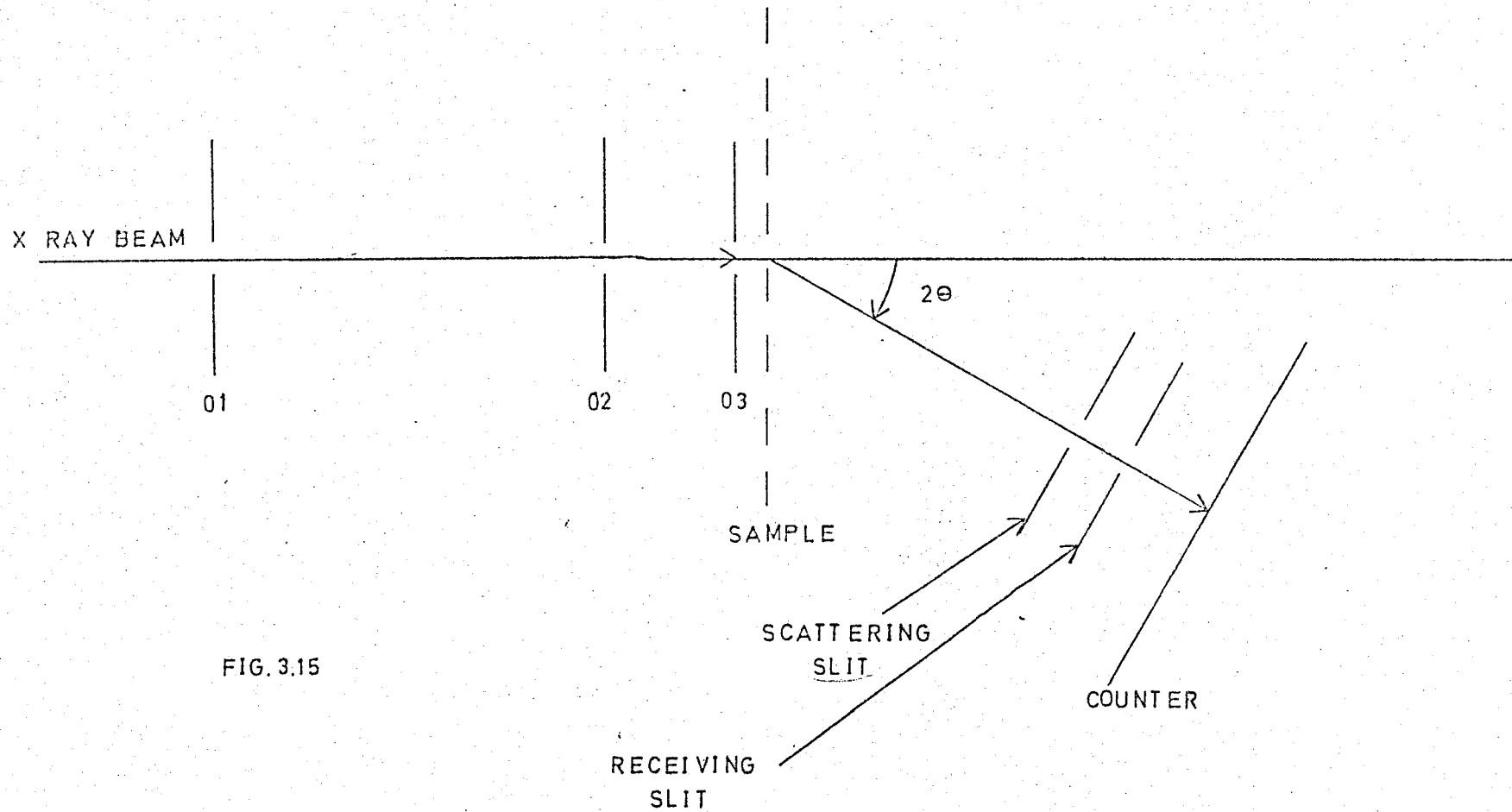


FIG. 3.15

determined by placing the sample in an absorbing position behind the receiving slit. For pin-hole optics with film detection, illustrated in Figure (3.16), slit O3 was removed and slits O1 and O2 were replaced by point collimators P1 and P2. Much of the main beam and parasitic scattering were absorbed by the backstop (B). The x-rays scattered by the sample were recorded on the film (R) in the plane of registration. The sample to plane of registration distance was 30.5 cm.

Surface area measurements of the crystalline phase were made on the hydrogenated polymer B1 using slit collimation. The methods of Porod (139-40) and Debye (141) were employed as described in Chapter 2. Lattice parameters (of the macrolattice) and orientation effects in the block copolymer were analyzed using both slits and pin-holes. The Bragg Equation (3.28) was used to calculate spacings:

$$n\lambda = 2d \sin \Theta \quad (3.28)$$

where n is an integer 1, 2, 3, . . .

λ is the wavelength of $\text{CuK}\alpha$ radiation (1.542\AA).

d is the spacing.

Θ is half the reflection angle.

The measured intensity at 2Θ should be multiplied by $(2\Theta)^2$ to account for the three-dimensional scattering occurring for all orientations of the lattice (138). However, this correction was unnecessary for the diffraction curves encountered, due to their sharpness. Measurements were taken with the x-ray beam perpendicular to the faces and edges of each sample. Considering that the samples

PIN-HOLE COLLIMATION WITH FILM DETECTION

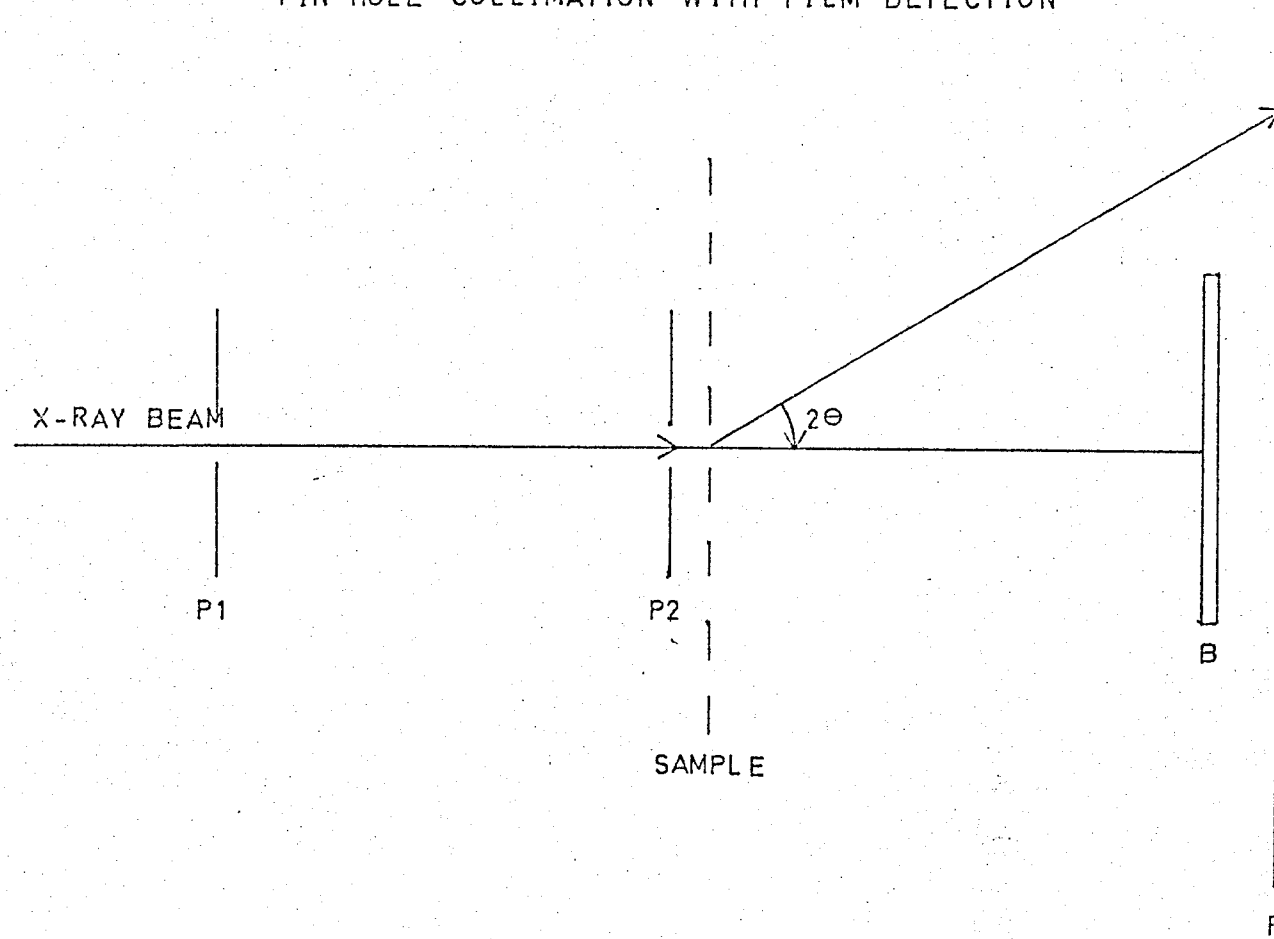


FIG. 3.16

were cast and moulded into sheets, the faces are defined as the two surfaces of largest area. In order to get varying exposures, with film detection, four photographic films were stacked on top of each other in the film cassette. The film was then exposed to the scattered x-rays over a week-long period.

An orientation function $\langle \cos^2 \phi \rangle$ was obtained for some of the block copolymer samples using Equation (3.29) (136-7):

$$\langle \cos^2 \phi \rangle = \frac{\int_0^{\pi/2} I(\phi) \sin \phi \cos^2 \phi \, d\phi}{\int_0^{\pi/2} I(\phi) \sin \phi \, d\phi} \quad (3.29)$$

where $I(\phi)$ is the maximum intensity of reflection at angle ϕ from the reference axis. $I(\phi)$ was measured with a Joyce-Loebl Microdensitometer (Mk. III B). The nature of the orientation function has been described more fully in Chapter 2.

Maximum resolution for determining spacing d was 1000 Å using counter detection but was limited to 500 Å with film detection due to the diameter of the backstop. Using counter detection, the reflection angle was determinable to $\pm .005$ degrees. With film detection, the distance of the scattering from the main beam was measurable to $\pm .005$ cm which means that spacings were determinable to approximately $\pm 2\%$.

CHAPTER 4 RESULTS

SECTION A HYDROGENATED POLYMERS

4.A.1 Dynamic Mechanical Measurements

Dynamic mechanical data were plotted at 10, 1 and 0.1 Hz from 160°K to 300°K for most of the samples and to 360°K for sample B1.

Dynamic modulus-temperature plots are illustrated in Figures (4.A.1) to (4.A.8). A large decrease in the modulus of at least one order of magnitude, is observed for each sample as the T_g of the polymer is traversed. In the rubbery plateau region the modulus decreases fairly rapidly with increasing temperature. As will be demonstrated later, this decrease in modulus coincides with melting in the crystalline phase.

Figures (4.A.9) through (4.A.16) are plots of $\tan \delta$ versus temperature for each sample. The maxima observed at low temperatures coincide with the step-like modulus decrease, mentioned above, indicating a T_g process. Further observation shows that these maxima have different magnitudes and occur at different temperatures for each sample. A higher temperature maximum is also observed for Sample B1, Figure (4.A.11), which coincides with this copolymer's melting point.

FIG. 4.A1

SAMPLE A1

- X 10 Hz
- O 1
- △ 0.1

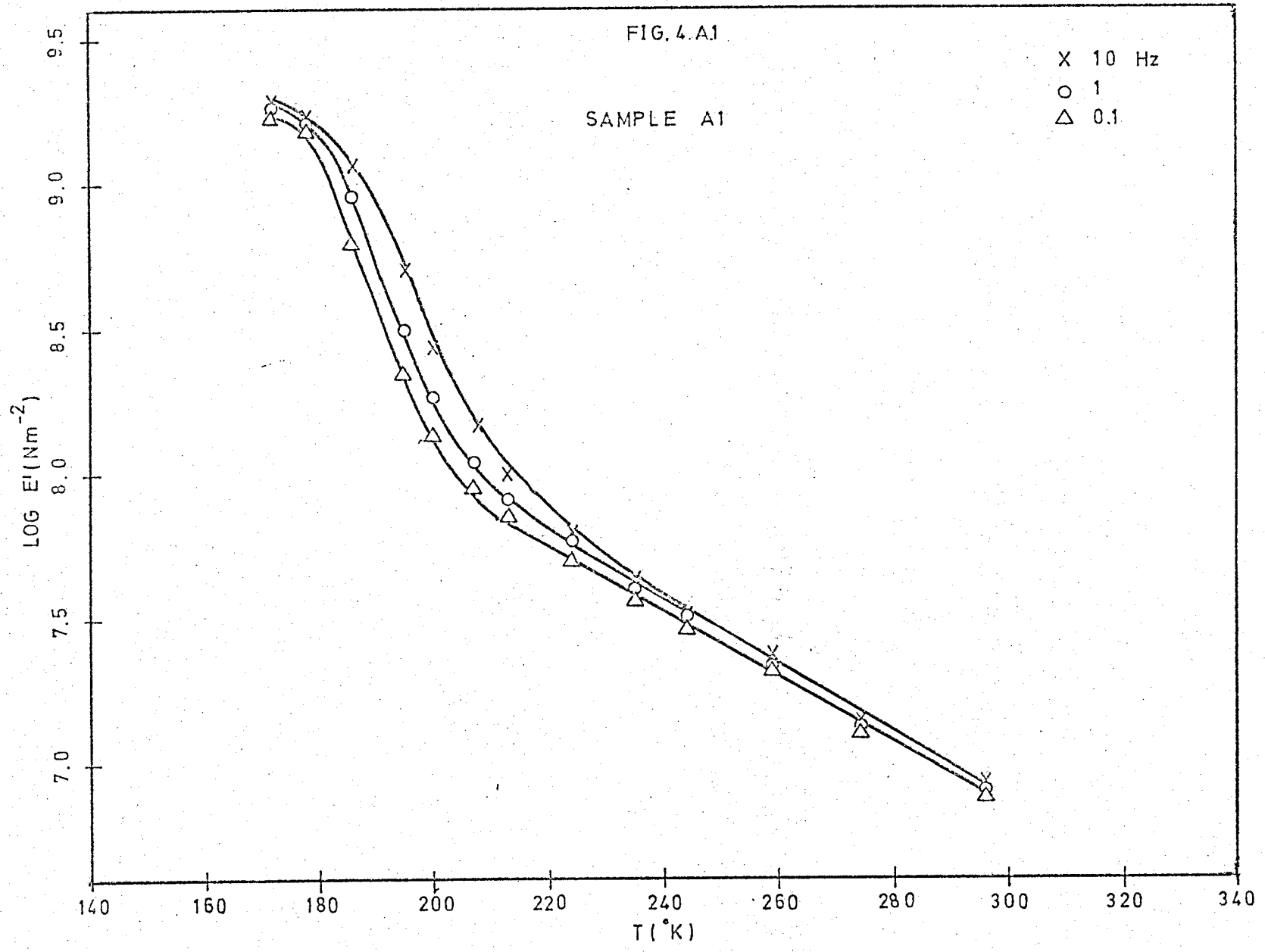


FIG.4.A.2

SAMPLE A2

X 10 Hz
O 1
Δ 0.1

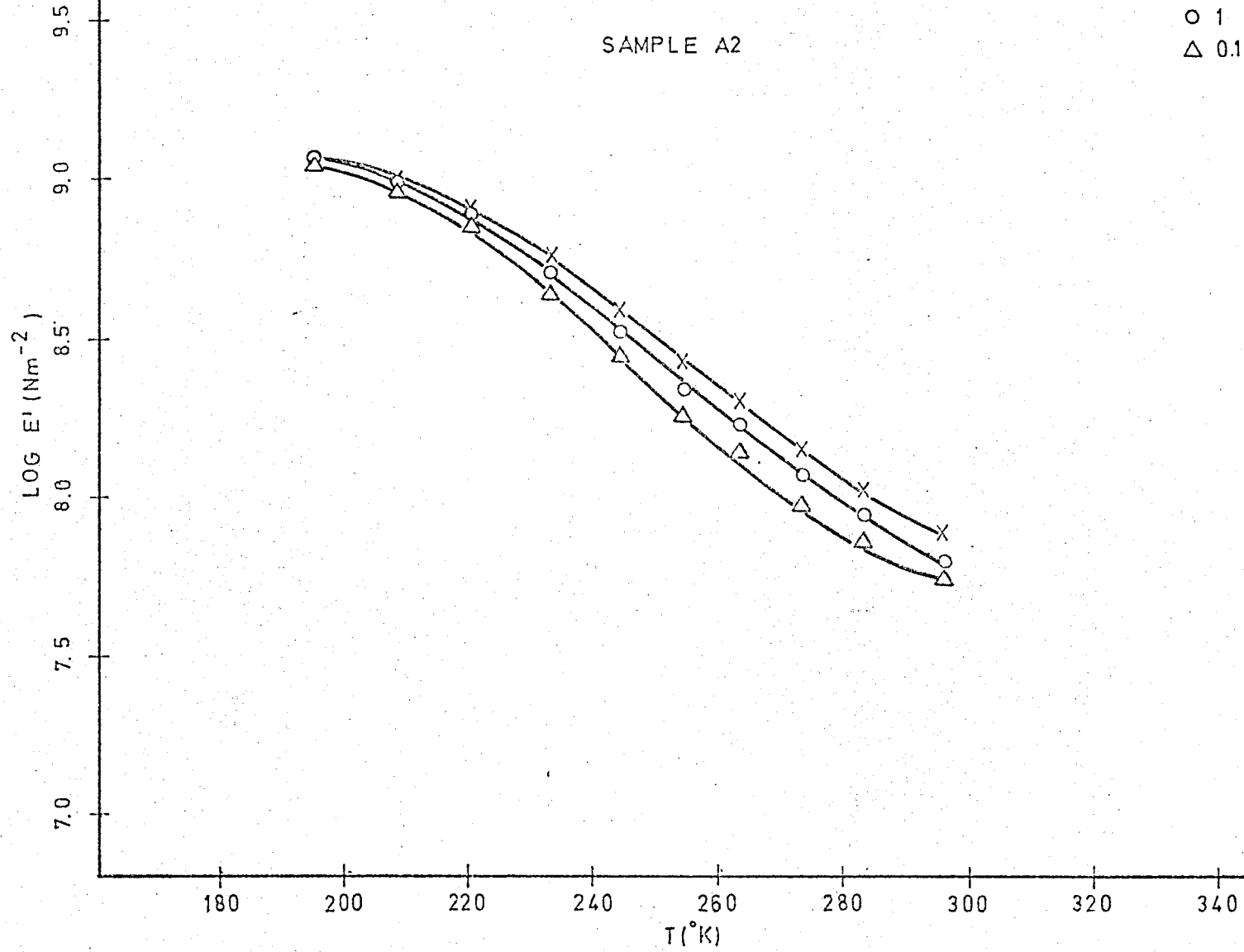
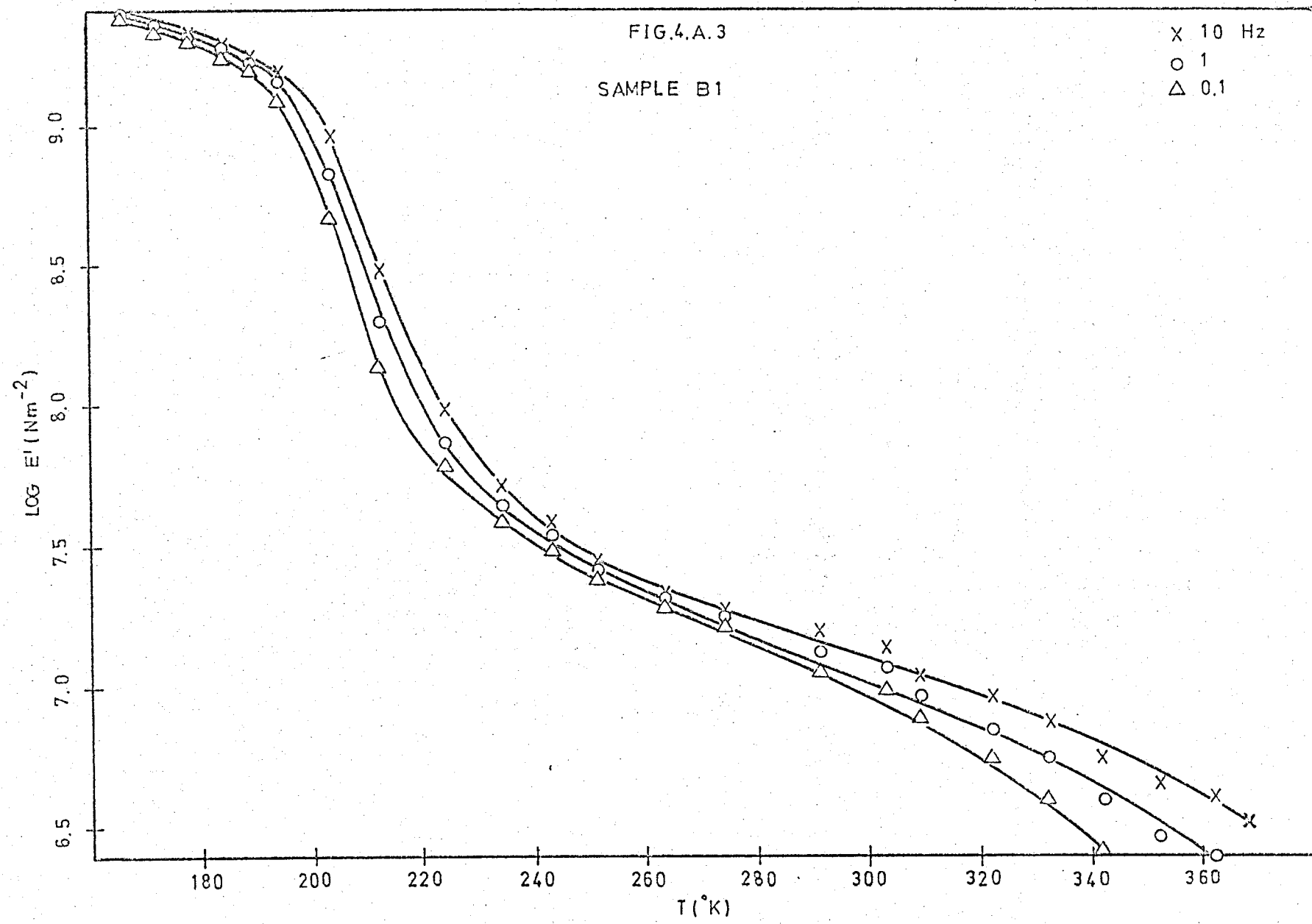
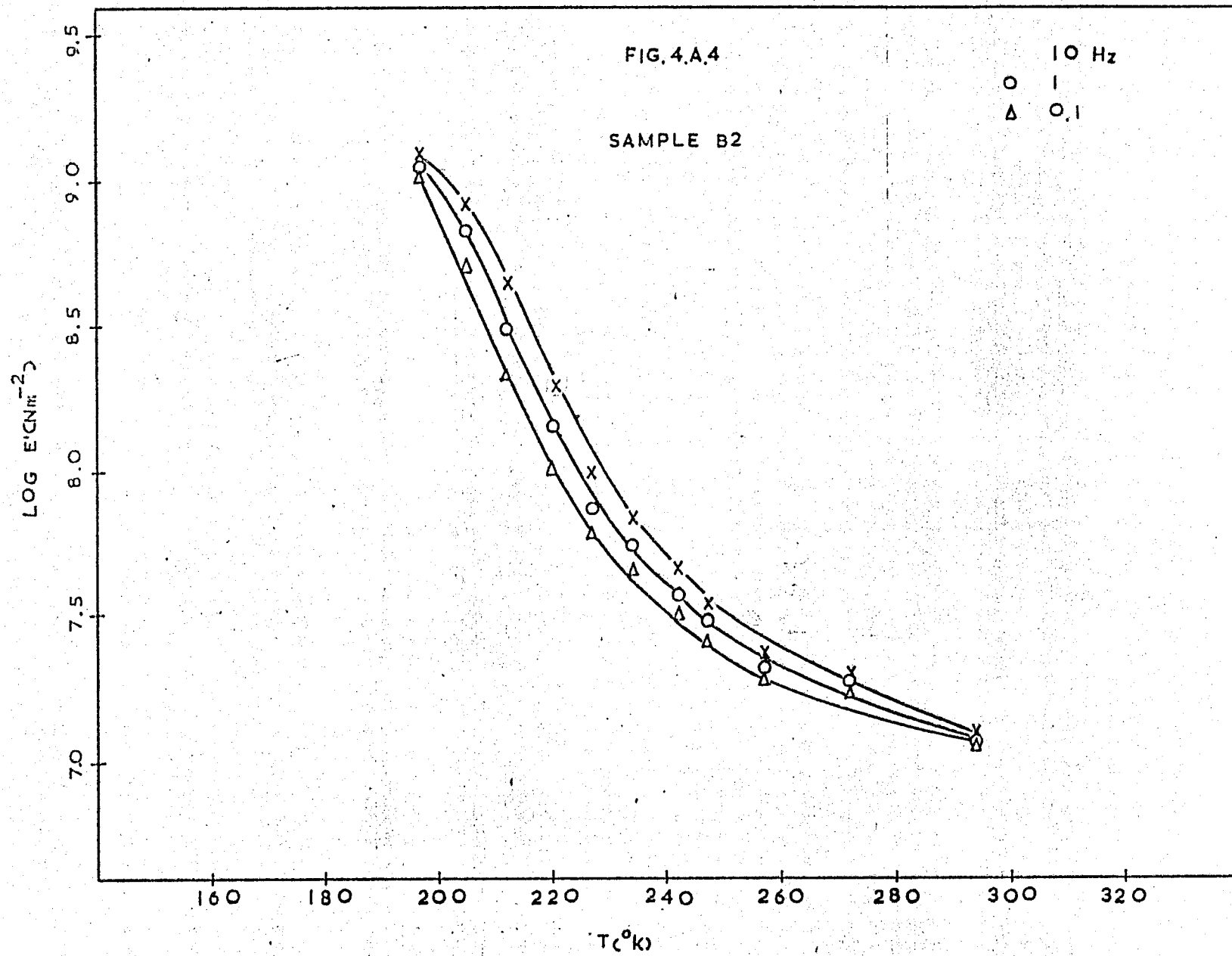


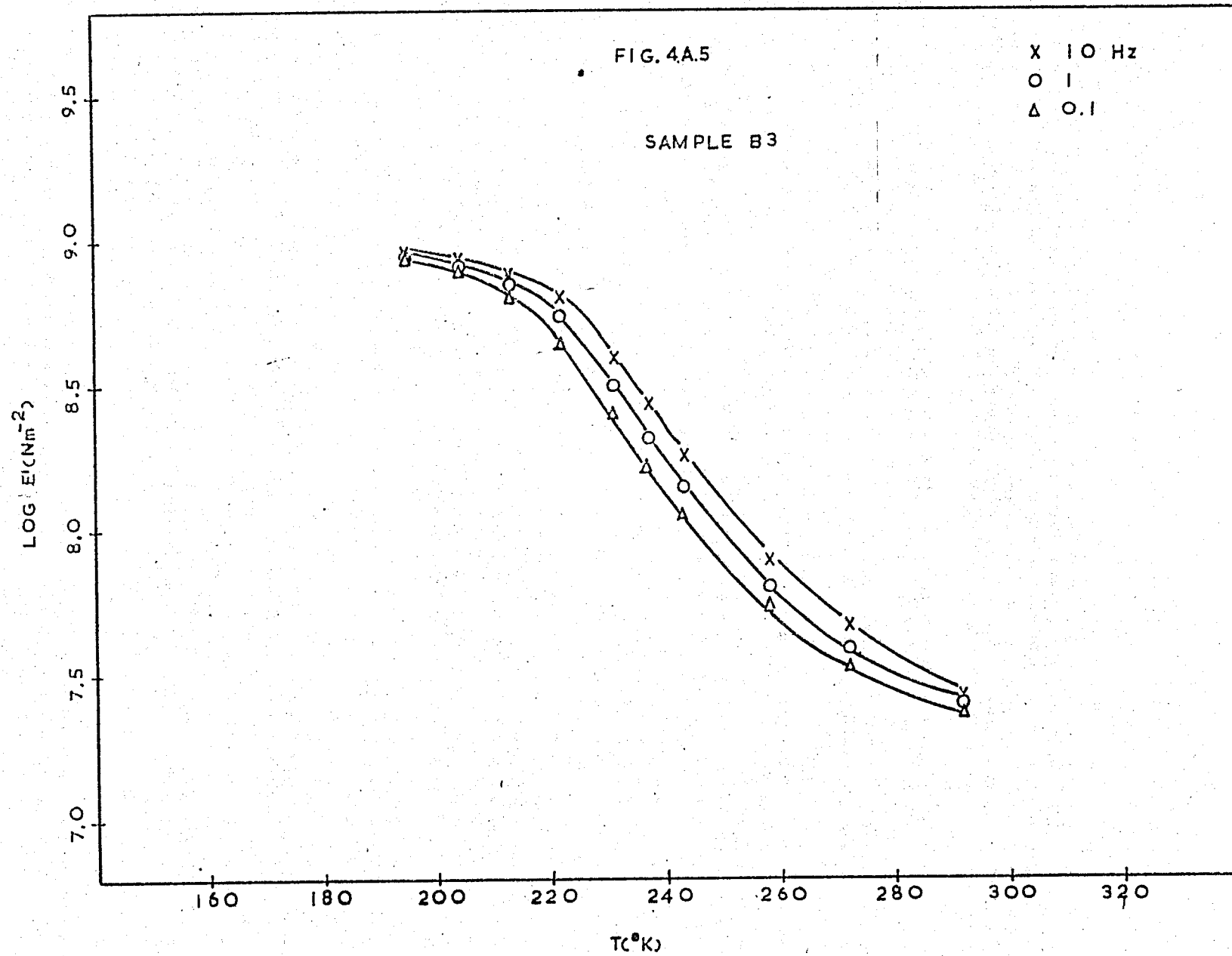
FIG.4.A.3

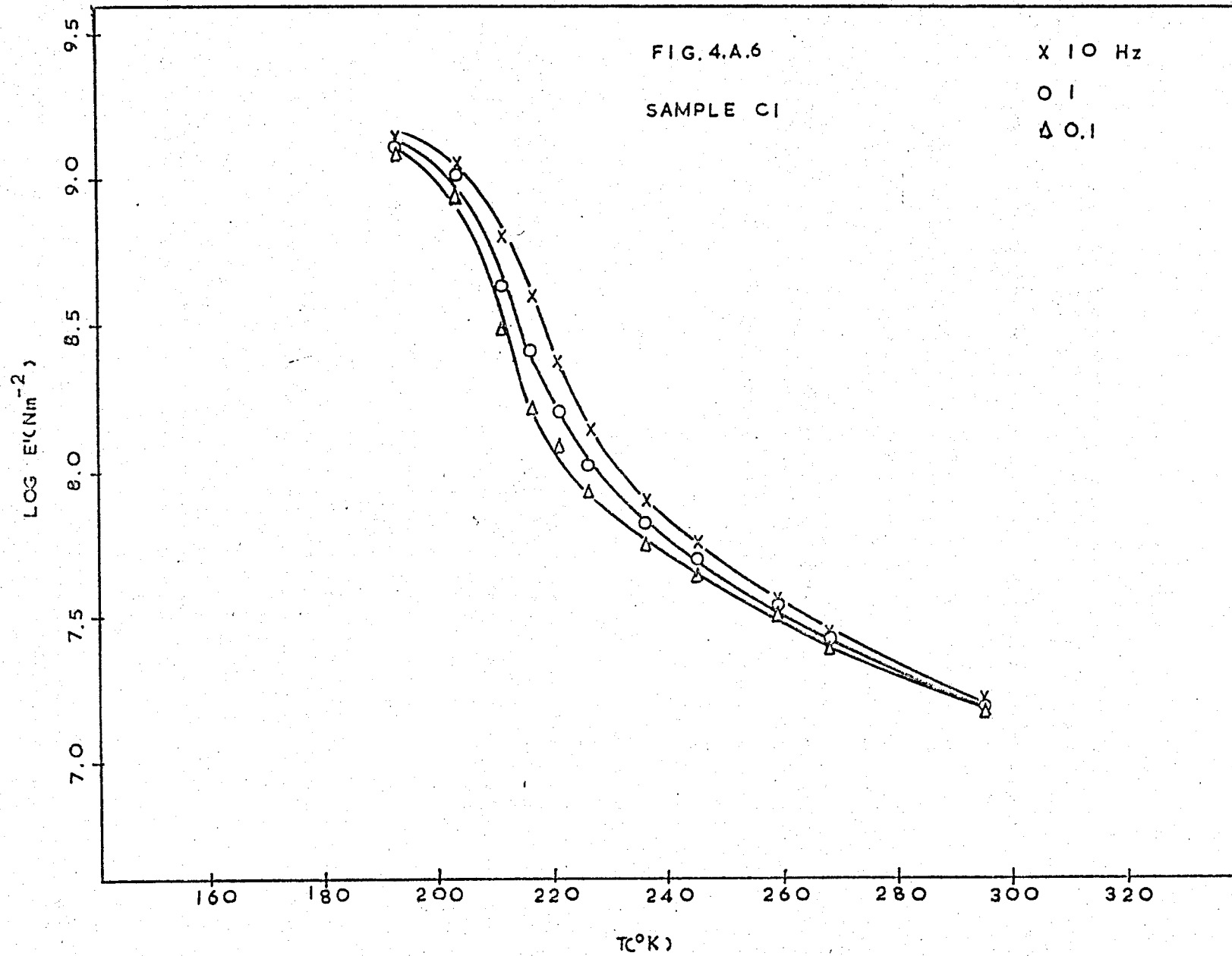
SAMPLE B1

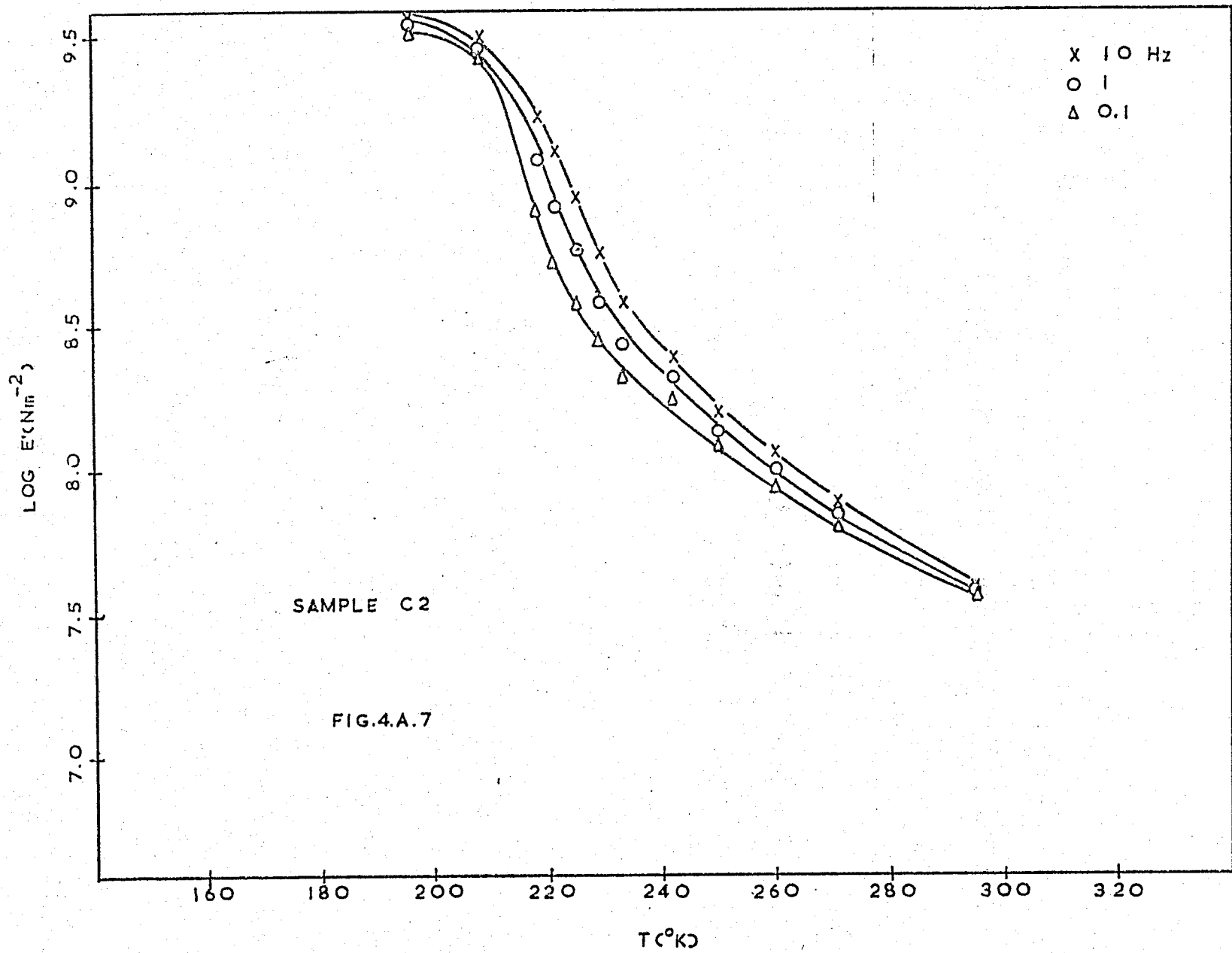
X 10 Hz
 O 1
 Δ 0.1

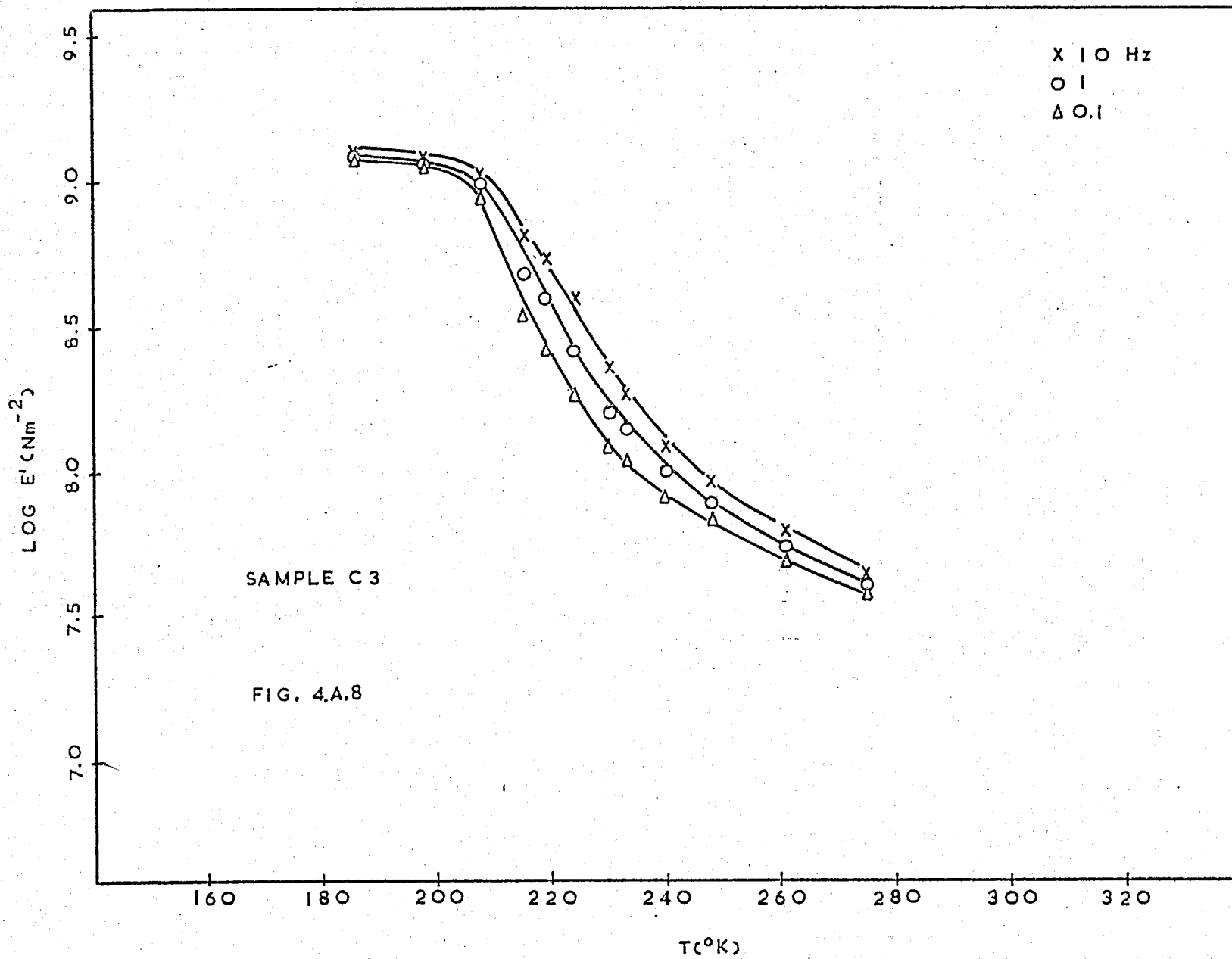












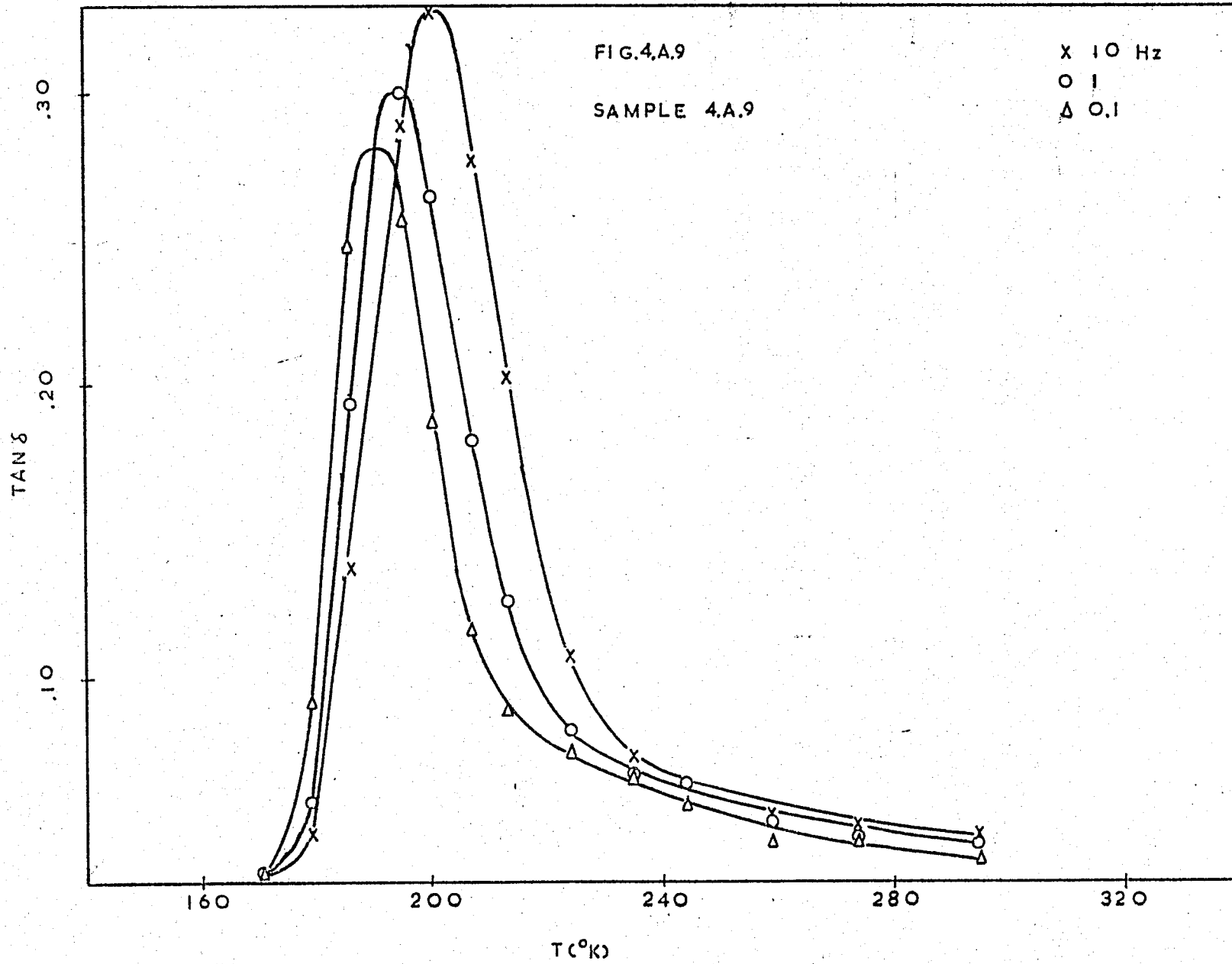


FIG. 4A.10

SAMPLE A2

Δ 10 Hz
O 1
X 0.1

TAN δ
.20
.10
.00

200 240 280 320
T(°K)

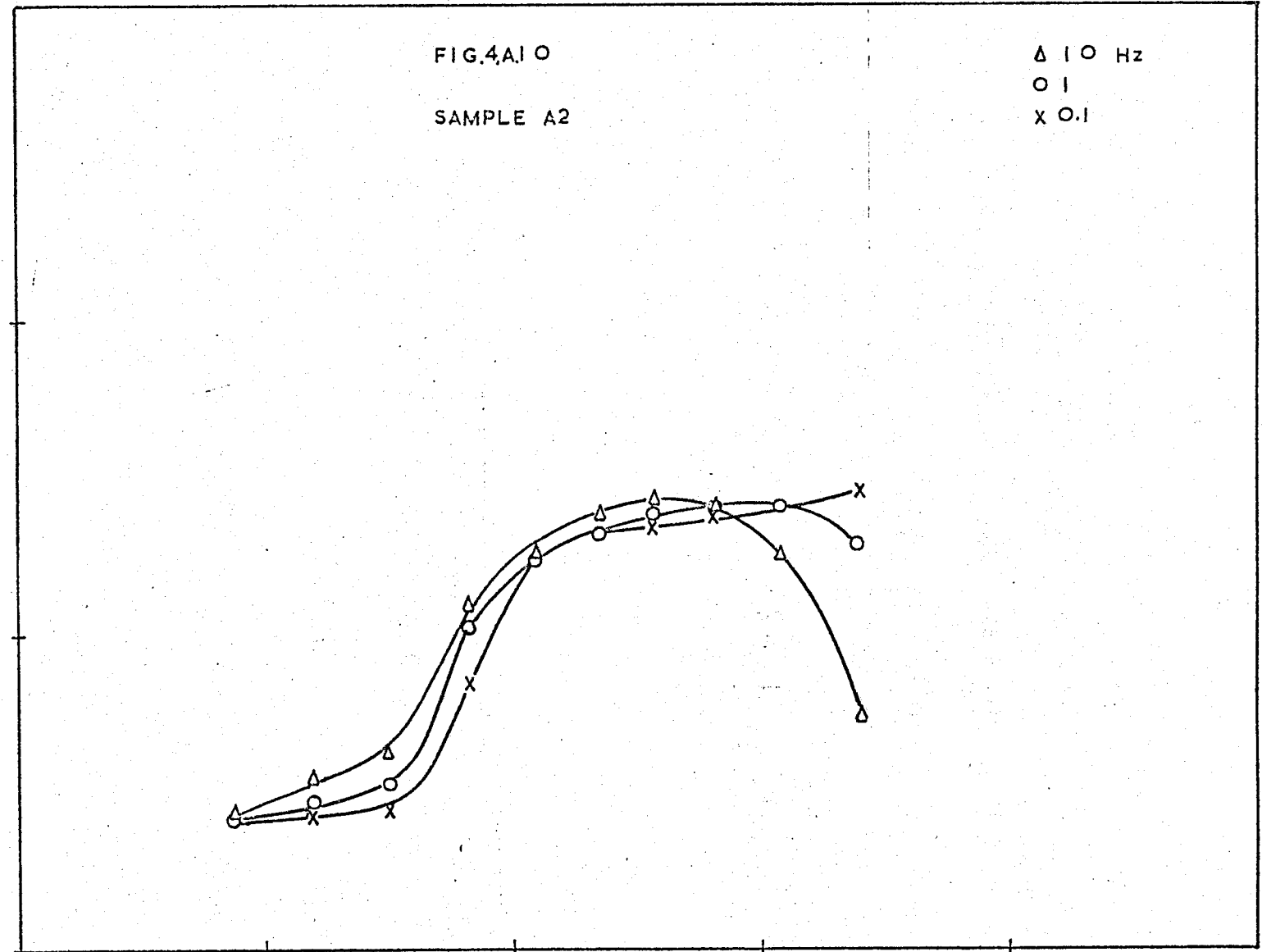
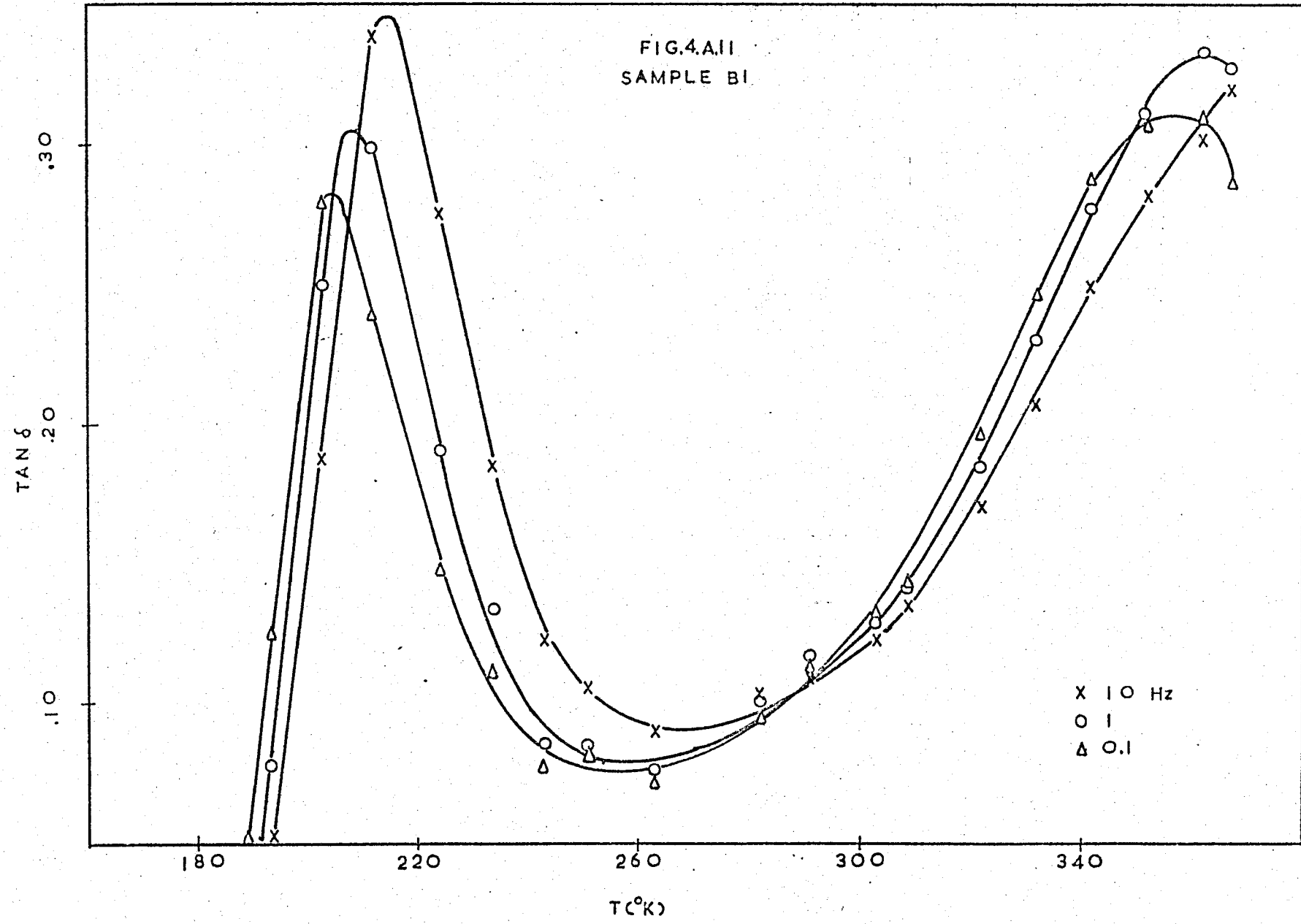


FIG.4.A.11
SAMPLE B1



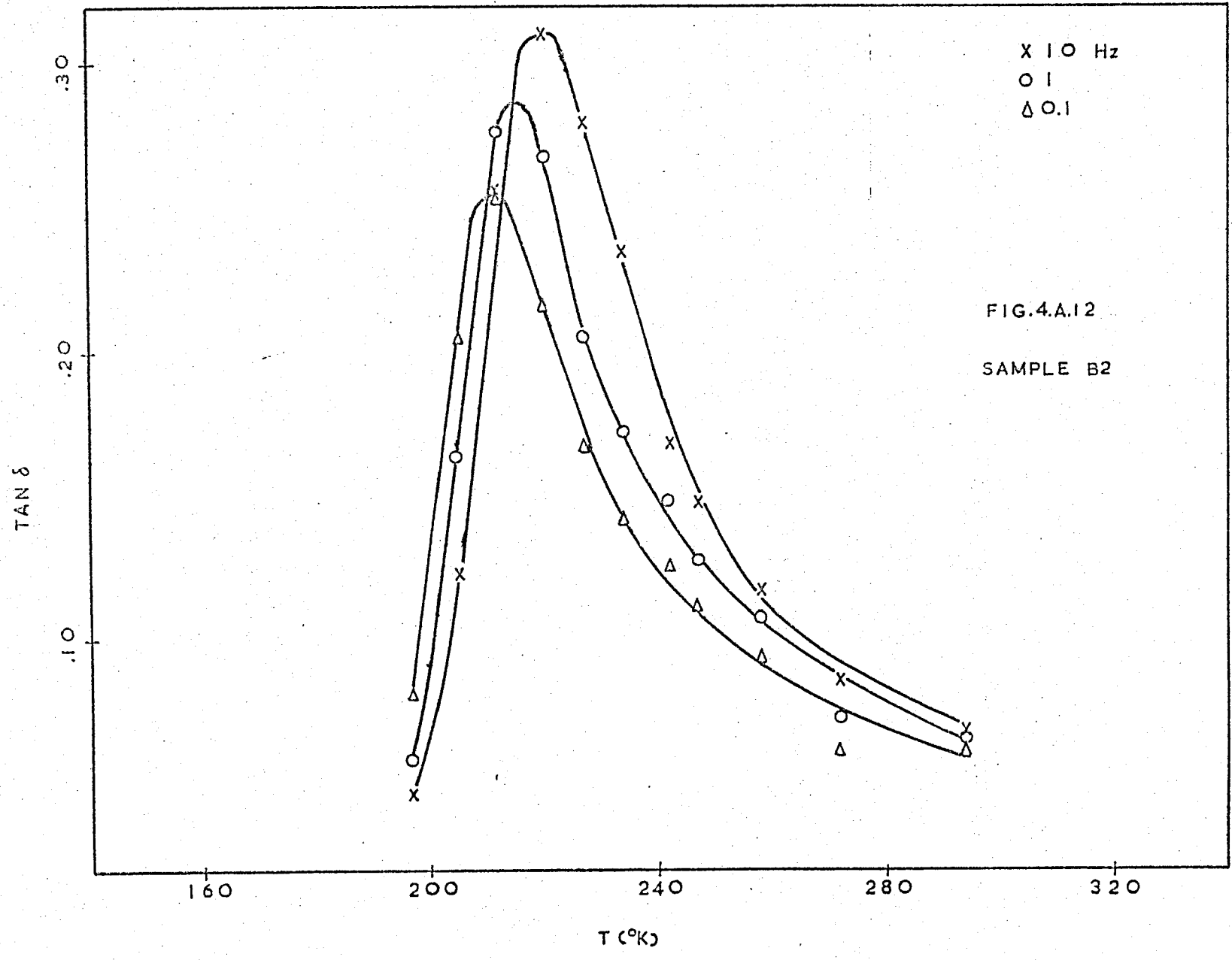


FIG. 4.A.13

SAMPLE B3

X 10 Hz

O 1

Δ 0.1

TAN δ

.20

.10

.00

180

220

260

300

T(°K)

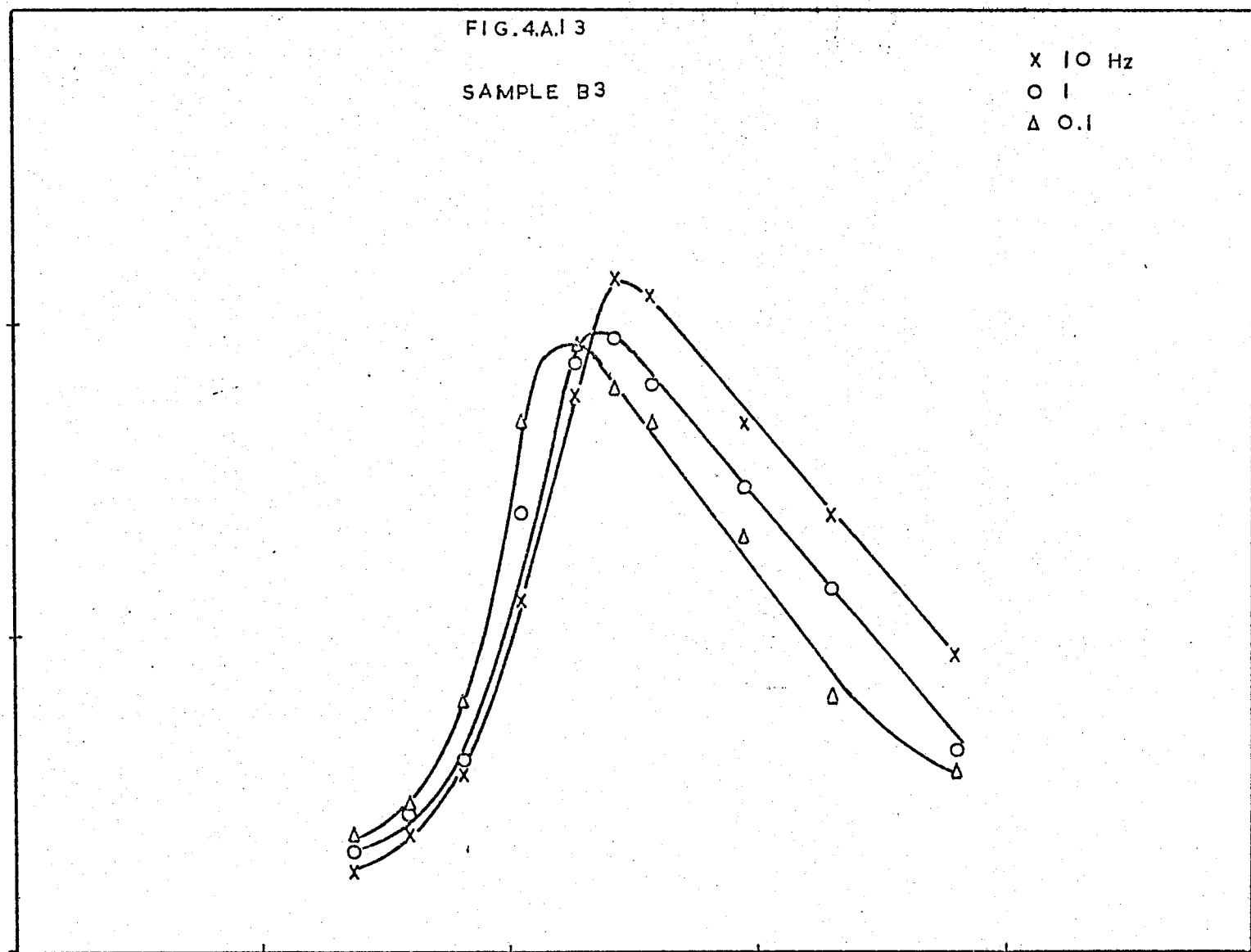
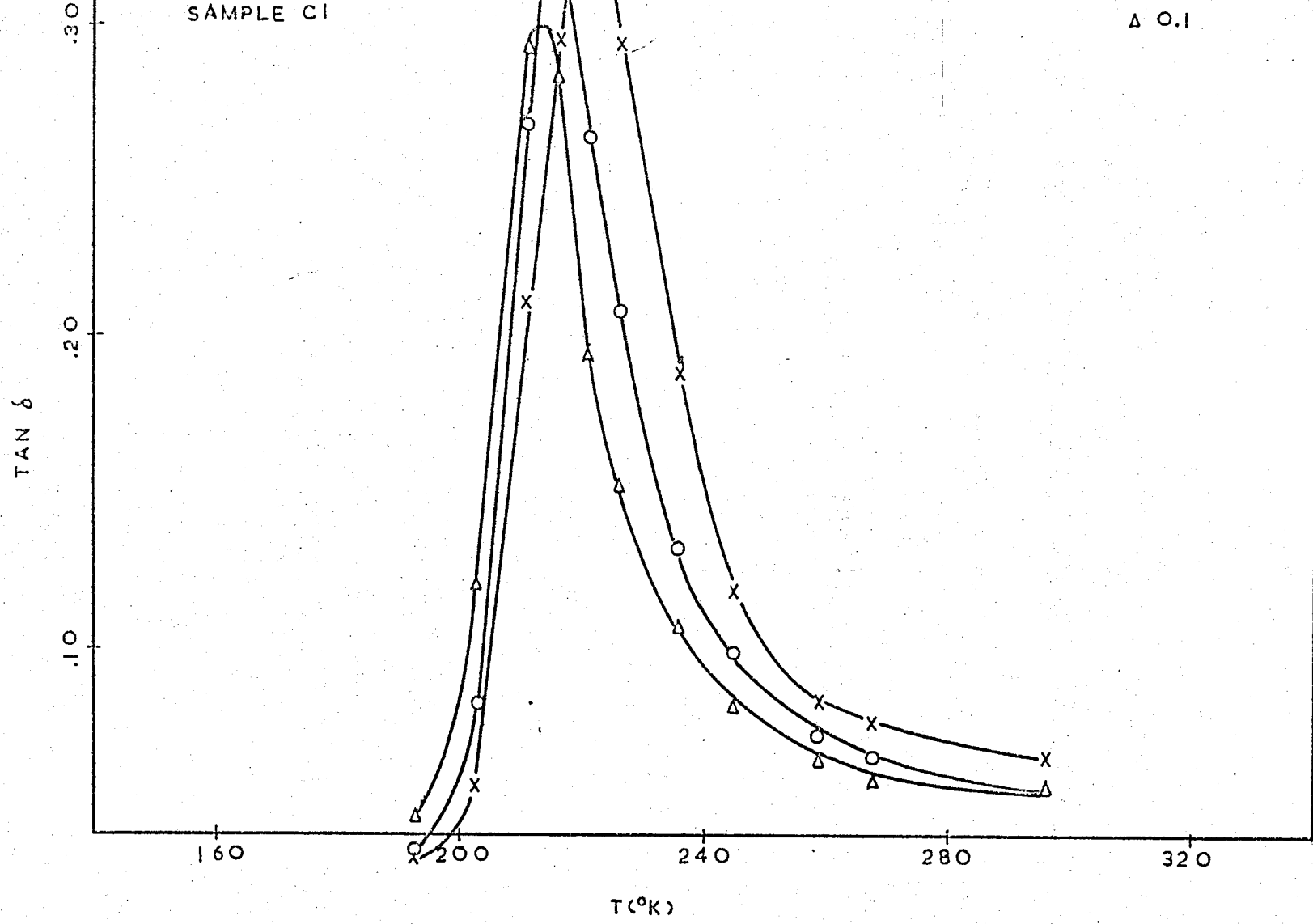


FIG.4.A.14
SAMPLE C1

X 10 Hz
O 1
Δ 0.1



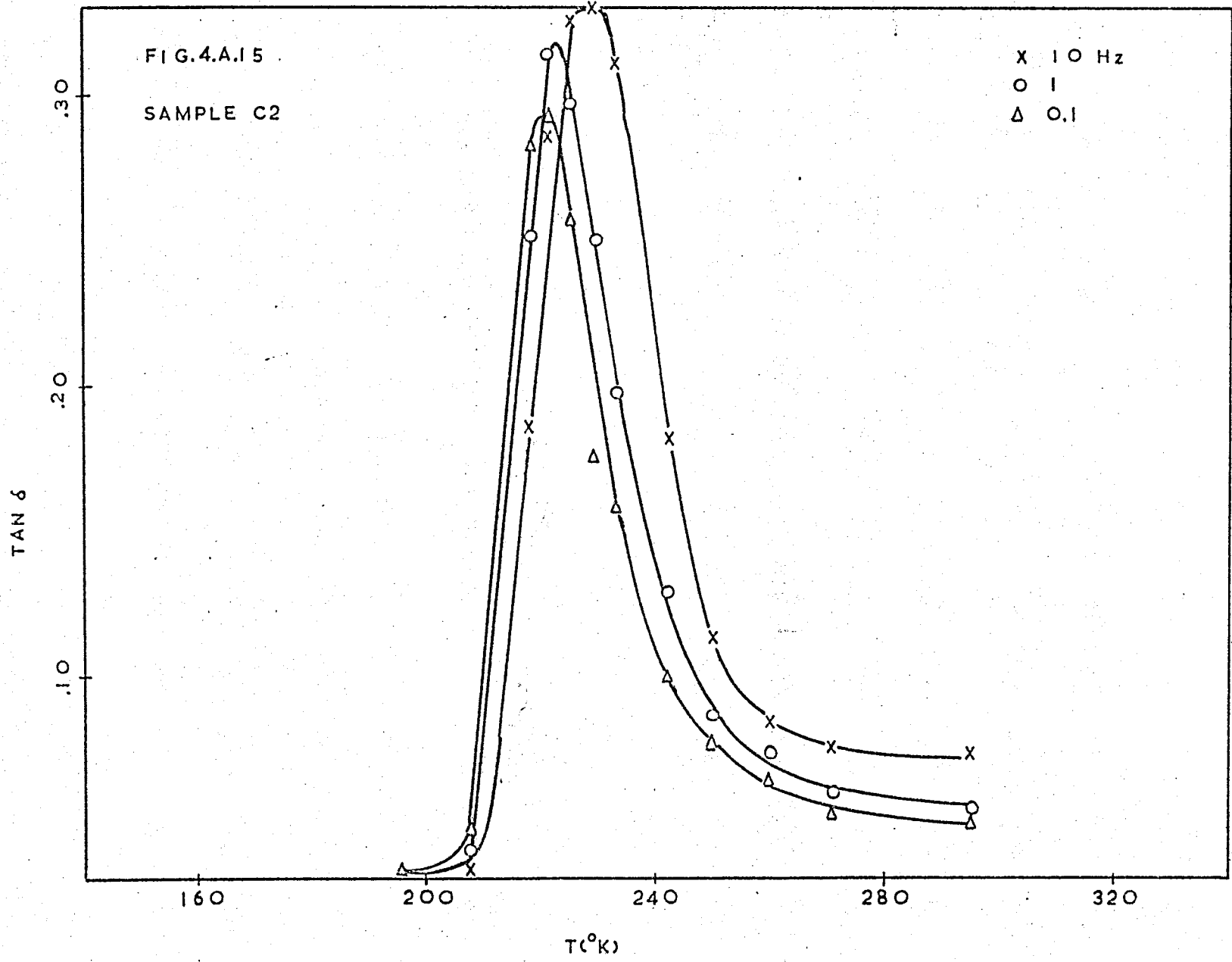


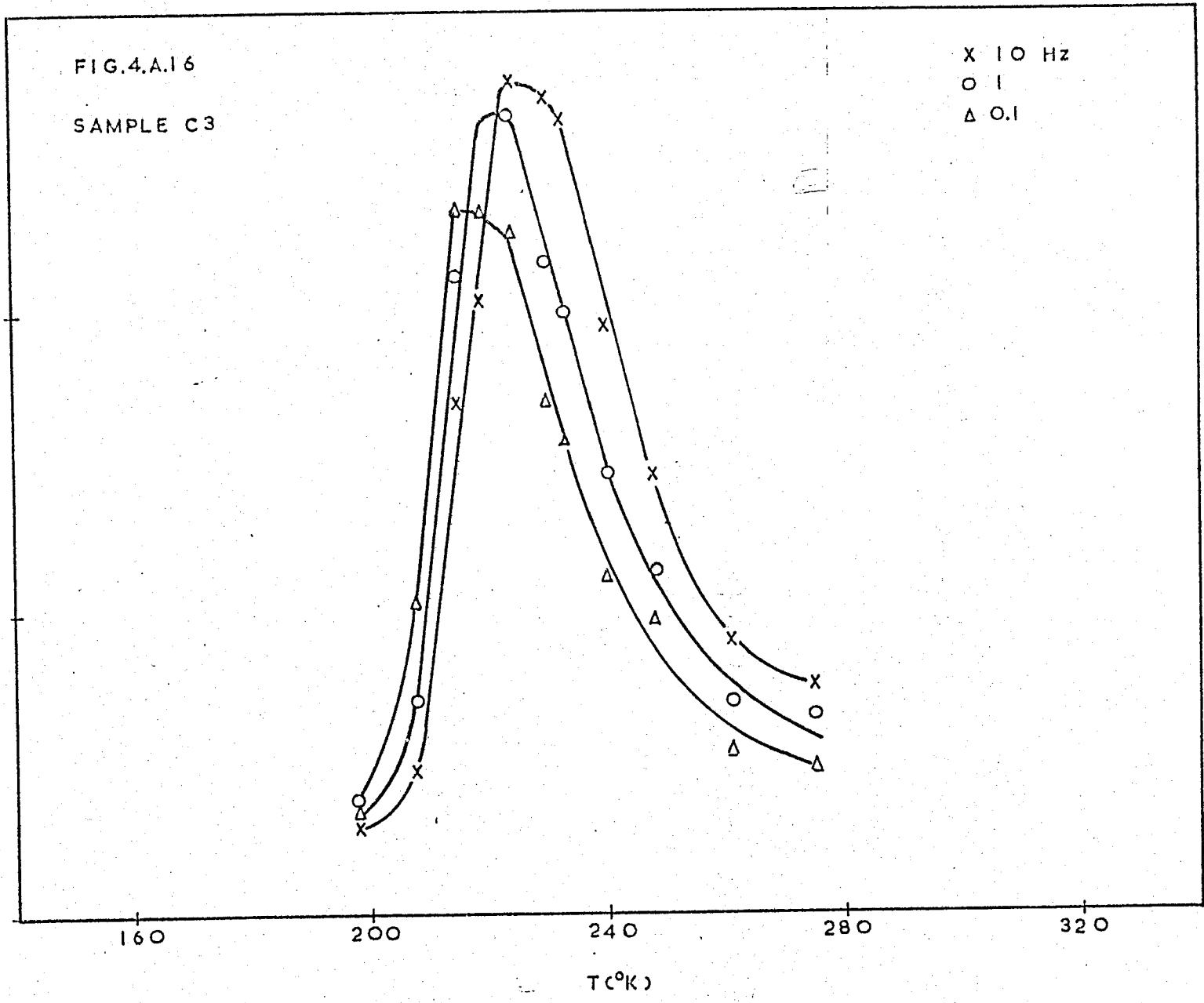
FIG.4.A.16

SAMPLE C3

X 10 Hz
O 1
Δ 0.1

TAN δ
.20
.10
.00

160 200 240 280 320
T(°K)



4.A.2 Differential Scanning Calorimetry

Figures (4.A.17) to (4.A.19) are DSC scans for base polymers A to C, respectively. All samples had the same thermal history; they were cooled slowly from the melt to 323°K, held there for one hour, and subsequently allowed to cool slowly to room temperature where they were held for several weeks. Immediately prior to scanning, the samples were quench-cooled, at ca. 10°K per minute, to 153°K. Endothermic peaks are observed at ca. 315°K and 335°K to 345°K.

w_c , T_g and T_m for each sample are summarized in Table (4.A.1). T_g and T_m were extrapolated to zero sample mass and therefore the table values do not necessarily agree with the values found directly from the figures.

TABLE 4.A.1 DSC Data for Hydrogenated Polymers

SAMPLE	T_g (°K)	T_m (°K)	w_c at 293°K
A1	205	369	.048
A2	250	373	.227
B1	211	363	.071
B2	221	361	.089
B3	227	363	.150
C1	223	361	.087
C2	223	363	.088
C3	221	360	.136

FIG.4.A.17

POLYMER A

A1 ———

A2 ·····

EXOTHERM ← ΔT → ENDOTHERM

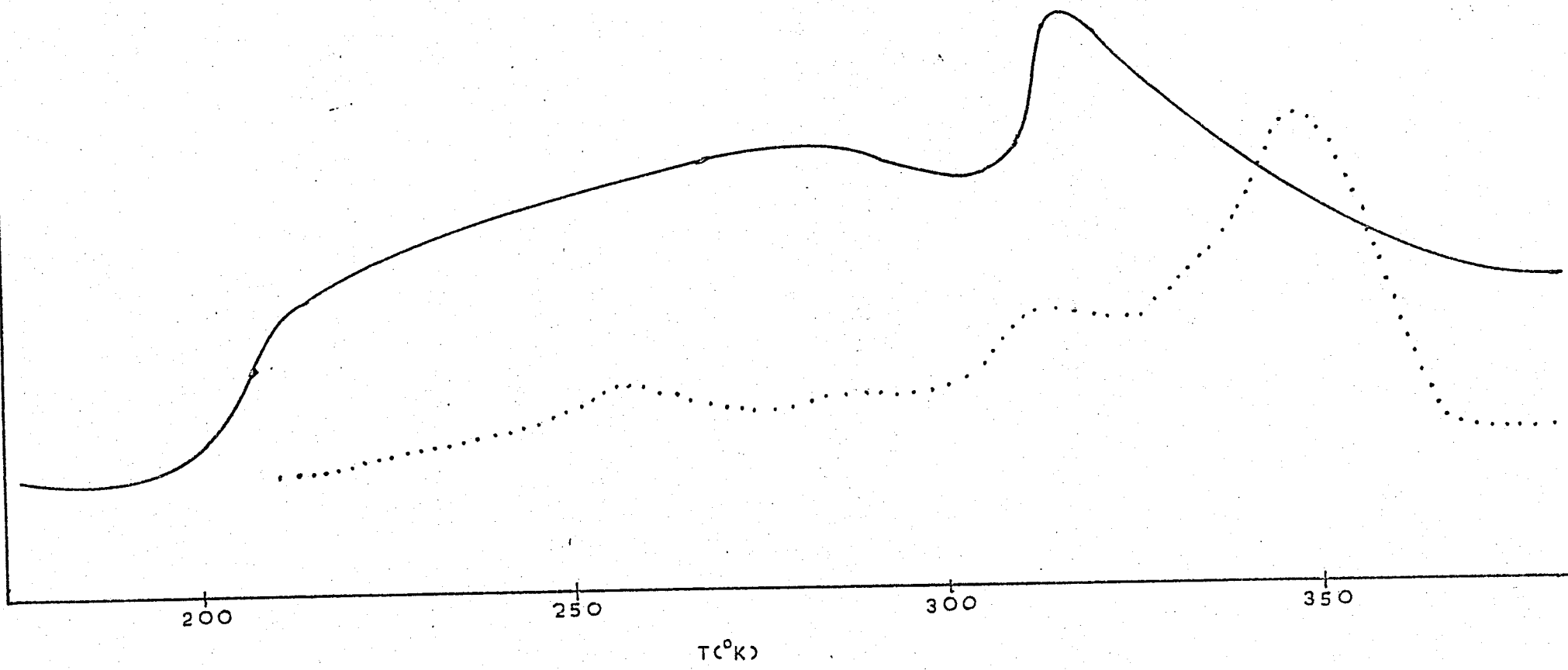


FIG.4.A.18

POLYMER B

B1 ———

B2 ·····

B3 - - -

EXOTHERM ← ΔT → ENDOTHERM

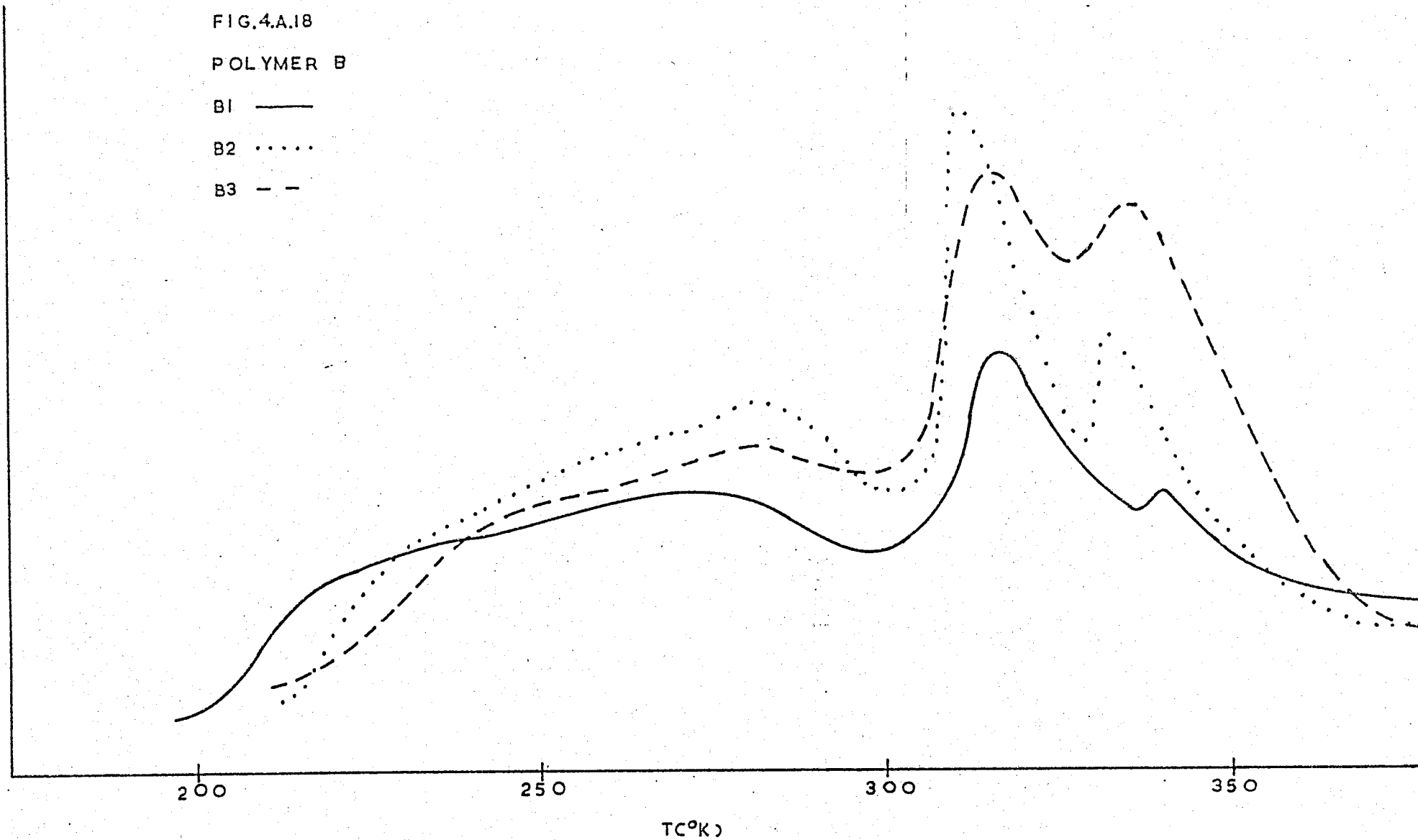


FIG.4.A.19

POLYMER C

C1

C2

C3

EXOTHERM ← AT → ENDOTHERM

200

250

300

350

T(°K)

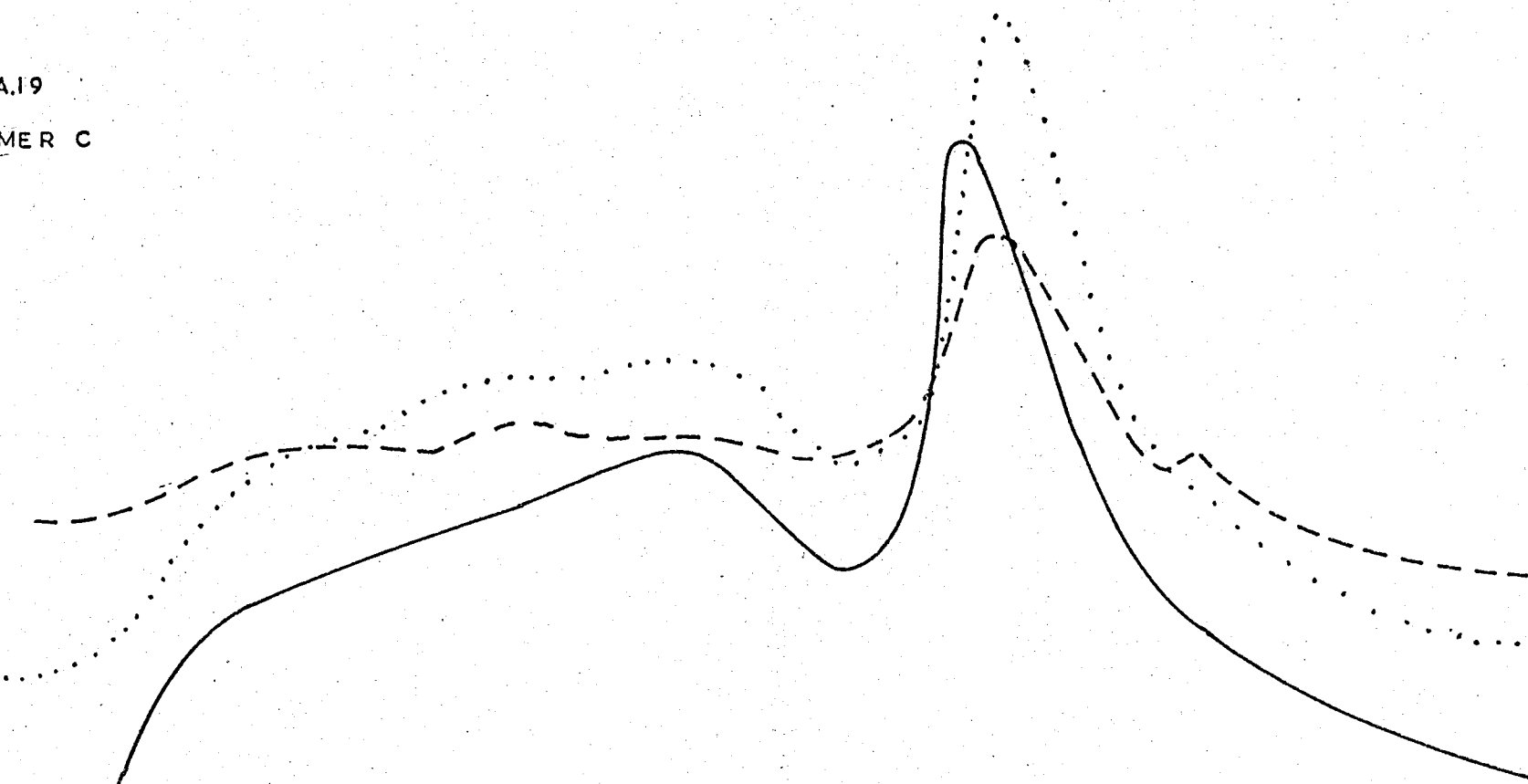


Figure (4.A.20) shows the effect of different thermal histories on the DSC scans for Sample B1. For curve 1, the sample has been cooled from the melt to 323°K , held there for one hour, then cooled to room temperature and held there for several weeks; peaks are observed at 315°K and 351°K . For curve 2, the polymer was cooled from the melt to room temperature and held there for several weeks; one peak at 315°K is observed. The polymer in curve 3 has been cooled from the melt to 323°K and held there for one hour; only one peak at 351°K is observed. The diffuse endothermic area below the lowest crystallization temperature was transformed into a series of peaks when the sample was program cooled below room temperature by holding it at each 10°K interval between room temperature and 233°K for one hour. Each sample was quenched (10°K per minute) to 153°K prior to scanning.

FIG.4.A.20

SAMPLE BI

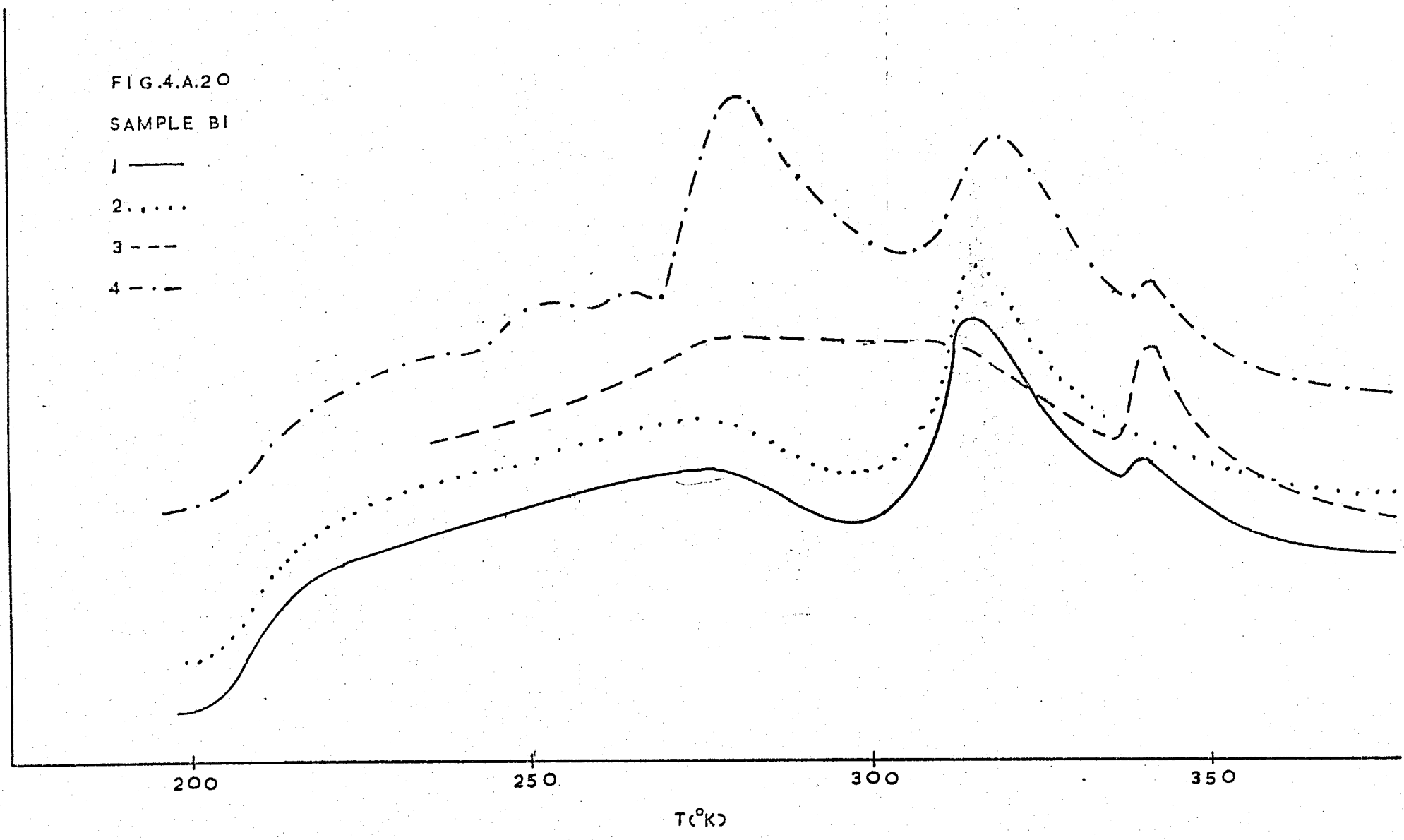
1 ———

2

3 - - -

4 - · - ·

EXOTHERM ← ΔT → ENDOTHERM

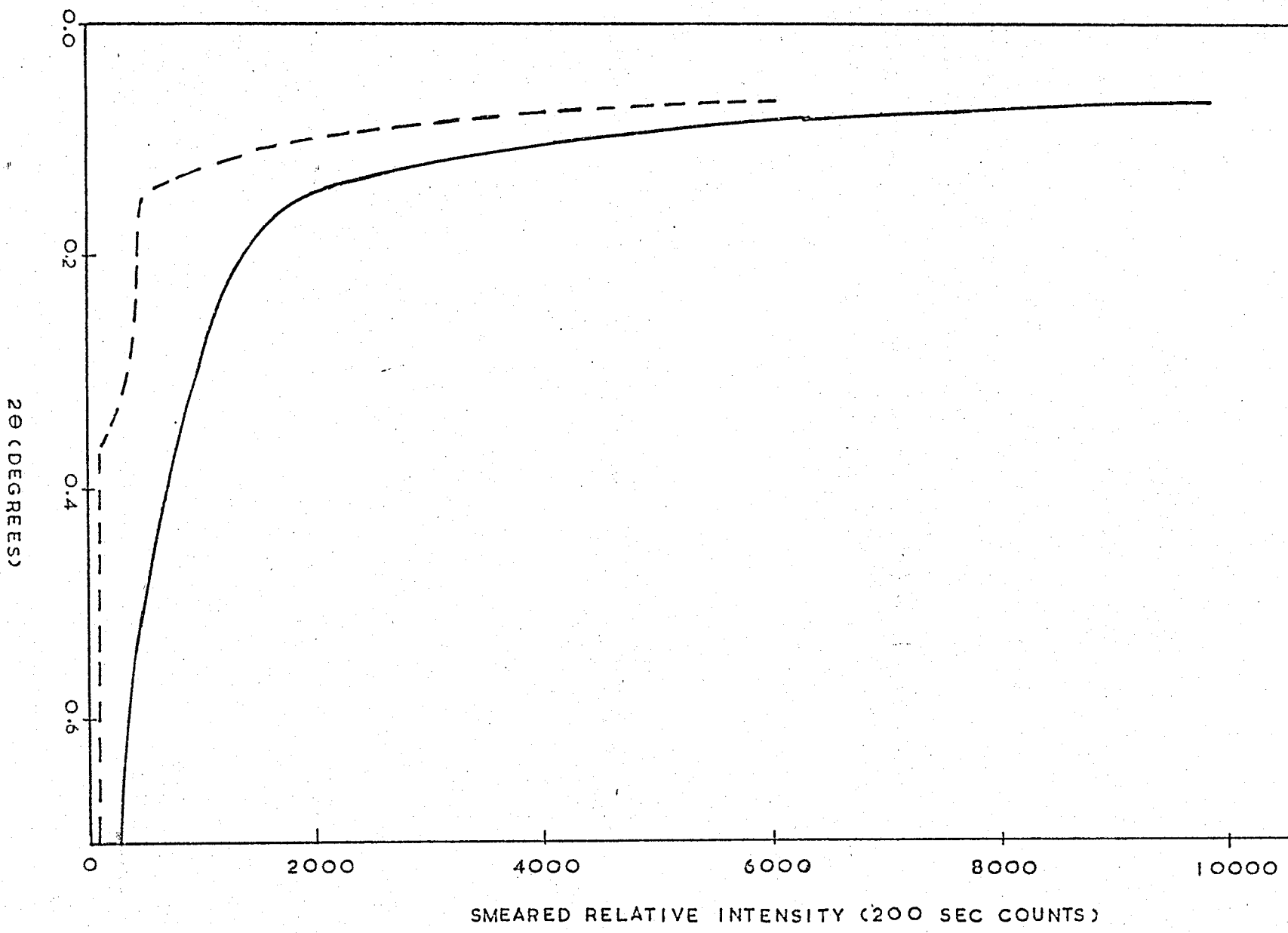


4.A.3 Small Angle X-ray Scattering

The sample and parasitic scattering for Sample B1 are shown in Figure (4.A.21). The diffuse nature of the scattering indicates the lack of order in the system.

FIG. 4,A.21
SAXS FOR
SAMPLE B1

SAMPLE SCATTERING ———
PARASITIC SCATTERING - - -

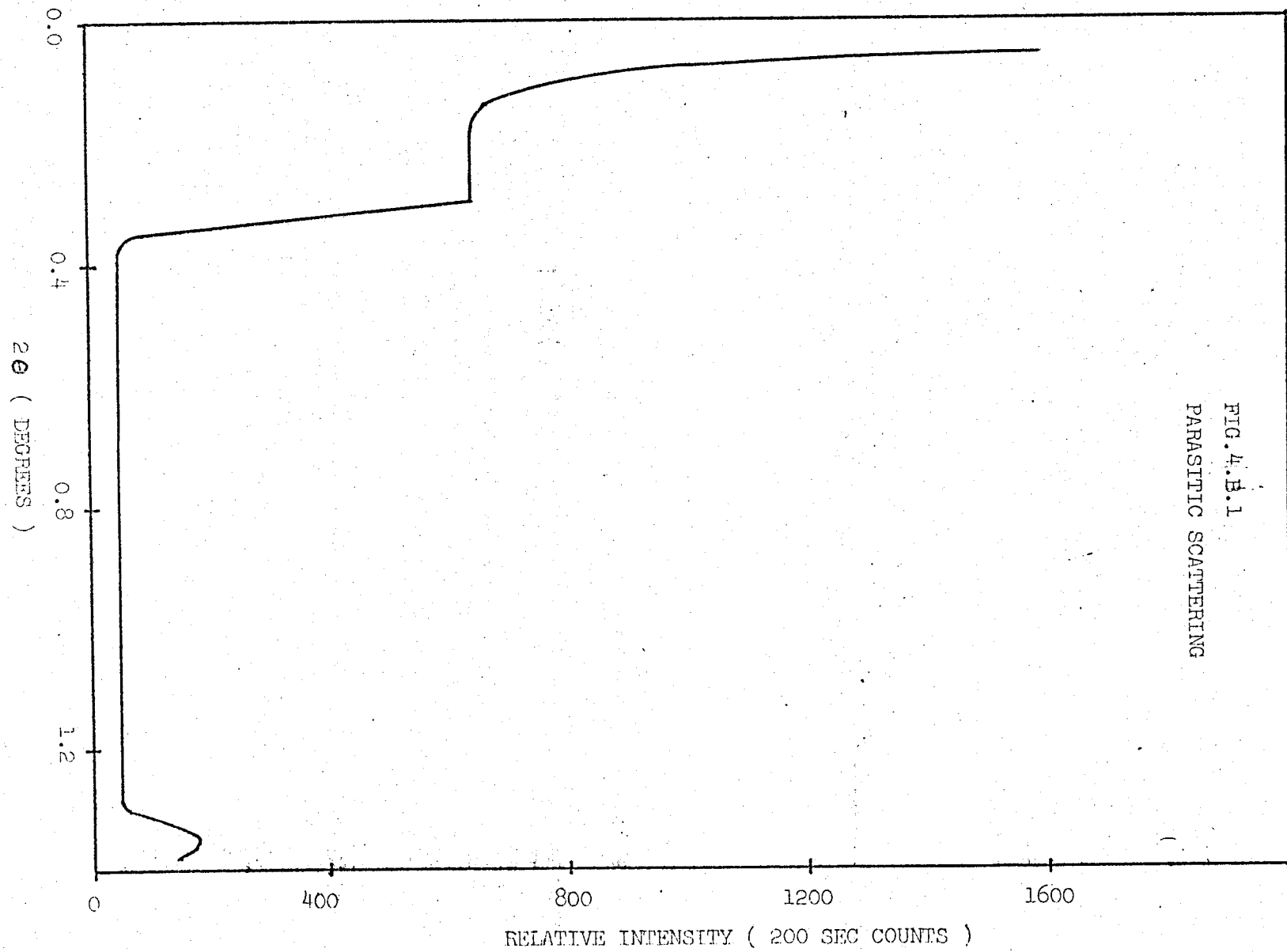


SECTION B SILOXANE BLOCK COPOLYMERS

4.B.1 Small Angle X-ray Scattering

The SAXS for the siloxane copolymer samples was determined using both slit and pin-hole collimation. The data is shown in Figures (4.B.1) to (4.B.6). The sample was mounted such that the beam was either normal to the faces or an edge and the faces were vertical.

The slit optics data is shown in Figures (4.B.1) to (4.B.5). Since all sample thicknesses were approximately the same, Figure (4.B.1) is used to illustrate the parasitic scattering obtained to 1.4 degrees. The sample minus the parasitic scattering is illustrated in the remaining figures. All four samples show different spacings and/or intensity differences in the scattering for the beam normal to the edge and face. Figure (4.B.2) shows the first and second reflection orders for the benzene cast sample when viewed through an edge. The intensity for the face view is approximately 1/10th that of the edge view. The first order reflection for this sample swollen with silicone oil is also shown. Three reflection orders are shown for the face view of the moulded sample, Figure (4.B.3). The two highest orders are also illustrated with a longer counting time. There is virtually no detectable scattering for the face view. Figures (4.B.4) and (4.B.5) for the cyclohexane cast sample, show marked differences in both scattered intensity and spacings before and after taking the sample above the T_g of the organic phase. There are also differences in the scattering for face and edge views.



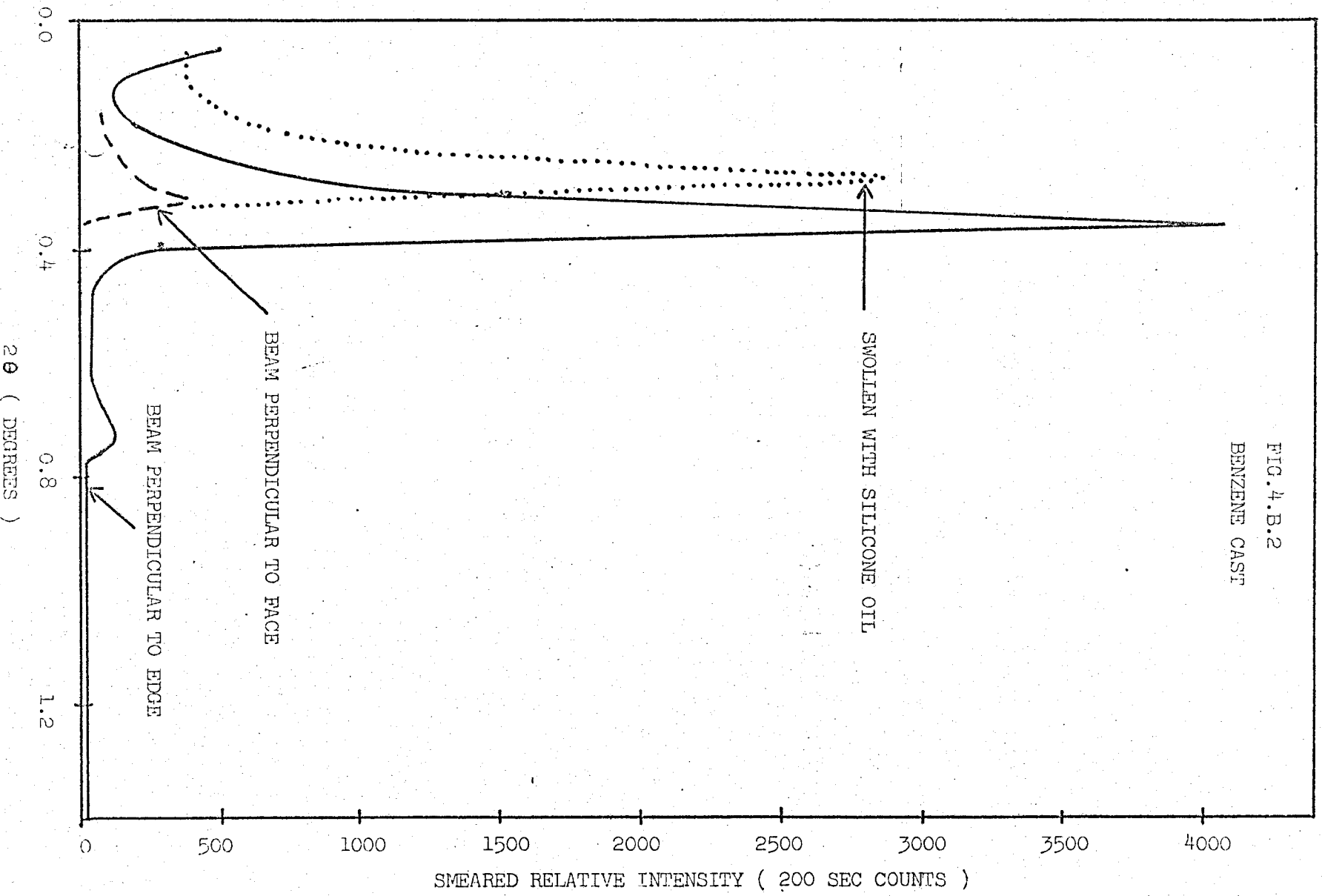


FIG.4.B.2
BENZENE CAST

FIG.4.B.3

MOULDED

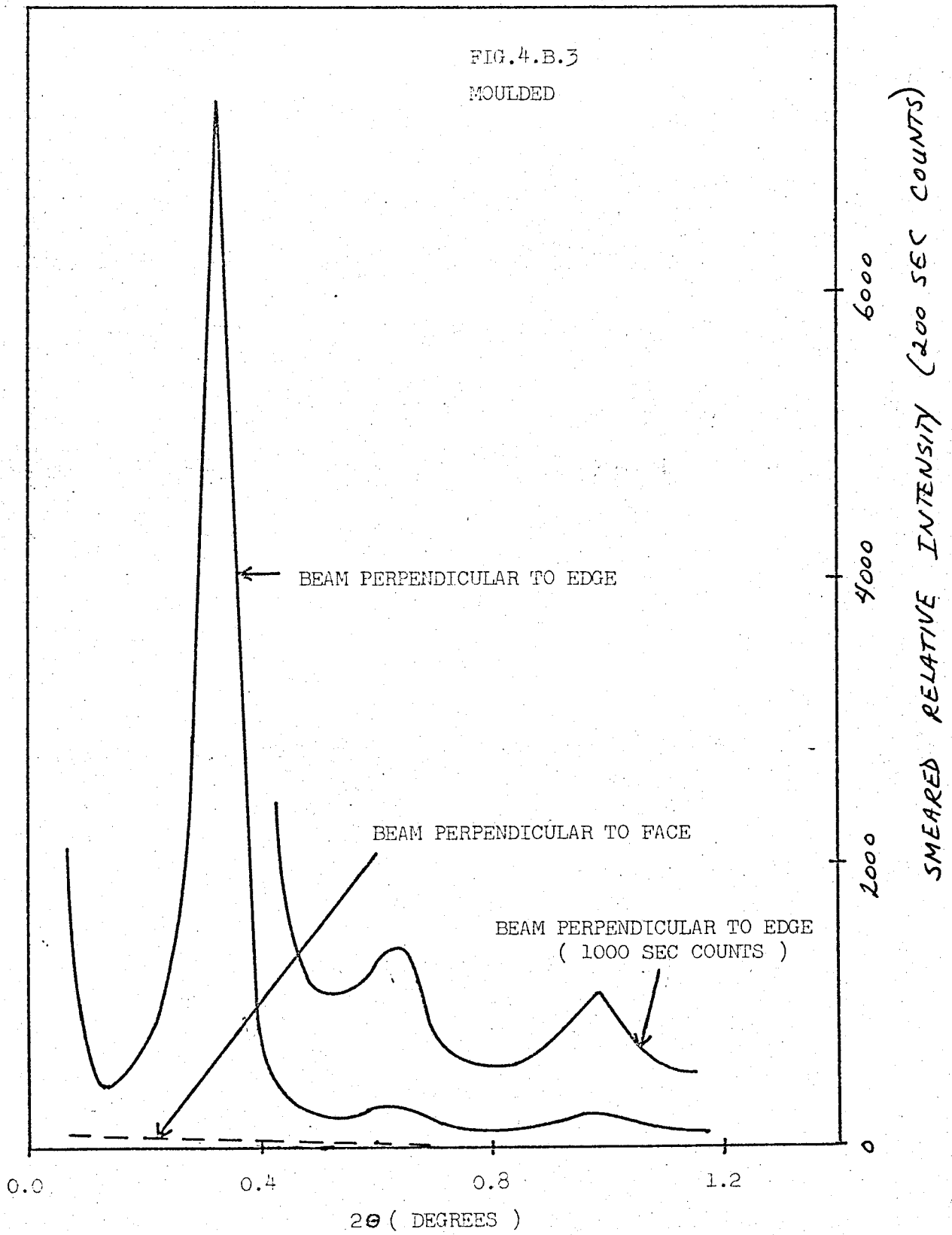


FIG.4.B.4
CYCLOHEXANE CAST

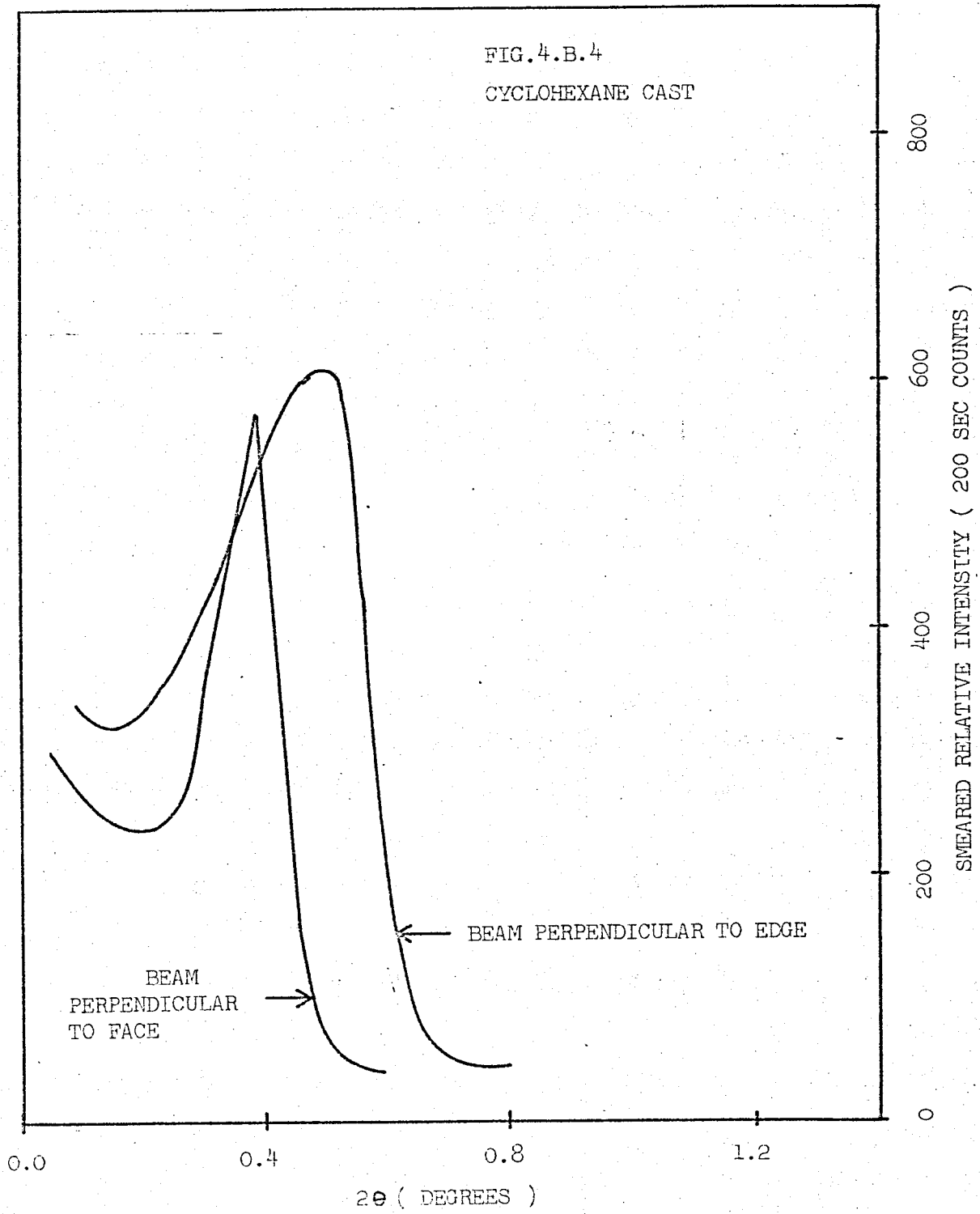


FIG.4.B.5

CYCLOHEXANE CAST - TAKEN ABOVE T_g
BEAM PERPENDICULAR TO FACE

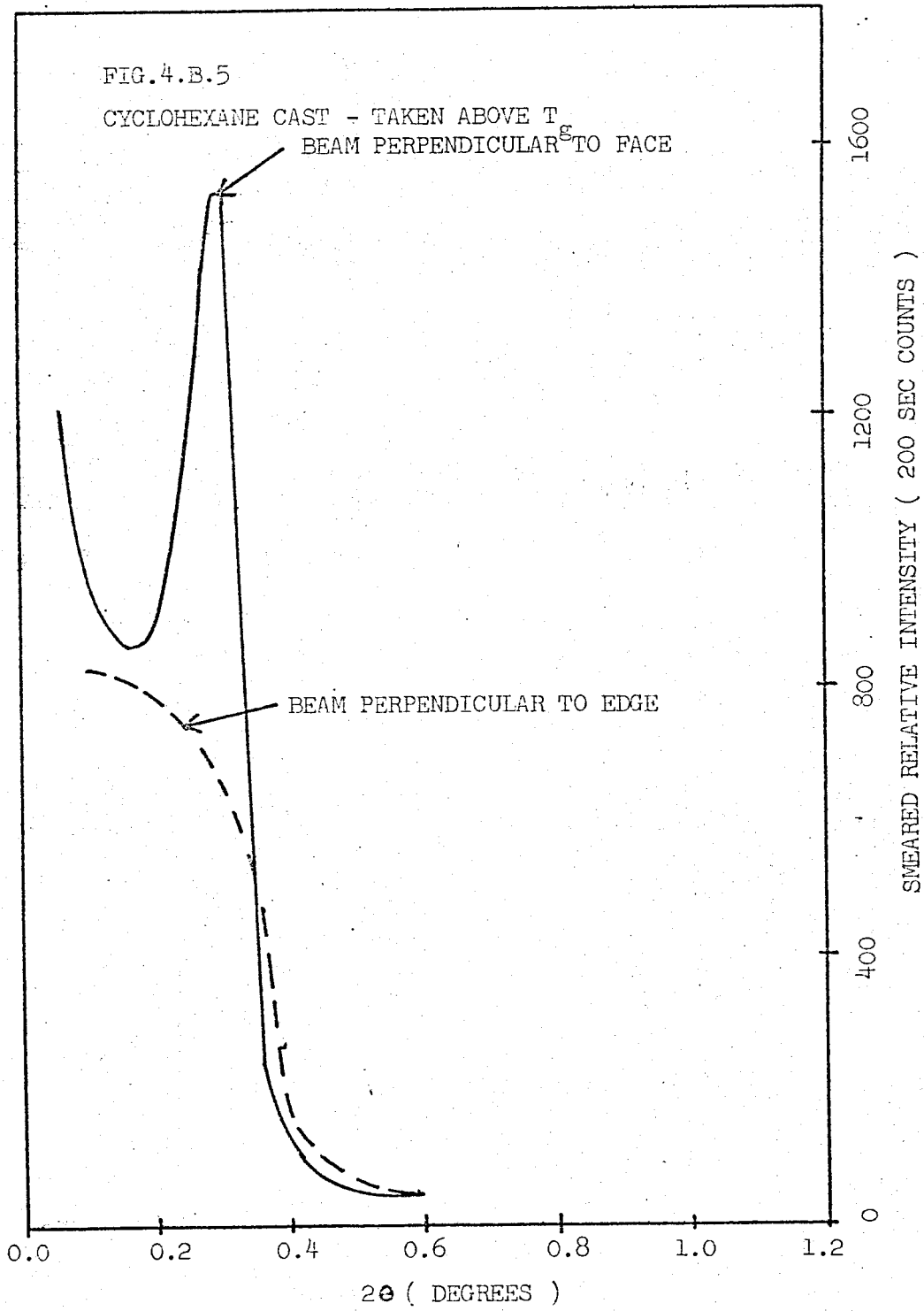




FIG.4.B.6.a

INTENSITY TOO WEAK TO SHOW
UP ON PHOTOGRAPH.

FIG.4.B.6.b

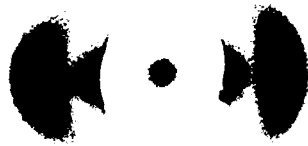


FIG. 4.B.6.c



FIG. 4.B.6.d

FIG.4.B.6.e



FIG.4.B.6.f



FIG.4.B.6.g



FIG.4.B.6.h

The pin-hole photographs, Figures (4.B.6.a) through (4.B.6.h), are consistent with the slit data and give more information about sample orientation and macro-lattice parameters (from higher order reflections). The spacings from pin-hole and slit data are summarized in Table (4.B.1).

TABLE 4.B.1 Bragg Spacings of the Macro-Lattice

SAMPLE	PLANE NORMAL TO X-RAY BEAM	O R D E R	BRAGG SPACING (\AA)		
			PIN - HOLE		SLIT (SMEARED)
			EQUATOR	MERIDIAN	
Swollen	Edge	1	--	--	314 ± 6
Benzene Cast	Face	1	235 ± 5	235 ± 5	282 ± 3
	Edge	1	235 ± 5	247 ± 5	246 ± 4
		2	115 ± 2	--	121 ± 4
		3	77 ± 1	--	--
		4	57 ± 1	--	--
Moulded	Face	1	307 ± 6	307 ± 6	--
	Edge	1	275 ± 5	307 ± 6	272 ± 4
		2	143 ± 2	--	139 ± 1
		3	92 ± 2	--	89 ± 1
		4	70 ± 1	--	--
Cyclohexane Cast	Face	1	208 ± 4	208 ± 4	229 ± 3
	Edge	1	156 ± 3	208 ± 4	178 ± 2
		2	87 ± 1	116 ± 2	--
Cyclohexane Cast - Taken Above T_g	Face	1	273 ± 5	273 ± 5	296 ± 4
	Edge	1	275 ± 5	275 ± 5	--

Figures (4.B.6.a) and (4.B.6.c) are edge views for the benzene cast and moulded samples, respectively. The equatorial arcs and ratios of consecutive orders indicate the presence of lamellae preferentially oriented parallel to the sample faces. The arcs in the moulded sample are more closely centred about the equators and the entire diffraction pattern is slightly elliptical in shape. Both photographs also show high intensity equatorial spots on the border of the backstop (500 \AA spacing). The complete absence of a peak at the corresponding angle (ca. 17°) for slit optics indicates that this scattering is not due to sample structure. The face views, show much weaker intensity scattering. The benzene cast sample, Figure (4.B.6.b), shows a circular pattern of uniform intensity, while the moulded sample, Figure (4.B.6.d), shows a circular pattern with two higher intensity arcs.

The edge view for the cyclohexane cast sample, Figure (4.B.6.e), shows an elliptical pattern with four higher intensity arcs at an angle of about 45° to the equator. This has changed to a circular pattern with higher intensity meridional arcs when the sample was taken above the T_g of the organic phase, Figure (4.B.6.g). The face views, Figures (4.B.6.f) and (4.B.6.h), for both samples show circular, uniform intensity patterns.

4.B.2 Wide Frequency Scanning Dynamic Mechanical Measurements

A relaxation in the frequency plane of the benzene cast and moulded samples due to a lamellar slip mechanism was observed while the samples were rubbery. The modulus increases and $\tan \delta$ goes through a maximum with increasing frequency as shown in Figures (4.B.7) and (4.B.11.a), for the benzene cast and moulded samples, respectively. The reality of the relaxation was established by measuring the benzene cast sample at five different sample lengths (l) and comparing the resulting $\tan \delta$ measurements with those of moulded Kraton 101 and a steel bar; this is also shown in Figure (4.B.7). When the benzene cast sample is swollen with silicone oil, the shape and magnitude of the modulus - and $\tan \delta$ - temperature plots changes, Figure (4.B.9). The relaxation is not observed for the cyclohexane cast sample, Figure (4.B.12.a). The temperature dependence of the frequency plane data is shown in Figures (4.B.8), (4.B.10), (4.B.11b) and (4.B.12.b).

The anisotropy in the benzene cast, moulded and cyclohexane cast samples is shown in Figures (4.B.13) to (4.B.15), respectively. The stresses were applied in three directions as shown below.

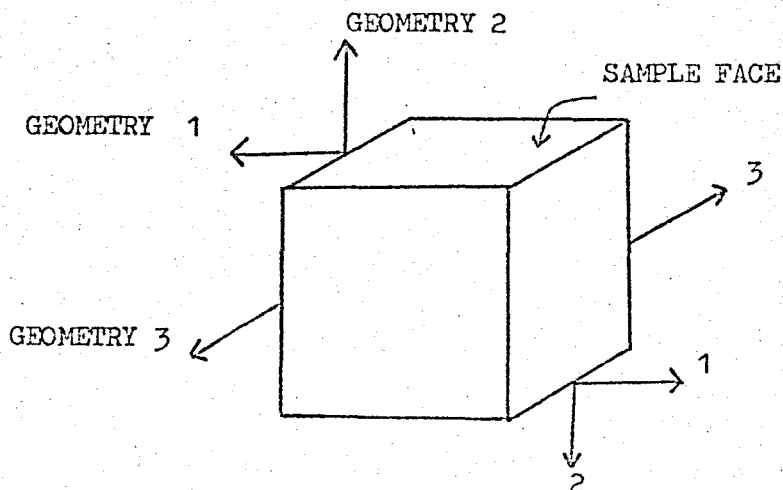


FIG. 4.B.7

- $l = 1.180$ cm.
- ⊙ $l = 1.000$ cm.
- ⊗ $l = 0.765$ cm.
- ⊘ $l = 0.471$ cm.
- × $l = 0.322$ cm.
- KRATON 101
- △ STEEL BAR

BENZENE CAST
294 °K

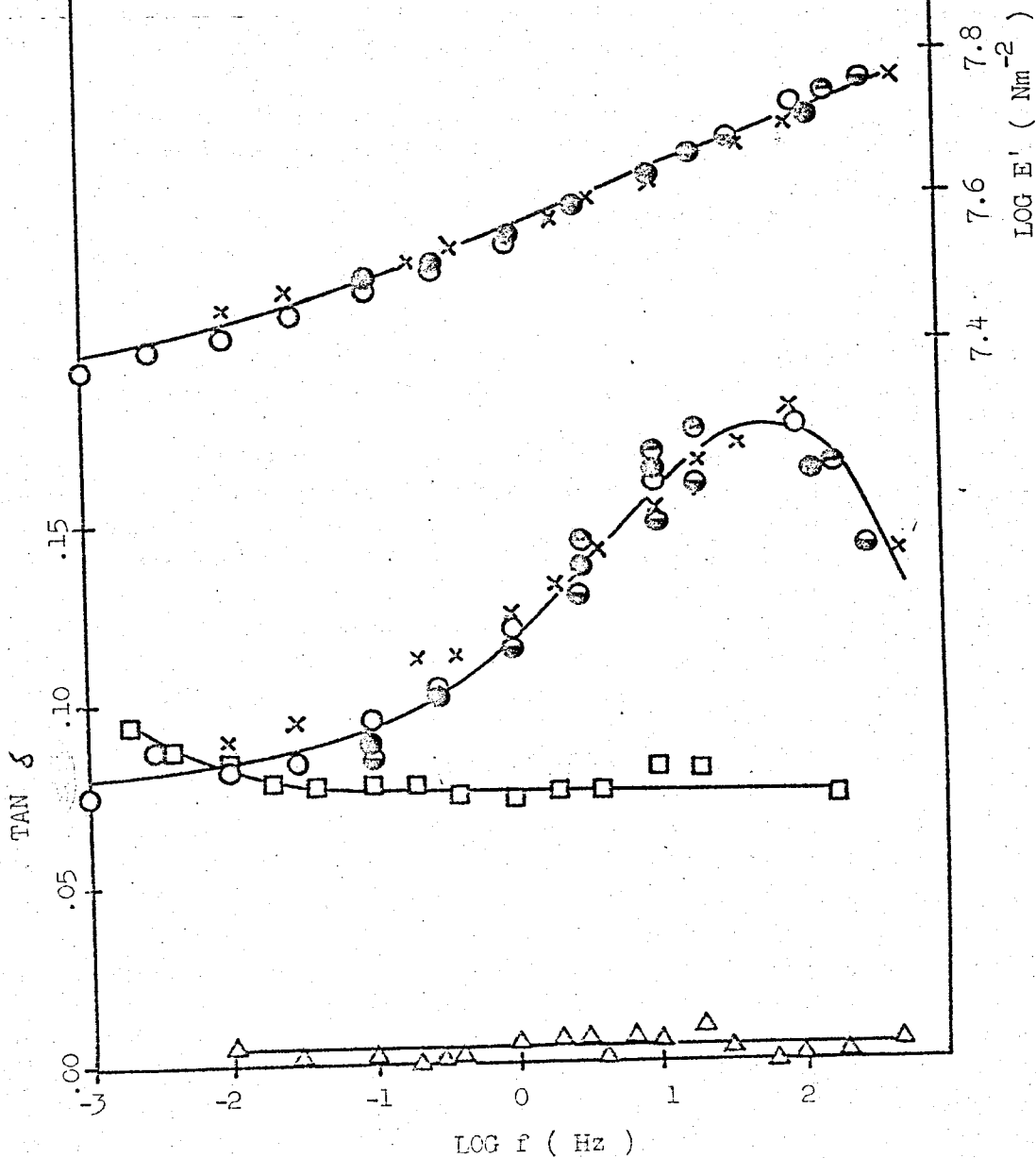


FIG. 4.B.8

BENZENE CAST

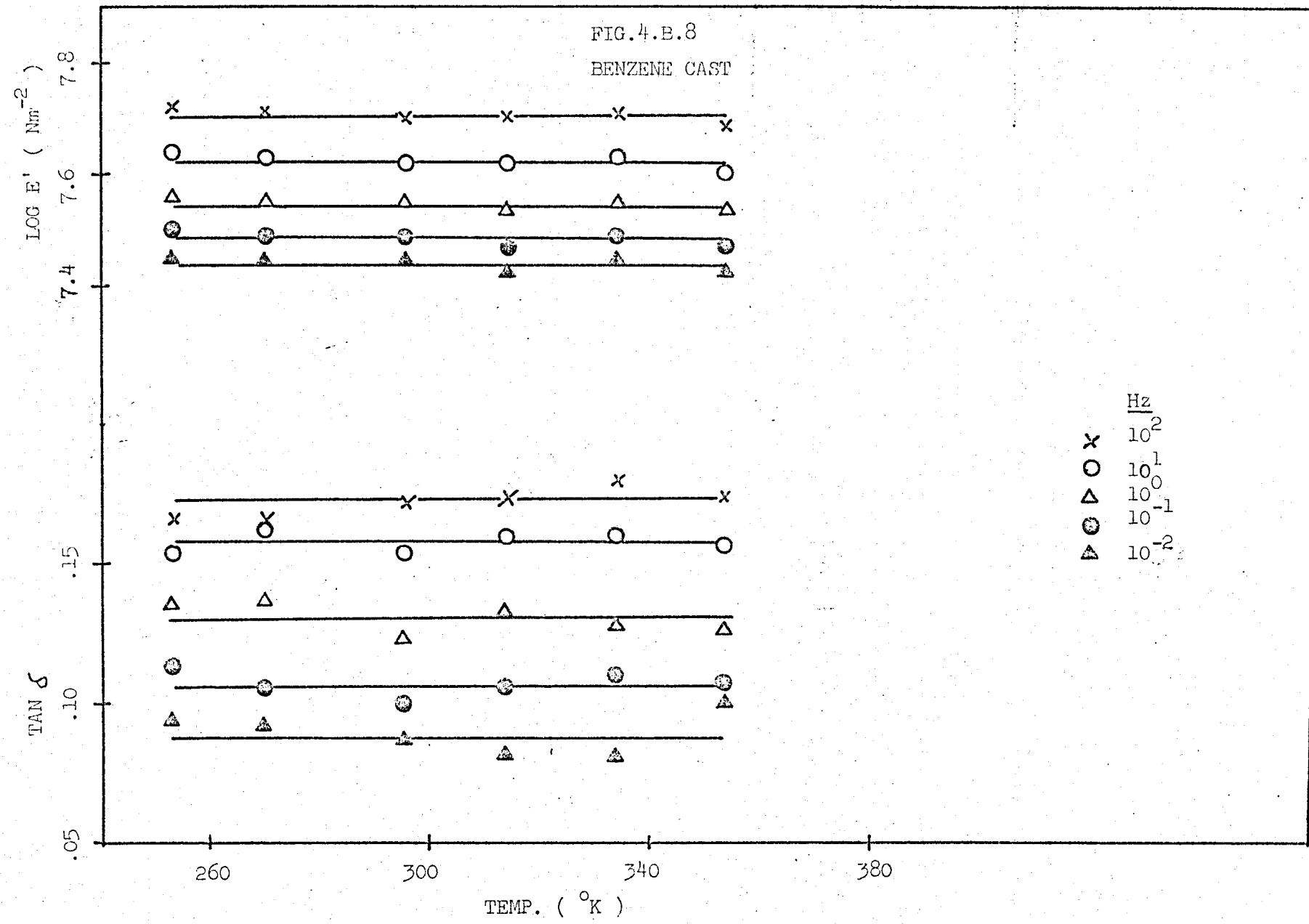


FIG. 4.B.9

BENZENE CAST (SWOLLEN)

293 °K

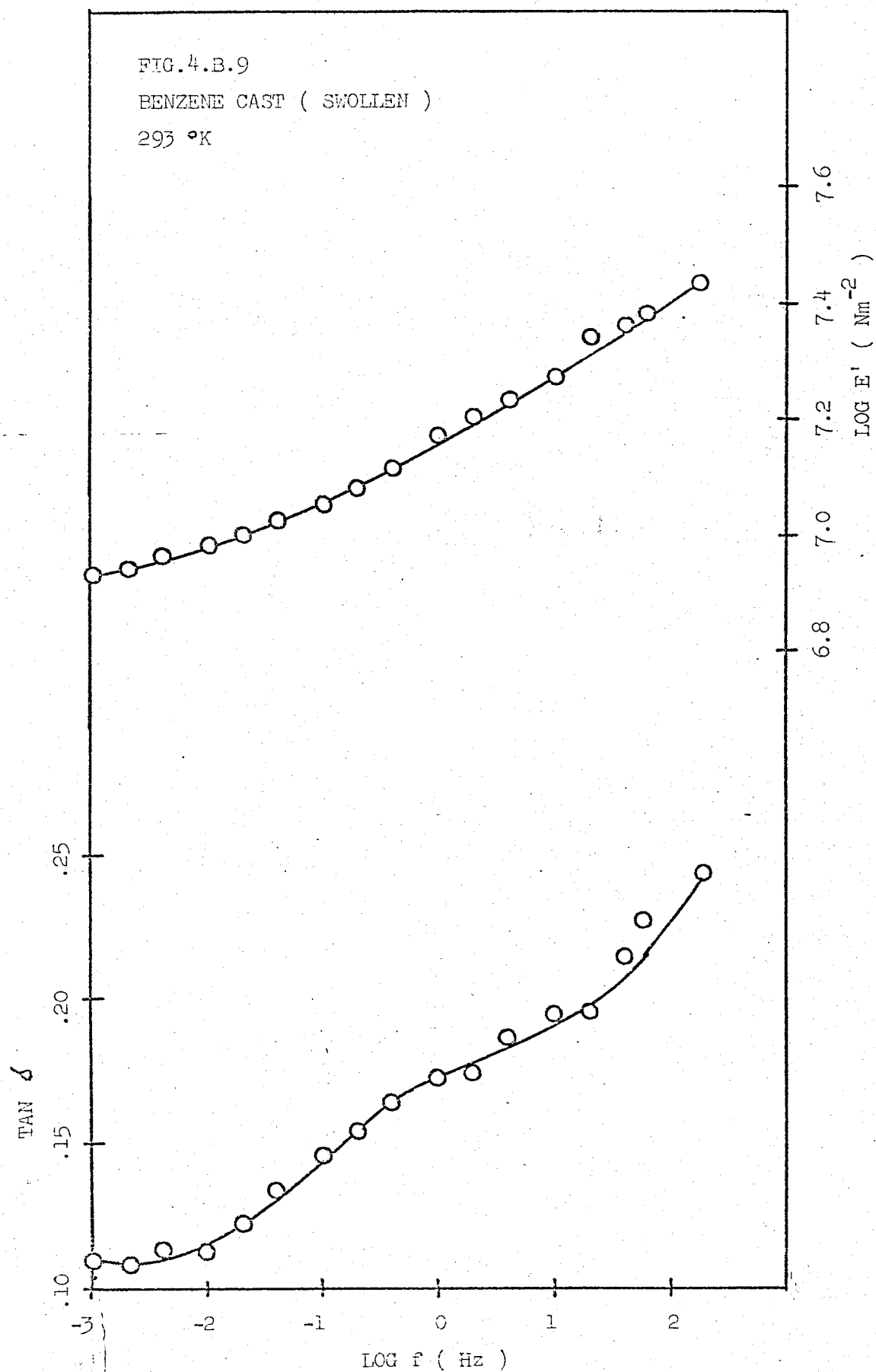
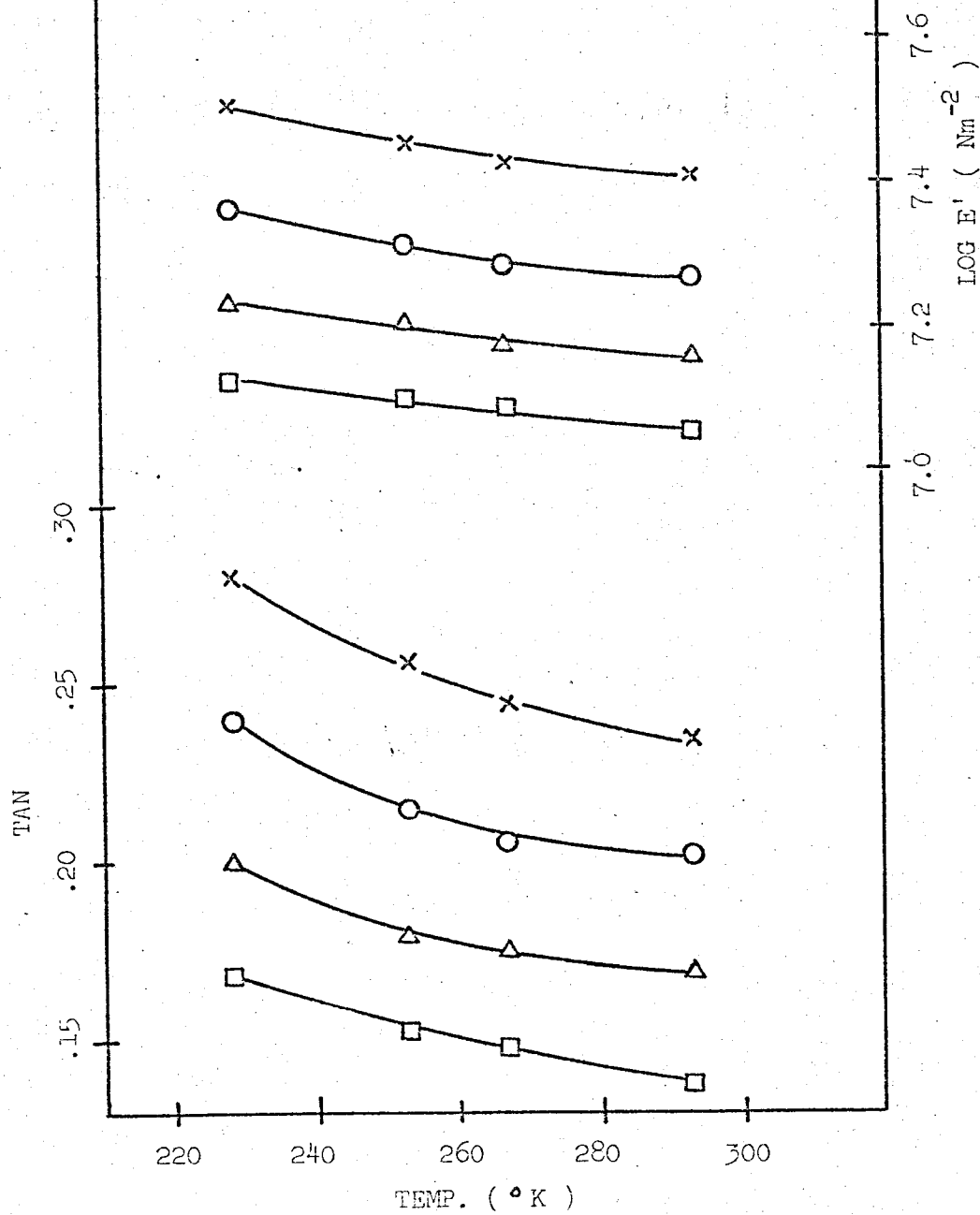
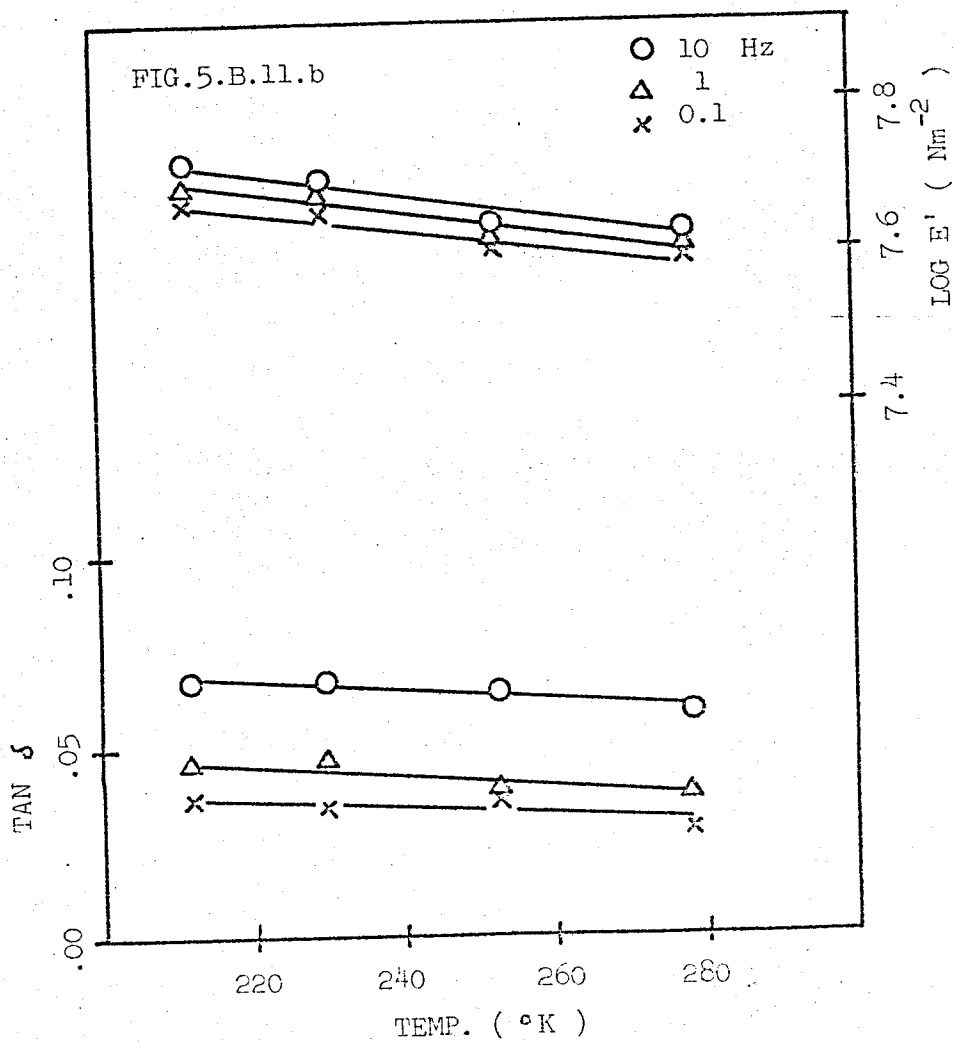
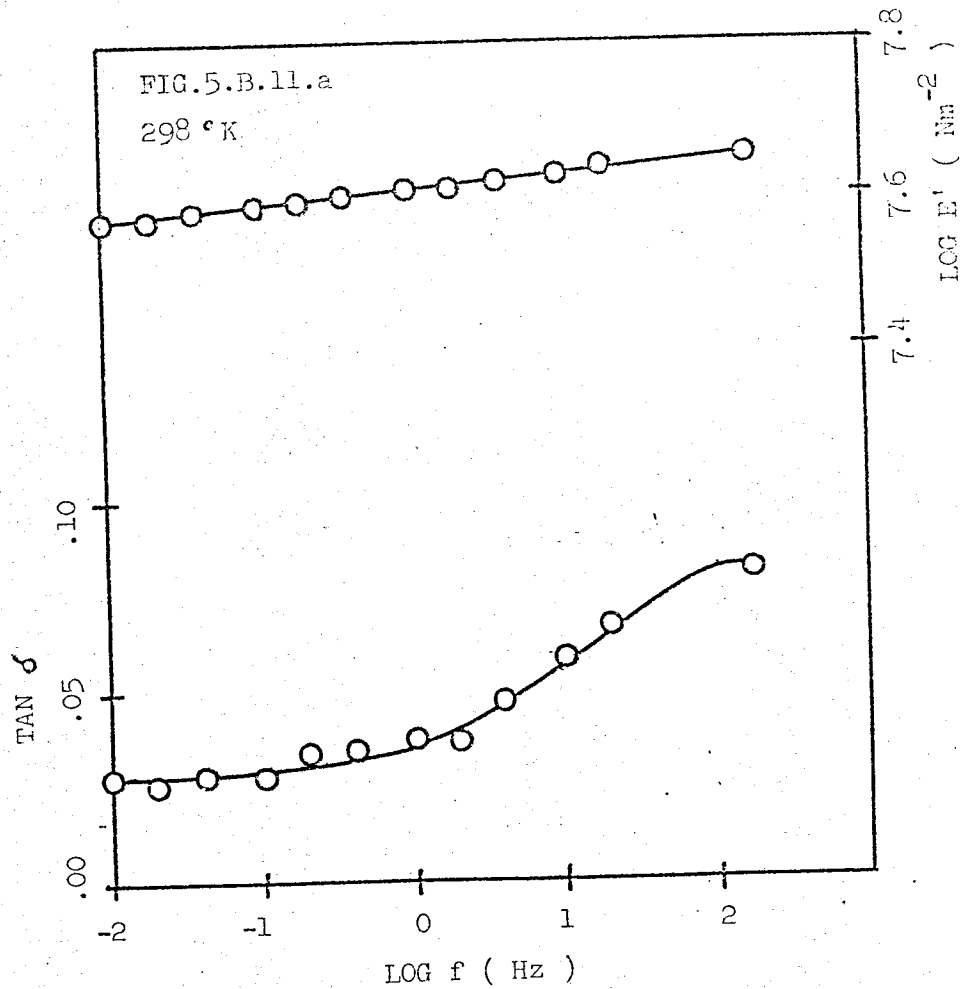


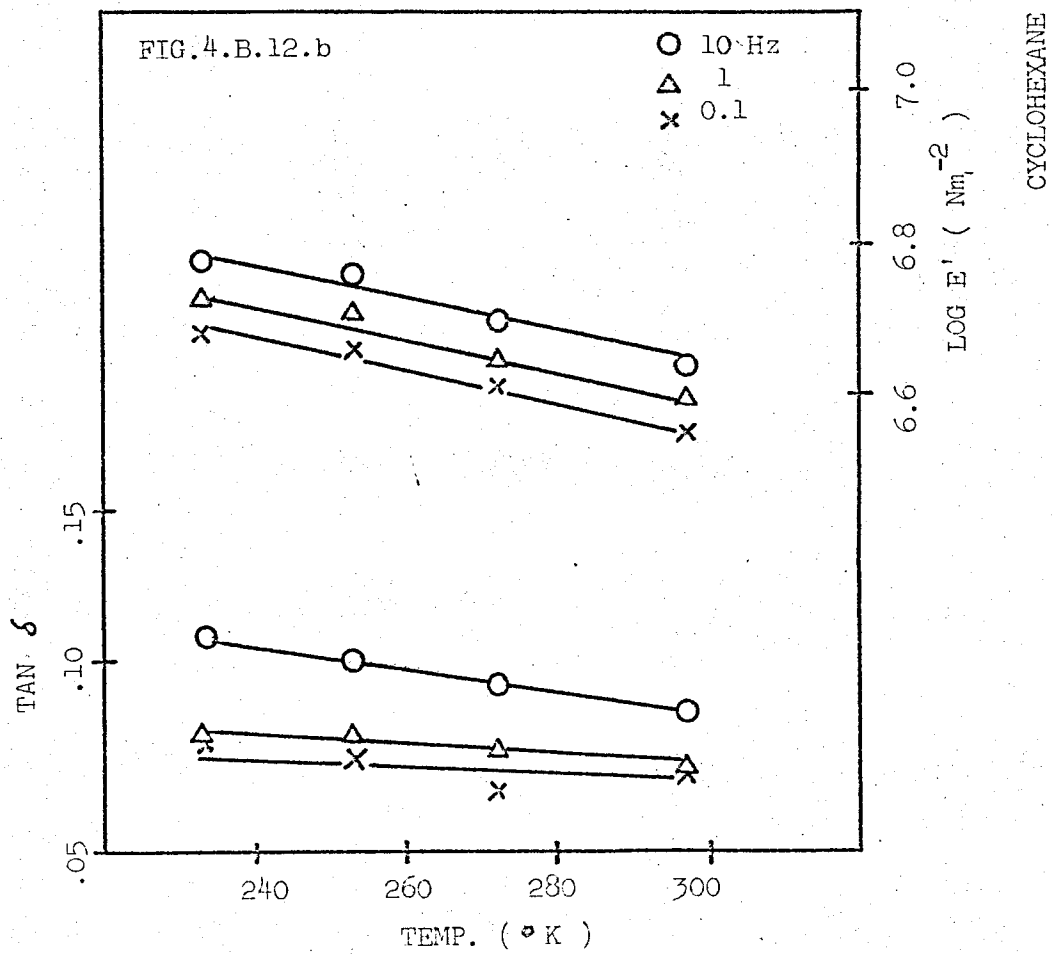
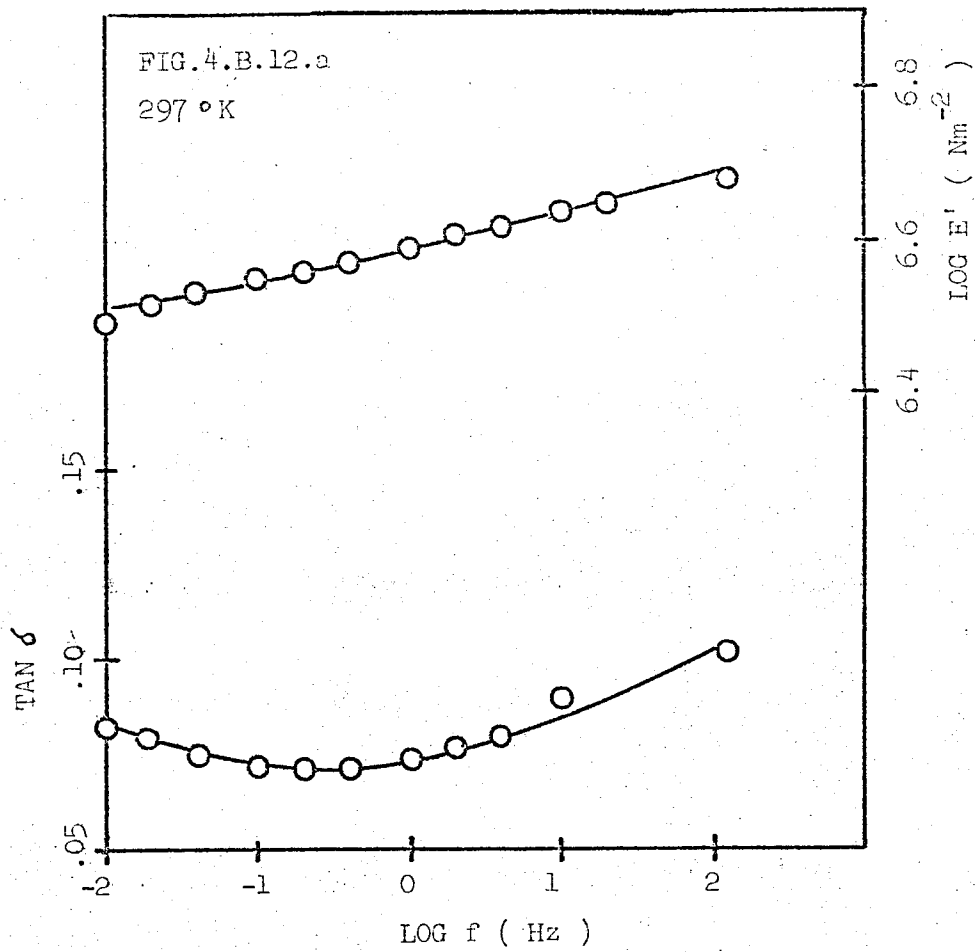
FIG. 4.B.10
 BENZENE CAST (SWOLLEN)

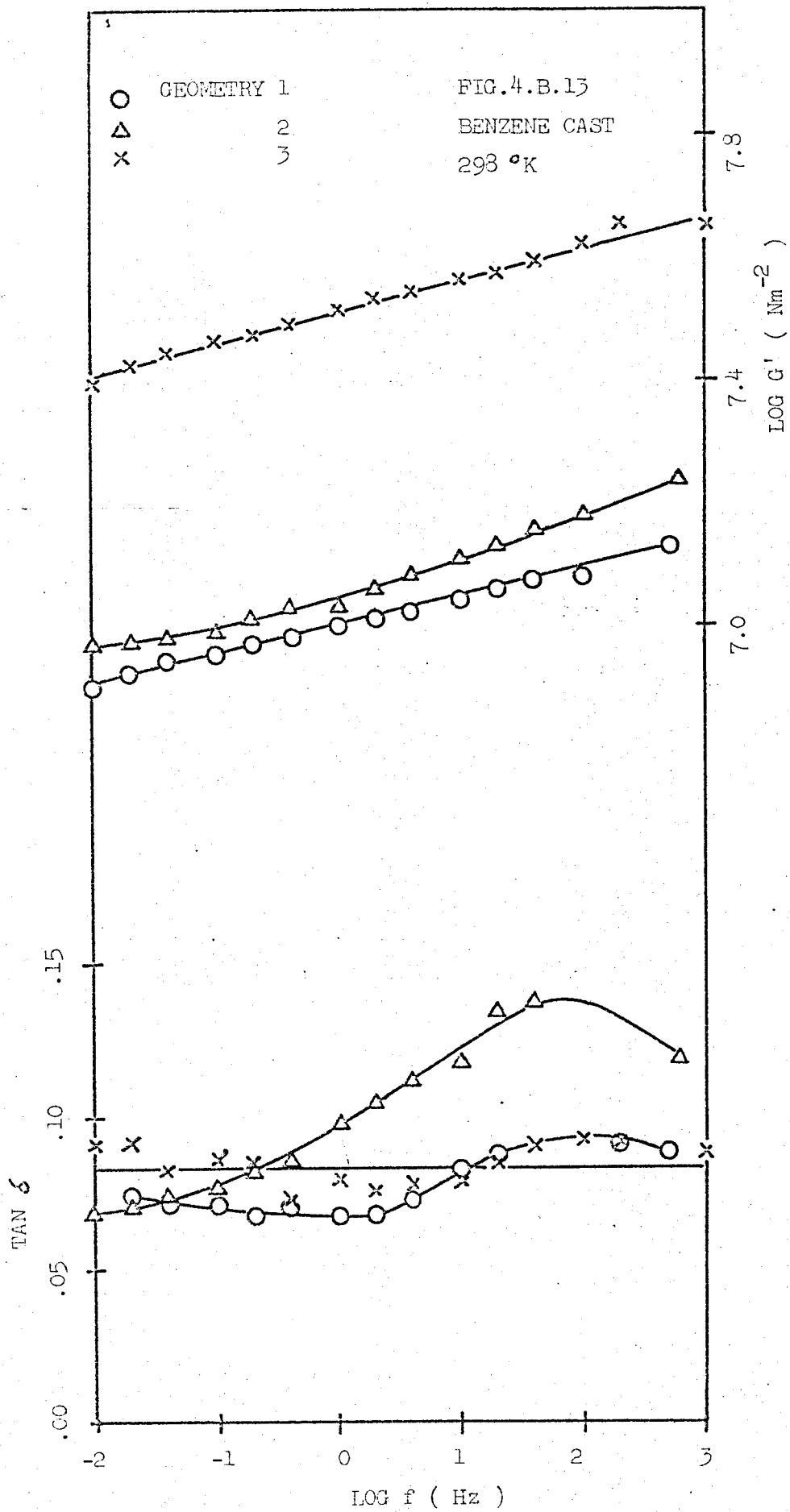
- x 10^4
- o 10^1
- Δ 10^0
- 10^{-1}

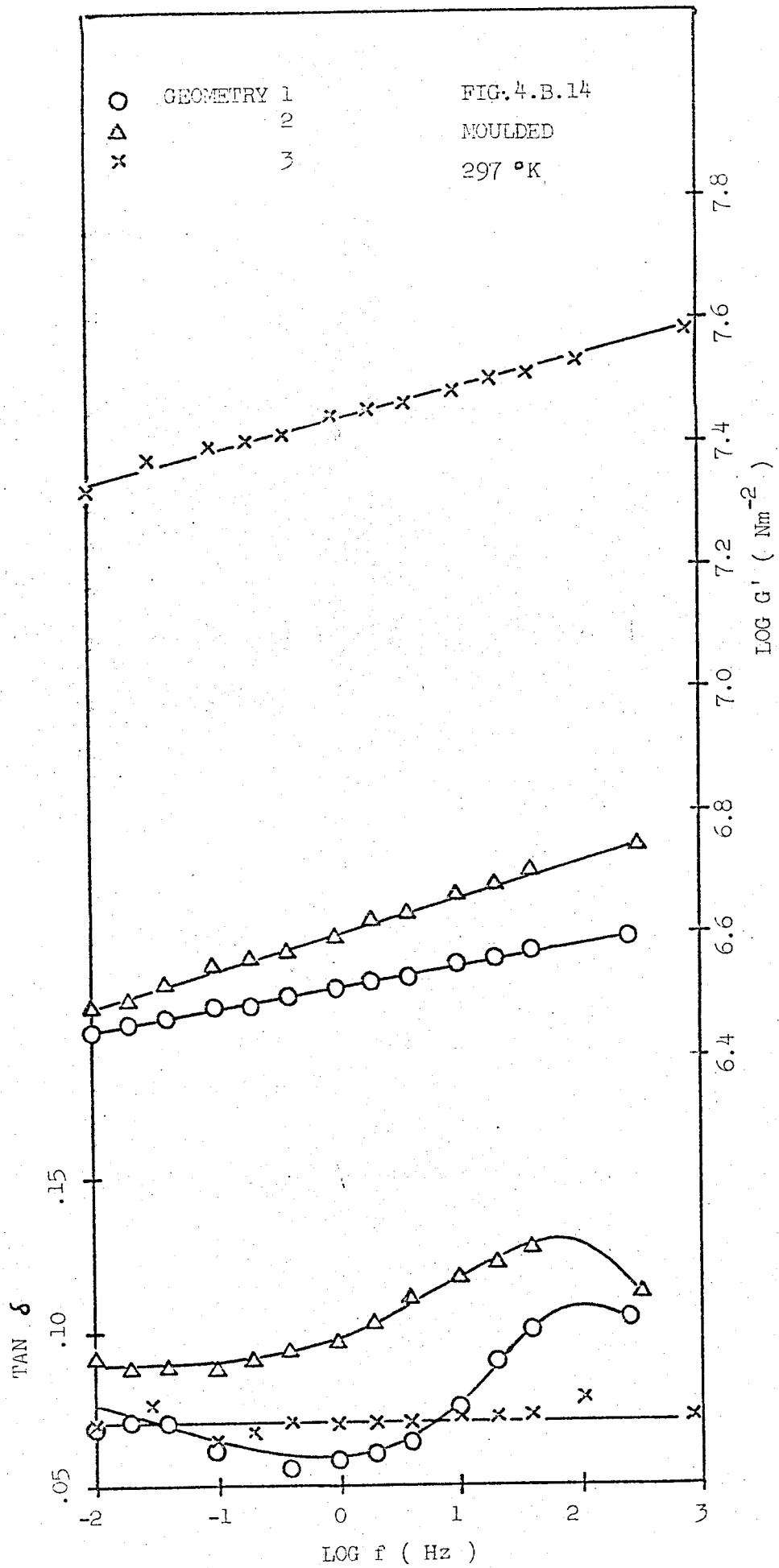


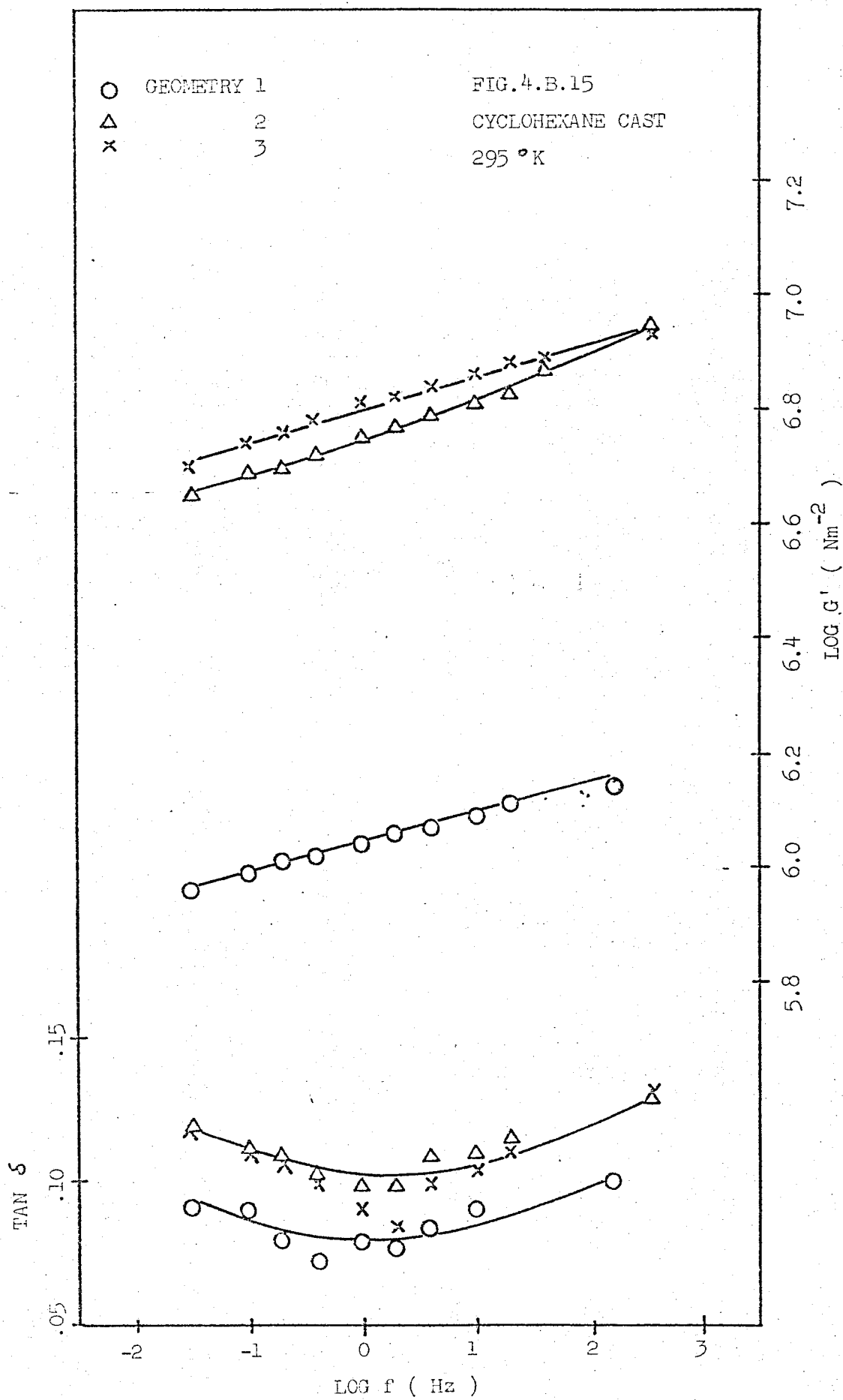


MOULDED

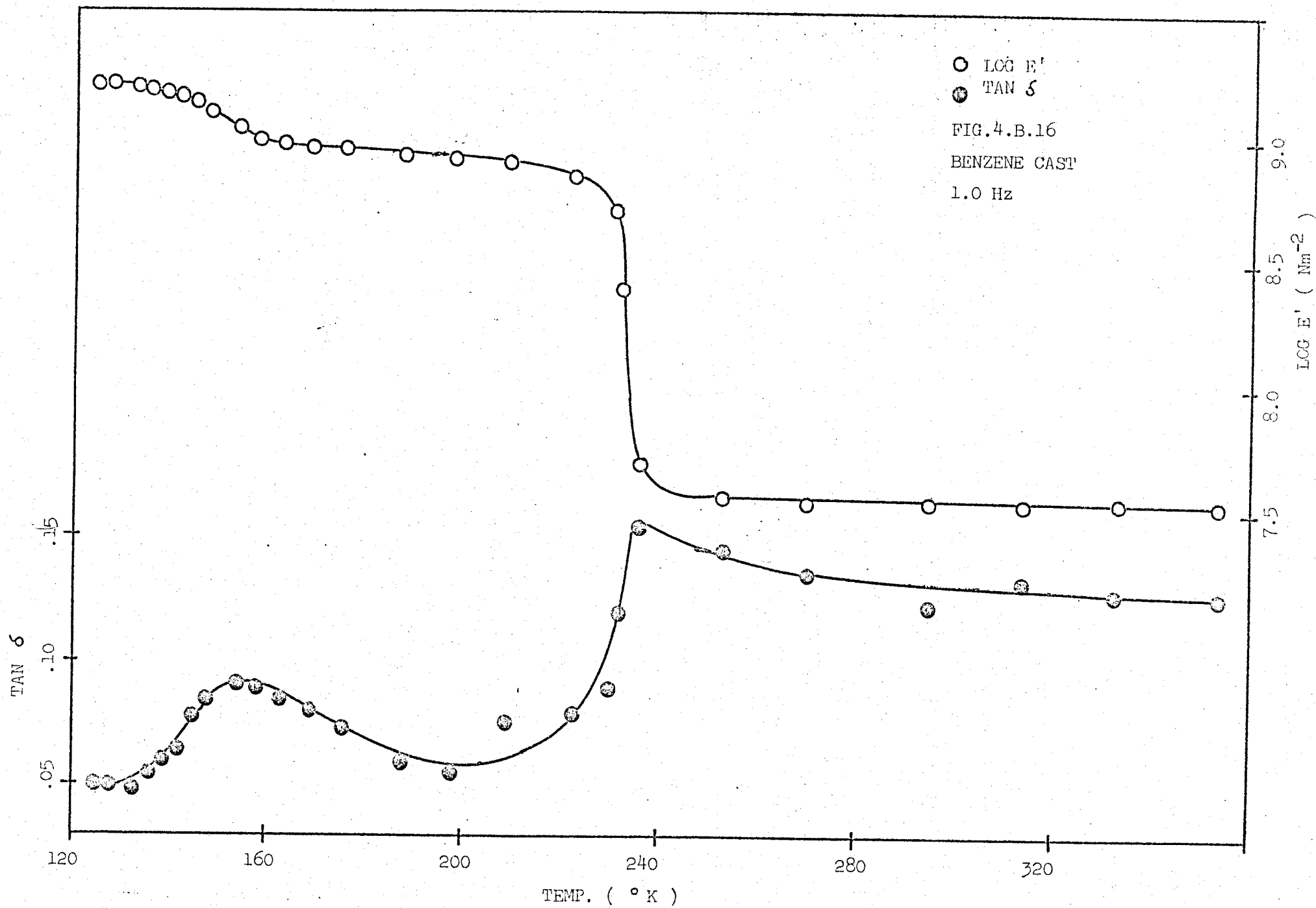


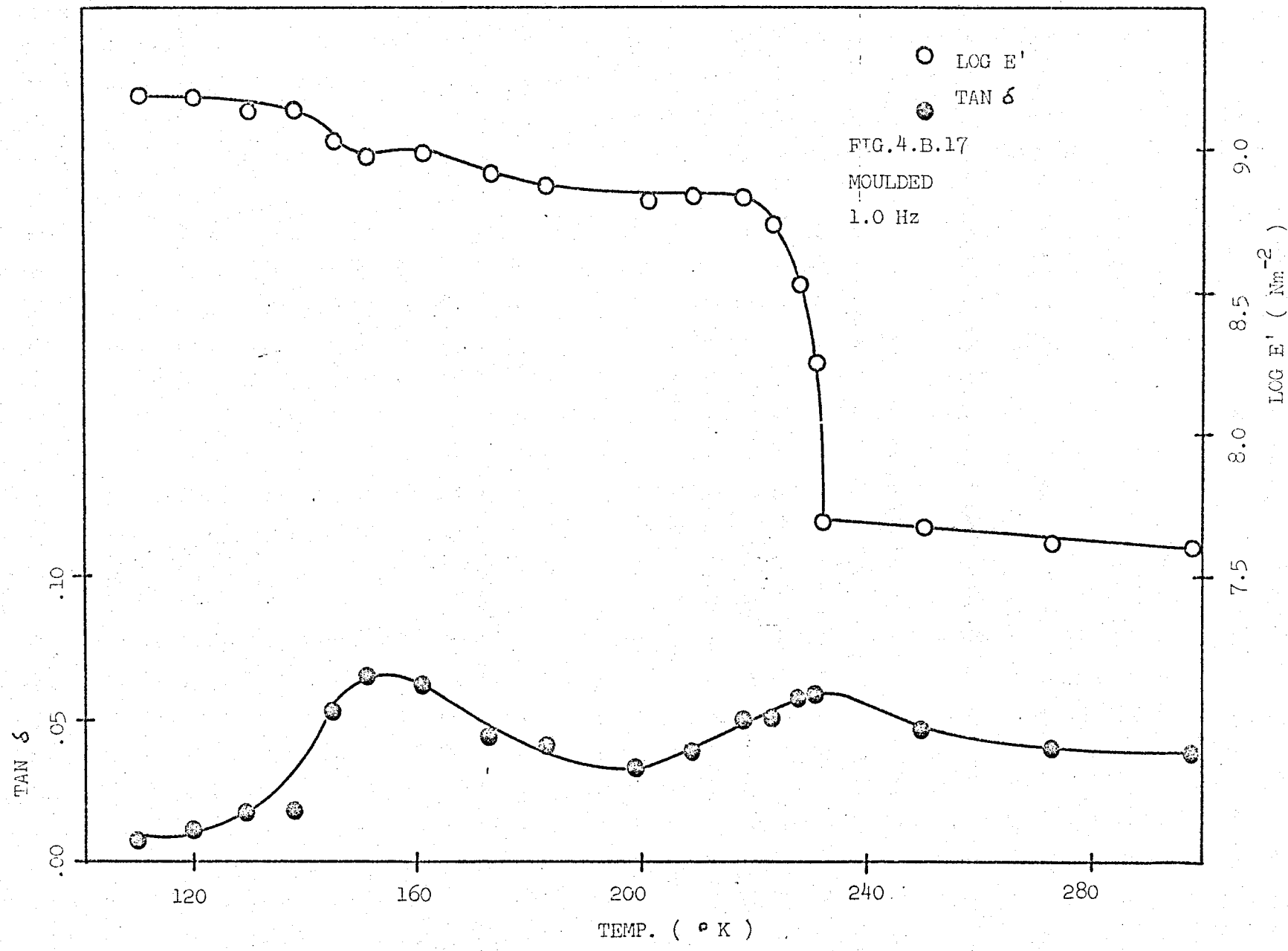


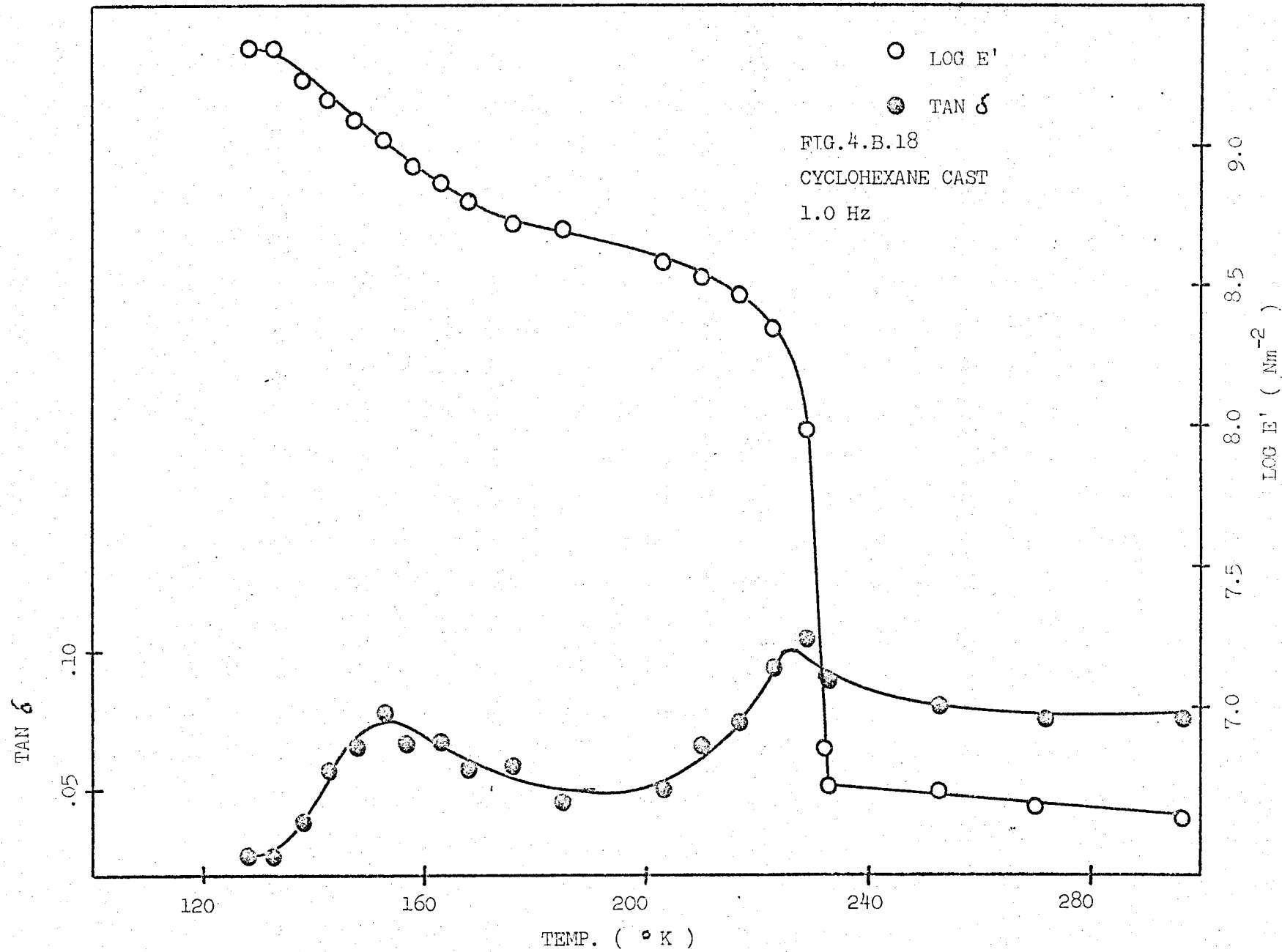


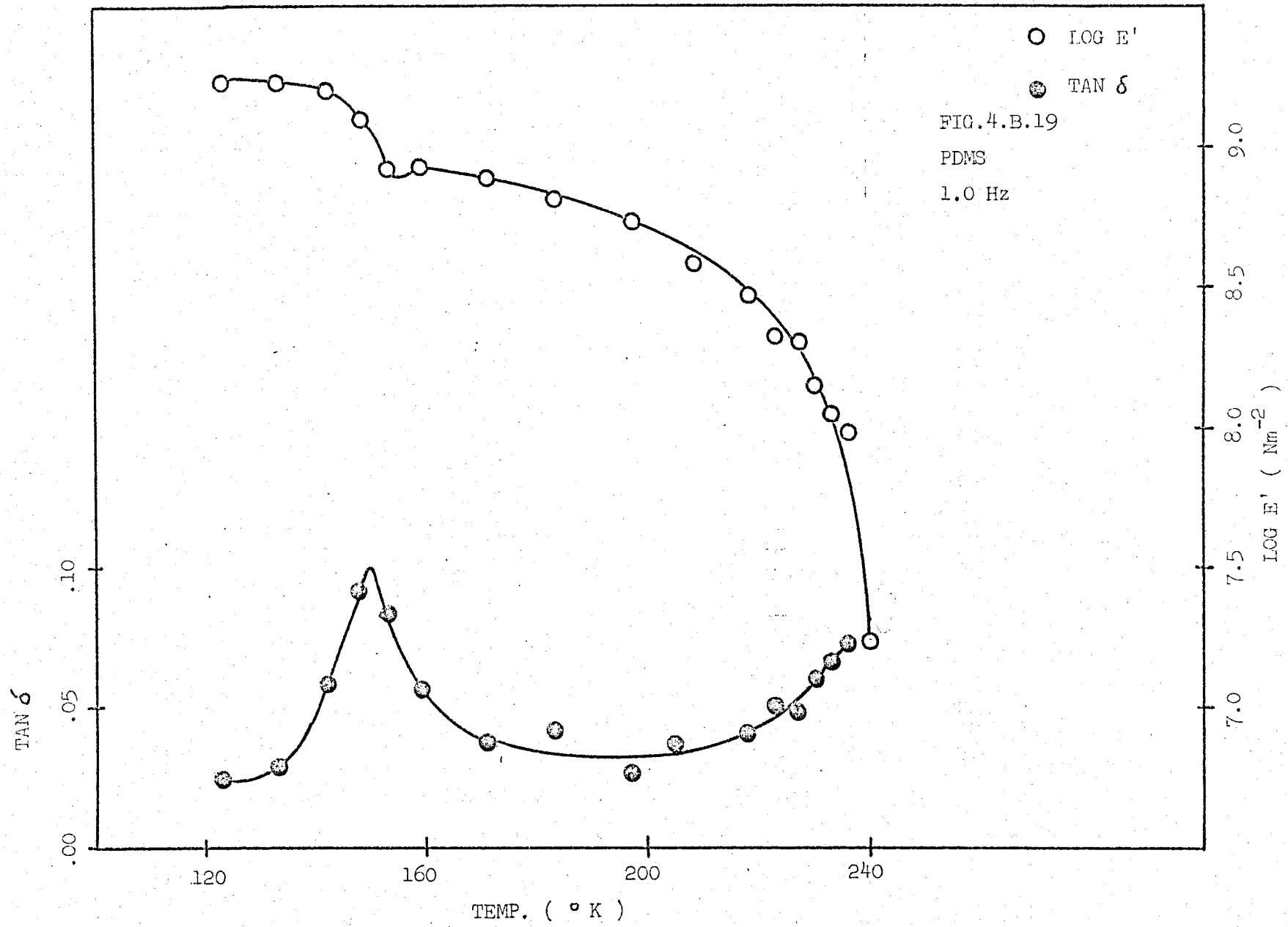


Figures (4.B.16) through (4.B.19) are graphs of E' and $\tan \delta$ versus temperature for the benzene cast, moulded and cyclohexane cast copolymer and the poly (dimethylsiloxane) homopolymer, respectively, at 1.00 Hz. In all graphs, the T_g process for the siloxane phase is indicated by a small decrease in E' and a $\tan \delta$ peak at ca. 150°K . The large decrease in E' accompanied by an increase in $\tan \delta$ from 230°K to 240°K is a consequence of melting in the siloxane phase.



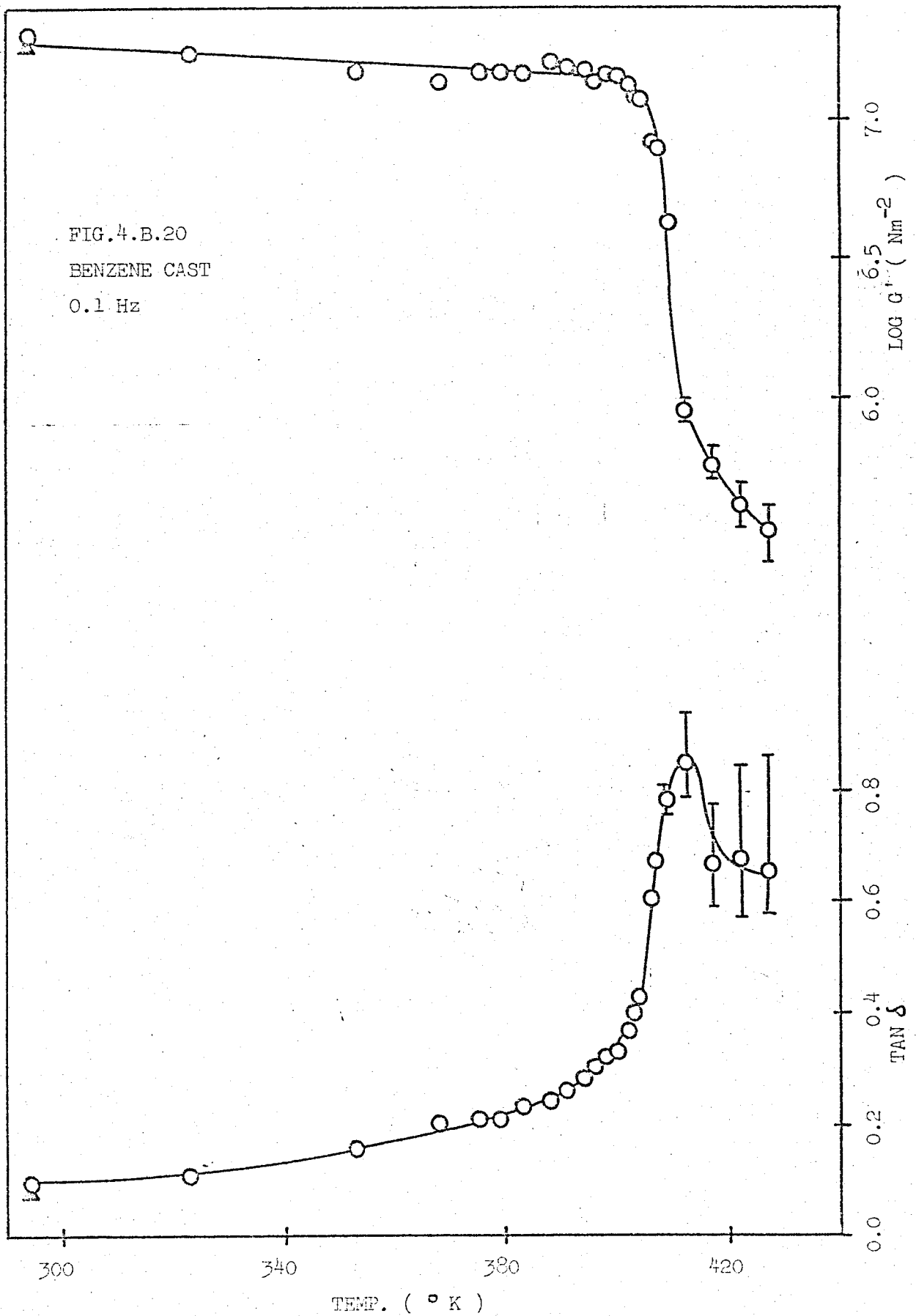






4.B.3 Torsion Pendulum Data

G' and $\tan \delta$ were measured on a torsion pendulum at ca. 0.1 Hz from ambient to the T_g of the organic phase for the benzene cast, moulded and cyclohexane cast samples, as shown in Figures (4.B.20) to (4.B.22). The maximum in $\tan \delta$ for the T_g process of the α - methylstyrene phase is observed to decrease in the order: benzene cast, moulded, cyclohexane cast. The magnitude of G' (rubber) minus G' (melt) also decreases in the same order. If the T_g is defined as the temperature at which $\log G' = 6.00$, then the T_g of the benzene cast sample is more than 10°K lower than for the moulded or cyclohexane cast samples. The bordered vertical lines on either side of some points indicate the uncertainty of the data.



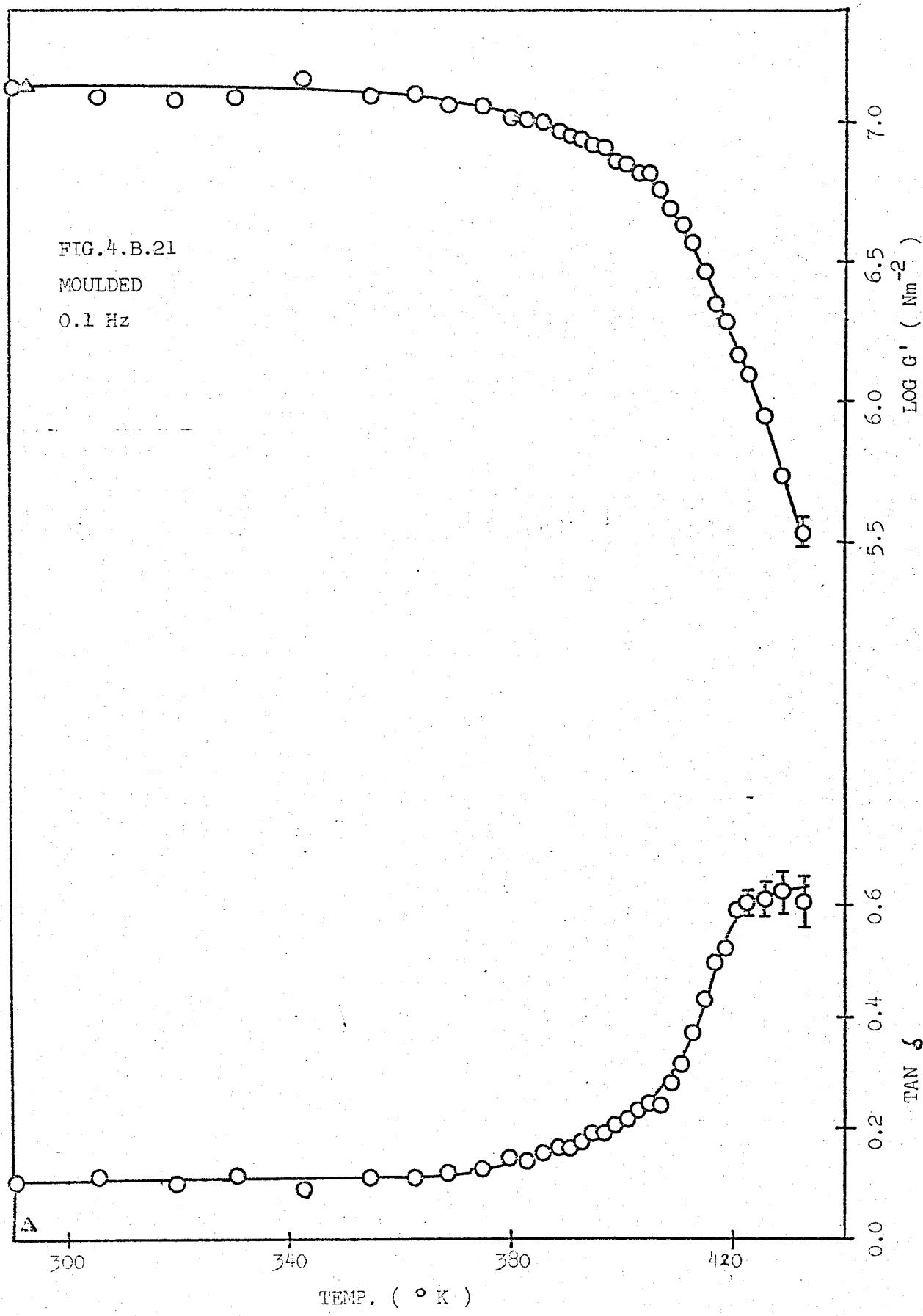
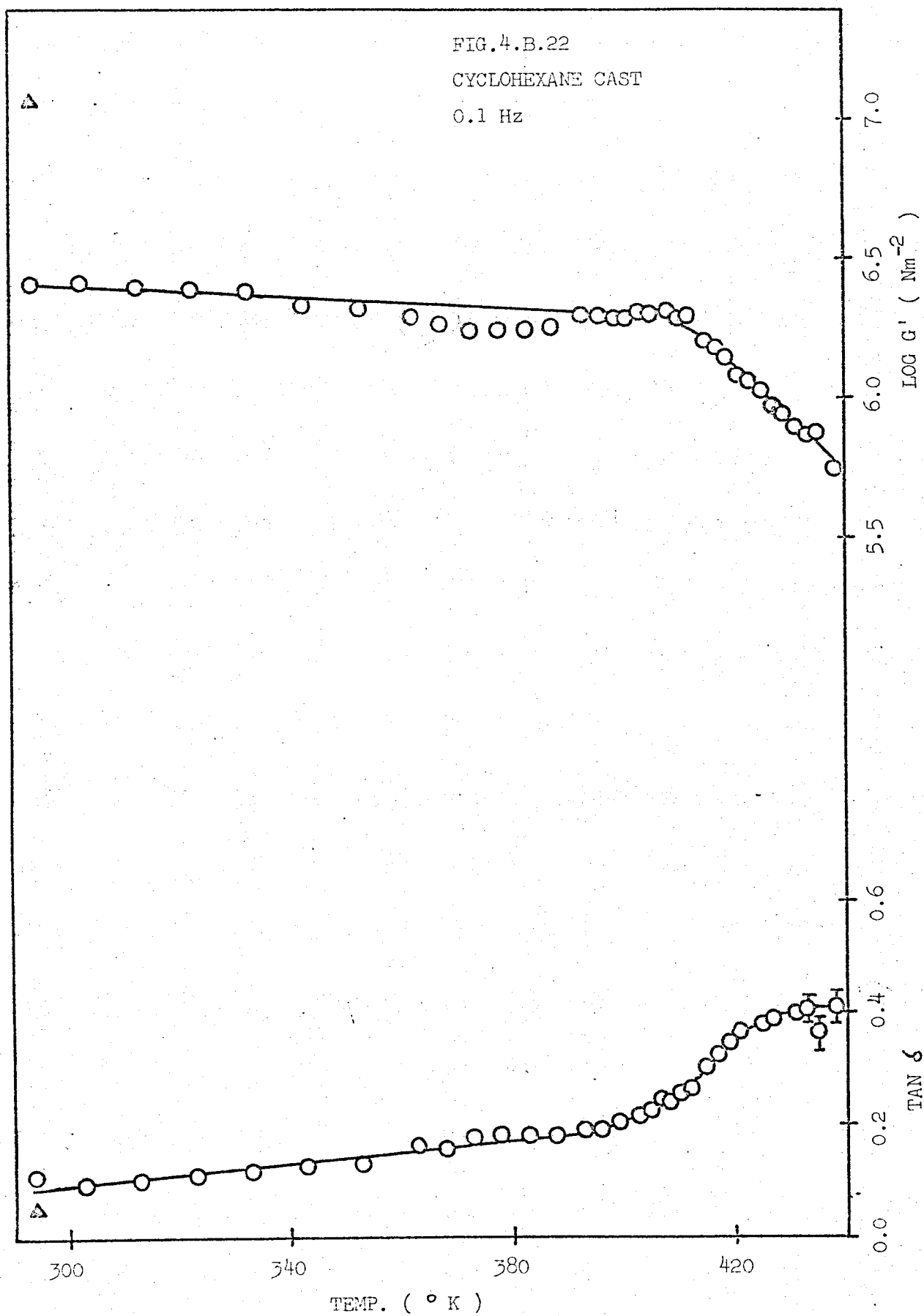


FIG. 4.B.22

CYCLOHEXANE CAST

0.1 Hz



4.B.4 Differential Scanning Calorimetry

DSC was used to study crystallinity in the siloxane phase. Melting (endothermic) peaks for the benzene cast, moulded and cyclohexane cast copolymer and the siloxane homopolymer (PDMS) are shown in Figures (4.B.23) to (4.B.25) for three different cooling rates. At cooling rate 1, the samples were cooled from ambient to 153°K at 10°K/min. prior to scanning. At cooling rate 2, they were cooled from ambient to 153°K at 1.4°K/min. At cooling rate 3, they were cooled from ambient to 194°K at 2°K/min. They were then held at this temperature for 12 hours prior to quenching to 77°K. At cooling rate 1, a small exothermic peak is observed for the cyclohexane cast copolymer.

Table (4.B.2) summarizes the DSC data in terms of melting peaks (T_p) and weight fraction crystallinity (w_c). For the copolymers, w_c is defined as the weight of crystalline siloxane divided by the total weight of the siloxane phase. T_p was determined by extrapolating to zero sample mass thus accounting for the discrepancies between the figures and the table.

FIG. 4.B.23

COOLING RATE 1

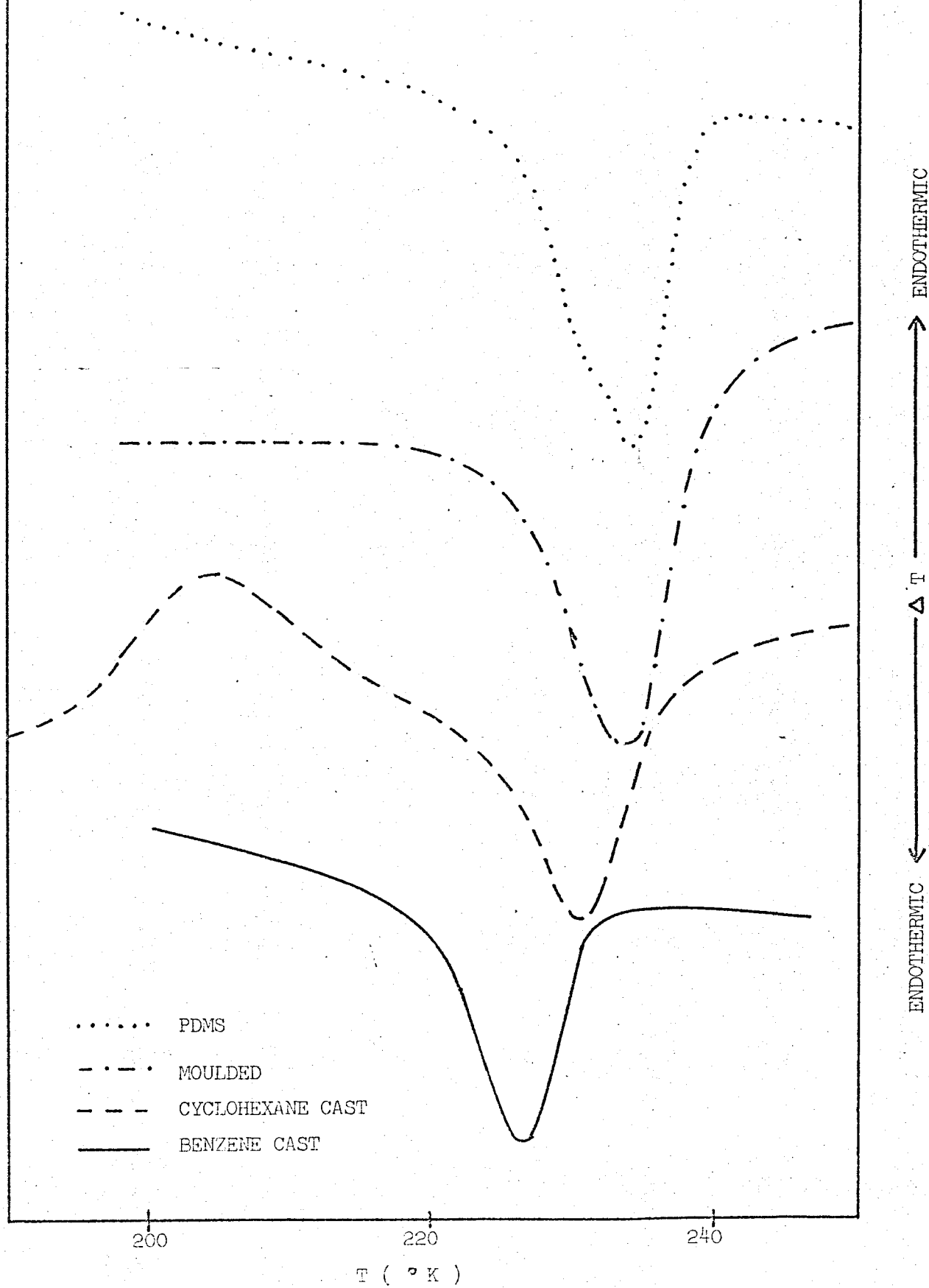


FIG. 4.B.24

COOLING RATE 2

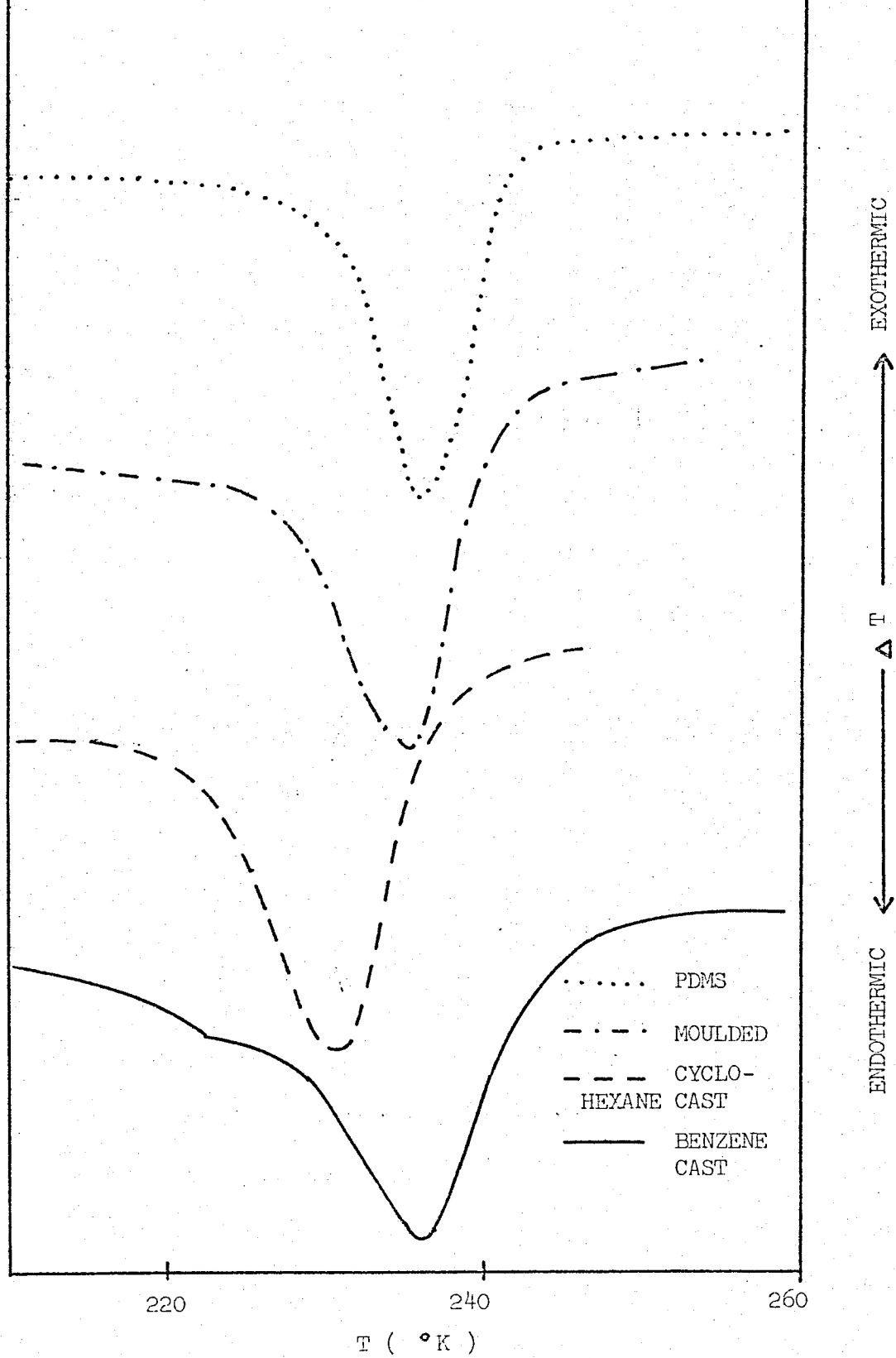


FIG. 4.B.25

COOLING RATE 3

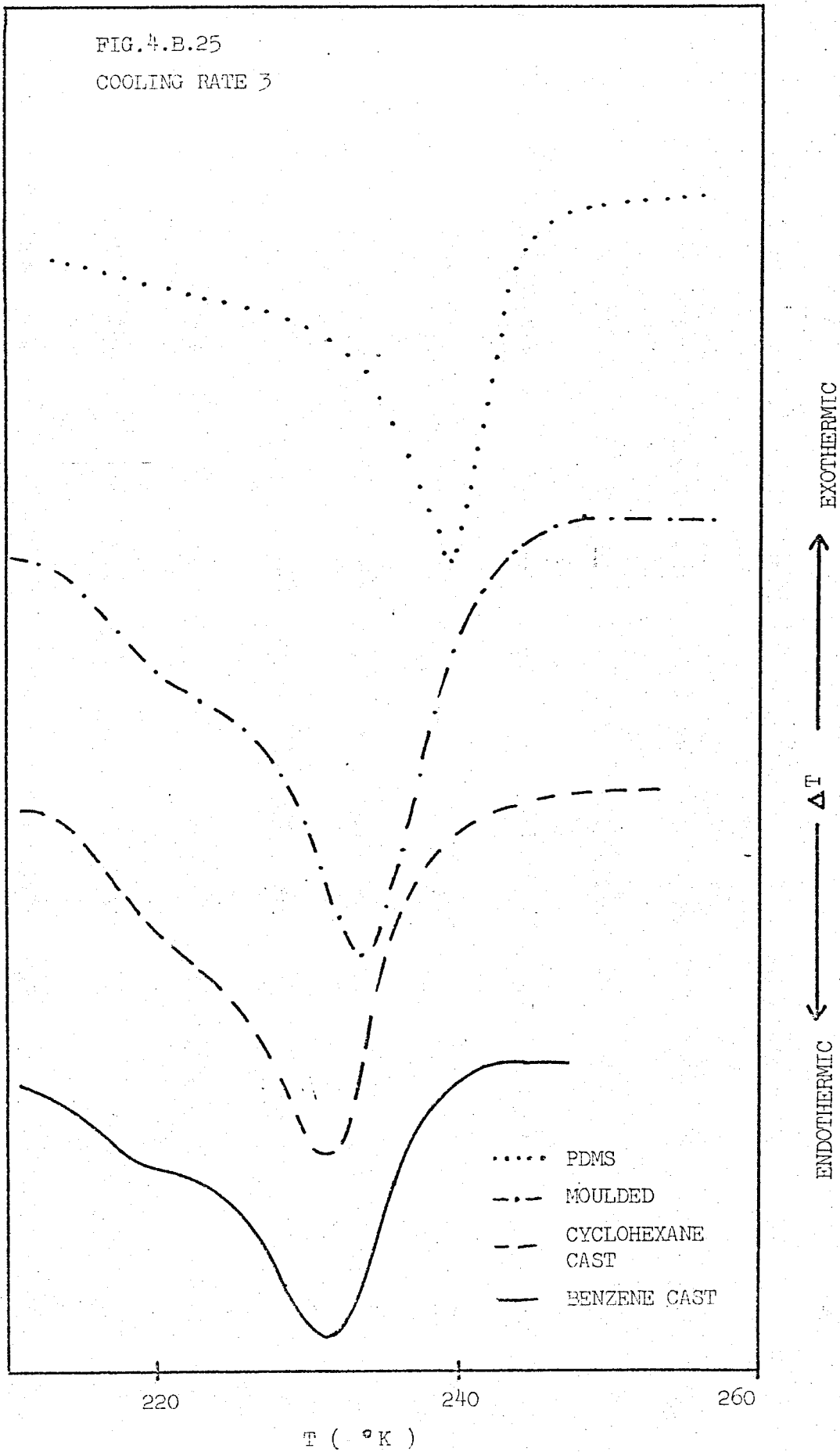


TABLE 4.B.2 Crystallinity in Poly (Dimethylsiloxane)

SAMPLE	COOLING RATE	T_p ($^{\circ}$ K)	w_c
Benzene Cast	1	227	.317
	2	229	.354
	3	228	.442
Cyclohexane Cast	1	225	.194
	2	226	.224
	3	228	.387
Moulded	1	229	.306
	2	231	.359
	3	229	.449
PDMS	1	231	.439
	2	231	.469
	3	236	.508

CHAPTER 5 DISCUSSION

SECTION A HYDROGENATED POLYMERS

5.A.1 Dynamic Mechanical Measurements

Log E' and $\tan \delta$ are plotted against temperature for each polymer in Figures (4.A.1) to (4.A.16). The $\tan \delta$ peaks associated with a large change in modulus are indicative of the glass transitions for each polymer. Table 5.A.1 shows that the $\tan \delta$ peak location at 0.1 Hz roughly coincides with the T_g calculated from DSC data. Table 5.A.1 also shows that for a particular base polymer the $\tan \delta$ peak loses height and is shifted to higher temperatures with increasing crystallinity. The decrease in peak height could be a consequence of less material undergoing a T_g process (158) but this hypothesis is not borne out by the increase in peak height in the order A1, B1, C1. In this case, as crystallinity increases peak height increases. The shift of T_g to higher temperatures is probably caused by increased strain on the amorphous chains due to increased crystallinity (159). The skewness of the $\tan \delta$ peaks is more pronounced with higher degrees of crystallinity but it is not certain how this arises.

The plots of log E' against T show no plateau regions above the glass transition. Instead, the modulus decreases quite rapidly with increasing temperature. It will be shown later in this chapter that the decrease in modulus is primarily a function of decreasing crystallinity. The DSC scans, Figures (4.A.17) to (4.A.20), show that there are very broad melting regions (wider than 100°K) for

each polymer in the region of modulus decrease. Thus there is a qualitative correlation between decreasing crystallinity and modulus.

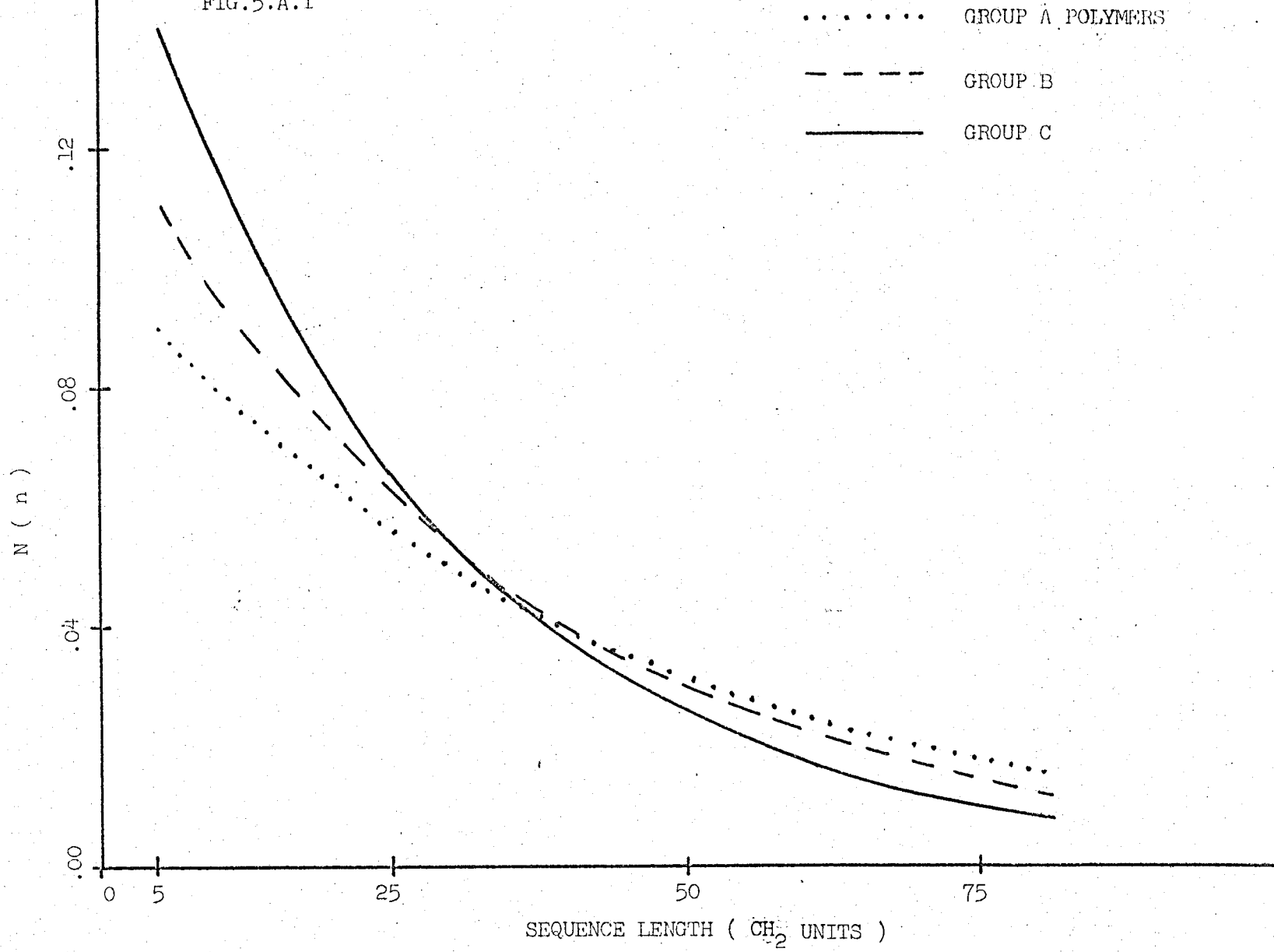
TABLE 5.A.1

SAMPLE	T _g (°K) DSC DATA	Tan δ PEAK AT 0.1 Hz (°K)	Tan δ PEAK HEIGHT	w _c AT 293°K
A1	205	190	.272	.048
A2	250	263	.144	.227
B1	211	205	.288	.071
B2	221	211	.254	.089
B3	227	228	.192	.150
C1	223	213	.311	.087
C2	223	220	.288	.088
C3	221	216	.244	.136

5.A.2 Melting Behaviour and DSC Scans

The existence of such a broad melting region is a consequence of copolymerization (84). When co-units (>CHR) are introduced randomly into the $(\text{CH}_2)_n$ chains, assuming 100% hydrogenation, the value of n becomes more varied with possible values ranging from 5 to the number of CH_2 units in the longest hydrogenated butadiene chain. The distribution of crystallizable sequence lengths (n) is shown in Figure (5.A.1) for the three base polymers assuming 100%

FIG. 5.A.1



hydrogenation. The fraction of sequence lengths at each value of n is (82):

$$N(n) = p^{n-1} (1-p) \quad (5.A.1)$$

where p is the probability of addition of butadiene monomer (non-vinyl). This equals the mole fraction of cis plus trans butadiene assuming random addition of co-units (vinyl and styrene). Since a number of crystallizable lengths are available and crystallite melting point is a function of crystallite length (81, 82), it is reasonable to assume that a broad melting range will occur.

As a consequence of the broad melting ranges of these polymers, allowance had to be made for the effect of temperature on the heat of fusion (ΔH_u) and the free energy of fusion (ΔF_u). ΔH_u was used to calculate the degree of crystallinity from DSC data and ΔF_u was used to calculate the length of the crystallites as a function of their melting points, as will be shown later. Considering the transition of bulk crystalline $(CH_2)_n$ to liquid $(CH_2)_n$, the heat and entropy (ΔS_u) of fusion at temperature T_m can be written (160):

$$\Delta H_u = \Delta H_u^o + \int_{T_m^o}^{T_m} \Delta C_p dT \quad (5.A.2)$$

$$\Delta S_u = \Delta S_u^o + \int_{T_m^o}^{T_m} \frac{\Delta C_p}{T} dT \quad (5.A.3)$$

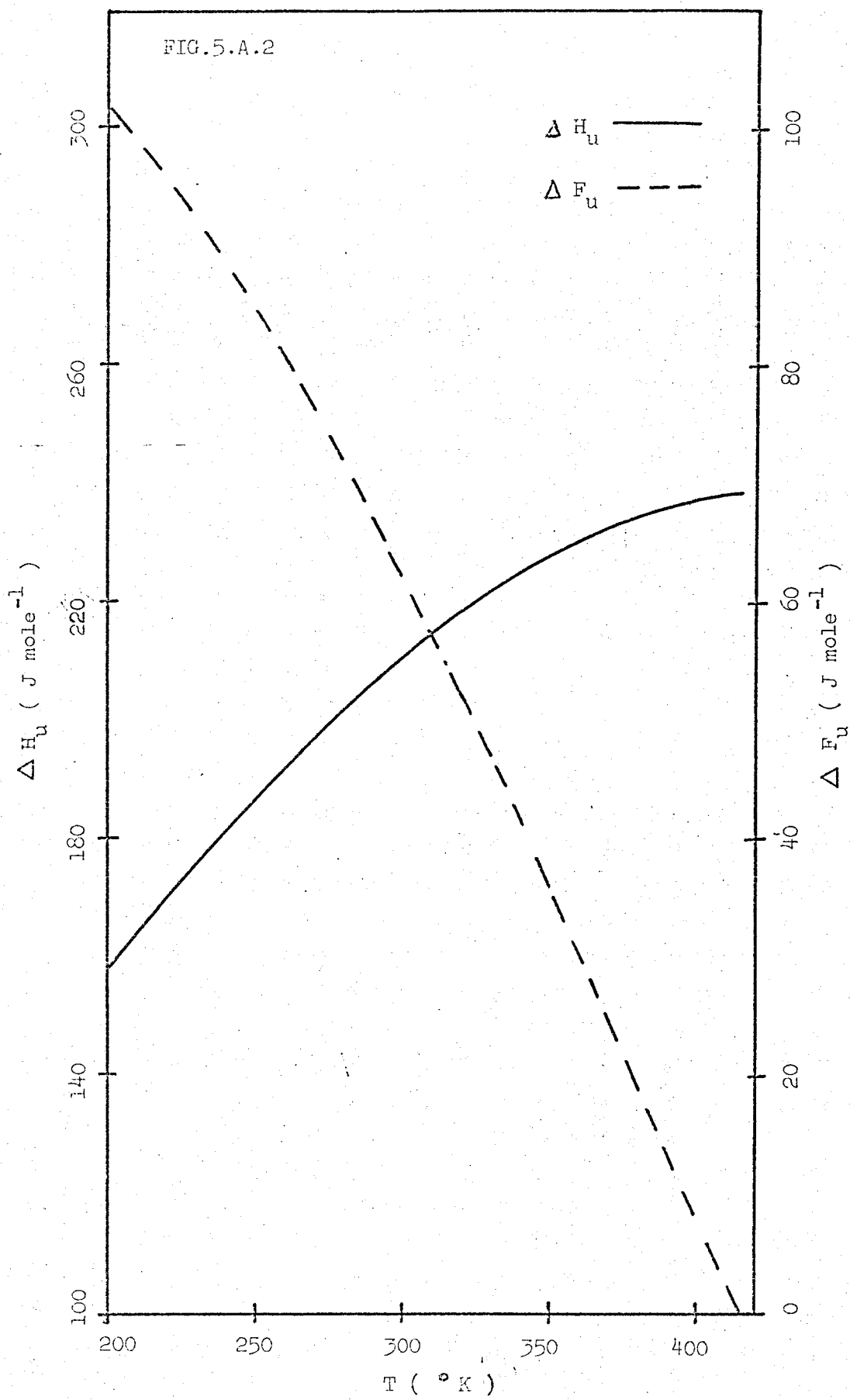
where T_m° is the equilibrium melting point of $(CH_2)_n$ crystals, n is infinite,

ΔH_u° , ΔS_u° are the heat and entropy of fusion at T_m° , respectively,

ΔC_p is the difference in specific heat between bulk crystalline and liquid $(CH_2)_n$ at a particular temperature. Since $\Delta F_u = \Delta H_u - T_m \Delta S_u$ then if ΔH_u and ΔS_u were constant with temperature, a plot of ΔF_u versus T would be linear. However, since ΔH_u and ΔS_u do vary with T , it will be shown that ΔF_u versus T is not linear. Broadhurst (161) has extrapolated thermodynamic data for highly purified n -paraffins to obtain ΔH_u and ΔF_u versus T from $200^{\circ}K$ to T_m° , which he assumed to be $414.3^{\circ}K$. This data is shown in Figure (5.A.2).

Interesting structural information can be drawn from studying the relationships between peaks in DSC scans, thermal history and fraction crystallinity. Figures (4.A.17) to (4.A.19) compare DSC scans of all polymers moulded as described in Section (3.1). There are two distinct peaks above room temperature, $311^{\circ}K$ to $315^{\circ}K$ and $328^{\circ}K$ to $347^{\circ}K$, which appear as a consequence of moulding conditions. The lower temperature peak is a result of annealing at room temperature for a period of weeks while the high temperature peak is a result of holding the polymer at $323^{\circ}K$ for an hour. Figure (4.A.20) illustrates this point by showing how varying thermal history affects the peak

FIG.5.A.2



positions in sample B1. The author assumes similar behaviour would occur using the other samples. To obtain curve 1, the sample was cooled from the melt to 323°K , held there for one hour, then cooled to room temperature and held there for several weeks. Two peaks appear at 315°K and 351°K . For curve 2, the polymer was cooled from the melt to room temperature and held there for several weeks. Only one peak appears at 315°K . The polymer in curve 3 was cooled from the melt to 323°K and held there for one hour; one peak appears at 351°K .

In all these curves a diffuse endothermic area appears between the T_g and room temperature which is due to shorter crystallites forming upon rapidly cooling (ca. $10^{\circ}\text{K}/\text{min.}$) the sample to 153°K before scanning. The existence of polyethylene crystallites below 268°K was postulated by Richards et. al. (162) for some ethylene-propylene rubbers in interpreting dynamic mechanical properties. X-ray and IR measurements verified this hypothesis.

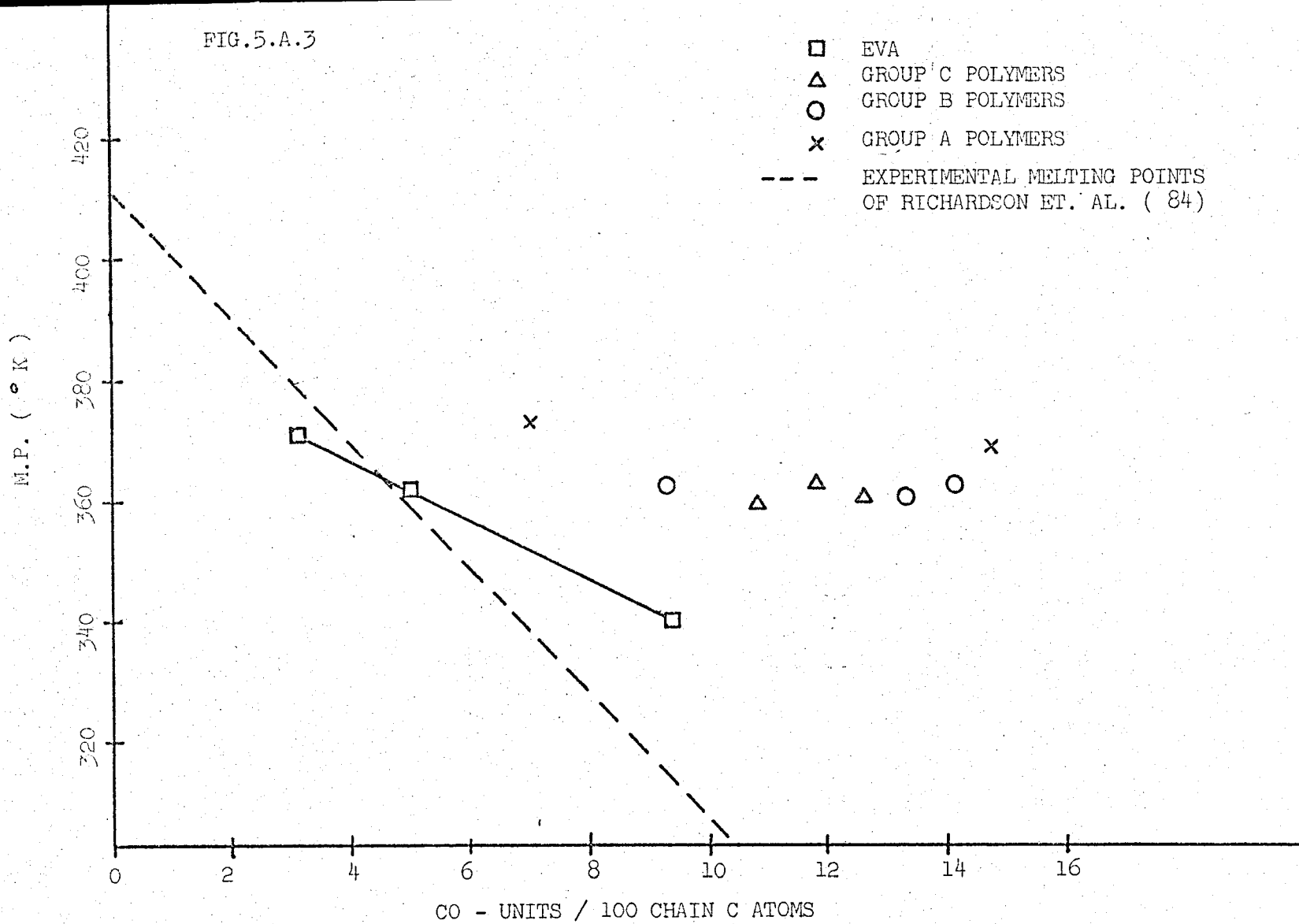
Curve 4 in Figure (4.A.20) represents the same material scanned in curve 1 which has been program cooled below room temperature by holding at each 10°K interval between room temperature and 233°K for one hour. The temperature variation is identical to that experienced by the sample during dynamic mechanical measurements. The once diffuse melting region is now a series of peaks corresponding to the various annealing temperatures. The crystallinity calculated from

curve 4 was used to calculate the modulus versus temperature curve shown later in this chapter.

Looking again at Figures (4.A.17) to (4.A.19), it can be seen that for a particular base polymer, as the degree of crystallinity increases, the ratio of the area of the low temperature to the high temperature peak decreases. This is logical, since at higher crystallinities one would expect more long sequences to be available for crystallization at the higher annealing temperature. Also, when comparing curves for different base polymers of similar crystallinity in Figures (4.A.18) and (4.A.19) it is evident that far less of a high temperature peak is present, if present at all, for the curves in Figure (4.A.19). Since the C base polymers, represented in Figure (4.A.19), have 7 mole % styrene compared with 3 mole % styrene for the B base polymers, Figure (4.A.18), not as many long crystallizable sequences are present in the C polymers for similar degrees of hydrogenation. Thus not as much crystallinity can be developed at the 323°K annealing temperature for the C polymers.

The melting points (T_m) of these polymers, determined by DSC, are quite high when compared with other copolymers where methylene units comprise the crystallizable segments, as shown in Figure (5.A.3). The experimental melting points of Richardson et. al. (84) are those for copolymers of ethylene randomly copolymerized with $CH_2 = CHR$, where R is $(-CH_2CH_3)$ and $(-CH_2CH_2CH_3)$, with melting points in this case determined dilatometrically. The data for the ethylene vinyl acetate (EVA) random copolymers was obtained in our laboratories using DSC. These samples were Imperial Chemical Industries (ICI)

FIG.5.A.3



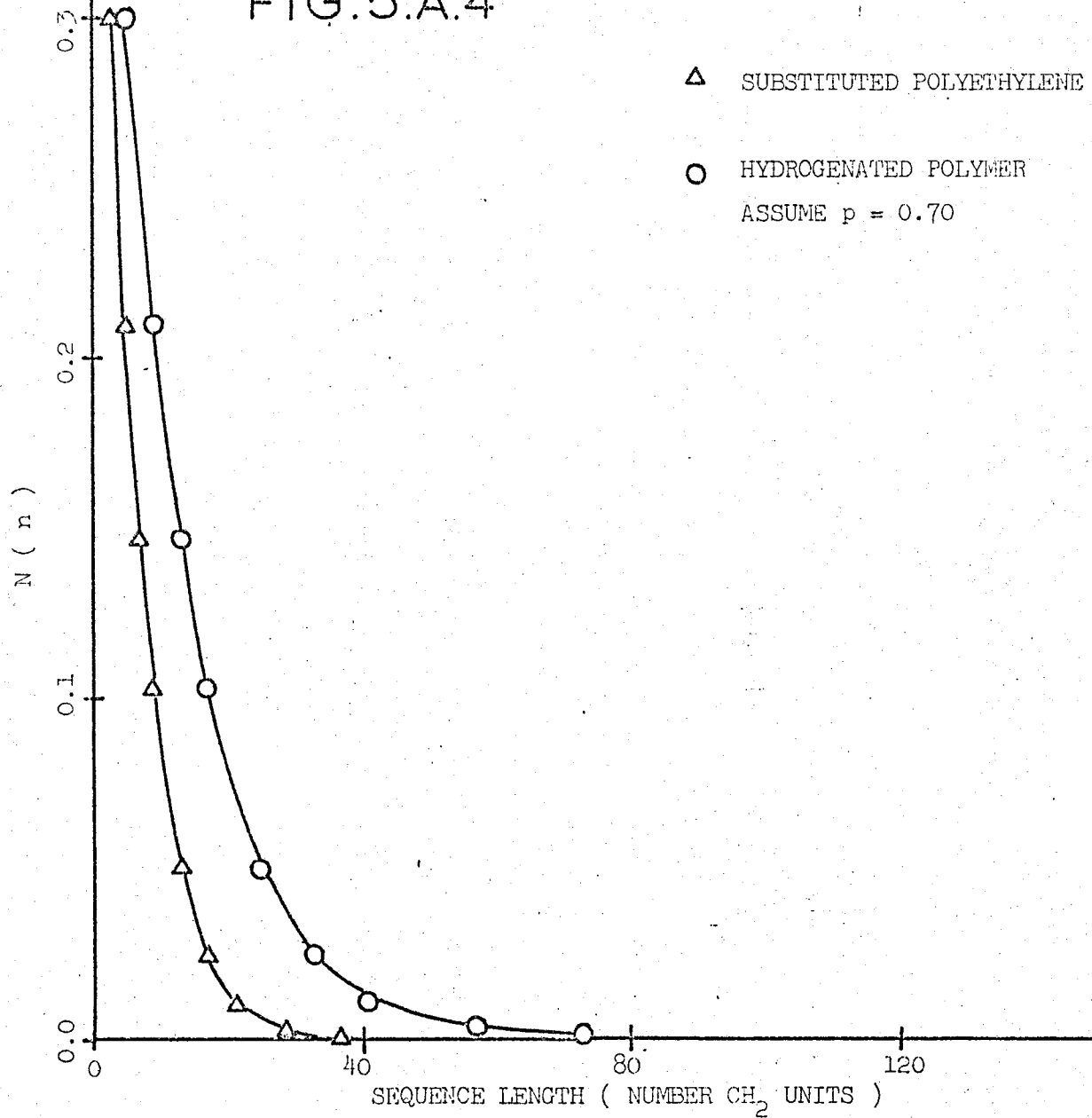
polymers characterized by nuclear magnetic resonance (NMR). Analysis of the spectra for sequence distributions showed them to be perfectly random (163). For the hydrogenated polymers, the number of co-units per 100 chain carbons includes the unsaturated chain carbons. See Appendix II for a sample calculation.

Figure (5.A.3) shows that the EVA copolymers have melting points which are a linear function of the number of co-units per 100 chain carbons. However, this line has a lower slope and y-axis intercept than do the copolymers of Richardson et. al. It is not clear why this is so. Considering that the ethyl and n-propyl substituted polyethylenes were crystallized extremely slowly (over a period of weeks) and then melted almost as slowly, one would have expected their melting points to be higher than the EVA polymers which were crystallized only by slow cooling, then melted at a heating rate of $15^{\circ}\text{K}/\text{min}$. It is not thought that DSC should give values of T_m so different from dilatometry. T_m has been defined the same way for both experiments and assuming the DSC was more sensitive, the EVA melting points should have a larger y-axis intercept and the same slope as the dilatometric melting points. Incorporation of ethyl and n-propyl groups into the crystal lattice might account for a melting point depression of the copolymers of Richardson, et. al. This seems unlikely, however, since Baker and Mandelkern (186), using the same samples supplied by these workers, have shown that the crystal lattice dimensions of n-propyl substituted copolymers, near their melting points, very closely approximate the lattice dimensions of Marlex HDPE (high density polyethylene) at the same temperature. Although Holdsworth and

Keller (1944) have concluded that both methyl and ethyl groups are incorporated into the polymethylene crystal lattice in crystals grown from dilute solution, their experimental evidence does not justify their conclusions for ethyl group incorporation. The basic flaw in their argument is their failure to show that ethyl groups expand the 'a' unit cell dimension of the polymethylene crystal structure whereas they show that methyl groups do this dramatically.

Figure (5.A.3) also shows that the melting points of the hydrogenated polymers lie above those of the ethyl and n-propyl substituted polyethylenes and the random EVA copolymers which have the same number of co-units per 100 chain carbons. This effect can be partially explained by comparing plots of sequence length distribution, $N(n)$, against sequence length, number of consecutive CH_2 units, for a hydrogenated polymer and a substituted polyethylene copolymer using Equation (5.A.1). For this example, assume $p = 0.70$ for both polymers, which is a measure of co-unit concentration. Recall that n is the number of monomer units between co-units. Since, for hydrogenated polymers the number of CH_2 units per sequence is about $4n + 1$ and for substituted polyethylene is $2n + 1$, more long sequences are present in the hydrogenated polymer for identical co-unit concentration as is shown in Figure (5.A.4). However, non-random distribution of co-units and/or non-random hydrogenation could also increase the polymer melting points. To test this hypothesis, the fraction of sequences of length m or greater, $f(m)$, is compared with the weight fraction crystallinity (w_c) at 353°K . m equals 18 is the

FIG.5.A.4



minimum crystallite length (expressed in number of butadiene monomer units) which can exist at 353°K. $f(m)$ can be derived from Equation (5.A.1):

$$f(m) = \sum_{n=m}^{\infty} N(n) = p^{m-1} \quad (5.A.4)$$

where, in this instance, p is the mole fraction of hydrogenated cis plus trans butadiene, assuming random hydrogenation and random vinyl and styrene distribution. m was found using methods explained later in this chapter. Table (5.A.2) compares w_c at 353°K to $f(m)$ where $m=18$. If hydrogenation and co-unit addition are random w_c would be expected to be considerably less than $f(m)$ since even under the most favourable conditions all sequences of length m or greater will not become part of crystallites of length m or greater. Inspection of Table (5.A.2) reveals that w_c is either greater than or approximately equal to $f(m)$ in most cases, thus verifying the non-random nature of these polymers.

TABLE 5.A.2

SAMPLE	w_c at 353°K	$f(m)$, $m=18$
A1	.004	.0007
A2	.090	.063
B1	.002	.0003
B2	.004	.0007
B3	.010	.018
C1	.002	.002
C2	.002	.004
C3	.004	.009

5.A.3 Surface Area of the Crystalline Phase

The modulus calculations performed in Section (5.A.4) require knowledge of the surface area of the crystalline phase (S_2). S_2 was calculated for sample B1 from the SAXS curve shown in Figure (4.A.21) using the methods of Porod (139-40) and Debye (141). A thorough description of both methods is found in Chapter 2. It should be recalled that Porod's method is generally applicable to any two phase system. However, Debye's method is limited to systems where the dispersed phase is of random size and shape which will give a linear relationship between $(I)^{-2/3}$ and $(2\Theta)^2$; (2Θ) is the angle of the scattered intensity (I) . S_2 is then computed from the slope and intercept of this line.

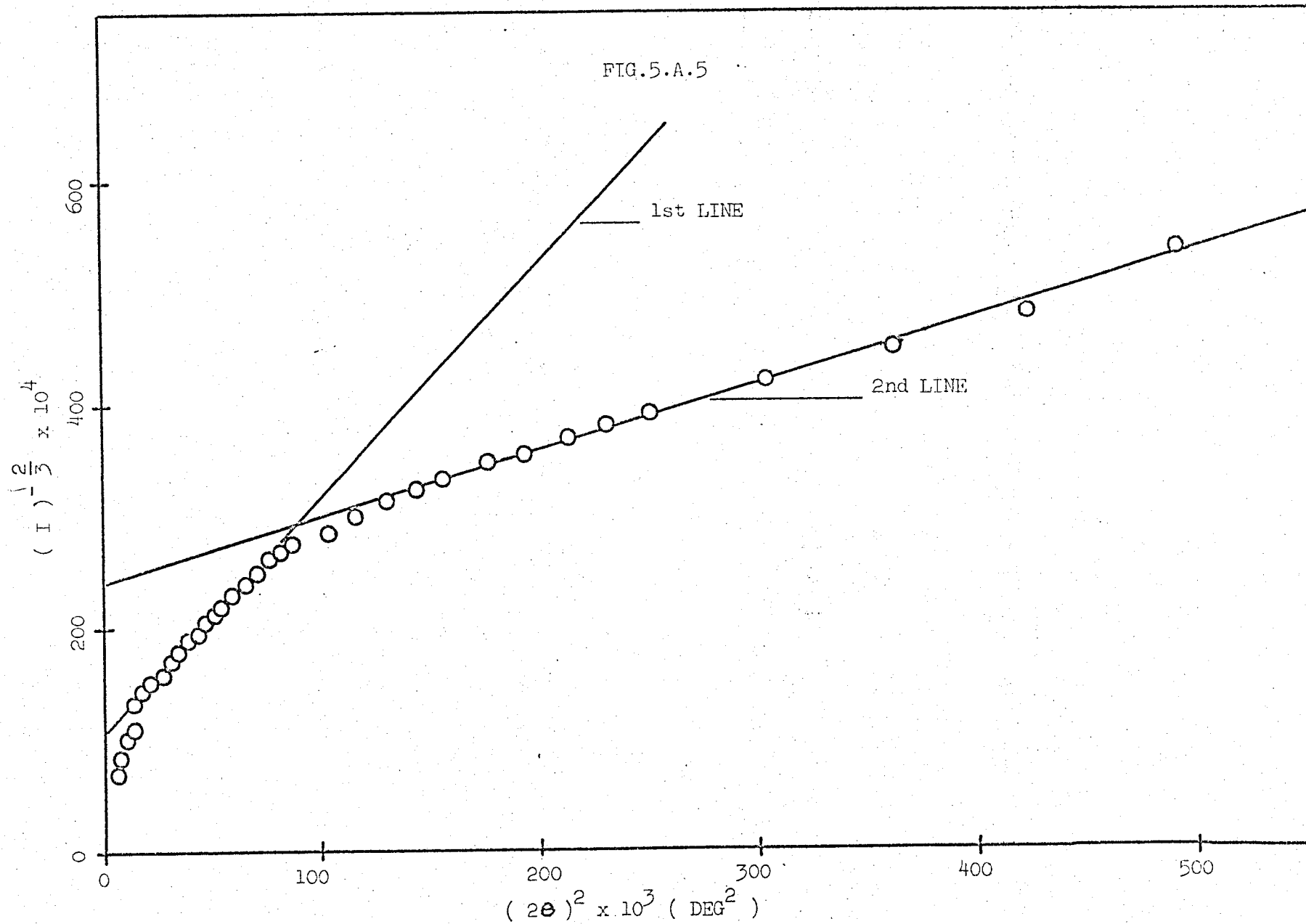
The Debye plot, $(I)^{-2/3}$ versus $(2\Theta)^2$, is shown in Figure (5.A.5) and illustrates the presence of two different straight lines, each with a linear regression correlation coefficient of .999. The values for S_2 from each line are:

$$\underline{\text{1ST LINE}} \quad S_2 = 52.9 \text{ (m}^2 \text{ g}^{-1}\text{)}$$

$$\underline{\text{2ND LINE}} \quad S_2 = 150 \text{ (m}^2 \text{ g}^{-1}\text{)}$$

Porod's method gives $S_2 = 179 \text{ (m}^2 \text{ g}^{-1}\text{)}$. At first glance it would appear that the 2nd line gives the best value of S_2 since it agrees most closely with S_2 from Porod's method. However, it was not possible to obtain the amorphous scattering for the sample and it has not been subtracted. Thus, the limiting value of $\tilde{I}(M)^3$ could be easily as much as one fourth the value used and under these conditions S_2 from Porod's method would agree most

FIG.5.A.5



closely with S_2 from the 1st line. Also, Debye plots usually give straight lines at values of (2θ) corresponding to the first line. Certainly it is inconclusive which Debye plot gives the true value of S_2 . Since S_2 from Porod's method is assumed to be too uncertain due to the lack of knowledge of the amorphous scattering at high angles, an average value of S_2 is taken from the two Debye plots:

$$S_2(\text{average}) = 101 \pm 50 \text{ m}^2 \text{ g}^{-1} \text{ polymer.}$$

5.A.4 Modulus Calculations

The moduli of all samples have been calculated and are compared with experimental values. Two basic assumptions were made in these calculations: (1) chain folding did not occur and (2) lamellar crystallites were not present. Substantial evidence upholds these assumptions thus indicating a fringed-micelle morphology. Flory et. al. (1965) have pointed out that folding of a copolymer crystallite chain is very unlikely since, " after deposition of a preferred sequence of (crystallizable) units, the formation of a loop or fold requires the presence of a second uninterrupted run of units of the same length immediately following the loop. The probability of two such sequences being found in close proximity in a single chain is low. More likely, the required sequence will be found in a neighbouring chain. When such a number of units does occur further down the same chain it will most probably participate in another crystallite. Hence repetitive participation in the same chain in a given crystallite can rarely occur in a copolymer. "

An attempt was made to grow spherulitic crystallites (lamellae radiating from a nucleation centre). Their presence would have been verified by observing birefringence under crossed polaroids. Polymer A2 was chosen for the experiment since it had the highest degree of crystallinity and, thus, thought to have the best chance of forming spherulites. Thin films were cast from xylene and thoroughly dried at 353°K under 1 torr pressure for 3 days with no sign of birefringence. The temperature was lowered to 333°K with no birefringence after 4 more days. The temperature was again lowered, this time to 313°K with no birefringence after another 3 weeks. 1 torr pressure was maintained throughout the experiment except when observing under the microscope.

It was shown, in Section (5.A.3), how the surface area of the crystalline phase of sample B1 was calculated from SAXS using Debye's method. It was stated that this method is only applicable to systems in which the dispersed phase consists of particles of random size and shape. Since a linear relationship between $(I)^{-2/3}$ and (2Θ) is obtained, lamellar crystallites are not likely to be present. The preceding statements therefore indicate that chain folded, lamellar crystallites are not formed and, thus, a fringed micelle morphology seems likely.

Since the polymers are high molecular weight (\bar{M}_n is 130,000 to 200,000) the effects of chain ends are negligible in modulus calculations. The modulus can then be calculated assuming that the number of crystalline sequences per unit volume (v_c / V) equals the number of amorphous chains bound by crystalline crosslinks per unit

volume (v/V). This assumption is a consequence of the lack of chain folding. Since all polymers studied had relatively low degrees of crystallinity and employing the fringed micelle model, the rigidity modulus (E) can be calculated from the theory of rubber elasticity:

$$E = 3 \left(\frac{v}{V} \right) \left(\frac{\langle r^2 \rangle_i}{\langle r^2 \rangle_o} \right) kT \quad (5.A.5)$$

where $\langle r^2 \rangle_i$ is the mean square chain displacement length in the absence of strain imposed by an external stress.

$\langle r^2 \rangle_o$ is the mean square chain displacement length for free chains unconstrained by unit junctions.

k is the Boltzmann constant.

T is absolute temperature.

For samples of low crystallinity $\frac{\langle r^2 \rangle_i}{\langle r^2 \rangle_o} \approx 1$ (165).

Thus,

$$E = 3 \left(\frac{v_c}{V} \right) kT \quad (5.A.6)$$

(v_c / V) can be calculated using DSC data. Consider all the crystallites of length l in a unit volume of polymer, one of which is represented by Figure (5.A.6.a). $(v_c / V)_l$ is the volume of these crystallites per unit volume of polymer. $(v_c / V)_l$ is defined as the number of crystalline sequences of length l per unit volume of polymer. A is the cross-sectional area of a crystalline chain. Define, $(v_c / V)_l A = f_l$, the volume fraction crystallinity of crystallites of length l . As was indicated earlier, l is a function

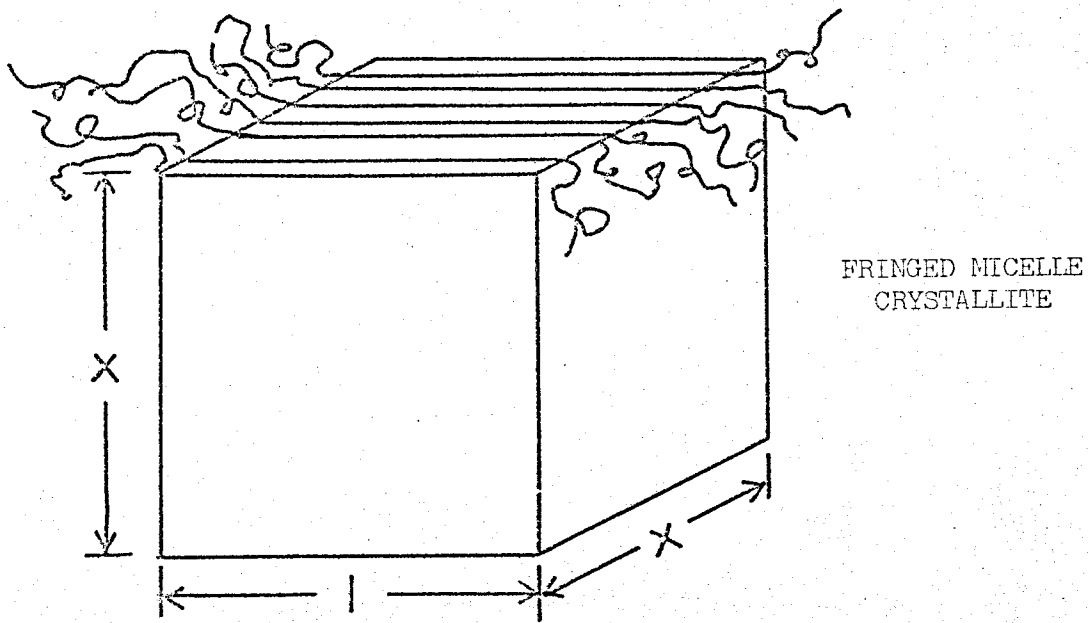


FIG. 5.A.6.a

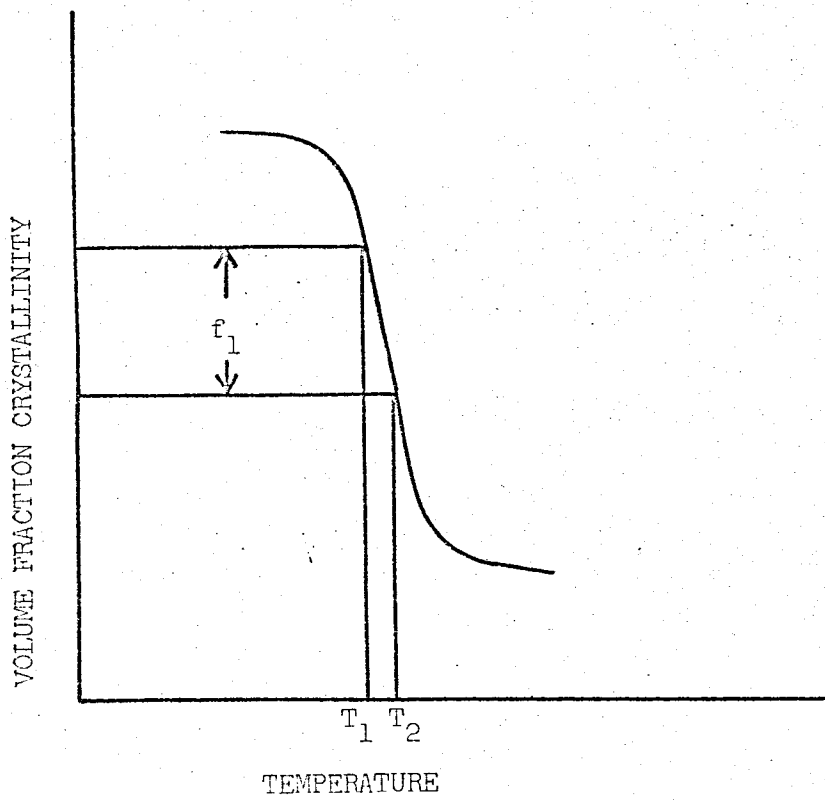


FIG. 5.A.6.b

of the crystallite melting point (T_m). Thus f_1 is the volume fraction crystallinity in a narrow temperature range T_1 to T_2 as is illustrated in Figure (5.A.6.b). But f_1 cannot be calculated directly from DSC data, which gives only weight fraction crystallinity (w_c). However by calculating w_c for successive temperature intervals, a plot of w_c versus T can be made. From this plot, w_1 , the weight fraction crystallinity between T_1 and T_2 can be calculated. f_1 can then be calculated from w_1 using Equation (5.A.7):

$$f_1 = \frac{w_c \rho_p}{\rho_c} \quad (5.A.7)$$

where ρ_p is the density of the polymer at $\frac{T_1 + T_2}{2}$.

ρ_c is the density of the crystalline phase, $.9988 \text{ g cm}^{-3}$ (166).

ρ_p was measured for each sample at $292.95 \pm .05^\circ \text{K}$ by flotation using methanol / water solutions in a 25 ml. pycnometer. Since,

$$\rho_A = \frac{\rho_p - w_c \rho_c}{(1 - w_c)} \quad (5.A.8)$$

where ρ_A is the density of the amorphous phase. ρ_p can be calculated at any temperature where w_c is known, assuming ρ_A and ρ_c are constant with temperature, using Equation (5.A.9):

$$\rho_p = w_c \rho_c + (1 - w_c) \rho_A \quad (5.A.9)$$

ρ_A can be calculated from ρ_c . In a polyethylene crystal, a single chain has the conformation illustrated in Figure (5.A.7.a).

Therefore,

$$x = 1.54 \text{ \AA}$$

$$\alpha = 109^{\circ}30'$$

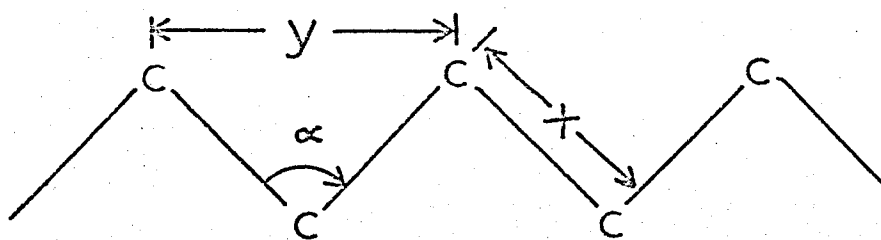


FIG.5.A.7.a

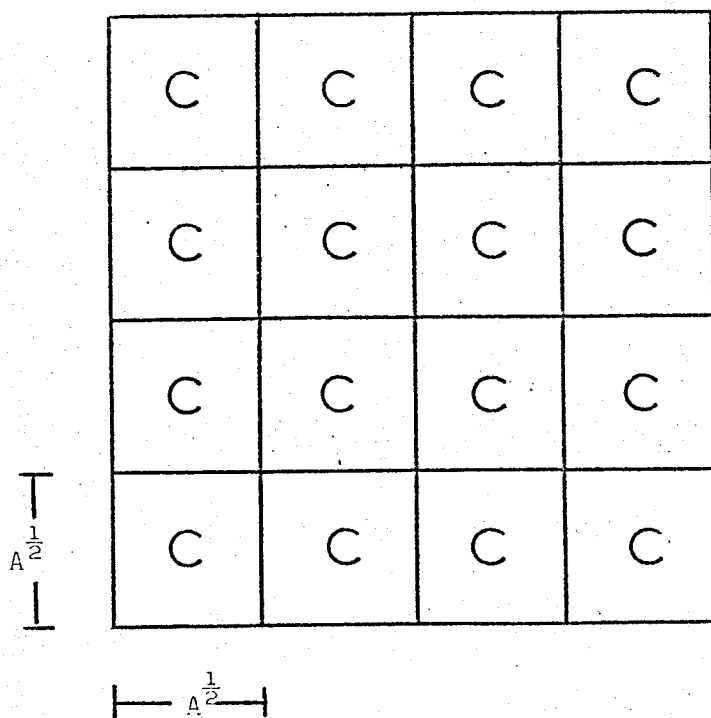


FIG.5.A.7.b

$$y = 2x \cos \alpha = 2.50 \text{ \AA}$$

Part of the cross-section of a crystallite can be represented by

Figure (5.A.7.b) where each chain has a cross-sectional area A .

Each CH_2 group thus occupies a volume $\frac{Ay}{2}$. The volume of a crystalline CH_2 unit can also be written:

$$\frac{M \rho}{N}$$

where M is the molecular weight of CH_2 .

N is Avogadro's number.

Therefore,

$$A = \frac{2M \rho}{yN} = 18.6 \times 10^{-20} \text{ m}^2$$

We now have:

$$\left(\frac{v_c}{V}\right)_1 = \frac{f_1}{1A} \quad (5.A.10)$$

where f_1 is known as a function of temperature and A is known.

l must now be calculated as a function of temperature. The free energy of formation ($\Delta \phi_c$) for the crystallite represented in Figure (5.A.6.a) is (167-8):

$$\Delta \phi_c = 2x^2 \sigma_e + 4xl\sigma - x^2 l \Delta F_u \quad (5.A.11)$$

where σ_e is the surface free energy of the crystallite faces perpendicular to chain extension.

σ is the lateral crystallite surface free energy.

ΔF_u is the free energy difference between the melt and the bulk crystalline phase.

Edge free energy terms are ignored. These would reflect the extra work required to cause a crystalline sequence to lie on a flat surface in from the sequence plane, rather than in the plane of the sequences or even outside it. At the melting point of this crystallite (T_m), $\Delta\phi_c = 0$ changing Equation (5.A.11) to:

$$2x \sigma_e + 4l \sigma - xl \Delta F_u = 0 \quad (5.A.12)$$

Rearranging Equation (5.A.12) gives:

$$l = \frac{2 \sigma_e}{x \Delta F_u - 4 \sigma} \quad (5.A.13)$$

Thus, the dependence of l on T_m can be established when x and ΔF_u are known as functions of T_m . Figure (5.A.2) illustrates the dependence of ΔF_u on T_m . It is not known how x varies with T_m but it is certainly unreasonable for $1/x$ to be constant with T_m since higher melting crystallites (with longer crystallizable sequences) are much more scarce than shorter crystallites, as shown in Figures (5.A.1) and (5.A.4). However, it is felt that a reasonable answer will be obtained if x is assumed to be constant as a function of T_m .

The problem thus condenses to choosing the appropriate value for x . A reasonable value can be calculated if the surface area of the crystalline phase is measured at a known degree of crystallinity. Sample B1 was chosen to illustrate this point. Assume that all crystallites can be represented by Figure (5.A.6.a) with average dimensions $x_a = x$ and $l_a = l$. The surface area per gram of polymer is then:

$$S_2 = n (2x_a^2 + 4l_a x_a) \quad (5.A.14)$$

where n is the number of crystallites per gram of polymer.

The weight fraction crystallinity is:

$$w_c = n l_a x_a^2 \rho_c \quad (5.A.15)$$

Dividing Equation (5.A.14) by (5.A.15) yields:

$$\frac{S_2}{w_c} = \frac{2x_a^2 + 4l_a x_a}{l_a x_a^2 \rho_c} \quad (5.A.16)$$

Solving Equation (5.A.16) for x_a gives:

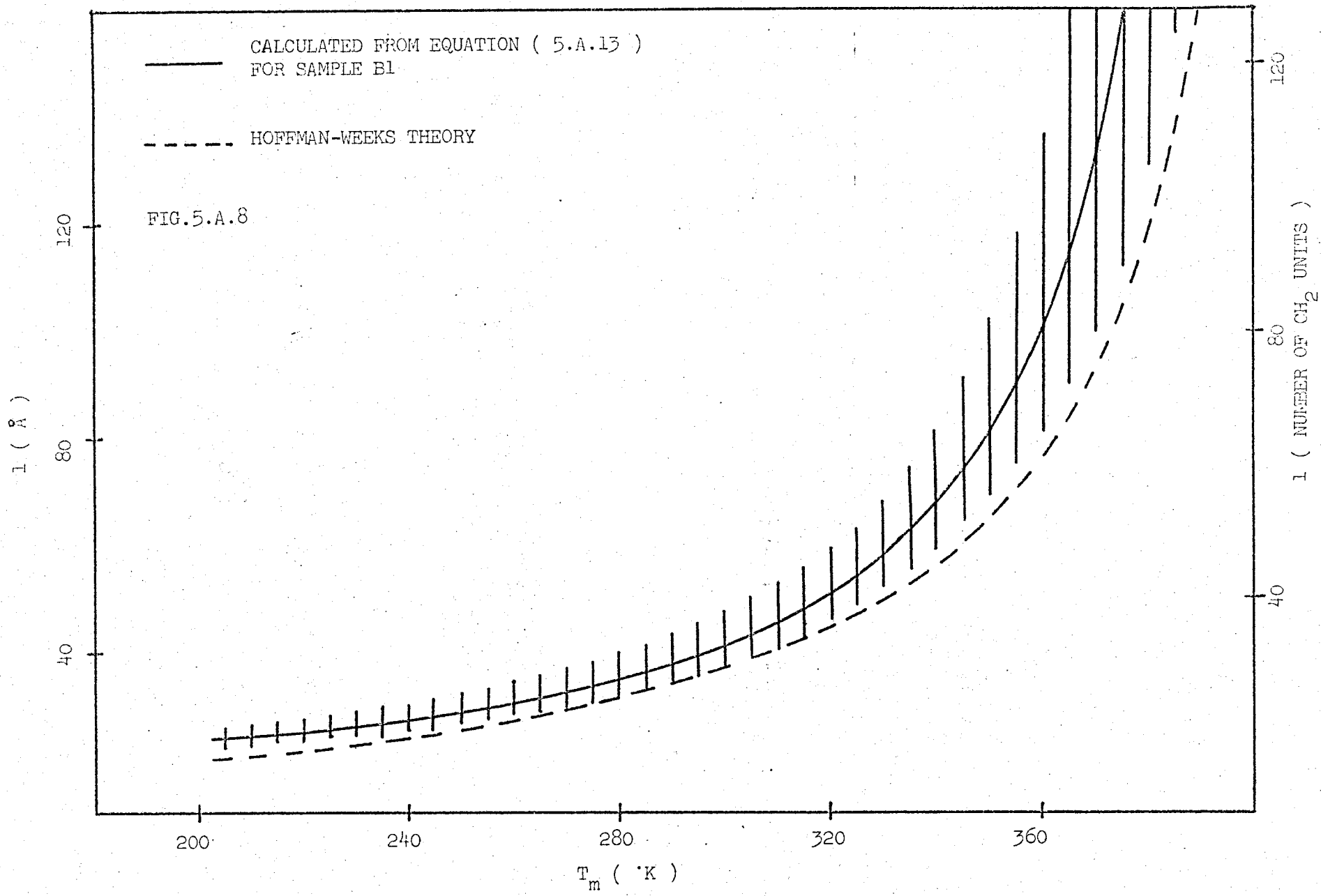
$$x_a = \frac{4l_a w_c}{l_a \rho_c S_2 - 2 w_c} \quad (5.A.17)$$

Since the main DSC peak for sample B1 occurs at 320°K, $l_a = 1$ and $x_a = x$ approximate the dimensions of those crystallites melting at 320°K. Thus, use $x = x_a$, $l = l_a$ and ΔF_u at 320°K in Equation (5.A.13). Combine this with Equation (5.A.14) to give:

$$l_a = \frac{2 w_c (\sigma_e - 0)}{\Delta F_u w_c - \sigma_c \rho_c S_2} \quad (5.A.18)$$

Substitute the value of l_a obtained from Equation (5.A.18) into (5.A.17) to determine x_a , which is assumed to remain constant over the melting range. This value of $x_a = x$ can then be used in Equation (5.A.13) to determine how l varies with T_m as shown in Figure (5.A.8). To calculate l , in meters, the following values are used:

$$\sigma_e = 7.99 \times 10^{-3} \text{ J m}^{-2} \text{ crystal (169)}$$



$$\sigma = 5.72 \times 10^{-4} \text{ J m}^{-2} \text{ crystal (168)}$$

$$w_c = .072 \text{ (g crystal) (g}^{-1} \text{ polymer), from DSC}$$

$$\rho_c = .9988 \times 10^{-6} \text{ (g crystal) (m}^{-3} \text{ crystal) (166)}$$

$$\Delta F_u = \text{J m}^{-3} \text{ crystal, Figure (5.A.2)}$$

$$S_2 = 101 \pm 50 \text{ (m}^2 \text{ crystal) (g}^{-1} \text{ polymer), Section (5.A.3).}$$

In Figure (5.A.8), the solid line represents the values of l calculated from Equation (5.A.13) using $S_2 = 101 \text{ m}^2 \text{ g}^{-1}$. The shaded area represents the uncertainty of the data using the extreme values of S_2 for the area's boundaries. This plot is compared with the values of l calculated from the Hoffmann-Weeks equation (82), the broken line in Figure (5.A.8):

$$l = \frac{2 \sigma_e}{\Delta F_u} \quad (5.A.19)$$

This equation is derived from Equation (5.A.12) assuming that x is at least three times larger than l , thus $4l \Delta < 2x \Delta_e$ and:

$$2x \sigma_e = xl \Delta F_u$$

which reduces to Equation (5.A.19).

In the Hoffman-Weeks treatment, ΔF_u is considered to vary linearly with temperature; thus the discrepancies between the two analyses at low values of T_m . At intermediate values of T_m , agreement between the two analyses is closest since, $x \approx 3l$ and in this region up to T_m^0 , ΔF_u is almost linear with temperature. At higher T_m , discrepancies become more pronounced because $x < 3l$. To illustrate this, assume $S_2 = 52.9 \text{ m}^2 \text{ g}^{-1}$ (lower limit of S_2).

The graph of l versus T_m in Figure (5.A.8) calculated from this value of S_2 corresponds to the lower limit of l . The lower limit of l starts to deviate from the Hoffman-Weeks curve for

$$l = 46\text{\AA} = \frac{x}{3}.$$

Errors in the calculation of l from T_m could result from:

- (1) Neglecting the effect of the edge free energy.
- (2) Neglecting the change of G_e with T_m (171).
- (3) Imperfections in the crystalline phase caused by possible incorporation of main chain double bonds and/or hydrogenated vinyl co-units into the crystal lattice (86,172-3). These might depress the melting points of crystallites formed well below the copolymer melting point.

(4) Not knowing exactly what the l/x ratio is at different T_m . Sizable errors would only be possible, however, where $l/x \gg 1/3$. Although l versus T_m has been calculated only for sample B1, it has been shown that in the regions of maximum crystallinity (315°K to 351°K) only small deviation from the Hoffmann-Weeks equation is observed and this equation will therefore be used to predict l for all samples.

Equation (5.A.10) can now be used to calculate $(v_c / V)_1$ since all terms are known. (v_c / V) can then be calculated using Equation (5.A.20):

$$\left(\frac{v_c}{V}\right) = \sum_1 \left(\frac{v_c}{V}\right)_1 \quad (5.A.20)$$

Combining Equations (5.A.20) and (5.A.6) gives:

$$E = 3kT \sum_1 \left(\frac{v_c}{V} \right) \quad (5.A.21)$$

Thus far the crystallites have been thought of merely as crosslinks. However, since they occupy a finite volume, they will contribute a factor $(1 + 2.5c + 14.1c^2)$ to the modulus (106,112,174), where c is the volume fraction of crystalline material. Equation (5.A.22) therefore becomes:

$$E = \left[3kT \sum_1 \left(\frac{v_c}{V} \right) \right] (1 + 2.5c + 14.1c^2) \quad (5.A.22)$$

Table (5.A.3) compares the experimental and calculated, from Equation (5.A.23), Young's moduli at 293°K. The experimental values are the dynamic storage moduli at 0.1 Hz. All calculated values are about an order of magnitude lower than experimental values which is in agreement with the findings of Nielsen and Stackton (174) and Flory et. al. (165), who did related calculations on similar systems.

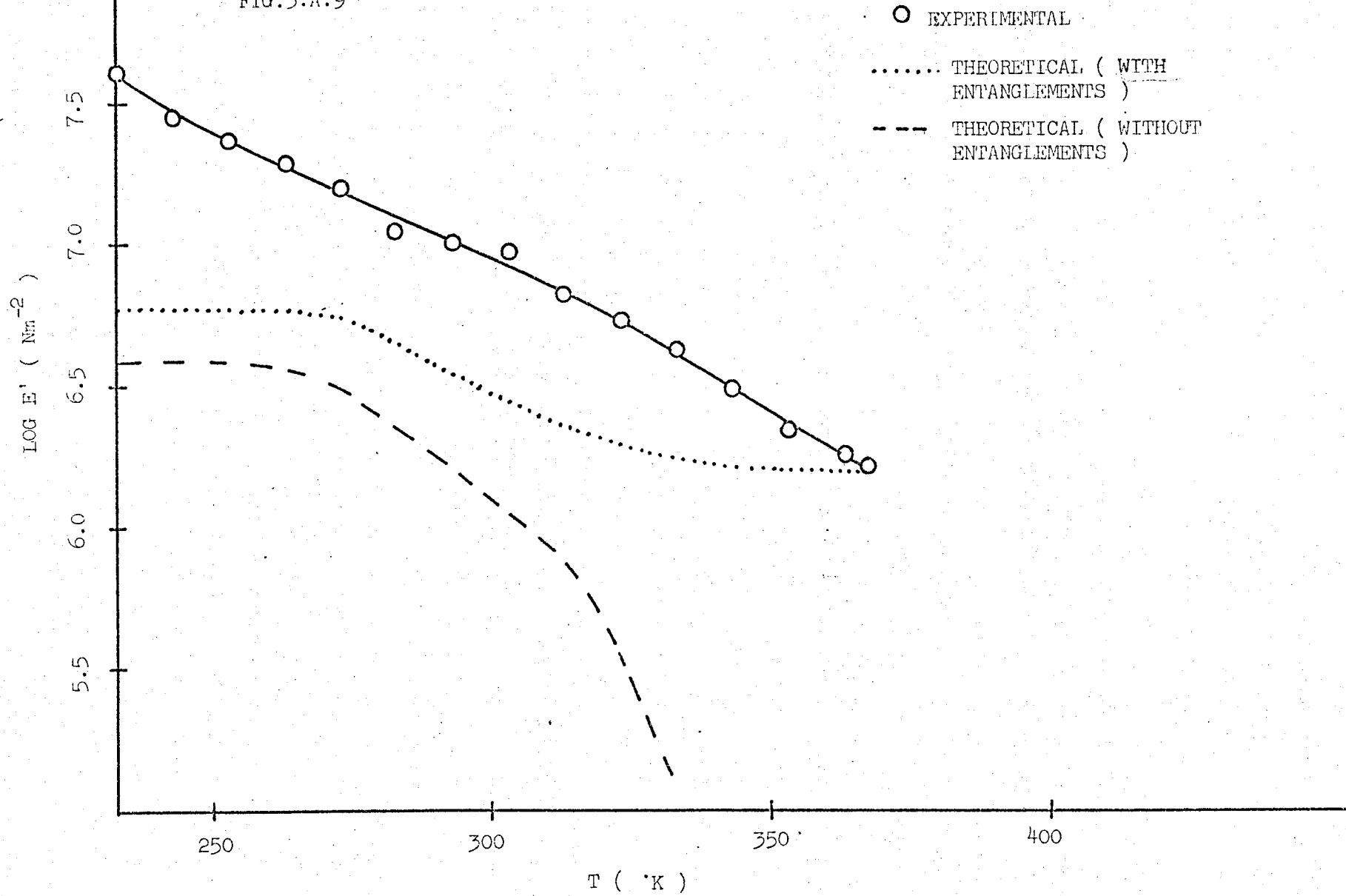
TABLE 5.A.3

SAMPLE	w_c at 293°K	E' (EXPERIMENTAL) Nm^{-2}	E (CALCULATED) Nm^{-2}
A1	.048	7.95×10^6	6.27×10^5
A2	.227	5.37×10^7	6.84×10^6
B1	.071	1.00×10^7	1.08×10^6
B2	.089	1.26×10^7	1.50×10^6
B3	.150	2.24×10^7	2.98×10^6
C1	.087	1.60×10^7	1.53×10^6
C2	.088	1.86×10^7	1.54×10^6
C3	.136	4.00×10^7	2.37×10^6

The basic assumption of crystallites acting as fillers and cross-links is indicated by the direct relationship between w_c and the magnitudes of the experimental and calculated moduli. However, large discrepancies exist between the experimental and calculated data.

In order to more carefully evaluate the reasons for these differences, the modulus of sample B1 will be calculated at various temperatures and compared with experimental values. f_1 was calculated from a DSC scan (curve 4, Figure 4.A.20) for a sample with similar thermal history to the dynamically tested specimen. The experimental modulus was the dynamic storage modulus at 0.1 Hz. Results are shown in Figure (5.A.9). Agreement between experimental and theoretical curves (broken line) is within an order of magnitude from 233°K to 303°K. Above 303°K, the calculated modulus falls off sharply. Chain entanglements appear to be a major cause of discrepancy, since the theoretical curve falls off so rapidly at low values of w_c (higher temperatures). The contribution to the modulus due to entanglements at a certain frequency and temperature can be calculated from the dynamic modulus if the sample is completely amorphous. If the polymer is heated to the molten state then cooled rapidly from the melt, while modulus measurements are taken, this entanglement contribution to the modulus can be determined at various temperatures below the copolymer melting point. If cooling is rapid enough to about 323°K, crystallinity will be negligible and the modulus will be due solely to entanglements. This experiment was carried out using sample B1 cooled from 363°K to 326°K within thirty

FIG.5.A.9



minutes. The results, in Table (5.A.4) show that very little modulus change occurred over the temperature range. Thus, the number of entanglements is approximately constant with temperature. The number of network chains per unit volume calculated from the modulus at 368°K was taken as the contribution to the modulus via entanglements. This number was added to (v_c / V) for each point on the broken line in Figure (5.A.9). The new theoretical curve (solid line), with the effect of entanglements considered is also shown in Figure (5.A.9) and displays much less discrepancy with the

TABLE 5.A.4

<u>E' (Nm⁻²) at 0.1 Hz</u>	<u>T(°K)</u>
1.15 x 10 ⁶	368
1.15 x 10 ⁶	362
1.20 x 10 ⁶	351
1.21 x 10 ⁶	347
1.25 x 10 ⁶	339
1.26 x 10 ⁶	326

experimental curve. Possible explanations for the remaining differences are:

(1) 0.1 Hz allows too short a time for the polymer to relax to its equilibrium modulus. This explanation most probably accounts for the increasing discrepancy below 263°K where the T_g process is starting, but certainly not above this temperature.

(2) Amorphous chains are in a state of strain in highly crystalline polymers (157,174). Maximum crystallinity for sample B1 is

only 18% at 233°K thus minimizing the likelihood of this possibility.

TABLE 5.A.5

$\Delta (v_c / V) \times 10^{-20}$ chains per cm^3	T(°K)
.42	353
1.09	343
1.47	333
2.63	323
3.24	313
4.03	303
4.11	293
4.19	283
4.29	273

(3) The data shown in Figure (5.A.8) might be wrongly predicting longer crystallites to melt at a particular temperature than actually do. Thus, the number of crystallites melting at a particular temperature is higher than predicted, making (v_c / V) , and the modulus, higher than predicted.

(4) The crystallites could be ordered in such a way as to have an additional reinforcing effect. This effect would be expected to become most apparent at higher degrees of crystallinity where interparticle interplay would be more likely to occur. The opposite situation has in fact occurred. At low degrees of crystallinity, the discrepancy between theory and experiment increased rapidly then leveled off at higher crystallinities.

(5) Crystallization might be increasing the number of entanglements which cannot relax at 0.1 Hz. The number of extra entangle-

ments needed to account for the difference between experimental and calculated moduli, $\Delta(v_c / V)$, between 273°K and 353°K are shown in Table (5.A.5). This data indicates that crystallization causes more permanent entanglements. If the data relating l to T_m were wrong, $\Delta(v_c / V)$ would continue to increase with decreasing temperature. Instead, a constant difference of approximately 4×10^{20} chains per cm^3 occurs between 273°K and 303°K. A sizable relaxation between 263°K and 369°K, Figure (4.A.11), can be accounted for by the relaxation of these entanglements as a function of increasing temperature and decreasing crystallinity.

SECTION B SILOXANE BLOCK COPOLYMERS

5.B.1 Polymer Morphology

The morphologies of the siloxane block copolymer samples prepared by casting from benzene and cyclohexane and moulding, were determined using SAXS and dynamic mechanical data.

BENZENE CAST

Table (5.B.1) shows the ratio of spacings of consecutive orders for the three samples. The incident x-ray beam was normal to the sample edges since this was the only way higher order reflections could be observed. The ratio of spacings for the benzene cast sample is approximately, 1: .500 : .333 : .250 , which is consistent only with a regular periodic arrangement of parallel lamellae of infinite lateral extension (143-4). The interlamellar spacing (d) is 235\AA . The pin-hole photographs, Figures (4.B.6.a) and (4.B.6.b) show equatorial arcs with the x-ray beam normal to the edges and a circular diffraction pattern of weak intensity with the beam normal to the edge. This indicates a ring oriented structure with preferential orientation of the lamellae perpendicular to the film thickness direction, which can be considered an orientation axis (Z) (175). Z is therefore normal to the sample faces. Since most of the reflected intensity is at the equators, in Figure (4.B.6.a), the slit smeared data shows a very sharp first - order peak, with a similar spacing as the pin-hole photographs and very little intensity at low angles. The orientation function, $\langle \cos^2 \phi \rangle$, calculated from Equation (3.29), was found to be .215 + .001. This represents an intermediate value between purely randomly oriented lamellae, $\langle \cos^2 \phi \rangle = .333$, and all

lamellae perpendicular to Z, $\langle \cos^2 \phi \rangle = 0$. Thus, although most of the lamellae are perpendicular to the thickness direction of the film, many are at all other orientations accounting for the diffraction pattern observed with the x-ray beam parallel to Z.

TABLE 5.B.1

SAMPLE	n	SPACING RATIO OF CONSECUTIVE ORDERS	
		PIN-HOLE OPTICS	SLIT OPTICS
BENZENE CAST	1	1	1
	2	.489	.492
	3	.328	---
	4	.242	---
MOULDED	1	1	1
	2	.520	.511
	3	.335	.327
	4	.254	---
CYCLOHEXANE CAST	1	1	1
	2	.558	---

The mechanical properties of the benzene cast system are also consistent with the aforementioned structure. Table (5.B.2) summarizes the dynamic moduli, shown in Figures (4.B.13) to (4.B.15) at 1.00 Hz, for the three possible shear deformations of all samples. The properties of the cyclohexane cast sample taken above its T_g are also shown. Log G' for geometries 1 and 2 of the benzene cast sample agree within experimental error and geometry 3 offers the most resistance to shear. This behaviour is predicted using the model of stacked lamel-

lae discussed in Section (2.7). Most of the lamellae in the benzene cast sample are stacked parallel to the sample faces, as shown in Figure (5.B.1.a); the shaded area represents the glassy phase. Since the glassy lamellae are interconnected only by very compliant rubbery chains, shearing in geometries 1 and 2 results merely in the lamellae slipping over one another, as shown in Figure (5.B.1.b), and the modulus will be little affected by their rigidity. This behaviour is quantitatively verified by Equations (2.56) and (2.61). Shearing in geometry 3, however, involves actual deformation of the glassy phase, accounting for the more than three-fold increase in modulus as shown by Equation (2.57).

TABLE 5.B.2

SAMPLE	GEOMETRY	LOG G' (Nm^{-2}) at 1.00 Hz
BENZENE CAST	1	7.00
	2	7.05
	3	7.51
MOULDED	1	6.51
	2	6.60
	3	7.44
CYCLOHEXANE CAST	1	6.04
	2	6.75
	3	6.81
CYCLOHEXANE CAST - TAKEN ABOVE T_g	1	7.04
	2	6.67
	3	6.93

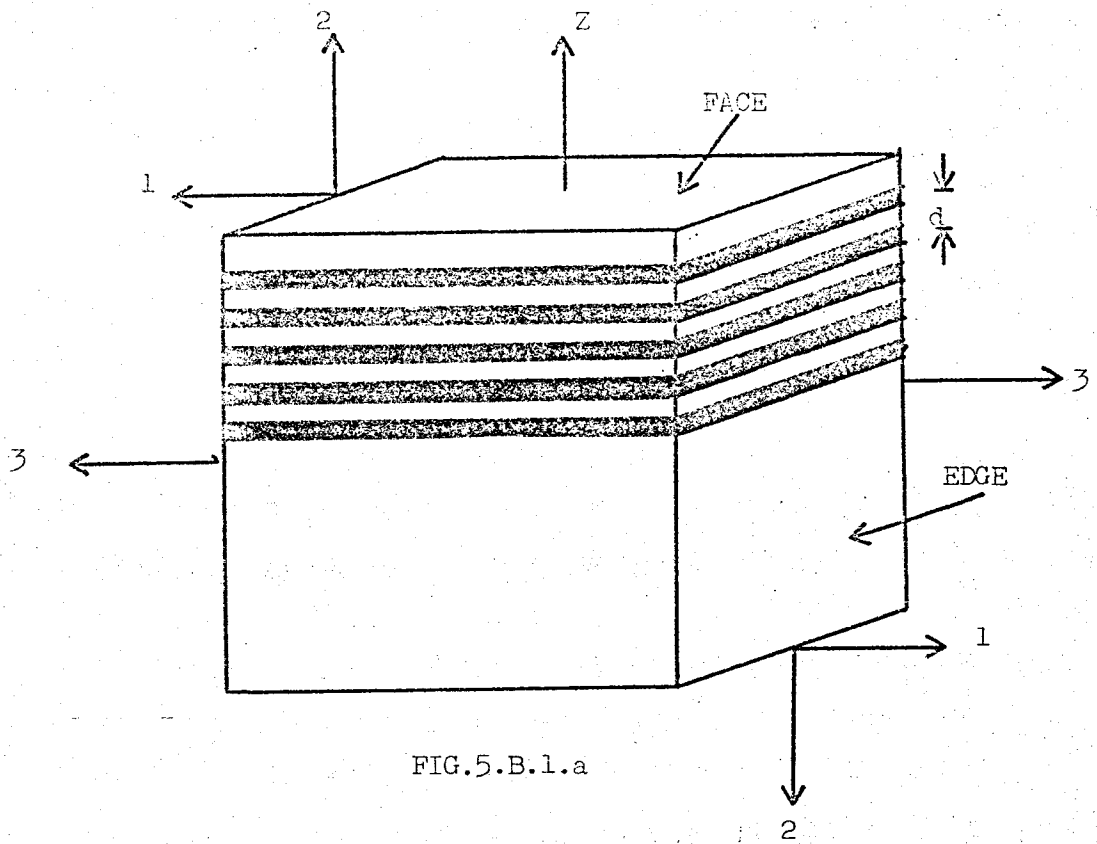


FIG.5.B.1.a

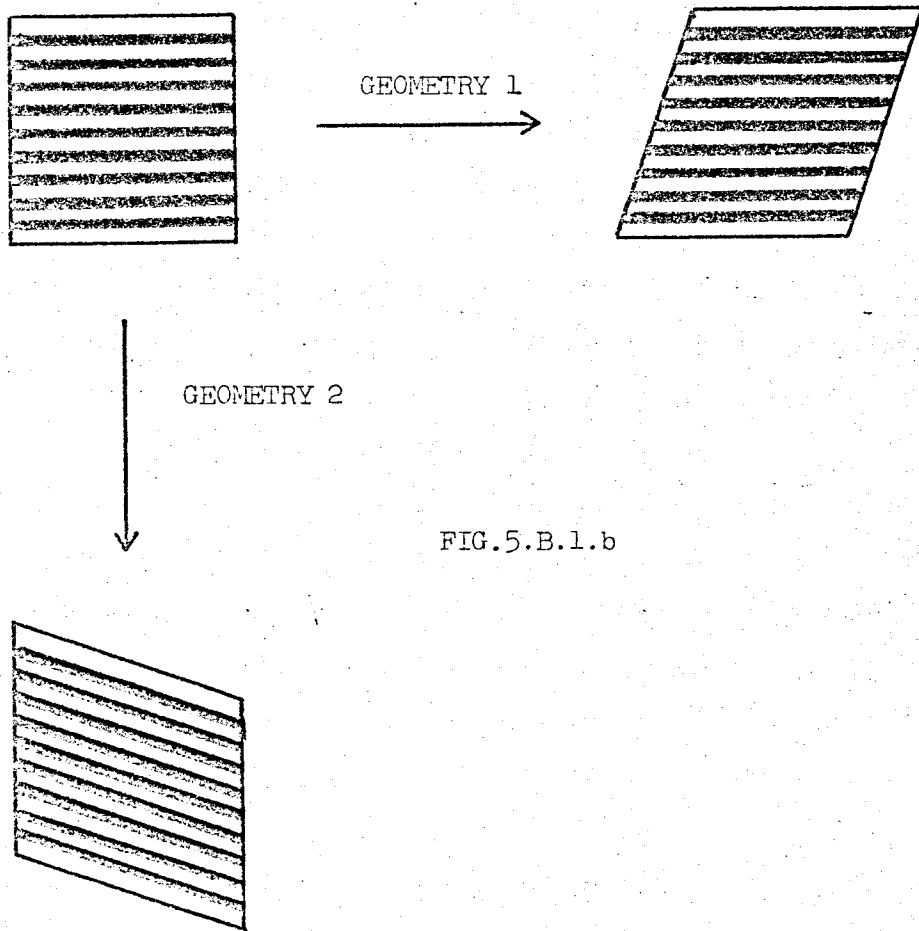


FIG.5.B.1.b

MOULDED

As in the benzene cast system, the ratio of spacings from Table (5.B.1) is consistent with the existence of parallel lamellae of infinite lateral extension. The pin-hole photographs, Figures (4.B.6.c) and (4.B.6.d), also indicate a primarily ring oriented structure with preferential orientation of the lamellae perpendicular to the film thickness direction, which can be considered an orientation axis (Z). Z is again normal to the sample faces. However, the orientation function, $\langle \cos^2 \phi \rangle$, in this case is .060 + .001. This indicates the more oriented nature of this sample with many more lamellae perpendicular to Z than for the benzene cast system. Figure (4.B.6.c) also shows an elliptical diffraction pattern with its long axis parallel to the equators. According to Table (4.B.1), the meridional interlamellar spacing is exactly the same as for the beam perpendicular to the face. This indicates that the interlamellar spacing for lamellae perpendicular to Z is 275Å while those few that are parallel to Z are 307Å apart. Figure (4.B.6.d) shows that the few lamellae parallel to Z are also preferentially oriented. However, such a small percentage are involved that there are no observed effects on the mechanical properties. Slit optics, with the beam perpendicular to the sample edge, shows a very sharp first order peak and two higher orders; see Figure (4.B.3). The sharpness of the first order peak and the agreement in position with the pin-hole photograph is a consequence of the type of orientation, as explained for the benzene cast system.

The mechanical properties shown in Table (5.B.2) again substan-

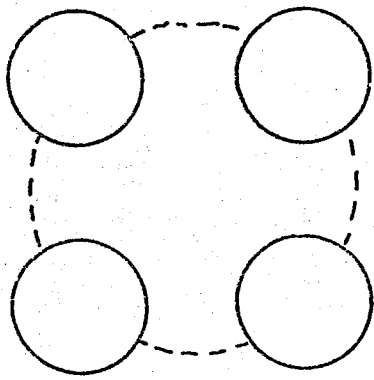
tiate the x-ray findings. Figures (5.B.1.a) and (5.B.1.b) can be used again to explain why the moduli of geometries 1 and 2, which are the same within experimental error, are softer than for geometry 3. However, geometries 1 and 2, for this system, are also softer than for the benzene cast system while geometry 3 shows the same modulus for both systems, within experimental error. It must be remembered that the benzene cast system, being less oriented, has substantially more lamellae in random orientations than the moulded sample. Shearing in geometries 1 and 2 results in deforming some of these lamellae which are parallel to Z, thus increasing the modulus of the system. Since the more oriented moulded sample has less of these lamellae parallel to Z, $\log G'$ would be expected to be less than for the benzene cast system.

CYCLOHEXANE CAST

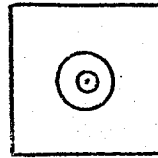
There is only one higher order reflection observed for this system as shown by Table (5.B.1). Therefore, the only definite statement that can be made about morphology is that it is a non-lamellar system since the spacing ratio of the two visible orders is 1: .558. The pin-hole photographs, Figures (4.B.6.e) and (4.B.6.f), show an elliptical diffraction pattern, with beam normal to a sample edge, and a circular pattern with the beam normal to a face. This again indicates a ring oriented system with Z perpendicular to the sample faces. The elliptical pattern in Figure (4.B.6.e) also shows four arcs of slightly higher intensity at 45° to the equator. Elliptical halos have been found at low draw ratios while stretching partially crystalline polymers such as poly(ethylene) (176) and poly(vinyl

alcohol) (177). The elliptical halos in the drawn polymers were postulated to be a result of preferentially distorting a statistically random orientation distribution of a regular, periodic lattice as shown in Figure (5.B.2.a). This figure illustrates a statistically isotropic distribution of lattice points and the resultant photograph expected from its first order reflection, Figure (5.B.2.a'), assuming the incident x-ray beam is normal to the paper surface. Figure (5.B.2.b) illustrates a distortion of the lattice with its resultant elliptical halo of reflection, Figure (5.B.2.b'), as a result of unidirectional stretching. Thus, a non-lamellar structure is indicated for the sample with uniform spacings (d_2) for the glassy domains when viewed through the face and narrower spacings (d_1) in one direction than in the other (d_2) when viewing through an edge. The orientation is seemingly a result of a unidirectional stress having been applied outwards and perpendicular to Z. Table (4.B.1) indicates that $d_1 = 156\text{\AA}$ and $d_2 = 208\text{\AA}$. The four maxima observed in Figure (4.B.6.e) indicate that one of the many orientations of the unoriented lattice, prior to "stretching", was favoured (178). The slit data, Figure (4.B.4), show that with the beam perpendicular to the sample edge, a much broader peak is obtained, while the photographs, both face and edge views, indicate the same degree of peak sharpness. This broadening of the slit peak is undoubtedly due to increased smearing caused by the elliptical nature of the scattering curve when the beam is perpendicular to the edge.

Using the rigidity moduli data in Table (5.B.2), a model based on interconnected spheres has been constructed, which is also consistent with the x-ray data. The model is illustrated in Figure (5.B.3).

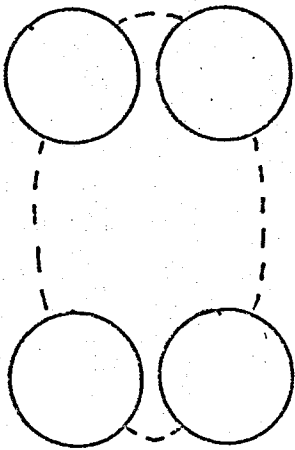


(a)

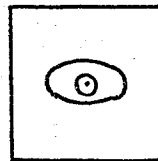


(a')

↑
STRETCHING DIRECTION



(b)



(b')

FIG. 5.B.2.

Figure (5.B.3.a) shows the system viewed through an edge, with the sample faces at the top and bottom of the illustration. The shorter interparticle spacings (d_1) are parallel to Z, while d_2 are perpendicular to Z, as a result of stresses applied outwards and perpendicular to Z. The glassy interconnections are postulated to result from the stress perpendicular to Z deforming the glassy phase while it was still soft with absorbed solvent. No connections were thought to form between closely spaced spheres because of the oriented nature of the applied stress. Since cyclohexane is a preferential solvent for the siloxane phase, the organic phase became glassy while the siloxane phase was still quite swollen. The interconnections would thus counteract the effect of the rubbery chains trying to force the spheres back to an equilibrium situation of equidistant interparticle distances. The view through the sample face, Figure (5.B.3.b), shows equidistant interparticle distances (d_2) with randomly interconnected spheres. Shearing in geometry 1 would result in a very soft modulus, as observed, since the layers of interconnected spheres can slide over one another quite easily because of the absence of vertical interconnections. However, shearing in geometries 2 and 3, whose moduli are identical within experimental error, results in deforming some interconnections leading to the higher observed modulus.

CYCLOHEXANE CAST - TAKEN ABOVE T_g

While performing the torsion pendulum analysis on the cyclohexane cast sample, the sample was taken above the T_g of the organic phase, to 440°K, and left above the T_g for approximately two

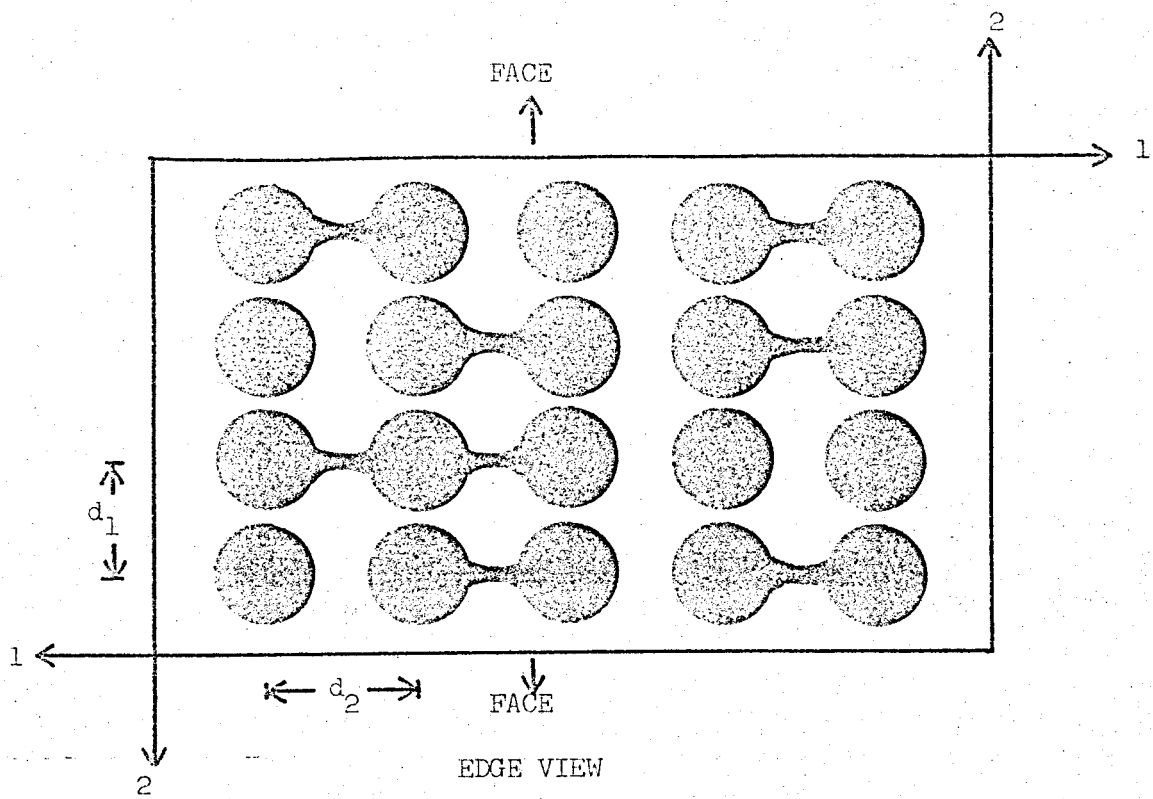


FIG. 5.B.3.a

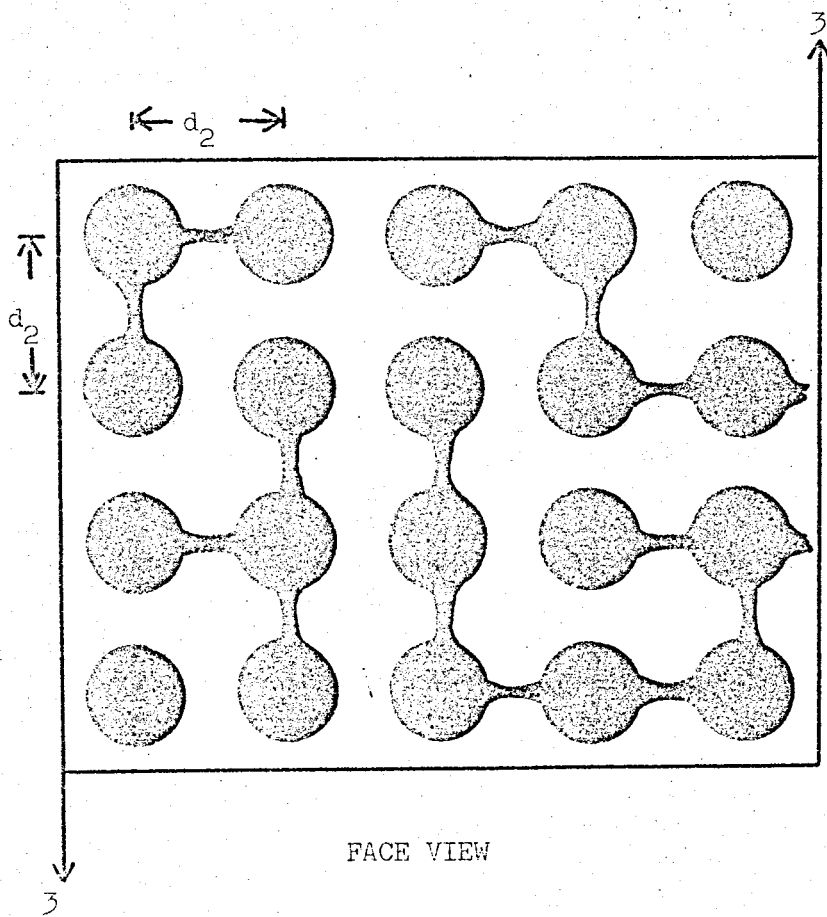
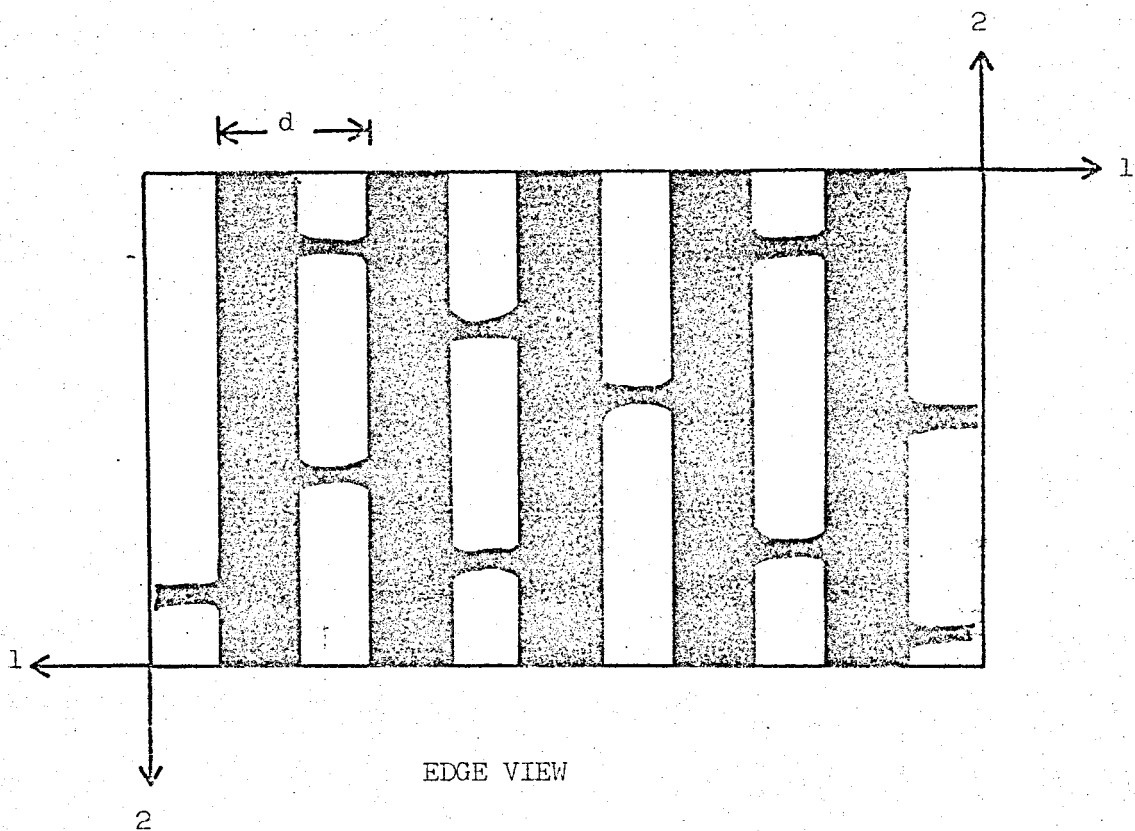


FIG. 5.B.3.b

hours before being allowed to cool slowly to room temperature. When it had reached room temperature, its physical properties and SAXS were found to differ markedly from those taken prior to the heat treatment. A model has been proposed, illustrated in Figures (5.B.3.b) and (5.B.4), consistent with most of the observed data.

The pin-hole photograph, Figure (4.B.6.g), with meridional arcs, indicates a layered structure preferentially oriented perpendicular to the sample faces when viewing through an edge. This is shown in Figure (5.B.4). The step-like scattering curve obtained with slit collimation and beam normal to the sample edge, Figure (4.B.5), is undoubtedly a consequence of the smearing effect due to the higher intensity meridional arcs. Figure (4.B.6.h), although showing the same interparticle spacing as through the edge does not indicate an oriented structure when viewing through the face.

Combining the x-ray data with the fact that G' in geometry 1 is an order of magnitude higher than for the untreated sample, the development of strong interconnections between the formerly closely spaced spheres seems likely. The following explanation is a possible description of the formation of such a structure. While the system is below the T_g of the organic phase, the siloxane chains connected to widely spaced particles are under strain, as discussed previously. Once the organic phase becomes mobile (above its T_g), the strained chains initiate movement to an equilibrium conformation, accounting for the change to a circular diffraction pattern, Figure (4.B.6.g), when viewing through an edge. Also, those spherical domains which were closely spaced have a high probability of blending together due to their proximity, once mobile, and it seems



EDGE VIEW

FIG. 5.B.4

probable that they might form cylinders perpendicular to the sample faces via this mechanism. It is thought that the glassy interconnections present prior to the heat treatment remain. This structure is illustrated in Figures (5.B.3.b) and (5.B.4) which are face and edge views, respectively. In this case, $d_2 = d = 275\text{\AA}$. G' in both geometries 2 and 3 is not greatly increased by heat treatment. This should be expected, since in both cases the movement of the cylinders past one another is retarded by the interconnections. It is not clear, however, why G' in geometry 2 is almost half that of geometry 3.

POSSIBLE MECHANISMS FOR THE FORMATION OF THE VARIOUS MORPHOLOGIES

The formation of an oriented structure for the compression moulded system is in agreement with the findings of Lewis and Price (120) and Keller and coworkers (117,118,119). Both sets of workers found orientation in styrene-butadiene-styrene (SBS) systems caused by melt flow. Lewis and Price observed this in compression moulded samples, while Keller et. al. made their findings on an extruded plug. It is therefore proposed that the moulded siloxane block copolymer became oriented via melt flow.

Orientation in the solution cast systems is in agreement with the findings of Krigbaum et. al. (121), who observed orientation in two solution cast SBS systems. The author has found a similar "orange peel" surface texture in the benzene cast system described by these workers. The cyclohexane cast surface, however, was smooth. Krigbaum and coworkers proposed a mechanism of density gradients within the solution and/or surface tension effects as the

basis for formation of oriented structures. This is also a possible explanation for the effect in the siloxane copolymer. In the cyclohexane cast system, however, the elliptical scattering has been previously described as appearing to result from stresses applied outwards and parallel to the film faces. These stresses could arise as a result of volume contraction, from solvent evaporation, acting with the adhesion of the film edge to the glass evaporating dish to produce a drawn film. The issue appears confused by the findings of Lewis and Price (120) who observed that only isotropic films were formed by casting two SBS samples from benzene. However, their polymers were of low styrene content (26% to 28%) whereas the polymer of Krigbaum and coworkers contained 53% styrene. Since the siloxane block copolymer had a reasonably high glassy phase content (38%), the possibility of the weight fraction of the glassy phase affecting polymer orientation seems plausible.

Since lamellae are formed by moulding and slowly casting from benzene (a good solvent for both phases), it appears that for this particular polymer this is the equilibrium morphology. Meier (97) predicts that a lamellar morphology is present when $1 < M_B / M_A < 3.33$, where M_B , M_A are the molecular weights of the siloxane and α - methylstyrene phases, respectively. In this system $M_B / M_A = 1.67$ which is in agreement with the prediction. A non-lamellar structure for the cyclohexane cast system is consistent with the findings of Saam and Fearon (22). They found that cyclohexane, being a preferential solvent for the siloxane phase, caused the glassy phase to "precipitate" first, in a less continuous structure than for toluene (a good solvent for both phases) cast

systems.

5.B.2 Rubbery Relaxation

The benzene cast and moulded samples display a small relaxation while in the rubbery state. This relaxation is present in certain shear sandwich geometries and in the bending geometries as seen in Figures (4.B.7), (4.B.11.a), (4.B.13) and (4.B.14). A lamellar slip model, similar to the one described by McCrum and Morris (177) for poly(ethylene), is proposed to explain the phenomenon.

A lamellar slip model is proposed for three reasons:

- (1) The relaxation is absent in the non-lamellar (cyclohexane cast) system, as shown in Figures (4.B.12.a) and (4.B.15).
- (2) It is absent for lamellar systems in which the mechanical properties are dominated by deformation of the glassy lamellae, as shown for geometry 3 in Figures (4.B.13) and (4.B.14).
- (3) It is present only in cases where lamellar slip can occur.

The systems displaying this relaxation contain glassy lamellae of thickness L and modulus G , separated by rubber layers, of thickness l and viscosity η . If an oscillating stress is applied such that the lamellae will slip past each other, there is a frequency at which deformation of the glass becomes easier than pushing the lamellae through the viscous medium. This concept can be illustrated using a single relaxation time (τ) model, in which it can be shown that (177):

$$\tau = \frac{K L \eta}{l G} \quad (5.B.1)$$

where K is a constant depending on geometrical factors affecting the rigidity of the glassy lamellae. Assume that prior to the onset of the relaxation, the system possesses a dynamic rigidity modulus $G' = G_R$. Also assume that at the conclusion of the relaxation, $G' = G_U$. Thus, for this single relaxation time model, at any frequency (ω) ()::

$$G' = G_R + \frac{(G_U - G_R) \omega^2 \tau^2}{1 + \omega^2 \tau^2} \quad (5.B.2)$$

$$\tan \delta = \frac{(G_U - G_R) \omega \tau}{(G_U G_R)^{1/2} (1 + \omega^2 \tau^2)} \quad (5.B.3)$$

$$\omega_{\max} = \frac{1}{\tau} \quad (5.B.4)$$

where ω_{\max} is the frequency of the $\tan \delta$ maximum.

To gain an appreciation for the magnitudes of the quantities affecting the relaxation, ω_{\max} is calculated as follows:

Assume:

$$K = 3$$

$$G = 10^9 \text{ Nm}^{-2}$$

$$\eta = 10^7 \text{ poise}$$

$$\left(\frac{L}{l}\right) = .538$$

The dynamic viscosity ($\eta = 10^7$ poise) was determined from G'' in geometry 2 at 10^{-2} Hz using Equation (5.B.5) (18/):

$$\eta = \frac{G''}{\omega} \quad (5.B.5)$$

$\left(\frac{L}{l}\right)$ equals $\frac{\phi}{1-\phi}$, where ϕ is the volume fraction of the glassy phase. $\left(\frac{L}{l}\right)$ was thus calculated using the values of .970 and 1.08 g cm⁻³ for the densities of the siloxane (182) and glassy (183) phases, respectively. ω_{\max} was then calculated from Equation (5.B.4), to be 90 Hz, which is very close to the experimentally determined value (100 Hz). It is observed that ω_{\max} for the benzene cast and moulded systems, in the various shear and bending geometries remains constant. This is to be expected for the model proposed since ω_{\max} is affected by $\left(\frac{L}{l}\right)$, η and G which of course remain the same under the conditions stated.

SWOLLEN SAMPLE

The benzene cast sample was swollen with silicone oil (Hopkin and Williams MS 2000/50 cs) of \bar{M}_n 2000 and density .96 g cm⁻³. Silicone oil was chosen because of its non-volatile nature and low solubility parameter (δ), compared with poly(α - methylstyrene); see Table (5.B.3). Thus, the siloxane phase of the block copolymer was preferentially swollen without disrupting the lamellar structure. This permitted the effects of changing the viscosity and thickness of the rubbery phase on the rubbery relaxation to be studied.

TABLE 5.B.3

<u>POLYMER</u>	<u>$(\text{cal}/\text{cm})^{\frac{1}{2}}$ (184)</u>
Silicone Oil	4.9 - 5.9
Poly(dimethylsiloxane)	7.3 - 7.6
Poly(α - methylstyrene)	8.6 - 9.7

Several benzene cast samples were placed in the oil, at room temperature, and left there for many weeks to attain equilibrium swelling. The average sample weight increase was $16.3 \pm 1.1\%$. The first order SAXS slit-smear peak is shown in Figure (4.B.2). The sharpness of the peak and the assumption of the same orientation present in the unswollen sample, makes desmearing unnecessary. The smeared spacings for both swollen and unswollen samples, from Table (4.B.1), were used to determine L , l and (L / l) as shown in Table (5.B.4). In calculating these quantities it was assumed that L was constant as a function of swelling.

TABLE 5.B.4

SAMPLE	$d(\text{\AA})$	$L(\text{\AA})$	$l(\text{\AA})$	(L / l)
UNSWOLLEN	246	86	153	.538
SWOLLEN	314	86	228	.377

The dynamic properties of the swollen sample, measured in bending geometry, are shown in Figure (4.B.9). In order to discuss the relaxation in terms of Young's modulus, let E' , E_R and E_U replace G' , G_R and G_U , respectively, in Equations (5.B.2) and (5.B.3).

Thus:

$$E' = E_R + \frac{(E_U - E_R)\omega^2 \tau^2}{1 + \omega^2 \tau^2} \quad (5.B.6)$$

$$\tan \delta = \frac{(E_U - E_R)\omega \tau}{(E_U E_R)^{\frac{1}{2}} (1 + \omega^2 \tau^2)} \quad (5.B.7)$$

Figure (4.B.9) shows that E' , for the swollen sample, is much lower than for the unswollen sample at low frequencies where the oil-filled rubbery phase is contributing substantially to the modulus. Thus, E_R is lower for the swollen polymer due to plasticization. With increasing frequency, the swollen modulus increases much faster than the unswollen. It is expected that at a high enough frequency the limiting modulus for the unswollen sample is approached, since deformation of the glassy domains dominates the sample stiffness at high frequencies. Thus, E_U is thought to be approximately the same for the swollen and unswollen polymer.

The plot of $\tan \delta$ versus frequency for the swollen polymer shows that the peak position (ω_{\max}) has moved to a higher frequency and $\tan \delta$ is greater than for the unswollen polymer. Both of these effects can be explained using Equations (5.B.4) and (5.B.7). ω_{\max} is dependent on τ , which is smaller for the swollen sample, since (L/l) and η have decreased while (K/G) has stayed the same. This decrease in τ pushes ω_{\max} to higher frequencies. This can be demonstrated quantitatively as follows. Assume K and G remain the same as for the unswollen sample, 3 and 10^9 Nm^{-2} , respectively. (L/l) is given in Table (5.B.4) as .377. The viscosity of the swollen rubbery phase, η_s , can be calculated from a knowledge of the viscosity of the unswollen rubbery phase, $\eta = 10^7$ poise, and the viscosity of the silicone fluid, $\eta_F = 5 \times 10^{-2}$ poise, using Doolittle's viscosity equation (185, 186):

$$\ln \eta = A + B \frac{1}{F} \quad (5.B.8)$$

where A is assumed to remain constant for poly (dimethylsiloxane) of any molecular weight.

B approximates unity.

η , f are the viscosity and fractional free volume of the measured sample.

The relationships between fractional free volume and viscosity for the swollen and unswollen siloxane and the silicone fluid can therefore be written:

$$\ln \eta_S = A + \frac{1}{f_S} \quad (5.B.9)$$

$$\ln \eta = A + \frac{1}{f} \quad (5.B.10)$$

$$\ln \eta_F = A + \frac{1}{f_F} \quad (5.B.11)$$

where η_S , η , η_F are the viscosities of the swollen and unswollen siloxane and silicone fluid, respectively.

f_S , f , f_F , are the fractional free volumes of the swollen and unswollen, siloxane and silicone fluid, respectively.

It was empirically determined that the following equation is approximately correct based on the weight fraction dependence of free volume:

$$\frac{1}{f_S} = \frac{1}{f} - \omega_F \left(\frac{1}{f} - \frac{1}{f_F} \right) \quad (5.B.12)$$

where ω_F is the weight fraction of silicone fluid in the swollen siloxane phase.

Combining Equations (5.B.9) and (5.B.12) gives:

$$\ln \eta_S = A + \frac{1}{f} - \omega_F \left(\frac{1}{f} - \frac{1}{f_F} \right) \quad (5.B.13)$$

Therefore, combining Equations (5.B.10), (5.B.11) and (5.B.13) η_S was calculated to be 8×10^7 poise. This would make ω_{\max} for the swollen sample equal to 1500 Hz, which is consistent with the experimental data.

The magnitude of $(E_U - E_R)^{\frac{1}{2}}$, in Equation (5.B.7), is the primary factor controlling the magnitude of $\tan \delta$. A change in τ merely shifts the $\tan \delta$ curve along the frequency plane and $(E_U - E_R)$ is relatively insensitive to changes in E_R . Therefore, since $(E_U - E_R)^{\frac{1}{2}}$ is so much smaller for the swollen sample, the smaller $\tan \delta$ for the unswollen sample is expected.

TEMPERATURE DEPENDENCE

The swollen, moulded and cyclohexane cast samples all show a remarkably small variation in E' and $\tan \delta$ over a 60°K temperature range, as shown in Figures (4.B.10), (4.B.11) and (4.B.12.b). Even more remarkably, however, E' and $\tan \delta$ for the benzene cast system remain constant over a 100°K temperature range, as shown in Figure (4.B.8). This is quite unexpected behaviour for polymers when considering the principles of time-temperature superposition presented in Section (2.5). Several authors (72-79) have reported the lack of fit of viscoelastic properties for block copolymers to master curves via a Williams-Landel-Ferry transform. However, to the best of the author's knowledge, such a dramatic deviation from time-temperature superposition, as presented in this work, has never been reported.

Looking at Equations (5.B.6) and (5.B.7), it is evident that the magnitudes of E' and $\tan \delta$ depend on the magnitudes of E_R , E_U and τ . It is therefore the interplay between these three quantities as a function of temperature that will dictate the temperature dependence of E' and $\tan \delta$. E_R and E_U are both dependent on the moduli of the glassy and rubbery phases. From the theory of rubber elasticity, the modulus of a crosslinked, flexible network can be expected to increase with increasing temperature while the glassy modulus remains approximately constant. E_U and E_R would thus be expected to increase with temperature. The relaxation time for this model (τ) is described by Equation (5.B.1). With increasing temperature:

- (1) η , the viscosity of the rubbery phase, would decrease.
- (2) (L / l) would decrease, since the coefficient of expansion for a rubber is greater than for a glass.

Thus, τ decreases with temperature. It can therefore be envisaged that the decrease in τ could be balanced by the increase in E_U and E_R in such a way as to keep E' and $\tan \delta$ constant, or nearly constant, as a function of temperature.

5.B.3 Temperature Dependence of Dynamic Mechanical Properties

The dynamic properties were measured below 373°K on the wide frequency scanning apparatus and above ambient on the torsion pendulum.

WIDE FREQUENCY SCANNING APPARATUS

Log E' and $\tan \delta$ for the benzene and cyclohexane cast, and moulded copolymers and the poly (dimethylsiloxane) homopolymer were measured as a function of temperature, as shown in Figures (4.B.16)

to (4.B.19), respectively. The T_g of the siloxane phase, as indicated by a small $\tan \delta$ peak and slight drop in modulus, occurs at about 150°K. This figure is in agreement with quoted values (187-8).

Above the T_g of the siloxane phase there is a plateau in E' prior to melting in the siloxane phase. During the melting process greater than an order of magnitude decrease in E' occurs, with maximum slope of the $\log E'$ temperature curve occurring between 230°K and 240°K. This is in agreement with T_p obtained by DSC, shown in Table (4.B.2), and with literature values (188-90). It is odd that Saam and Fearon (22) found no siloxane crystallinity by torsional braid analysis for a $(BAB)_x$ styrene-dimethylsiloxane block copolymer. Their measurements covered the temperature range 73°K to 473°K and their modulus-temperature plot shows only the styrene and siloxane glass transitions. However, Noshay and coworkers (18, 24) have shown that small siloxane block molecular weights (ca. 5000) in poly(sulphone) and (α -methylstyrene) / dimethylsiloxane block copolymers, show no crystallinity, whereas larger block molecular weights (ca. 20,000) do show crystallinity.

At the onset of siloxane melting, for the three copolymer samples, $\tan \delta$ is shown to increase then level off. This is undoubtedly due to the start of the lamellar slip relaxation brought about by the increased mobility upon melting of the rubbery phase.

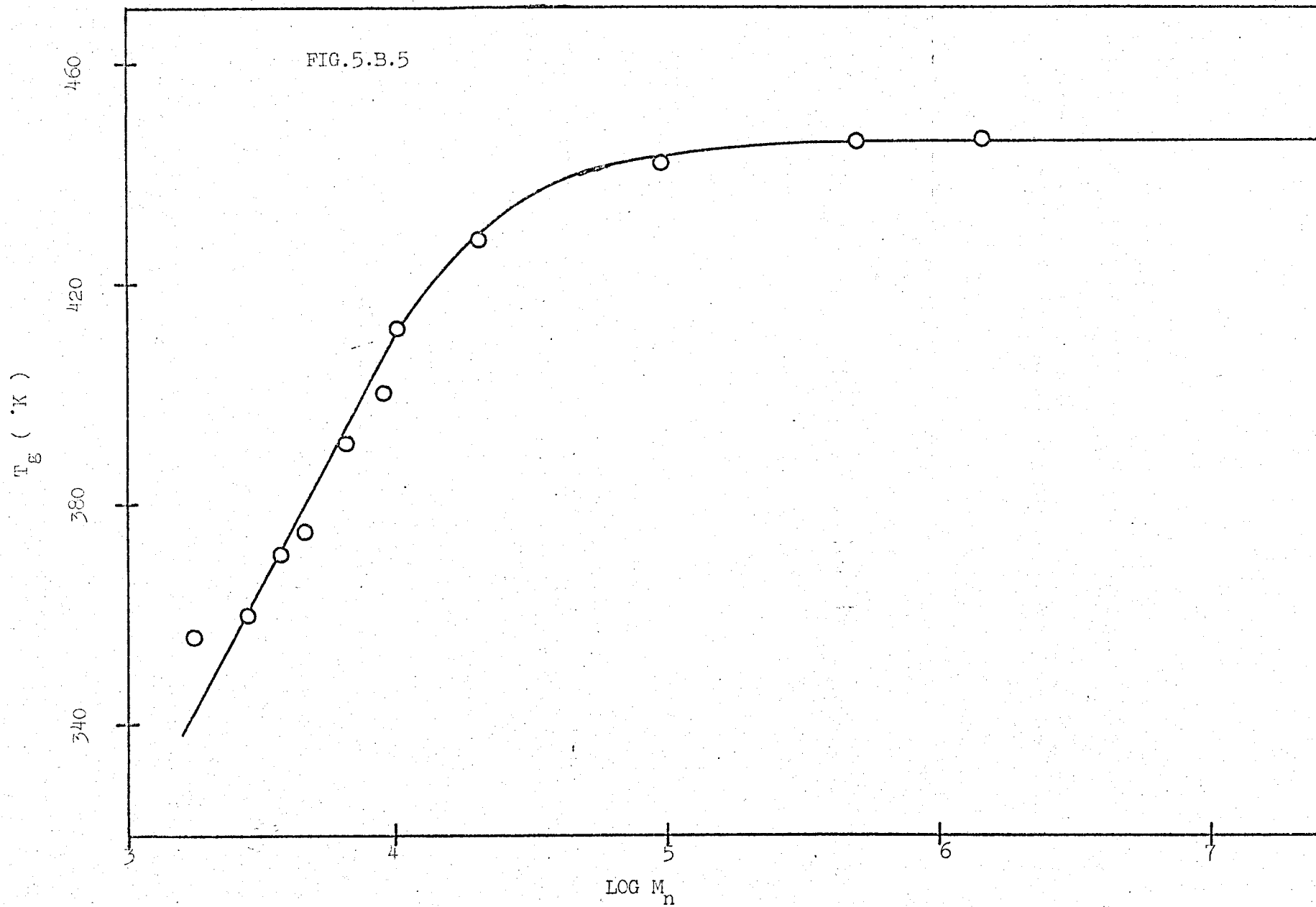
TORSION PENDULUM ANALYSIS

Plots of $\log G'$ (torsion) and $\tan \delta$ versus temperature are shown for the benzene cast, moulded and cyclohexane cast samples in

Figures (4.B.20) to (4.B.22). In each figure, a rubbery plateau region precedes ^e the T_g of the organic phase. The filled triangles represent data taken after the sample had gone through the T_g . Only in the case of the cyclohexane cast sample is G' , after T_g , much different than prior to T_g . This change in G' is due to the morphology change discussed in Section (5.B.1).

Because of the high damping in each sample above the T_g , it is difficult to decide exactly where the transition is. For this reason, the temperature at which $\log G'$ is 6.00 is arbitrarily chosen as the T_g . Thus, 412°K, 424°K and 426°K are the values for the T_g of the benzene cast, moulded and cyclohexane cast samples, respectively. Figure (5.B.5) is a plot of T_g versus \bar{M}_n for poly (α -methylstyrene) using the data of Cowie and Toporowski (191). For a \bar{M}_n of 9000 (\bar{M}_n of each glassy sequence in this copolymer), Figure (5.B.5) predicts a T_g of 408°K. Clearly, the values for the block copolymer are much higher (even when allowing for the effects of experimental time scale). However, the effect of molecular weight on T_g can be explained using the Free Volume Theory (101). Specifically, free volume around chain ends is taken to be greater than that around chain middles because of imperfect packing at the chain ends. Since increasing the free volume decreases the T_g , decreasing \bar{M}_n will have the same effect. In the block copolymer, although the \bar{M}_n of each α -methylstyrene sequence is 9000, only half the chain ends present in the homopolymer of the same \bar{M}_n are in each sequence. Thus, from chain end considerations, these sequences should have the equivalent T_g of a homopolymer of $\bar{M}_n = 18,000$, which is

FIG. 5.B.5



427°K according to Figure (5.B.5). This is in very good agreement with the T_g 's of the moulded and cyclohexane cast samples. The T_g of the benzene cast system is, however, more than 10°K lower than the others. This is thought to be due to a plasticization effect in the α - methylstyrene phase caused by a small residual benzene content in spite of the rigorous drying conditions. The sharpness of the transition makes phase mixing at the interface (72,176) or partial orientation within the glassy domains (157) seem unlikely.

There is a decrease in relaxation strength for the benzene cast, moulded and cyclohexane cast samples, in that order. This is in line with the decreasing modulus drop from the rubbery to the melt phase, in the same order. The lamellar samples are the stiffest, in torsion since the glassy phase, being more continuous in these systems, has a larger contribution to the total modulus. Thus the smaller modulus drop for the cyclohexane cast system. In Section (5.B.1) the benzene cast sample was shown to have more lamellae perpendicular to the sample faces than the moulded sample. These lamellae are deformed in torsion thus accounting for the higher G' , in the rubbery state, for the benzene cast sample.

5.B.4 Crystallinity in the Siloxane Phase

Figures (4.B.23) to (4.B.25) show the DSC scans for the copolymer samples and the siloxane homopolymer subjected to three different cooling histories. T_p , extrapolated to zero sample mass, and $(\omega)_c$ for each sample are summarized in Table (4.B.2) for the different cooling rates.

An exothermic peak on the low temperature side of the scan for

the cyclohexane cast sample at cooling rate 1 indicates that the siloxane chains crystallize more slowly for this than the other samples. The unique orientation in this system, discussed in Section (5.B.1), puts more strain on the siloxane chains in this copolymer. This might account for the slower crystallization rate. Lower ω_c and T_p for the cyclohexane cast system, when compared to the other copolymer systems, can also be accounted for by this extra strain in the rubbery phase (159).

ω_c and T_p for all copolymer samples are lower than for the homopolymer. More strain exists in the siloxane chains of the copolymer. It is caused by the chains being tied to the glassy domains and having tetrafunctional branch points. This strain is partially responsible for the lower values of ω_c and T_p as discussed in the previous paragraph. The presence of branching has also been found to cause the same effect (84).

The variation of ω_c with cooling rate shows that a large degree of crystallinity develops quickly (primary stage) followed by a slower rate of development (secondary stage). This agrees with the findings of Moskalenko et. al. (192) who studied the crystallization kinetics of poly(dimethylsiloxane). They found that the primary stage takes place rapidly (a few minutes). The subsequent secondary stage was found to last several hours or even days.

CHAPTER 6 CONCLUSIONS

HYDROGENATED POLYMERS

These polymers were shown to consist of poly (ethylene) crystallites dispersed in a rubbery poly (butadiene) matrix. SAXS indicated that the crystallites are of random size and shape. It was also pointed out that chain folding is improbable, thus implying a fringed-micelle morphology.

Copolymerization by units rejected from the crystalline lattice led to crystallizable sequences, and thus crystallites, of varying length. The dependence of T_m , the copolymer melting point, on crystallite length was quantitatively demonstrated thus explaining the observation of broad melting ranges (greater than 100°K).

The melting points of these copolymers were found to be much higher than those of random copolymers of poly (ethylene). This was thought to be due to the non-random placement of co-units and/or non-random hydrogenation.

The rubbery modulus was calculated from the theory of rubber elasticity assuming that the crystallites act as crosslinks and filler particles. Discrepancies between the calculated values and experiment were proposed to be caused by the formation of more permanent entanglements in the rubbery matrix brought about by crystallization.

SILOXANE BLOCK COPOLYMERS

The morphology of the block copolymer was determined by SAXS

and dynamic mechanical properties. The benzene cast and moulded samples consisted of alternating lamellae of glassy, poly (α -methylstyrene) and rubbery poly (dimethylsiloxane) phases. These lamellae were preferentially oriented parallel to the sample faces, the moulded sample displaying the most orientation.

The cyclohexane cast sample was found to be non-lamellar and oriented so that the siloxane chains were more strained than in the other copolymer systems. When this sample was taken above the organic phase T_g , a marked morphological change occurred as a result of this strain.

A relaxation in the frequency plane was observed for the benzene cast and moulded systems at temperatures where rubbery behaviour was found. A lamellar slip mechanism was proposed and a single relaxation time model postulated. Preferentially swelling the siloxane phase of the benzene cast sample changed the relaxation in a predictable way. The model was also used to explain the temperature independence of the relaxation in the benzene cast system.

The presence of crystallinity in the siloxane phase complicated the dynamic modulus - and loss tangent - temperature curves. The two-step modulus-temperature curves normally encountered for two-phase amorphous systems were not present. Crystallinity was so high that the T_g process for the siloxane phase was almost masked and a large modulus drop (greater than an order of magnitude) was observed when melting occurred. Lower temperature melting peaks and lower degrees of crystallinity were observed for the copolymers when compared with crystallinity in the homopolymer. It was proposed

that this was the result of the presence of more strain in the copolymer siloxane chains due to the presence of crosslinks.

REFERENCES

1. D.S. Campbell, Paper presented at Conf. on New Flexible Polymers and Cross Links, London (Oct. 1972).
2. E.W. Duck, J.R. Hawkins and J.M. Locke, Paper presented at Conf. on Flexible Polymers and Cross Links, London (Oct. 1972).
3. E.W. Duck, J.R. Hawkins and J.M. Locke, Journal of the IRI, 6, No. 1 (1972).
4. S.L. Cooper and A. Tobolsky, Textile Res. J., 36, 800 (1966).
5. S.L. Cooper and A. Tobolsky, J. Appl. Polym. Sci., 10, 1837 (1966).
6. S.L. Cooper and A. Tobolsky, J. Appl. Polym. Sci., 11, 1361 (1967).
7. S.L. Cooper, D.S. Huh and W.J. Morris, I. & E. Chem. R. & D., 7, 248 (1968).
8. S. Bonotto and R.K. Walton, Mod. Plastics, 5, 143 (1963).
9. C.S. Schollenberg, U.S. Pat. 2,871,218 (January, 1959).
10. Polymer Age, 3, 177 (1972).
11. M. Brown and W.K. Witsiepe, Rubber Age, 35 (March, 1972).
12. R.M. Prosser and W.K. Witsiepe, Paper presented at Conf. on New Flexible Polymers and Cross Links, London (Oct., 1972).
13. W.H. Buck and R.J. Cella, Polymer Preprints, 14, 98 (1973).
14. J.T. Bailey, E.T. Bishop, W.R. Hendricks, G. Holden and N.R. Legge, Rubber Age, 98 69 (1966).
15. R.D. Deanin, S.P.E.J., 23, 45 (1967).

16. L.J. Fetters and M. Morton, *Macromolecules*, 2, 453 (1969).
17. G. Karoly, *Block Polymers*, ed. S.L. Aggarwal, Plenum Press, New York (1970), p.153.
18. M. Matzner, A. Noshay and J.E. McGrath, *Polymer Preprints*, 14, 68 (1973).
19. J.C. Saam, D.J. Gordon and S. Lindsey, *Macromolecules*, 3, 1 (1970).
20. J.W. Dean, *J. Polym. Sci.*, B8, 677 (1970).
21. W.G. Davies and D.P. Jones, *I. & E. Chem. Prod. Deve.*, 10, 168 (1971).
22. J.C. Saam and F.W.G. Fearon, *I. & E. Chem. Prod. Dev.*, 10, 10 (1971).
23. M.J. Owen and T.C. Kendrick, *Macromolecules*, 3, 458 (1970).
24. A. Noshay, M. Matzner, G. Karoly and G.B. Stampa, *J. Appl. Polym. Sci.*, 17, 619 (1973).
25. A. Noshay, M. Matzner and C.N. Merriam, *Polymer Preprints*, 12, 247 (1971).
26. A. Noshay, M. Matzner and C.N. Merriam, *J. Polym. Sci.*, A1, 9, 3147 (1971).
27. M. Matzner and A. Noshay, U.S. Pat. 3,579,607 (May 18, 1971).
28. M. Matzner, A. Noshay, L.M. Robeson, C.N. Merriam, R. Barclay and J.E. McGrath, NASA Conf. on Polymers for Unusual Service Conditions (Nov. 30, 1972).
29. R.P. Kambour, *op. cit.* ref. 17, p.263.
30. H.A. Vaughn, *J. Polym. Sci.*, B7, 569 (1969).
31. D.G. Le Grand, *J. Polym. Sci.*, B7, 579 (1969).

32. R.P. Kambour, *J. Polym. Sci.*, B7, 573 (1969).
33. D.G. Le Grand, *Trans. Soc. of Rheology*, 15, 541 (1971).
34. P.C. Juliano, U.S. Pat. 3,663,350 (May 16, 1972).
35. P.C. Juliano, D.E. Floryan, R.W. Hand and D.D. Karttunen, 19th Sagamore Conf. on Block and Graft Copolymers (Sept. 5-8, 1972).
36. J.V. Dawkins, Block Copolymers, ed. D.C. Allport and W.H. Janes, Applied Science, Bristol (1973), Ch. 8A and B.
37. M.J. Folkes and A. Keller, The Physics of Glassy Polymers, Applied Science, Barking, Essex (1973), Ch. 10.
38. G. Holden, Block and Graft Copolymerization, ed. R.J. Ceresa, Wiley - Interscience, Bristol (1973), Ch.6.
39. P.J. Flory, *Trans. Faraday Soc.*, 57, 829 (1961).
40. L.R.G. Treloar, The Physics of Rubber Elasticity, 2nd Ed., Clarendon Press, Oxford (1958).
41. L.R.G. Treloar, *Proc. Royal Soc. (London)*, B139, 506 (1952).
42. J.J. Aklonis, W.J. MacKnight and M. Shen, Introduction to Polymer Viscoelasticity, Wiley - Interscience, New York (1972).
43. J.D. Ferry, Viscoelastic Properties of Polymers, Wiley, New York (1961).
44. N.G. McCrum, B.E. Read and G. Williams, Anelastic and Dielectric Effects in Polymeric Solids, Wiley, Bristol (1967).
45. A.E.H. Love, A Treatise on the Mathematical Theory of Elasticity, 4th Ed., Cambridge University Press, New York (1927).

46. H. Lamb, Hydrodynamics, Dover, New York (1945).
47. L. Boltzmann, Prog. Ann. Erg., 7, 624 (1876).
48. B. Gross, Mathematical Structure of the Theories of Visco-elasticity, Hermann, Paris (1953).
49. H. Leaderman, Rheology - Theory and Applications, Ed. F. Eirich, Vol. II, Academic Press, New York (1958), Ch. 1.
50. H. Leaderman, Elastic and Creep Properties of Filamentous Materials, Textile Foundation, Washington (1943).
51. D.R. Bland, The Theory of Linear Viscoelasticity, Pergamon, London (1960).
52. E. Weichert, Ann. d. Phys., 50, 335 (1893).
53. J.J. Thomson, Applications of Dynamics to Physics and Chemistry, Macmillan, London (1888), Ch.8.
54. M.G.Sharma, Testing of Polymers, Vol. I, Ed. J. Schmitz, (1965), p. 148.
55. P.E. Rouse, J. Chem. Phys., 21, 123 (1956).
56. F. Bueche, J. Chem. Phys., 22, 603 (1954).
57. W.L. Peticolas, Rubber Chem. Tech., 36, 1422 (1963).
58. M. Shen, W.F. Hall and R.E. De Wames, Rubber Chem. Tech., 45, 638 (1972).
59. J.D. Ferry, R.F. Landel and M.L. Williams, J. Appl. Phys., 26, 359 (1955).
60. M.L. Williams, J. Polym. Sci., 62, 57 (1962).
61. A.V. Tobolsky and D.B. Dupre, Adv. Polym. Sci., 6, 103 (1969).
62. H. Leaderman, Textile Res. J., 11, 171 (1941).

63. A.V. Tobolsky and R.D. Andrews, *J. Chem. Phys.*, 11, 125 (1943); *J. Polym. Sci.*, 3, 669 (1948).
64. A.V. Tobolsky, *Properties and Structure of Polymers*, Wiley, New York (1960).
65. J.D. Ferry, *J. Am. Chem. Soc.*, 72, 3746 (1950).
66. J.D. Ferry, E.R. Fitzgerald, M.F. Johnson and L.D. Grandine, *J. Appl. Phys.*, 22, 717 (1951).
67. M.L. Williams, R.F. Landel and J.D. Ferry, *J. Am. Chem. Soc.*, 77, 3701 (1955).
68. E.R. Fitzgerald, L.D. Grandine and J.D. Ferry, *J. Appl. Phys.*, 24, 650 (1953).
69. L.D. Grandine and J.D. Ferry, *J. Appl. Phys.*, 24, 679 (1953).
70. M.L. Williams and J.D. Ferry, *J. Colloid Sci.*, 9, 479 (1954).
71. W.C. Child and J.D. Ferry, *J. Colloid Sci.*, 12, 327 (1957).
72. J.F. Beecher, L. Marker, R.D. Bradford and S.L. Aggarwal, *J. Polym. Sci.*, C26, 117 (1969).
73. G.L. Wilkes and R.S. Stein, *J. Polym. Sci.*, A2, 7, 1525 (1969).
74. T.L. Smith and R.A. Dickie, *J. Polym. Sci.*, C26, 163 (1969).
75. T.L. Smith, op. cit. ref. 17.
76. C.W. Childers and G. Kraus, *Rubber Chem. Tech.*, 40, 1183 (1967).
77. E. Fischer and J.F. Henderson, *J. Polym. Sci.*, C26, 149 (1969).
78. E. Fischer and J.F. Henderson, *Rubber Chem. Tech.*, 40, 1373 (1967).

79. M. Shen and D.H. Kaelble, J. Polym. Sci., E8, 149 (1970).
80. L. Mandelkern, Crystallization of Polymers, McGraw - Hill, New York (1964).
81. P.J. Flory, J. Chem. Phys., 17, 223 (1949).
82. J.D. Hoffman and J.J. Weeks, J. Res. NBS, 66A, 13 (1962).
83. P.J. Flory, Trans. Faraday Soc., 51, 848 (1955).
84. M.J. Richardson, P.J. Flory and J.B. Jackson, Polymer, 4, 221 (1963).
85. C.H. Baker and L. Mandelkern, Polymer, 7, 7 (1966).
86. C.H. Baker and L. Mandelkern, Polymer, 7, 71 (1966).
87. B. Lotz and A.J. Kovacs, Kolloid - Z., 209, 97 (1966).
88. B. Lotz, A.J. Kovacs, G.A. Bassett and A. Keller, Kolloid - Z., 209, 115 (1966).
89. M.H. Theil and L. Mandelkern, J. Polym. Sci., A-2, 8, 957 (1970).
90. J.H. Hildebrand and R.L. Scott, The Solubility of Non-Electrolytes, Reinhold, New York (1950).
91. S. Krause, J. Polym. Sci., A-2, 7, 249 (1969).
92. S. Krause, Macromolecules, 3, 84 (1970).
93. U. Bianchi, E. Pedemonte and A. Turturro, Polymer, 11, 268 (1970).
94. D.J. Meier, J. Polym. Sci., C26, 81 (1969).
95. D.F. Leary and M.C. Williams, J. Polym. Sci., B8, 335 (1970).
96. R.T. La Flair, IUPAC Symposium, Boston; published as supplement to Pure Appl. Chem., 8, 195 (1971).

97. D.J. Meier, *Polymer Preprints*, 11, 400 (1970).
98. H. Kromer, M. Hoffmann and G. Kampf, *Ber. Bunsenges, physik. Chem.*, 74, 859 (1970).
99. T. Inoue, T. Soen, T. Hashimoto and H. Kawai, *op. cit. ref.* 17, p.53.
100. D.G. Le Grand, *J. Polym. Sci.*, B8, 195 (1970).
101. T.G. Fox and P.J. Flory, *J. Appl. Phys.*, 21, 581 (1950).
102. M. Gordon and J.S. Taylor, *J. Appl. Chem.*, 2, 493 (1952).
103. M. Baer, *J. Polym. Sci.*, A-2, 417 (1964).
104. M.L. Miller, *Canad. J. Chem.*, 36, 309 (1958).
105. Y. Iwakura, Y. Taneda and S. Uchida, *J. Appl. Polym. Sci.*, 5, 108 (1961).
106. H. Smallwood, *J. Appl. Phys.*, 15, 758 (1944); *Rubb. Chem. Tech.*, 21, 667 (1948).
107. A. Einstein, *Ann. Physik*, 19, 289 (1906); 34, 1591 (1911).
108. J. Weiss, *Trans. Inst. Rubb. Ind.*, 18, 32 (1942).
109. H. Smallwood, *Rubb. Chem. Tech.*, 18, 892 (1945).
110. E. Guth and O. Gold, *Phys. Rev.*, 53, 322 (1938).
111. L. Cohan, *India Rubber World*, 117, 343 (1947); *Rubb. Chem. Tech.*, 23, 635 (1950).
112. E. Guth, *J. Appl. Phys.*, 16, 20 (1945); *Rubb. Chem. Tech.*, 18, 596 (1945); *Proc. Rubb. Tech. Conf. 2nd*, Heffer, London, 1948, p.353.
113. M. Takayanagi, H. Harima and Y. Iwata, *Memoirs of the Faculty of Engineering, Kyushu University*, 23 (1963).

114. M. Takayanagi, Proc. 4th International Congress on Rheology, Part I (1965), p.161.
115. T. Okamoto and M. Takayanagi, J. Appl. Polym. Sci., 23C, 597 (1968).
116. K. Fujino, Y. Ogawa and H. Kawai, J. Appl. Polym. Sci., 8, 2147 (1964).
117. A. Keller, E. Pedemonte and F.M. Willmouth, Kolloid Z. u. Z. Polymere, 238, 25 (1970).
118. M.J. Folkes and A. Keller, Polymer, 12, 222 (1971).
119. A. Keller, J. Dlugosz, M.J. Folkes, E. Pedemonte, F.P. Scalisi and F.M. Willmouth, J. de Phys., 32, C5a, 295 (1971).
120. P.R. Lewis and C. Price, Polymer, 12, 258 (1971).
121. W.R. Krigbaum, S. Yazgan and W.R. Tolbert, J. Polym. Sci., Polym. Phys. Ed., 11, 511 (1973).
122. J. Thomson, Proc. Phil. Soc. (Glasgow), 13, 464 (1882).
123. H. Benard, Rev. Gen. Sci. Pure Appl., 11, 1261, 1309 (1900); Ann. Chem. Phys., 23, 62 (1901).
124. J.R.A. Pearson, J. Fluid Mech., 4, 489 (1958).
125. I.M. Ward, Mechanical Properties of Solid Polymers, Wiley - Interscience, Bristol (1971), Ch.10.
126. M. Takayanagi, K. Imada and T. Kajiyama, J. Polym. Sci., C-15, 263 (1966).
127. Z.H. Stachurski and I.M. Ward, J. Polym. Sci., A-2, 6, 1083 (1969).
128. Z.H. Stachurski and I.M. Ward, J. Polym. Sci., A-2, 6, 1817 (1969).

129. Z.H. Stachurski and I.M. Ward, *J. Macromol. Sci.*, B3(3), 427 (1969).
130. Z.H. Stachurski and I.M. Ward, *J. Macromol. Sci.*, B3(3), 445 (1969).
131. A. Guinier and G. Fournet, Small-Angle Scattering of X-rays, Wiley, New York (1955).
132. D. Hosemann and S.N. Bagchi, Direct Analysis of Diffraction by Matter, Interscience, New York (1962).
133. O. Kratky, *Angew. Chem.*, 72, 467 (1960).
134. G. Porod, *Fortschr. Hochpolymer Forsch.*, 2, 363 (1961).
135. W.D. Statton, Newer Methods of Polymer Characterization, ed. B. Ke, Wiley, New York (1964), Ch.6.
136. L.E. Alexander, X-ray Diffraction Methods In Polymer Science, Wiley, New York (1969).
137. M. Kakudo and N. Kasai, X-ray Diffraction by Polymers, Kodansha, Tokyo (1972).
138. C.G. Vonk and G. Kortleve, *Kolloid - Z. u. Z. Polymere*, 220, 19 (1967).
139. G. Porod, *Kolloid - Z.*, 124, 83 (1951).
140. G. Porod, *Kolloid - Z.*, 125, 51 (1952).
141. P. Debye, H.R. Anderson and H. Brumberger, *J. Appl. Phys.*, 28, 679 (1957).
142. F.P. Warner, D.S. Brown and R.E. Wetton, *Polymer*, 13, 575 (1972).
143. V. Luzzatti, H. Mustacchi, A. Skoulios and F. Husson, *Acta Cryst.*, 13, 660 (1960).

144. F. Husson, H. Mustacchi and V. Iuzzatti, *Acta Cryst.*,
13, 668 (1960).
145. Op. cit. ref. 137, Ch. 10 and 14.
146. P.H. Hermans, Contribution to the Physics of Cellulose
Fibers, Elsevier, Amsterdam (1946).
147. Z.W. Wilchinsky, Advances in X-ray Analysis, Vol. 6,
Plenum Press, New York (1963).
148. W.G. Davies and D.P. Jones, *Polymer Preprints*, 447 (1970-71).
149. W.G. Davies, B. Elliott and T.C. Kendrick, U.S. Pat.
3,481,898.
150. E.E. Bostick, U.S. Pat. 3,483,270.
151. A.S. Tan, Ph.D. Thesis, University of Loughborough (1970).
152. R.E. Wetton, M.Sc. Thesis, University of Manchester (1960).
153. L.E. Nielsen, Mechanical Properties of Polymers, Reinhold,
New York (1964).
154. R.S. Rivlin and D.W. Saunders, *Transactions IRI*, 24,
295 (1949).
155. W.J. Read, *J. Appl. Mech.*, 17, 349 (1950).
156. ASTM D2236 - 27 (1970).
157. K. Schmieder and K. Wolf, *Kolloid - Z.*, 127, 65 (1952).
158. Op. cit. ref. 44, p. 140.
159. W.R. Krigbaum, R.J. Roe and K.J. Smith, *Polymer*, 5,
533 (1964).
160. G.W. Castellan, Physical Chemistry, Addison - Wesley,
Reading, Massachusetts (1964), pp. 127 and 165.

161. M.G. Broadhurst, J. Res. NBS, 67A, 233 (1963).
162. J.R. Richards, R.G. Mancke and J.D. Ferry, J. Polym. Sci.,
B2, 197 (1964).
163. Characterized by Dr. M. Cudby, ICI Plastics Div.
164. P.J. Holdsworth and A. Keller, J. Polym. Sci., 5B,
605 (1967).
165. P.J. Flory, J.B. Jackson, R. Chaing and M.J. Richardson,
Polymer, 4, 237 (1963).
166. P.R. Swann, J. Polym. Sci., 42, 525 (1960).
167. J.I. Lauritzen and ^{J.D.}Hoffman, J. Res. NBS, 64A, 73 (1960).
168. J.D. Hoffman and J.I. Lauritzen, J. Res. NBS, 65A, 297 (1961).
169. Average of values from references 165 and 170.
170. J.D. Hoffman, SPE Trans., Oct., 315 (1964).
171. M.J. Richardson, Trans. Faraday Soc., 61, 1876 (1965).
172. E.A. Cole and D.R. Holmes, J. Polym. Sci., 46, 147 (1960).
173. P.R. Swann, J. Polym. Sci., 56, 409 (1962).
174. L.E. Nielsen and F.D. Stockton, J. Polym. Sci., A1, 1995 (1963).
175. Op. cit. ref. 137, pp. 238 and 245.
176. N. Kasai and M. Kakudo, J. Polym. Sci., A2, 1955 (1964).
177. N. Kasai, M. Kakudo and T. Watase, Kogyu Kagaku Zasshi,
59, 786 (1956).
178. Op. cit. ref. 137, p. 405.
179. B.I. Tikhomirov, I.A. Klopotova and A.I. Yakubchik,
Eur. Polym. J. (Supplement), 561 (1969).
180. Op. cit. ref. 44, pp. 106 - 7.

181. Op. cit. ref. 43, p.33.
182. Hsiang - Shih and P.J. Flory, *Macromolecules*, 5, 758 (1972).
183. J.M.G. Cowie and P.M. Toporowski, *Eur. Polym. J.*, 5,
493 (1969).
184. J. Brandrup and E.H. Immergut, ed., Polymer Handbook,
Interscience, New York (1966), pp. IV 347 - 367.
185. A.K. Doolittle, *J. Appl. Phys.*, 22, 1471 (1951).
186. A.K. Doolittle, *J. Appl. Phys.*, 28, 901 (1957).
187. C.M. Huggins, L.E. St. Pierre and A.M. Bueche, *J. Phys. Chem.*,
64, 1304 (1960).
188. Yu. K. Godovskii, V. Yu. Levin, G.L. Slonimskii, A.A. Zhdanov
and K.A. Andrianov, *Polym. Sci. USSR*, 11, 2778 (1969).
189. S.M. Ohlberg, L.E. Alexander and E.L. Warrick, *J. Polym. Sci.*,
27, 1 (1958).
190. E.L. Warrick, *J. Polym. Sci.*, 27, 19 (1958).
191. J.M.G. Cowie and P.M. Toporowski, *Eur. Polym. J.*, 4, 621
(1968).
192. V.A. Moskalenko, V. Yu. Levin, D. Ya. Tsvankin, A.A. Zhdanov,
K.A. ANDrianov, G.L. Slonimskii and F.A. Galil - Ogly,
Polym. Sci. USSR, 13, 3017 (1971).
193. E.P. Goldberg, *J. Polym. Sci.*, C-4, 707 (1963).
194. S.H. Merrill, *J. Polym. Sci.*, 55, 343 (1961).
195. K.P. Perry, W.J. Jackson Jr. and J.R. Caldwell, *J. Appl.*
Polym. Sci., 9, 3451 (1965).

APPENDIX I

Derivation of Relationships For Wide Frequency Scanning Dynamic Mechanical Apparatus

Equation (3.1) describes the oscillatory motion of a rectangular beam undergoing bending deformation:

$$M\ddot{x} + kE^*x + Ax = F_p \exp(i\omega t) \quad (3.1)$$

Solving Equation (3.1) for x gives (52):

$$x = \frac{F_p \exp[i(\omega t - \beta)]}{\left[(kE' + A - M\omega^2)^2 + k^2 E''^2 \right]^{1/2}} \quad (A.1)$$

$$\text{where } \beta = \tan^{-1} \left[\frac{kE''}{kE' + A - M\omega^2} \right] \quad (A.2)$$

If only peak force (F_p) and peak amplitude (x_p) are considered, Equation (A.1) becomes:

$$\frac{F_p}{x_p} = \left[(kE' + A - M\omega^2)^2 + k^2 E''^2 \right]^{1/2} \quad (A.3)$$

Solving Equations (A.2) and (A.3) for E' and E'' gives:

$$E' = \frac{1}{k} \left(\frac{F_p}{x_p} \cos\beta - A + M\omega^2 \right) \quad (A.4)$$

$$E'' = \frac{1}{k} \left(\frac{F_p}{x_p} \sin\beta \right) \quad (A.5)$$

Next, it will be shown that F_p and x_p are functions of V_i and V_o , respectively, so that all quantities in Equations (A.4) and (A.5)

are experimentally measurable. V_o is proportional to x_p :

$$x_p = BV_o \quad (A.6)$$

where B is a constant of the transducer system. F_p is proportional to V_i :

$$F_p = NV_i \quad (A.7)$$

where N is a constant dependent on the strength of the magnet and the properties of the coil. Combining Equations (A.4) and (A.5) with Equations (A.6) and (A.7) and defining $C = \frac{N}{kB}$ gives E' and E'' in terms of measurable quantities:

$$E' = C \left(\frac{V_i \cos \beta}{V_o} \right) - \frac{A}{k} + \frac{M\omega^2}{k} \quad (A.8)$$

$$E'' = C \left(\frac{V_i \sin \beta}{V_o} \right) \quad (A.9)$$

$$\tan \delta = \frac{E''}{E'} \quad (A.10)$$

Equations (A.9) and (A.10) are identical to Equations (3.4) and (3.5), respectively.

At a certain frequency (ω_o), depending on the rigidity of the sample, the vibrating system will possess an amplitude resonance. With no sample mounted in the drive clamp the system will resonate at (ω_R). The suspension rigidity term (A) is related to ω_R by:

$$A = M\omega_R^2 \quad (A.11)$$

Combining Equations (A.8) and (A.11) gives Equation (3.3).

At ω_o , $V_o \gg V_i$ so that Equation (A.8) becomes:

$$E'_S = \frac{M}{k} (\omega_o^2 - \omega_R^2) \quad (\text{A.12})$$

where E'_S is the Young's modulus of the sample at ω_o . Since ω_o and ω_R can be measured very accurately, E'_S can be calculated.

At ω_o the loss tangent ($\tan \delta_o$) of the oscillating system is (153):

$$\tan \delta_o = \frac{\omega_1 - \omega_2}{\omega_o} \quad (\text{A.13})$$

where ω_1, ω_2 are the frequencies at which the amplitude of vibration is $\frac{1}{\sqrt{2}}$ times the maximum amplitude. The oscillating system includes the sample and the suspension wires. Thus:

$$\tan \delta_o = \frac{kE_S'' + A''}{kE_S' + A'} \quad (\text{A.14})$$

where kE_S'', A'' are the out of phase restoring forces per unit displacement of the sample and suspension wires at ω_o , respectively.

kE_S', A' are the elastic restoring forces per unit displacement of the sample and wires at ω_o , respectively.

Since,

$$A'' \ll kE_S''$$

and

$$kE_S' + A' = M\omega_o^2 \quad (\text{A.15})$$

therefore,

$$\tan \delta_o = \frac{kE_S''}{M\omega_o^2} \quad (\text{A.16})$$

From Equations (A.9) and (A.10), the loss tangent of the sample at resonance ($\tan \delta_S$) is:

$$\tan \delta_S = \frac{E_S''}{E_S'} = \frac{kE_S''}{M \omega_o^2 - \omega_R^2} \quad (\text{A.17})$$

Thus, combining Equations (A.16) and (A.17):

$$\tan \delta_S = \tan \delta_o \left(\frac{\omega_o^2}{\omega_o^2 - \omega_R^2} \right) \quad (\text{A.18})$$

Equations (3.6) and (3.7) are identical to Equations (A.12) and (A.18), respectively. Equation (3.8) results from the combination of Equations (A.10) and (A.18).

APPENDIX II

Calculating the Number of Co-units Per 100 Chain Carbons

The number of co-units per 100 chain carbons, for the hydrogenated polymers, was calculated as shown in the following illustration for Sample B1. Tables (3.1) and (3.2) show that for each 100 monomer units there are 9 vinyl, 3 styrene and 88 cis + trans units. This corresponds to 18 vinyl, 18 styrene and 352 cis + trans chain carbons or a total of 376 chain carbons. There are 97 butadiene monomers. Polymer B1 is 57% hydrogenated. Since all vinyl double bonds are hydrogenated prior to any cis or trans double bonds (179), all the remaining double bonds are in the chains. Thus, there are 9 hydrogenated vinyl, 3 styrene and $.43 (96) = 41$ chain double bonds acting as co-units. Therefore,

$$\frac{\text{No. co-units}}{100 \text{ chain carbons}} = \frac{53}{376} = 14.1$$

